

**FLOW ACCELERATED CORROSION IN  
SINGLE AND DUAL S-SHAPE BENDS  
UNDER SINGLE AND TWO PHASE  
ANNULAR FLOW CONDITIONS**

FLOW ACCELERATED CORROSION IN SINGLE AND  
DUAL S-SHAPE BENDS UNDER SINGLE AND TWO  
PHASE ANNULAR FLOW CONDITIONS

By

Hazem Mazhar, M. A. Sc., B. Sc.

A Thesis

Submitted to the School of Graduate Studies in Partial  
Fulfillment of the Requirements for the Degree of Doctor of  
Philosophy

McMaster University

© Copyright Hazem Mazhar, Sept. 2013

DOCTOR OF PHILOSOPHY (2013)  
MCMASTER UNIVERSITY  
MECHANICAL ENGINEERING  
HAMILTON, ONTARIO

TITLE: Flow Accelerated Corrosion in Single and  
Dual S- shape Bends under Single and  
Two Phase Flow Conditions

AUTHOR: Hazem Mazhar

SUPERVISOR: Professor\ Chan Ching  
Department of Mechanical Engineering

SUPERVISOR: Associate Professor\ James Cotton  
Department of Mechanical Engineering

Number of Pages xxi, 230



# **ABSTRACT**

---

Flow Accelerated Corrosion (*FAC*) is defined as a flow enhanced mass transfer phenomenon that results in pipe wall thinning of the piping system and results in abrupt failure in some cases. *FAC* is controlled by the transport of corrosion species from the wall to the bulk fluid and is determined by the local distribution of the mass transfer coefficient. The overall objective of this research is to investigate the mass transfer in pipe bends arranged in single and dual S- shape configurations under single and annular two phase flow conditions. A novel wall dissolving mass transfer technique was developed to measure the local mass transfer distribution under a Schmidt number ( $Sc$ ) of 1280, which mimics the level of carbon steel in water in industrial applications. Flow field measurements using Particle Image Velocimetry (*PIV*) and flow visualizations using laser induced fluorescence were performed to understand the causal relation between the mass transfer and the flow dynamics.

The mass transfer in single  $90^\circ$  bends under single phase flow was measured for a range of  $Re$  from 40,000 to 130,000. Three regions of elevated mass transfer rates were determined in the single bend, (i) near the inlet to the bend inner wall, (ii) midway on the bend inner wall sides and (iii) near the outlet of the bend outer wall. The maximum mass transfer enhancement relative to the upstream pipe was found to occur near the outlet of the single bend outer wall and spans over the first part of the downstream pipe with a magnitude of approximately 1.8. The surface roughness of the test sections were determined at the end of each experiment and found to be in the fully rough wall region.

The mass transfer coefficient at the high mass transfer locations was found to scale as  $Re^{0.92}$ . The maximum enhancement was found to be independent of  $Re$  for the range of  $Re$  studied here.

For the dual S- shape bends, tests were performed for different separation distances  $L/D$  of 0, 1 and 5. The  $L/D=0$  case were tested for a range of  $Re$  from 40,000 to 130,000. The maximum mass transfer enhancement relative to the upstream pipe was found to occur when there was no separation distance between the bends. This maximum occurred at the transition from the first bend outer wall to the second bend inner wall with a magnitude of approximately 3.2. The mass transfer enhancement was found to decrease when the separation distance between the two bends was increased. A second region of high mass transfer enhancement was found to occur midway on the second bend inner wall in the form of two symmetric regions shifted from the centerline with a magnitude of 2.8.

The effect of air and water superficial velocities for annular flow in the range of  $J_v= 22$ - $29.5$  m/s, and  $J_L= 0.17$ - $0.41$  m/s on the mass transfer in single and dual S- shape bends was determined. The maximum mass transfer was found to occur midway on the centerline of the bend outer wall for the single bend case. This location corresponded to the entrained liquid droplet impingement and anticipated high velocity region due to liquid film thinning. A second high mass transfer region was observed on the latter part of the bend outer wall. The effect of the air superficial velocity on the mass transfer enhancement was more significant than the effect of the water superficial velocity.

The maximum mass transfer enhancement in the S- shape bend geometry under annular two phase flow was found to always occur on the first bend outer wall at a similar location to the single bend case. The mass transfer in the second bend was lowest for the zero separation distance between the bends, and increased with an increase in the separation distance. The maximum mass transfer in the second bend occurred near the outlet of the second bend outer wall with a magnitude of approximately 60% of that in the first bend when the separation distance was zero. The maximum mass transfer in the second bend was found to increase with an increase in separation distance to reach approximately 85% of that in the first bend for  $L/D=40$ . The location of the maximum region was observed to shift in the upstream direction as the separation distance was increased to approach the location of the single bend maximum near  $L/D=40$ .

Flow field measurements showed matching of the areas with high mean flow velocity on the inlet portion of the single bend inner wall. The high velocity stream was observed to shift toward the outer wall near the bend outlet. Similar features were observed in the first bend of the S- shape configuration. The flow velocity increased significantly near the transition from the first bend outer wall to the second bend inner wall of the dual S-shape bend. High turbulent kinetic energy was measured near the outlet of the single bend outer wall and inner wall. Similar kinetic energy distribution was observed on the first bend of the S- shape. The turbulent kinetic energy downstream of the first bend increased to approximately twice that in the first bend and was observed to travel from the outlet of the first bend inner wall to the second bend inner wall. For two phase annular flow, the phase redistribution visualization showed liquid separation from the core flow and

deposition on the bend wall. Three locations of deposition were observed (a) on the first bend outer wall near  $\phi_1$  of  $50^\circ$ , (b) between the  $50^\circ$  and the outlet of the first bend (c) on the latter part of the second bend outer wall.

# **ACKNOWLEDGEMENTS**

No Words can really express how grateful the author is to those who have contributed to the success of this work. The author would like to express his gratitude toward his supervisors Dr. Chan Ching and Dr. James Cotton for their guidance and support throughout the course of this Ph.D. program which have proved to be invaluable. The author is also grateful to other members of the supervisory committee, Dr. Tullis and Dr. Kish for their valuable suggestions and comments during the course of the study.

Gratitude is also extended to the technicians Mr. Ron Lodewyks, Mr. Mark Mackenzie, Mr. Jim McLaren, Mr. Joe Verhaeghe, JP Talon, and Mr. Michael Lee for their patient help and technical advice. The author would like to express great appreciation to Dr. Ewing, Dr. Sadek and Dr. El Gammal for their technical and personal support.

My accomplishment wouldn't have been possible without the support and love of my family and friends, especially my wife Dina, whose love and understanding and patience have been the source of my energy during the course of this work.

# **TABLE OF CONTENTS**

---

<b>Abstract</b>	v
<b>Acknowledgement</b>	viii
<b>Table of contents</b>	ix
<b>List of figures</b>	xiii
<b>List of tables</b>	xxi
<b>1 Introduction</b>	<b>1</b>
1.1 Motivation	1
1.2 Objectives	2
1.3 Scope of work	3
1.4 Thesis outline	6
1.5 A note to the reader	7
<b>2 Literature review</b>	<b>8</b>
2.1 Introduction	8
2.2 Flow Accelerated Corrosion	8
2.3 Mass transfer	10
2.3.1 Mass transfer measurement methods	10
2.3.2 Mass transfer in straight pipes	13
2.3.3 Mass transfer in bends under single phase flow	15
2.3.4 Mass transfer in bends under two phase flow	18
2.4 Flow characteristics in bends	20
2.4.1 Flow characteristic for single phase flow	20

2.4.2	Flow characteristics for two phase flow	24
2.5	Research motivation	30
<b>3</b>	<b>Experimental investigation of mass transfer in 90° pipe bends using a dissolvable wall technique</b>	<b>31</b>
	Abstract	32
3.1	Introduction	33
3.2	Experimental facility and experimental methodology	36
3.3	Mass transfer in single 90° bends	43
3.4	Roughness analysis	51
3.5	Summary and conclusion	55
3.6	References	56
<b>4</b>	<b>Mass transfer in dual pipe bends arranged in an S-configuration</b>	<b>62</b>
	Abstract	63
4.1	Introduction	64
4.2	Experimental facility	67
4.3	Results and discussion	73
4.4	Effect of Reynolds number	83
4.5	Roughness discussion	84
4.6	Conclusions	91
4.7	References	92
<b>5</b>	<b>Flow field characteristics in single and dual S- shape 90° bends</b>	<b>95</b>
	Abstract	95

5.1 Introduction	96
5.2 Experimental facility and methodology	98
5.3 Results and discussion	104
5.4 Conclusions	114
5.5 References	115
<b>6 Mass transfer in single bends under annular two phase flow conditions</b>	<b>118</b>
Abstract	119
6.1 Introduction	120
6.2 Experimental facility and methodology	123
6.3 Results and discussion	129
6.4 Conclusions	141
6.5 References	142
<b>7 Mass transfer in S-shape dual pipe bends under annular two phase flow conditions</b>	<b>144</b>
Abstract	145
7.1 Introduction	146
7.2 Experimental methodology	149
7.3 Results and discussion	155
7.4 Flow visualization	164
7.5 Conclusions	171
7.6 References	171
<b>8 Summary and Conclusions</b>	<b>177</b>

8.1 Thesis summary	177
8.2 Conclusions	179
8.2.1 Mass transfer in single and S- shape bends under single phase flow	179
8.2.2 Mass transfer in single and dual bends under annular two phase flow	181
8.3 Research contributions	179
8.4 Recommendations for future work	180
<b>Appendix A: Uncertainty analysis</b>	<b>183</b>
<b>Appendix B: Material properties</b>	<b>188</b>
<b>Appendix C: Comparison of single and two phase mass transfer</b>	<b>195</b>
<b>Appendix D: Processing Matlab routines</b>	<b>199</b>
<b>References</b>	<b>221</b>

# **LIST OF FIGURES**

---

2.1: Surface morphology change with increase in Reynolds number (a) $2 \times 10^5$ (b) $7 \times 10^4$ (c) $3 \times 10^4$	<b>14</b>
2.2: FAC examples of copper models 180° bend single-phase flow	<b>16</b>
2.3: FAC examples of copper models 180° bend two-phase annular flow	<b>20</b>
2.4: Secondary flow structure generated by the bend geometry	<b>22</b>
2.5: Secondary flow structure generated by the bend geometry $Re=5000$	<b>22</b>
2.6: flow pattern in U shaped pipe under different flow regimes	<b>27</b>
2.7: Proposed phase redistribution model for a) gas core flow pattern, (b) liquid film and entrainment flow pattern	<b>28</b>
2.8: Sequence of images showing frequent detachment of R134a liquid film from the inner wall	<b>29</b>
3.1: Schematic of the test facility showing the main components of the flow loop	<b>38</b>
3.2: Schematic of the test section showing the sections plane relative to, (a) streamwise orientation (b) crosswise orientation	<b>38</b>
3.3: Stream wise Sherwood number profiles along the centerline for (a) outer wall (b) inner wall of the bend section at $Re=70,000$ , $Sc=1280$ .	<b>43</b>
3.4: Typical mass transfer distribution over the entire single bend test section. (a) outer wall side view and (b) inner wall side view, measured for $Re=70,000$ , $Sc=1280$	<b>44</b>
3.5: Profiles of $Sh/Sh_{pipe}$ along the (a) outer wall side and (b) inner wall side of the bend. plotted along the centerline.	<b>46</b>

3.6: Azimuthal profiles of $Sh/Sh_{pipe}$ along the streamwise direction along the bend curvature for a) bend outer wall side, b) bend inner wall side for $Re$ of $\nabla$ 40,000, $\square$ 60,000, $\circ$ 70,000, $\blacktriangleleft$ 100,000, $\blacklozenge$ 130,000	<b>47</b>
3.7: Physical images of the test sections showing the inner wall side, at Reynolds numbers of a) $Re=40,000$ , b) $Re=60,000$ and c) $Re=130,000$	<b>49</b>
3.8: Variation of the local maximum Sherwood number with Reynolds number, $-\cdot-$ $0.005 Re Sc^{0.33}$ [11], $- -$ $0.007 Re^{0.96} Sc^{0.33}$ [13], $\dots$ $0.0165 Re^{0.86} Sc^{0.33}$ [10], $—$ $0.01 Re^1 Sc^{0.33}$ [2]	<b>50</b>
3.9: Variation of mass transfer enhancement in the bend compared with existing data for the same radius of curvature ( $r/D=1.5$ ) and different Schmidt numbers	<b>50</b>
3.10: Relative roughness pattern in the upstream pipe for $Re=40,000$ , (a) 2-d roughness height pattern (b) Spatial distribution of the roughness undulations from the physical sample scan	<b>52</b>
3.11: Development of average relative roughness with time in the upstream pipe at $Re=70,000$	<b>53</b>
3.12: Variation of the roughness evaluated based on the peak to valley at the upstream pipe, inlet to bend inner wall and at the outlet of the bend outer wall with different Reynolds numbers	<b>54</b>
3.13: Variation of the roughness scale in the upstream pipe with Reynolds number	<b>54</b>
4.1: Schematic of the test facility showing the main components of the flow loop	<b>68</b>
4.2: Schematic of the test section showing the section planes relative to (a) streamwise orientation (b) crosswise orientation in the first bend (c) crosswise orientation in the second bend	<b>69</b>
4.3: Local Sherwood number distribution at $Re=70,000$ and $Sc=1280$ for separation distances of $L/D= 0, 1$ and $5$ , arranged from left to right. (a) Side view consisting of the	

first bend outer wall and second bend inner wall (b) Side view consisting of the first bend inner wall and second bend outer wall	<b>75</b>
4.4: Scan images of the test sections for separation distances of (a) $L/D=0$ (b) $L/D=1$ (c) $L/D=5$ for the two test section sides (i) consisting first bend outer wall and second bend inner wall (ii) consisting first bend inner wall and second bend outer wall	<b>77</b>
4.5: Profiles of $Sh/Sh_{pipe}$ along the (a) first bend outer wall and second bend inner wall (b) first bend inner wall and second bend outer wall	<b>79</b>
4.6: Azimuthal profiles of $Sh/Sh_{pipe}$ at different locations along the dual bend profile for separation distances of $0D$ , $1D$ and $5D$ , arranged from left to right	<b>81</b>
4.7: Variation of peak mass transfer enhancement $Sh_{peak}/Sh_{pipe}$ separation distance	<b>83</b>
4.8: Azimuthal profiles of $Sh/Sh_{pipe}$ along the streamwise direction along the bend for $L/D=0$ at $Re$ of $\blacksquare$ 40,000, $\bullet$ 60,000, $\blacktriangleleft$ 70,000, $\blacktriangledown$ 100,000, $\blacklozenge$ 130,000	<b>86</b>
4.9: Variation of the local maximum Sherwood number with Reynolds number, $\text{---} 0.01 Re Sc^{0.33}$ , $\text{-- --} Re^{0.92}$ , $\text{---} \cdot 0.0165 Re^{0.86} Sc^{0.33}$ , $\text{.....} 0.007 Re^{0.96} Sc^{0.33}$	<b>87</b>
4.10: Variation of mass transfer enhancement in the S- bend compared with existing data for a single bend ( $r/D=1.5$ ) and U- bend ( $r/D=2.5$ ).	<b>87</b>
4.11: Relative roughness distribution contours for separation distances of (a) $L/D = 0$ (b) 1 (c) 5 for (i) first bend outer wall and second bend inner wall (ii) first bend inner wall and second bend outer wall	<b>89</b>
4.12: Variation of the relative roughness at different locations along the bend for the different separation distances ( $L/D$ ).	<b>90</b>
4.13: Variation of the relative roughness at the upstream pipe, inlet to bend inner wall and at the outlet of the bend outer wall with Reynolds numbers for $L/D=0$ .	<b>90</b>

5.1: The main components of the test facility, (a) schematic of the main components of the flow loop (b) schematic and picture of the <i>PIV</i> setup	<b>101</b>
5.2: Schematic of the test section showing the section planes relative to (a) streamwise orientation (b) crosswise orientation in the first bend (c) crosswise orientation in the second bend	<b>102</b>
5.3: Velocity profiles in the upstream pipe, (a) comparison of profiles at different locations with, (b) comparison of the profile from the two sides of the pipe (Symmetry check)	<b>105</b>
5.4: Velocity field in single bend (a) contour along symmetry plane (b) normalized velocity profiles at different angular locations for ◉ Re=40,000, ▶ Re=70,000	<b>106</b>
5.5: Turbulent kinetic energy distribution in single bend (a) T.K.E contour at midplane (b) cross sectional profiles of T.K.E for ◉ Re=40,000, ▶ Re=70,000	<b>108</b>
5.6: Velocity field in the S- shape dual bends (a) T.K.E contour at midplane (b) cross sectional profiles of T.K.E for ◉ Re=40,000, ▶ Re=70,000	<b>110</b>
5.7: Crosssectional velocity contours at different location along the S-shape bend curvature for Re=70,000	<b>112</b>
5.8: Turbulent kinetic energy distribution in the S- shape dual bends (a) T.K.E contour at midplane (b) cross sectional profiles of T.K.E for ◉ Re=40,000, ▶ Re=70,000	<b>113</b>
6.1: Schematic of the test facility showing the main components of the flow loop	<b>125</b>
6.2: Schematic of the test section showing the section planes relative to (a) streamwise orientation (b) crosswise orientation	<b>125</b>
6.3: Comparison of the (a) mass removal and (b) mass transfer coefficient for different initial water bulk concentrations for $J_v=24.5$ and $J_L=0.28$ m/s	<b>130</b>

6.4: Effect of (a) water velocity and (b) air velocity on the Sherwood number distribution in the $90^\circ$ bend with a radius of $1.5D$ under annular flow conditions, (a) $J_v \sim 29.0$ m/s, $J_L = 0.18, 0.28$ and $0.41$ m/s, (b) $J_L = 0.28$ m/s, $J_v = 22, 24.5$ and $29.5$ m/s	<b>131</b>
6.5: Streamwise Sherwood number profiles along the (a) outer wall and (b) inner wall for $J_L = 0.28$ m/s and different $J_v$ .	<b>133</b>
6.6: Streamwise Sherwood number profiles along the (a) outer wall and (b) inner wall for $J_v \sim 29.0$ m/s and different $J_L$ .	<b>134</b>
6.7: Azimuthal profiles of the Sherwood number for $J_L = 0.28$ m/s and $J_v = 29.5$ m/s (—), $24.5$ m/s (— →), $22$ m/s (.....).	<b>137</b>
6.8: Azimuthal profiles of the Sherwood number for $J_v = 29.5$ m/s and $J_L = 0.41$ m/s (—), $0.28$ m/s (— →), $0.18$ m/s (.....).	<b>138</b>
6.9: Effect of air and water superficial velocities on the mass transfer enhancement over straight pipe ( $Sh/Sh_{pipe}$ ) for different annular flow conditions, (a) at the first peak, compared with [11] results, (b) at the secondary peak. Note: Numbers in bold represent the current results	<b>140</b>
7.1: Schematic showing the principle components of the test facility	<b>152</b>
7.2: Schematic of the test section showing the section planes relative to (a) streamwise orientation (b) crosswise orientation in the first bend (c) crosswise orientation in the second bend	<b>152</b>
7.3: Mass transfer distribution in the S-shape dual bend at $L/D$ from 0 to 40 for (a) first bend outer (b) second bend outer for $J_v = 29$ m/s and $J_L = 0.28$ m/s and $Sc = 1280$	<b>157</b>
7.4: Profiles of Sherwood number along the centerline of (a) first bend outer (b) second bend inner wall (c) first bend inner wall and (d) second bend outer wall.	<b>159</b>

7.5: Azimuthal profiles of $Sh$ at different locations along the bend curvature for separation distances of $L/D$ of — 0, - - -1, .....5, — . -10, - - - 20, — 40, ∇ Single bend	<b>161</b>
7.6: Effect of separation distance $L/D$ on (a) maximum enhancement factor and (b) location of maximum enhancement in first and second bend.	<b>163</b>
7.7: Mass transfer distribution in S dual bend with change in (a) air superficial velocity for $J_V = 29, 24.5$ and $22$ m/s and $J_L=0.28$ m/s (b) water superficial velocity for $J_L = 0.17, 0.28$ and $0.41$ m/s and $J_V\sim 29$ m/s for $L/D=0$ .	<b>164</b>
7.8: Azimuthal Sherwood profiles with change in (a) air superficial velocity for $J_V = 29, 24.5$ and $22$ m/s and $J_L=0.28$ m/s (b) water superficial velocity for $J_L = 0.18, 0.28$ and $41$ m/s and $J_V\sim 29$ m/s, for $L/D=0$ .	<b>166</b>
7.9: Variation of mass transfer enhancement for the different annular flow conditions for (a) first bend and (b) second bend	<b>167</b>
7.10: Different realizations of the phase redistribution at (a) the first bend (b) cross section near the outlet of the first bend and (c) at second bend, using laser induced fluorescence for $J_V=29$ m/s and $J_L=0.28$ m/s	<b>169</b>
7.11: Schematic of (a) the proposed model for the phase redistribution depicted from flow visualization in contrast with physical images of the surface topography for (b) first bend outer wall and second bend inner wall and (c) first bend inner wall and second bend outer wall	<b>170</b>
8.1: Schematic of the dual bend with different angular orientations	<b>185</b>
B.1: Material composition analysis (sample C)	<b>192</b>
B.2: Material composition analysis (sample A)	<b>193</b>

B.3: Material composition analysis (sample B)	<b>194</b>
B.4: SEM microscopic image of the gypsum cast micro structure dendrites with magnifications of (a) 500x (b) 1000x (c) 2000x	<b>196</b>
B.5: Calibration of the water electrical conductivity variation with dissolution	<b>197</b>
C.1: Test conditions located on the two phase flow map	<b>200</b>
C.2: Comparison of the mass transfer coefficient for single and two phase flow in a straight pipe	<b>202</b>

# **LIST OF TABLES**

---

2.1: Geometries investigated using electrochemical methods	<b>12</b>
2.2: Summary of the mass transfer correlations for fully developed pipes	<b>14</b>
2.3: Summary of the mass transfer correlations for bends	<b>17</b>
3.1: Nomenclature of quantities and terms	<b>39</b>
4.1: Nomenclature of quantities and terms	<b>71</b>
5.1: Nomenclature of quantities and terms	<b>103</b>
6.1: Uncertainty in flow conditions	<b>123</b>
6.2: Factors affecting total uncertainty	<b>123</b>
6.3: Experimental test conditions	<b>123</b>
6.4: Nomenclature of quantities and terms	<b>126</b>
7.1: Nomenclature of quantities and terms	<b>152</b>
A.1: Recording parameters	<b>189</b>
B.1: Summary of the different material constituents from different random samples	<b>195</b>
C.1: Test matrix and void fractions estimated based on Martinelli's Model [25]	<b>199</b>

# CHAPTER 1

---

## Introduction

### 1.1. Motivation

The tragic accident in 1986 at the nuclear power station “Surry-USA” brought attention to Flow Accelerated Corrosion (*FAC*). A rupture in one of the condensate system bends resulted in four fatalities and costly repairs and lost revenue (Dooley, 1997). The rupture was attributed to *FAC*., which is a serious safety and reliability problem facing aging power generation plants, especially nuclear power plants (*NPP*). *FAC* is a slow piping degradation process caused by the flowing fluid damaging or thinning the protective layer of piping components. This phenomenon results in severe wear and thinning of large areas of piping and fittings that can lead to sudden and catastrophic failures. There are two mechanisms responsible for *FAC*: (i) an electrochemical process known as corrosion that depends on the chemistry of the flowing fluid and its conditions resulting in a thin porous oxide layer, and (ii) removal of the oxide layer by diffusion to the adjacent moving fluid. This process continues to occur leading to the thinning and failure of the piping component. The thinning rate and therefore the component life time is dependent on the mass transfer which is primarily dependent on the flow hydrodynamics within the piping component.

Pipe degradation can be caused by *FAC* or Erosion Corrosion (*EC*) wear. In *FAC* the removal of the oxide layer is by diffusion of mass to the flow, while in Erosion-Corrosion it is due to the

effect of the mechanical surface stresses, (e.g. shear stresses) created by the moving fluid (Robinson, 1999) that is able to produce surface wear. In many cases the two phenomena can take place at the same time, especially in two phase flow. However, in *FAC* the mass transfer is the rate limiting factor for pipe wall thinning (Poulson, 1988). There have been numerous studies of *FAC* and the parameters affecting *FAC*, because of the economic importance and safety considerations of the phenomena. Most studies focused on the water chemistry, such as the effect of the *PH* level of the flowing water on the rate of corrosion and the control of mass transfer through the *PH* level (Dooley, 1997). There have been fewer studies on the role of hydrodynamics in *FAC*.

## 1.2. Objectives

The flow hydrodynamics can affect the mass transfer distribution and in turn the *FAC*. The objective of the current study is to investigate the effect of flow hydrodynamics on the mass transfer in pipe bends. The specific objectives are;

1. To develop a mass transfer measurement technique taking into account the surface development under high Schmidt number ( $Sc$ )
2. To investigate the detailed mass transfer distribution in single  $90^\circ$  bends under single and two phase annular flow conditions
3. To investigate the effect of separation distance between two bends arranged in a back to back S-configuration configuration on the mass transfer enhancement and distribution under single and two phase flow conditions

4. To characterize the flow field in single and back to back S-configuration bends using Particle Image Velocimetry (*PIV*) measurements
5. To characterize the two phase redistribution in single and back to back bends under annular flow conditions through flow visualization using Laser Induced Fluorescence (*LIF*)
6. To elicit the responsible mechanisms for mass transfer enhancement for single and annular two phase flow conditions

### **1.3. Scope of the work**

The collection of articles composing this thesis represents the first experimental study of local mass transfer in short radius single and dual S-shape bends using dissolving wall methods. The study examines the effect of Reynolds number, for Re range of 40,000 to 130,000, on the mass transfer distribution and the peak mass transfer enhancement. In addition, the current investigation studied the effect of different annular two phase flow conditions on the mass transfer distribution. The effect of the separation distance between the bends in the dual S-shape configuration was also investigated under single and two phase flow conditions.

#### **1.3.1. Experimental investigation of mass transfer in 90 degree pipe bends using a dissolvable wall technique**

The mass transfer in single 90° bends and the effect of Reynolds number on the mass transfer is presented in this article. Experiments were performed in the fully rough wall region for Reynolds number in the range 40,000 to 130,000. The mass transfer at the peak locations scaled with

Reynolds number as  $Re^{0.92}$ . The maximum mass transfer enhancement, relative to the upstream pipe, was found to be independent of Reynolds number. The relative roughness was observed to decrease with Reynolds number.

### **1.3.2. Mass transfer in dual pipe bends arranged in an S-configuration**

The second article examines the mass transfer in S- shape dual bend. In particular the effect of the separation distance between the dual bends and Reynolds number on the mass transfer distribution was determined. The maximum mass transfer enhancement is found to occur when there is no separation distance between the bends with a magnitude of 3.2 over straight pipe. The enhancement decreased as the separation distance was increased. The Reynolds number exponent scaling was found to be similar to that in the single bend case.

### **1.3.3. Flow field characteristics in single and S-shape dual bends under single phase flow**

The flow field measurements in single and dual S- shape bends are discussed here. Particle Image Velocimetry (*PIV*) measurements were performed in different planes in the test section to understand the flow field characteristics and correlate it to the mass transfer distributions. Areas of high mean and secondary flow velocities were found to correspond to those of high mass transfer. High turbulent kinetic energy regions are found to correspond to high mass transfer at

some locations and low mass transfer in other locations. Highest mean flow velocity is observed near the inlet to the second bend inner wall in the S- shape dual bend case which corresponds to the highest mass transfer location.

#### **1.3.4. Mass transfer in Single bends under annular two phase flow conditions**

This article focuses on the mass transfer in single  $90^\circ$  bends under annular two phase air-water flow conditions. The location of the maximum mass transfer is found to agree with existing predictions in the literature. The air and water superficial velocities were varied to investigate the effect of each on the maximum mass transfer enhancement. The mass transfer was found to change significantly with the air superficial velocity; however, the water superficial velocity effect was not insignificant.

#### **1.3.5. Mass Transfer in S-shape dual pipe bends under annular two phase flow conditions**

The effect of annular two phase flow conditions on mass transfer in S- shape dual bends is presented here. The effect of separation distance between the bend on the mass transfer pattern and distribution is also discussed in this article. The maximum mass transfer is found to always occur in the first bend under all separation and all annular flow conditions. The mass transfer pattern in the second bend was significantly different to that in the first bend. Flow visualization

using laser induced fluorescence was performed to correlate the mass transfer pattern to the two phase redistribution within the bend.

#### **1.4. Thesis outline**

This thesis is made up of five journal articles outlined previously that comprise the results section of the thesis along with other supplementary chapters which provide a survey of related literature and context for the research, as well as conclusions and recommendations. Chapter 2 provides a more comprehensive overview of past studies in the area of flow accelerated corrosion and flow dynamics and mass transfer in bends. Chapter three contains the first journal article titled “Experimental investigation of mass transfer in 90° pipe bends using a dissolvable wall technique” which presents the mass transfer measurement methodology and application to measurements in a single 90° bend. Chapter four is the journal article titled “Mass transfer in dual pipe bends arranged in an S-configuration” which presents the results of the mass transfer in dual bends arranged in an S- configuration. The third journal article titled “Flow field characteristics in single and dual S- shape 90° bends“ is presented in chapter five. This chapter addresses the correlation of the flow field distribution and the mass transfer topography in single and dual S- bends. The journal article titled ”Mass transfer in single bends under annular two phase flow conditions” is presented as chapter six. This article focuses on the mass transfer in a single 90° bend for a range of annular two phase air-water flow conditions. The article titled “Mass transfer in dual S- Shape bends under annular two phase flow conditions” is the seventh and final results chapter. The mass transfer in dual bends arranged in an S- configuration for different separation distances and different annular flow conditions are presented in this chapter.

The correlation of the mass transfer topography to the phase redistribution obtained from Laser Induced Fluorescence (*LIF*) visualization is also presented here. The conclusions and recommendations for future work are presented in chapter 8. It also includes a list of the contributions to the current state of knowledge. Appendix A provides an analysis of the uncertainty of the experimental measurements performed during the course of this thesis. Appendix B provides information about the properties of the material used to perform the experiments and material contents. Appendix C presents a comparison of the mass transfer coefficient for single and annular two phase flow. Appendix D outlines the main Matlab data reduction routines used to obtain mass transfer coefficients.

## **1.5. A note to the Reader**

As a result of the editorial requirements of publishing a series of separate journal articles, there is some overlap of material contained in this thesis. In particular, the sections of each journal article pertaining to the experimental facility and measurement methodology contain significant repetition. The literature review sections of each article also contain similar material. However, each of these review sections is targeted, and does contain more specific references related to the work presented in each paper. In addition, the experimental methodology applied in the current research is described in each article but is less detailed after the first article. Finally, the conclusions reached in Chapter 8 are a summary of the conclusions contained of the five articles.

# **CHAPTER 2**

---

## **Literature Review**

### **2.1. Introduction**

This section of the thesis provides a comprehensive review of the relevant studies in the literature on Flow Accelerated Corrosion, and flow and mass transfer in pipe bends. The literature reviewed in each journal article is relatively brief to fit the publication requirements. To provide more insight and greater context to the work performed in this thesis, a more detailed literature review is presented in this section. The literature is broadly divided into: (i) a review of factors affecting Flow Accelerated Corrosion, (ii) mass transfer in pipe bends under single phase and two phase flows.

### **2.2. Flow Accelerated Corrosion**

Flow accelerated corrosion (*FAC*) is affected by a complex interplay between several factors, such as the flow chemistry, material properties, flow conditions (single and two phase) and the flow hydrodynamics. The available information on *FAC* rates are mostly based on industrial observations and statistical studies of pipe wall thinning inspections. Numerous experimental studies on *FAC* were focused on the cycle chemistry (Dooley, 1997). The flow chemistry such as

the *PH* level in the water affects the rate of the electrochemical corrosion process and so affects the *FAC* process. The water *PH* level can be optimized for minimum *FAC* rate (Dooley, 1997). Corrosion inhibitors such as chromates and nitrites at high concentrations which act as passive inhibitors have been tested and proven to limit the rate of *FAC* (Postlethwaite, 1979). Several studies addressed the effect of the material properties (Dooley, 1997). The addition of a very small percentage [ $<1\%$ ] of chromium to the carbon steel resulted in drastic reductions in the rate of *FAC*; however, this is more suitable for newly designed plants (Elliot, 2004), since the piping components in older plants have predominantly carbon steel pipe with variable unknown Chromium content. Computer codes were developed based on this data as well as the plant inspection data to predict the most susceptible areas and develop plans for inspection; however, *FAC* is still not reliably predicted and can cause abrupt and severe damage to piping components (Pietralik 2008)

*FAC* is classified as piping degradation resulting from mass dissolution of the wall protective corrosion layer and is limited by the wall mass transfer rates. Although flow hydrodynamics plays an important role in the mass transfer rate and thus *FAC*, very few investigations have been devoted to study its effects on *FAC*. Among the different flow parameters, *FAC* is found to be dependent on:

- a) Mean flow velocity and shear stress near the wall, which affects the boundary layer and mass removal rate.
- b) Turbulence intensity; which is reported to significantly affect *FAC* in both single and two phase flows as it enhances mixing and transport rates between the wall layer and bulk flow (Poulson, 1999).

The effect of turbulence intensity is still unclear since it was reported to reach a peak at intermediate  $Re$  where the  $FAC$  continues to increase (Poulson, 1993).

Repeated Nuclear Power Plant inspections around the world have shown that piping components located downstream of pipe singularities, such as sudden expansion/contractions, orifices, valves and bends are most prone to  $FAC$ . This is attributed to the severe changes in flow direction as well as the development of secondary flow instabilities downstream of these singularities (Chen et. al, 2006). Pipe bends, of interest here, are arguably one of the most common components in piping systems exhibiting  $FAC$  problems, and are the principal focus of this study. There have been only a few studies of mass transfer in pipe bends under single phase flows. There is even less research to understand the mass transfer under two phase flow conditions. In order to understand the mass transfer in bends, the flow dynamics under single and two phase flows in bends are also reviewed.

## **2.3. Mass transfer**

### **2.3.1. Mass transfer measurement methods**

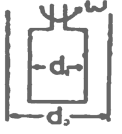
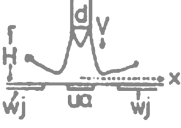
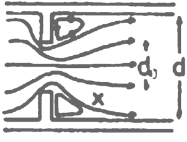
The mass transfer is represented by the non-dimensional Sherwood number ( $Sh$ ) which is a function of Reynolds number ( $Re$ ) and Schmidt number ( $Sc$ ). Mass transfer can be obtained from either analogy with heat transfer or through experimental measurements which are typically performed using electrochemical methods or dissolving wall methods. The Chilton - Colburn analogy has been used to relate heat and mass transfer data as summarized by Coney (1980). Despite the similarity of the two phenomena, mass transfer results in a change in the surface morphology which in turn changes the mass transfer rates and results in discrepancies between

the heat and mass transport rates (Poulson, 1988). The other key drawback is the difference in the ratio of the thickness of the boundary layers. Heat transfer experiments are usually performed at Prandtl numbers ( $Pr$ ) less than about 10, while for mass transfer the Schmidt number ( $Sc$ ) is typically in the range 100 to 3000 (Poulson, 1986).

Electrochemical methods, known as the limiting current density technique ( $LCDT$ ), have been used to measure mass transfer in different geometries (Poulson, 1983). Among the different geometries that have been studied are rotating disc, rotating cylinder, impinging jet, straight pipe and downstream of an orifice. The mass transfer correlations developed in these studies are listed in Table 2.1. The applicability of the  $LCDT$  technique is limited to simple geometries as a uniform distribution of the applied current is a prerequisite for the success of this technique, which is difficult to attain in complex geometries. In addition this technique doesn't allow for surface development to mimic some practical mass transfer applications.

Dissolving wall methods using sections made of or coated with a dissolvable material in some specific solution have been used to measure mass transfer. Typical material-fluid combinations were Transcinnamic acid in Water, Benzoic acid in Glycerin/Water mixtures (Poulson 1988), Naphthalene in Air (Sparrow et. al, 1986) and Plaster of Paris in water. Wilkin et. al. (1983) utilized the dissolution of Plaster of Paris in water to investigate the mass transfer in straight pipes and in  $90^\circ$  bends. Test sections were cast out of Plaster of Paris with water as the working fluid. The dissolution rate of Calcium Sulfate ( $CaSO_4$ ) into water is higher than the transport by diffusion into the bulk solution (Raines and Dewers, 1997), thus it provides diffusion controlled mass transfer environment. Since the mass transfer in steel pipes is also considered to be a transport controlled phenomenon, the dissolution of Calcium Sulfate in water was used to mimic

**Table 2.1: Geometries investigated using electrochemical methods- adapted (Poulson 1983)**

Rotating discs		$Sh_{smooth}=0.6205 Re^{0.5} Sc^{0.33}$	Levich (1962)
		$Sh_{rough}=0.0078 Re^{0.9} Sc^{0.33}$	Mohr (1976)
Rotating cylinder		$Sh_{smooth}=0.079 Re^{0.7} Sc^{0.356}$	Eisenberg (1954)
		$Sh_{rough}=[1.25+5.76*\log(d/\epsilon)]^{0.7} Re Sc^{0.356}$	Kappesser (1971)
Impinging Jet		$Sh_{UA}=1.12 Re^{0.5} Sc^{0.33}(H/d)^{0.51}$ $Sh_{WJ}=0.65 Re^{0.84} (x/d)^{-1.2}$	Tsang (1978) Trass (1976)
Nozzle or Orifice		$Sh_{max}=0.27 Re^{0.67} Sc^{0.33}$	Coney (1980)
		$Sh_x/Sh_{pipe}=1+A_x[1+B_x(Re^{0.66}/0.0165*Re^{0.86}-21)]$ Where: $A_x, B_x$ are constants, depend on distance from the orifice	
		$Sh_{max}=0.286 Re^{0.65} Sc^{0.33}$	Poulson (1986)
Straigh pipe		$Sh_{smooth}=0.0165 Re^{0.86} Sc^{0.33}$	Berger (1977)
		$Sh_{smooth}=0.026 Re^{0.82} Sc^{0.33}$	Poulson (1986)
		$Sh_{rough}=0.02 Re^{0.9} Sc^{0.33}$	Wilkin (1983)

*FAC*. The surface of Plaster of Paris was found to reach a quasi-steady roughness pattern in a short period of time (Blumberg 1970). The roughness pattern obtained with Plaster of Paris was found to be similar to that observed in steel pipes in industrial applications, (Pietralik 2012).

### **2.3.2. Mass transfer in straight pipes**

Numerous studies have been performed to measure the mass transfer in straight pipes. Some of the obtained mass transfer correlations are summarized in table 2.2. The mass transfer process is always accompanied with a change in the surface roughness of the test specimen and thus a change in the mass transfer rate. The roughness scale is a function of the Reynolds number of the flow, as shown in figure 2.1. The increase in the roughness scale results in an increase in the mass transfer coefficient ( $Sh$ ) until it reaches the fully rough region where the  $Sh$  becomes independent of the roughness scale and follows a constant Reynolds number exponent (Dawson and Trass, 1972). The  $Sh$  for a fully rough pipe is found to be 2 to 4 times the mass transfer rate for smooth pipes (Postlethwaite and Lotz, 1988). Dawson and Trass (1972) investigated the effect of surface roughness on the development of both the hydrodynamic and mass transfer profiles under different relative roughness ( $e/D$ ) and Schmidt number ( $Sc$ ). Generally, for  $Sc > 1$  the Reynolds number required for surfaces to be considered fully rough from the hydrodynamic point of view is larger than that required for them to be considered fully rough from the diffusion point of view and becomes even greater with increasing  $Sc$ . Above a certain Reynolds number, referred to as critical Reynolds number, the wall is considered fully rough and the mass transfer coefficient is found to be independent of the roughness height  $e/D$  (Dawson and Trass, 1972). The dimensionless roughness scale  $e^+$  at which

**Table 2.2: Summary of the mass transfer correlations for fully developed pipes**

Smooth wall	$Sh_{\text{smooth}}=0.0165 Re^{0.86} Sc^{0.33}$	Berger (1977)
Smooth wall	$Sh_{\text{smooth}}=0.026 Re^{0.82} Sc^{0.33}$	Poulson (1986)
Rough wall	$Sh_{\text{rough}}=0.02 Re^{0.9} Sc^{0.33}$	Wilkin (1983)
Rough wall	$Sh_{\text{rough}}=0.005 Re Sc^{0.33}$	Blumberg (1970)
Rough wall	$Sh_{\text{rough}}=0.007 Re^{0.96} Sc^{0.33}$	Postlethwaite and Lotz (1988)

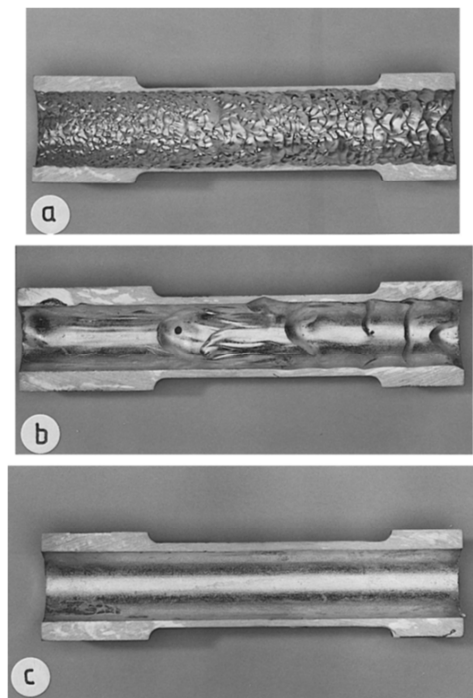


**Figure 2.1: Surface morphology change with increase in Reynolds number (a)  $2 \times 10^5$  (b)  $7 \times 10^4$  (c)  $3 \times 10^4$  (Poulson, 1993)**

straight pipes are considered fully rough is found to be approximately 10 to 30 (Dawson and Trass, 1972, Postlethwaite and Lotz, 1988).

### 2.3.3. Mass transfer in bends under single phase flow

The mass transfer in bends is affected by a number of factors including the bend radius relative to the pipe diameter ( $r/D$ ), angle of curvature ( $\Phi$ ), flow Reynolds number ( $Re$ ) and Schmidt number ( $Sc$ ). Mass transfer studies on long radius bends (Coney, 1980, Wilkin et. al, 1983) and short radius bends (Achenbach 1976) and (Sparrow and Chrysler, 1986) have been performed under turbulent flow conditions. The results are in agreement on the location and shape of the peak mass transfer regions, with the maximum mass transfer occurring near the outlet of the bend outer wall. The enhancement was reported to increase as  $r/D$  was decreased, which was attributed to the fact that increasing the bend acuteness would result in higher turbulence levels and in turn higher mass transfer.

The angle of curvature of the bend affects the development of the swirling flow structure and consequently the mass transfer enhancement. The effect of the bend angle of curvature on mass transfer was studied by Sprague et. al (1985) for bend angles of  $45^\circ$ ,  $90^\circ$  and  $180^\circ$  with an  $r/D = 2.72$ . The location of the maximum mass transfer was found to be midway through the bend on the outer wall for the  $45^\circ$  and  $90^\circ$  bends, and on the outer wall near the exit for the  $180^\circ$  bend.

Poulson (1988) investigated the mass transfer in  $180^\circ$  bends using *LCDT*, as shown in figure 2.2. The wear topology was in the form of crosswise traces directed toward the midline. In this study, the bends were manufactured from straight copper tubing resulting in significant geometry changes and variations in wall thickness during the bending process.

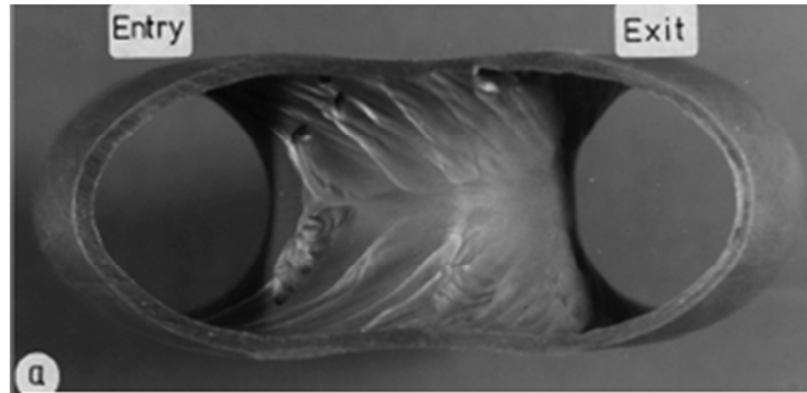


**Figure 2.2: FAC examples of copper models 180° bend single-phase flow - Poulson (1988)**

In this study, tests were run until pipe wall failure occurred. The overall mass transfer rate was determined by measuring the pipe weight before and after the test. The local mass transfer was evaluated by ultrasonic wall thickness measurements, especially at the failure locations. However, failure at a specific location may be due to the initial pipe wall thickness at this location and not because of a high local mass transfer level.

The transition to a fully rough wall, where the  $Sh$  becomes independent of roughness height, was found to occur at approximately  $Re=30,000$  for the 180° bend and at  $Re=50,000$  for the 45° bend (Sprague, 1985). The scaling of the  $Sh$  with  $Re$  was investigated by few studies as summarized in table 2.3. The average  $Sh$  over the entire bend section for  $r/D=8$  was found to scale as  $Re^{0.925}$  (Wilkin et. al, 1983), while the  $Sh$  at the peak location for short radius bends ( $r/D=1.5$ ) was found to scale as  $Re^{0.84}$  (Achenbach, 1976). The  $Sh$  at the peak location for long radius 180° bends ( $r/D$  of 2.5 and 7.3) was reported by Poulson (1993) to scale as  $Re^{0.86}$  for the smooth wall case and  $Re^1$  for the rough wall case.

**Table 2.3: Summary of the mass transfer correlations for bends**

Smooth wall (mass deposition)	$Sh_{\text{peak}}=0.018 Re^{0.84} Sc^{0.4}$	(Single bend)	Achenbach (1976)
Rough wall (mass removal)	$Sh_{\text{average}}=0.00923 Re^{0.925} Sc^{0.33}$	(Single bend)	Wilkin (1983)
Smooth wall (mass removal)	$Sh_{\text{peak}}=0.01 Re^1 Sc^{0.33}$	(U- shape dual bend)	Poulson (1988)
Rough wall (mass removal)	$Sh_{\text{peak}}=0.028 Re^{0.86} Sc^{0.33}$	(U- shape dual bend)	Poulson (1988)

The scaling of the mass transfer enhancement, defined as the local Sherwood number relative to that in a fully developed pipe for the same flow condition, with Reynolds number has been studied (Poulson, 1988, Coney, 1980, Wang and Shirazi 2001). There is a discrepancy in the results from the different studies since the mass transfer was normalized using either numerical, smooth or rough wall results. The enhancement was found to be independent of Reynolds number when normalized by the smooth wall results (Poulson, 1988) and (Coney, 1980) and scaled as  $0.71Re^{0.12}$  for the rough wall results (Poulson, 1988). An inverse scaling with Reynolds numbers was reported by Wang and Shirazi (2001) using numerical results. In bends, the Sherwood number scales with Reynolds number with a higher exponent than that of straight pipes. Therefore, the enhancement scaling with Reynolds number is expected to increase or at least remain constant with Reynolds number, which are contrary to the numerical results.

Computational studies have been performed on single bend under single phase flow conditions (Homicz, 2004). This study was oriented toward the prediction of *FAC* in pipe bends. The *RNG*- $(K-\epsilon)$  model was used, but was not coupled to the mass transfer equations. The mass transfer was

claimed to correlate only to the mean shear stress distribution with minor effect for turbulence kinetic energy. However, the effect of turbulent kinetic energy is found to be as important as the shear stress (Poulson, 1993). El-Gammal et. al (2010) performed numerical simulations on single bends using (*RSM*) turbulence model and standard wall functions for the near-wall zone. There were some discrepancies between the mass transfer predicted by simulations and those from experimental data, especially in the separation regions. This can be attributed to the difficulty of resolving the near wall region, especially for the diffusion boundary layer. Two locations of high mass transfer were reported: (i) near the inlet to the bend inner wall and (ii) near the outlet of the bend outer wall for a  $73^\circ$  bend, (Pietralik, 2013). In this study, the mass transfer obtained from numerical simulations was in good agreement in the pattern and locations of the maxima obtained from the industrial measurement.

#### **2.3.4. Mass transfer in bends under two phase flow**

Two phase liquid – gas flows are more frequent in power generation applications, where it usually occurs at high temperatures. *FAC* is usually higher in two phase flow than single phase flows (Dooley 1997). The high *FAC* level under two phase high temperature flow can be attributed to the decrease in the boundary layer thickness which results in an increase in the mass transfer in addition to the effect of liquid deposition and bubble entrainment which promote the turbulence level. The comparison of mass transfer in straight pipes under annular two phase flow and single phase flow at an equivalent surface shear stress yielded an enhancement of 1- 1.6 for the two phase flow over single phase flow (Poulson, 1991). The mass transfer enhancement for slug two phase flow relative to single phase flow at similar Reynolds number was reported to be approximately 3 times (Wang et. al, 2002). This enhancement was attributed to the effect of the

entrained bubbles and the effect of liquid slugs on enhancing the near wall turbulence and thus mass transfer.

The mass transfer in bends under liquid-gas two phase flow was found to increase with an increase in the void fraction due to the significant effect of the phase redistribution (Pecherkin, 2011). Thus, *FAC* studies were mostly focused on annular two phase flow conditions. The mass transfer in a 180° bend under a range of annular flow conditions was studied by (Poulson, 1991). The location of maximum wear, which corresponds to maximum local mass transfer rate, was found at approximately 45° to 50° from the bend inlet on the outer wall side as shown in figure 2.3. The mass transfer maximum was attributed to the effect of entrained droplet impingement on the bend outer wall. Mass transfer by erosion in Plaster test sections was reported by Poulson 1991 for gas superficial velocity of 60 to 70 m/s. The droplets impingement is reported to have significant effect on erosion without any film as is the case in mist flow systems (Malloy et. al, 2013). In the case of annular flow with sufficient film thickness the film tends to play a cushioning role in attenuating the effect of the impinging droplet on the mass transfer. The gas velocity threshold above which erosion contributes to the mass transfer is identified by Deffenbaugh and Buckingham (1989) and Hatori (2010) to be in the range of 70 to 125 m/s. The air superficial velocity had a significant effect on the mass transfer but the role of the water velocity is unclear in the results of (Poulson, 1991), showing it had a minor effect on the mass transfer (Koshizuk, 2010). The location of the maximum mass transfer along the bend is found to depend on the bend tightness ( $r/D$ ) and a correlation was proposed by Poulson (1991), to predict the location. The maximum mass transfer was found to move downstream when the radius of curvature of the bend was reduced. Numerical simulation of two phase flow is

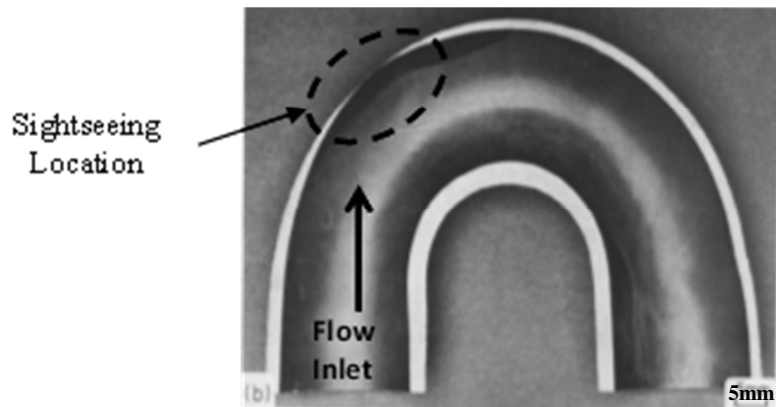


**Figure 2.3: FAC examples of copper models 180° bend two-phase annular flow**

**(Reproduced from Poulson, 1991)**

significantly more challenging than for single phase flows. One of these challenges is to accurately capture the discontinuous interfacial phenomenon, which may result in complex flow patterns and scales.

## **2.4. Flow characteristics in bends:**

### **2.4.1. Flow characteristic for single phase flow**

The flow in bends is significantly different to that in straight pipes since the flow is subjected to significant change in the flow direction, which due to centrifugal forces leads to the development of secondary flows, and flow separation. Weske et. al (1948) reported the flow dynamics in a sharp 90° bend under turbulent flow. The flow in sharp bends is affected by centrifugal forces that move the flow toward the outside radius through the center region of the flow. The pressure gradient due to this centrifugal force drives the flow again toward the inner radius. These two flows form double counter rotating vortices within the cross section of the bend, as shown schematically in figure 2.4. Meanwhile, the adverse pressure gradient along the inner radius may

lead to flow reversal and separation from the wall. The dynamics of the double counter rotating vortices is highly sensitive to the upstream conditions. Similar flow features were observed by Dean (1928) under laminar flow conditions.

Weske et. al (1948) reported shedding of the separation bubble downstream of the bend. However, this shedding was mainly driven by the acute  $90^\circ$  angle of the bend interior radius. Similar swirling vortices oscillation was reported by Tunstall and Harvey (1968). Rütten et. al (2005) performed large eddy simulations of flow in  $90^\circ$  bends and observed flow unsteadiness which they termed the “swirl switching” phenomenon that occurs within the bend curvature and lead to shedding of the separation bubble downstream of the bend exit, as shown in figure 2.5. The inlet flow condition in this study was unsteady sinusoidal velocity upstream of the bend inlet. The secondary flow structure is quite sensitive to the upstream condition (Weske, 1948); therefore the reported flow unsteadiness in the bend and its downstream may have been initiated by the entrance sinusoidal flow velocity distribution. The secondary flows induce a pressure drop along the bend that can significantly increase the wall mean and oscillatory shear stresses as well as the oscillatory pressure loads along the bend wall (Hassan, 1998). The secondary flows can also promote turbulence close to the wall and thus enhance the rate of mass transfer at the wall (Chen, 2006; Poulson, 1999).

The flow in dual bends is more complex than in single bends, due to the interaction of the flow dynamics within the two bends (Taylor et. al, 1984). This interaction in different dual bend orientations, e.g. U-, out of plane- and S- configurations, were studied by several investigators.

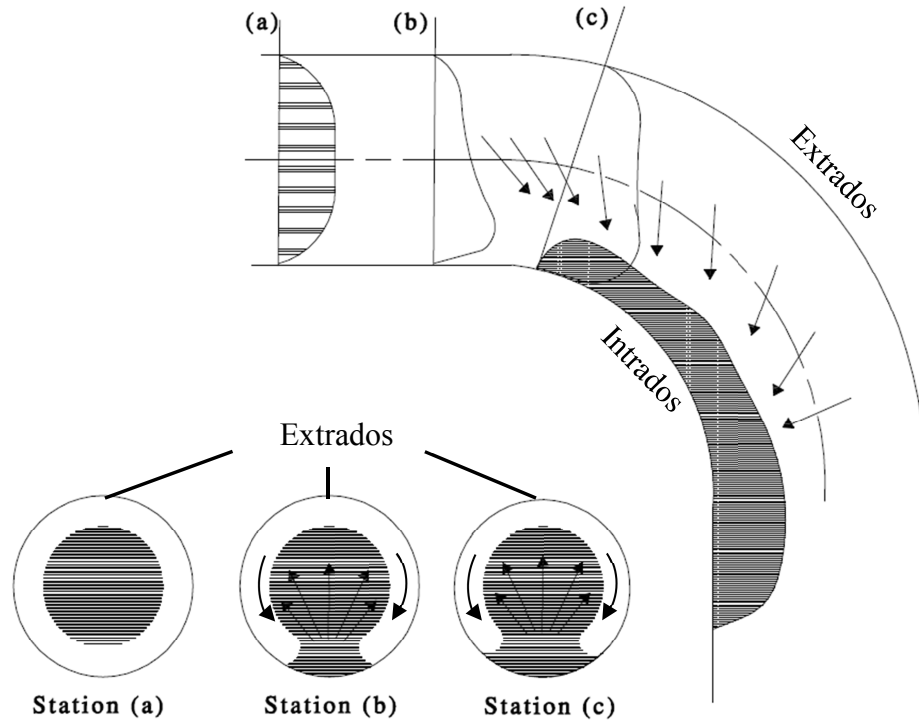


**Figure 2.4: Secondary flow structure generated by the bend geometry, (reproduced, Weske (1948))**

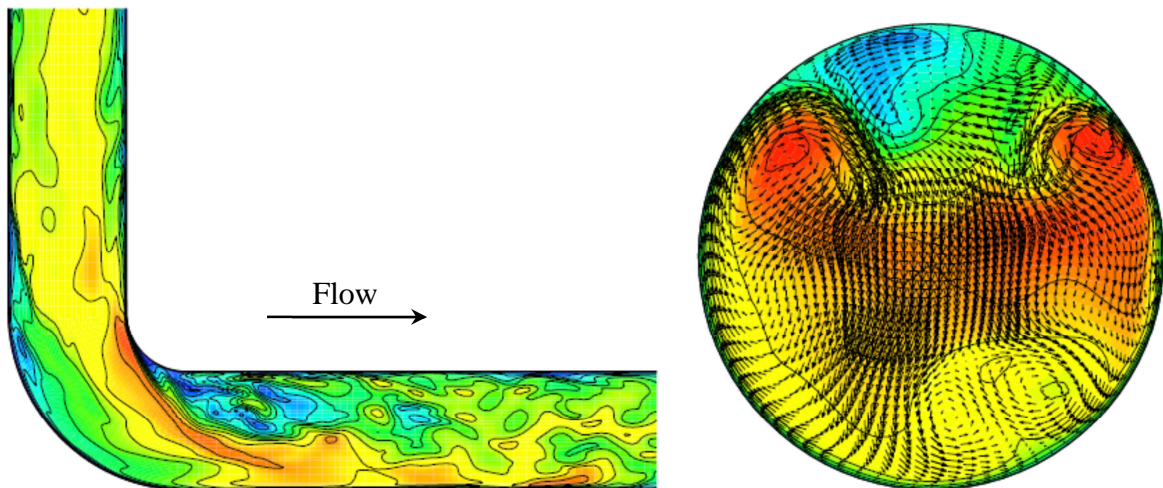


**Figure 2.5: Secondary flow structure generated by the bend geometry  $Re=5000$ , Rutten et. al (2001)**

The highest turbulence level and pressure drop was observed for the S- shape configuration compared to the U and out of plane dual bend configurations for turbulent flow conditions (Rudolf and Desova, 2007). This is likely due to the superimposition of the two acceleration motions, one due to shift of the high velocity core from the first bend inner wall to the outer wall near the inlet and another due to the acceleration on the second bend inner wall near the inlet.

The curvature direction of the bends is the same in the U- shape and partially the same in the out of plane configurations, which develops another pair of vortices in the same direction of the first bend vortices and allows for quicker velocity field recovery compared to the S configuration. Twin vortices are generated within the first bend of the S configuration, similar to that in a single bend. These are stretched along the curvature, decreasing in diameter and increasing in strength. Similar secondary flows are developed within the second bend, but in the opposite direction; the strength of the secondary flow in each bend will determine the prevailing flow structure in the entire S dual bend. The strength of these swirls will depend on the angle of curvature of each bend. Small angles of curvature resulted in suppression of the swirling structure in the second bend since the curvature is not large enough for the second bend to recover from the first swirl and develop its secondary vortices, for the case of laminar flow (Taylor et. al, 1984; Niazmand and Jaghargh, 2010). In this case two pairs of swirls turning in opposite directions were observed in the second bend and downstream of the dual bends. Very large angles could result in very strong vortices in the second bend that can diminish the intensity of vortices in the first bend. In dual 90° S-shape bends, the second bend could generate secondary structures that are able to overcome those generated in the first bend (Doorly and Sherwin, 2009). The effect of separation distance between the S- dual bends on the turbulence level was investigated by Yoshida et. al

(2008). The average turbulence level measured at several locations downstream of an S shape dual bend configuration is found to decrease with increasing separation distance from 0 to 1 diameter. The flow velocity field was found to be oscillating non-symmetrically in the cross section downstream of the dual bend shape. This asymmetry was attributed to the undeveloped flow admitted at the inlet to the S-bend.

#### **2.4.2. Flow characteristics for two phase flow**

Since the annular two phase flow is one of the most common flow regimes in power plant applications and is more prone to mass transfer and *FAC* as discussed in the preceding section, this section will be mainly focused on the dynamics of annular flows. Depending on the flow velocity of the liquid and gas constituents of the two phase flow, different flow regimes are obtained. The main gas liquid two phase flow regimes in a horizontal piping system (Taitel and Duckler, 1976) are:

**Bubbly flow:** high liquid flow rates and relatively small air flow rates usually results in numerous discrete bubbles in the continuous liquid stream.

**Slug flow:** increasing gas void fraction bubbles collide and coalesce and form larger gas voids which are comparable in dimension to the pipe diameter. These masses of gas voids are separated by slugs of liquid.

**Wavy flow:** for further increase in gas flow rate and void fraction, stratified flow forms where the bottom side of the pipe contains the liquid and the top side contains the gas flow. The gas tends to drag the surface of the liquid phase resulting in waviness in most cases and in this case the flow regime is called stratified wavy.

**Annular flow:** relatively high gas velocity results in high interfacial shear; once this shear force supersedes the gravity effect, the liquid is expelled from the core of the pipe toward the walls forming a film of liquid while the high velocity gas is flowing in the core region. Liquid entrainment and deposition between the film and the gas continuously occur resulting in entrained droplets of liquid in the gas core. The high velocity air core tends to create waviness in the liquid which in addition to the droplets deposition results in high turbulence level in the liquid film.

The hydrodynamics of two-phase liquid-gas flows in bends is more complex than in single-phase flows (Kim, 2007). This is because of the phase redistribution and the complex interactions between the gas phase and the liquid turbulence structures (Crawford, 2007). The latter mechanism plays a major role in the mass, momentum, and energy transfer between the two phases (Kim, 2007). The two-phase inlet flow regime will affect the phase redistribution and in turn affect the flow dynamics within the bends. For example, bubbles can significantly affect the turbulent kinetic energy close to the wall, affecting the wall shear stress and pressure. Jepson (1989) showed that high velocity slugs can cause high turbulence and shear forces at the pipe wall and thus enhance the destruction of the protective inhibitor film on pipe walls.

Studies on two phase flows in pipe bends were primarily devoted to understand the phase redistribution and evaluate the associated pressure drop along the bend curvature. Two phase air-water flows in different regimes, bubbly, stratified, plug and slug flows were investigated in a U shaped bend in different orientations (Usui, 1980). The redistribution of the two phases was correlated to the interaction between the gravity and centripetal forces. The development length for annular flow is significantly affected by the existence of pipe bends in the flow stream. For

flow through straight pipe, the entrance length is reported to be approximately 30 diameters by (Zhao et. al, 2013). The development length required downstream of a U- shape dual bend is reported to be longer than 30 pipe diameters which was the maximum length for the experiments by De Kerpel (2011) and more than 141 diameters by Da Silva Lima (2010). This could be due to the drastic two phase redistribution in bends, where most of the liquid phase collects on one side of the bend.

A modified Froude number ( $Fr_\phi$ ), representing the ratio of the centripetal forces at any angle along the bend to the radial component of the gravitational force at this location, equation 2.1, was used to combine the significance of each force and decide on the resulting flow pattern and phase redistribution (Usui, 1980).

$$Fr_\phi = \frac{V_{L\phi}^2}{\frac{\rho_L - \rho_G}{\rho_L} R_{L\phi} g |\cos \Phi|} \left[ 1 - \frac{\rho_G V_{G\phi}^2 R_{L\phi}}{\rho_L V_{L\phi}^2 R_{G\phi}} \right] \quad \dots \dots \dots \quad 2.1$$

The effect of the different flow patterns on the redistribution was reported as follows, figure 2.6:

- (a) Bubbly flow: the centrifugal force pushes the liquid phase toward the extrados and keeps the small percentage of the gaseous phase on the intrados side.
- (b) Stratified flow: the gravitational force moves the slow liquid phase toward the intrados on the downstream part of the bend.
- (c) Plug flow region: the tail part of the liquid plug becomes unstable.
- (d) Slug flow: flow reversal and flooding were observed, especially when a formed water slug is expelled by air flow.
- (e) Wavy flow: the centrifugal force was the major parameter in this regime. The liquid phase was pushed outward to the extrados and maintains the gas phase on the intrados.

- (f) Annular flow: Relatively stable flow was observed. The flow forms uniform rings around the axis of the bend cross section. The gravity effect is opposed by centripetal force and results in the uniform ring pattern.

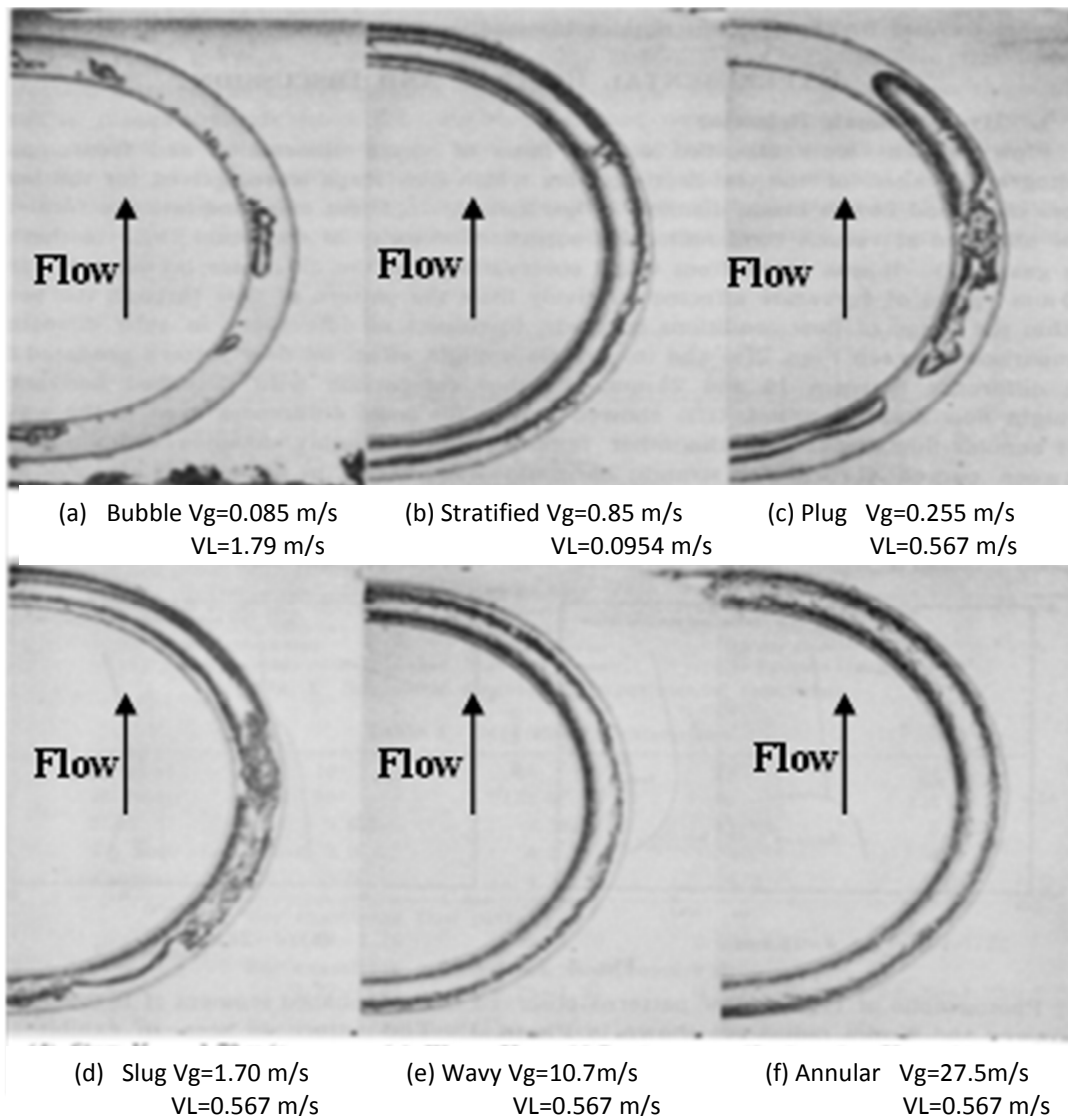


**Figure 2.6: Flow pattern in U shaped pipe under different flow regimes (Usui, 1980)**

In the case of annular two phase flow through horizontal bends, the gas flow in this case tends to follow similar swirling flow patterns to the single phase discussed above as proposed in the gas core region (Maddock et. al, 1974), figure 2.7. The entrained droplet in the upstream flow tends to deposit on the outer wall side near the sight seen location, where the upstream pipe centerline intersect with the bend outer wall. Liquid film collects on the outer wall after the location of the droplet deposition. Liquid re-entrainment on the latter part of the bend inner wall and deposition on the bend outer wall was observed. Frequent detachment of the liquid film from the bend inner wall is reported by Da Silva Lima and Thome (2012) as shown in figure 2.8.

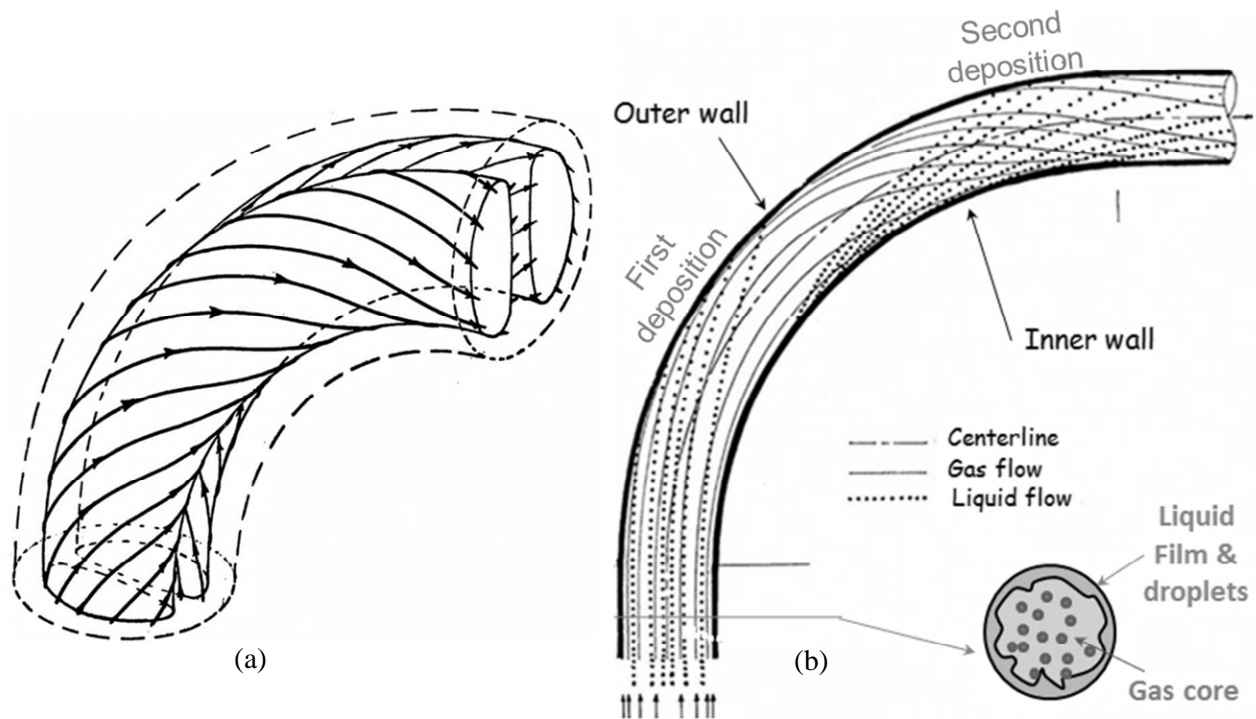


**Figure 2.7: Proposed phase redistribution model for a) gas core flow pattern, (b) liquid film and entrainment flow pattern, (Reproduced-Maddock et. al 1974)**

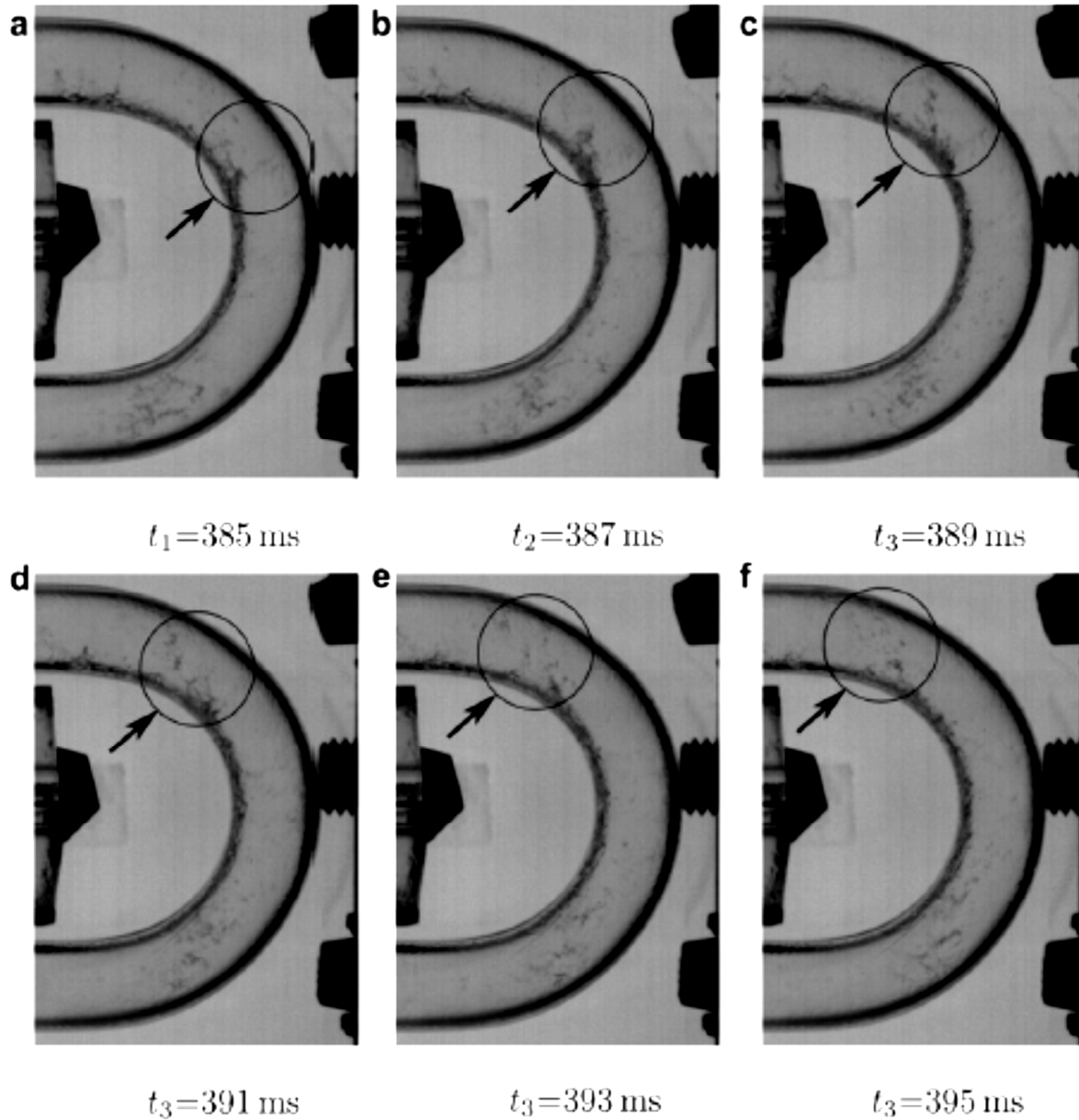


**Figure 2.8: Sequence of images showing frequent detachment of R134a liquid film from the inner wall (Da Silva Lima and Thome 2012)**

## 2.5. Research motivation

Despite the research done on the cycle chemistry to control *FAC* rates, the phenomenon is poorly understood. Mass transfer is the rate limiting process in the *FAC* phenomenon. The effect of flow hydrodynamics on mass transfer has received relatively little attention as shown in the preceding literature review. In particular, studies on mass transfer in pipe bends under high Schmidt number are very limited. The mass transfer in dual bends, which are common components in piping systems, has not been investigated previously. Pipe bends exist in piping systems in different configurations such as single, dual S-, U-, and out of plane configurations. Since these piping geometries represent a major component in most power generation plants, there is a strong incentive to further investigate this phenomenon. The single and dual S-shape bend configurations are the focus of this study. The results of the current research will eventually be utilized to develop and improve prediction tools for the *FAC* phenomenon in order to accurately and reliably predict the life time of the different piping geometries in power plants. Geometry factors based on the mass transfer enhancement factors in the critical areas, identified in the current research program, will be implemented in the component life time prediction codes to limit the risk of the phenomenon and also reduce the unnecessary frequent costly inspections on the entire plant connections and potentially avoid serious accidents.

## **CHAPTER 3**

---

### **Experimental investigation of mass transfer in 90° pipe bends using a dissolvable wall technique**

#### **Complete citation:**

H. Mazhar, D. Ewing, J. S. Cotton, C. Y. Ching, Experimental investigation of mass transfer in 90° pipe bends using a dissolvable wall technique, International Journal of Heat and Mass Transfer 65 (2013) 280–288

#### **Copyright**

Published with permission from the International Journal of Heat and Mass Transfer, 2013

#### **Relative Contributions:**

H. Mazhar: Performed all experiments, interpretation and analysis of the data and wrote the first draft of the manuscript including all figures and text.

D. Ewing: was involved in the interpretation and discussion of results.

J. S. Cotton: Co-supervisor of H. Mazhar and revised the initial drafts of the manuscript

C. Y. Ching: Co-supervisor of H. Mazhar and was responsible for the final draft submittal to the journal

**Abstract:**

The mass transfer in 90° angle bends was measured using a dissolvable wall technique using test sections cast from gypsum. The method allows the surface morphology to evolve producing a roughened surface to mimic practical mass transfer situations. The experiments were performed for standard 90° pipe bends, with a diameter of 2.54 cm and radius of curvature  $r/D=1.5$  at a Schmidt number of 1280 and Reynolds number in the range  $Re=40,000$  to 130,000. A mass transfer enhancement relative to the upstream pipe was observed on the bend inner wall near the inlet, on the side walls throughout much of the bend and on the bend outer wall near the outlet. A maximum mass transfer enhancement of approximately 1.85 times was observed on the bend outer wall near the bend outlet, which was independent of Reynolds number. The Sherwood number at the high mass transfer locations is found to scale as  $Re^{0.92}$ . The surface roughness in the upstream pipe and in the bend is found to decrease slightly with Reynolds number. The roughness scale  $e^+$  is estimated to be approximately 30 to 70 for the different Reynolds numbers.

### 3.1 Introduction

The mass transfer in turbulent flow through piping components plays an important role in Flow Accelerated Corrosion (*FAC*) in a number of practical applications. The mass transfer by diffusion of ions generated at the piping wall to the bulk flow determines the rate of *FAC*. This is different from erosion corrosion (*EC*) wear, where the mass removal process is dominated by mechanical forces, which is more prevalent in multiphase flows [1]. The dissolution mass transfer, in the *FAC* case, is typically limited by the turbulent transfer process in the flow and thus there is a need to investigate geometries with anticipated high regions of turbulence such as the flow downstream of orifices, valves and in bend geometries.

The mass transfer in bends, of interest here, is affected by a number of factors including the bend radius relative to the pipe diameter ( $r/D$ ), angle of curvature ( $\Phi$ ), flow Reynolds number ( $Re$ ) and Schmidt number ( $Sc$ ). Turbulent flow in bends is characterized by complex features such as flow acceleration, separation and generation of secondary flow structures in the form of swirling vortices [2]. The flow complexity in pipe bends increases the turbulence level and mass transfer [3]. The development and strength of the swirling flow is mainly affected by the radius and angle of curvature of the bend and Reynolds number.

Mass transfer studies on long radius [4, 5] and short radius bends [6, 7] under turbulent flow conditions have been performed. The results are in agreement on the location and shape of the peak mass transfer regions, with the maximum mass transfer occurring near

the outlet of the bend outer wall [4- 7]. The enhancement was reported to increase as  $r/D$  was decreased [3, 4, 6, 8], which was attributed to the fact that increasing the bend acuteness would result in higher turbulence levels and in turn higher mass transfer.

The angle of curvature of the bend affects the development of the swirling flow structure and consequently the mass transfer enhancement. The effect of the bend angle of curvature on mass transfer was studied by [9] for bend angles of  $45^\circ$ ,  $90^\circ$  and  $180^\circ$  with an  $r/D=2.72$ . The location of the maximum mass transfer was found to be midway through the bend on the outer wall for the  $45^\circ$  and  $90^\circ$  bends and on the outer wall near the exit for the  $180^\circ$  bend. The transition to a fully rough wall, a regime where the mass transfer coefficient starts to be independent of roughness height, was found to occur at approximately  $Re=30,000$  for the  $180^\circ$  bend and at  $Re=50,000$  for the  $45^\circ$  bend.

The scaling of the Sherwood number ( $Sh$ ) with Reynolds number was investigated by [5, 6, 10]. The average  $Sh$  over the entire bend section for  $r/D=8$  was found to scale as  $Re^{0.925}$  [5], while the  $Sh$  at the peak location for short radius bends ( $r/D=1.5$ ) was found to scale as  $Re^{0.84}$  [6]. The  $Sh$  at the peak location for long radius  $180^\circ$  bends ( $r/D$  of 2.5 and 7.3) was reported by [10] to scale as  $Re^{0.86}$  for the smooth wall case and  $Re^1$  for the rough wall case. The scaling of the mass transfer enhancement, defined as the local Sherwood number relative to that in a fully developed pipe for the same flow condition, with Reynolds number was studied by [3, 4, 8]. There is a discrepancy in the results from the different studies since the mass transfer was normalized using either numerical, smooth or rough wall results. The enhancement was found to be independent of Reynolds number when normalized by the smooth wall results [3, 4] and scaled as  $0.71Re^{0.12}$  for the rough

wall results [3]. An inverse scaling with Reynolds numbers was reported by [8] when using numerical results. In bends, the Sherwood number scales with Reynolds number with a higher exponent than that of straight pipes [5, 6, 11, 12]. Therefore, the enhancement scaling with Reynolds number is expected to increase or at least remain constant with Reynolds number, which are contrary to the results of [8].

The Chilton - Colburn analogy has been used to relate heat and mass transfer data as summarized by [4]. Despite the similarity of the two phenomena, mass transfer results in a change in the surface morphology which in turn changes the mass transfer rates and results in discrepancies between the heat and mass transport rates [10]. The mass transfer rate for a fully rough pipe is found to be 2 to 4 times the mass transfer rate for smooth pipes [11, 12, 13, 14]. Dawson and Trass [13] investigated the effect of surface roughness on the development of both the hydrodynamic and mass transfer profiles under different relative roughness ( $e/D$ ) and Schmidt number ( $Sc$ ). Generally, for  $Sc > 1$  the Reynolds number required for surfaces to be considered fully rough from the hydrodynamic point of view is larger than that required for them to be considered fully rough from the diffusion point of view and becomes even greater with increasing  $Sc$ . Above a certain Reynolds number, referred to as critical Reynolds number, the wall is considered fully rough and the mass transfer coefficient is found to be independent of the roughness height  $e/D$  [13]. The dimensionless roughness scale  $e^+$  at which straight pipes are considered fully rough is found to be approximately 10 to 30 [13, 14].

The objective of the current study is to develop and investigate the effect of Reynolds number on the mass transfer rate in pipe bends using a dissolvable wall technique. This

technique utilizes the dissolution of test sections cast with gypsum in water to measure the mass transfer rate. The methodology provides a  $Sc$  of 1280, similar to that for the diffusion of ferrous ions  $Fe^{+2}$  in water [14]. High  $Sc$  number mass transfer in short radius bends is not well covered in the literature. This technique allows for the surface roughness to develop with time to include the effect of surface roughness. Experiments were performed for Reynolds number in the range 40,000 to 130,000. The local surface wear topography is measured using a laser scanning technique at the end of each experiment and used to evaluate the local mass removal and mass transfer coefficient over the entire surface.

### **3.2 Experimental methodology and data reduction**

Experiments were performed in a 2.54 cm diameter flow loop shown schematically in figure 3.1. Water is circulated from a 100 liter reservoir through the test facility by a centrifugal pump. The flow rate is regulated by globe valves and measured by a turbine flow meter with an accuracy of  $\pm 1\%$  of the flow reading. The flow is passed through a perforated plate followed by a honey-comb before entering a straight pipe with a length of 165 cm leading to the test section. The flow exited the test section to a 75 cm long straight pipe before being directed back to the reservoir. The water temperature was measured in the reservoir and controlled to within  $\pm 0.5$  °C using a compensation cooling loop. The amount of Gypsum dissolved in the water during the experiment was determined by measuring the electrical conductivity of the water. A calibration experiment was performed to correlate the amount of dissolved Gypsum to the increase in conductivity of the water.

The gypsum bend test sections consisted of an upstream 20 cm long straight pipe, a standard 90° bend with a radius of curvature of 3.81 cm ( $r/D=1.5$ ) and a downstream 10 cm long straight pipe. The test section had a nominal diameter of 2.54 cm throughout. The test sections were cast over rubber cores covered by thin balloons that were held in place in a machined plastic mold. The segments of the test section are cast in succession with the bend cast first followed by the upstream and downstream straight pipes. The gypsum was generated by mixing Hydrocal ( $\text{CaSO}_4 \cdot 1/2\text{H}_2\text{O}$ ) with water that yields gypsum with a density of 1550 ( $\text{kg/m}^3$ ). A small amount of citric acid is added during the mixing stage to retard the curing process and facilitate the casting process. The mixture is left under a vacuum before casting to aid the release of trapped air bubbles in the mixture. The cast test sections were allowed to cure under ambient conditions and weighed periodically until the weight reached steady state, which typically took 15 days. Samples from the cured cast test sections were analyzed using X-ray diffraction and it was found to consist of almost 98% calcium sulfate compounds, with a minor percentage of other contents and 0% silica.

The test section was tested in the facility by running water through it at different Reynolds numbers for a specific period of time. After each test, the test section was allowed to dry until the weight again reached a constant value, in typically 5 to 10 days.

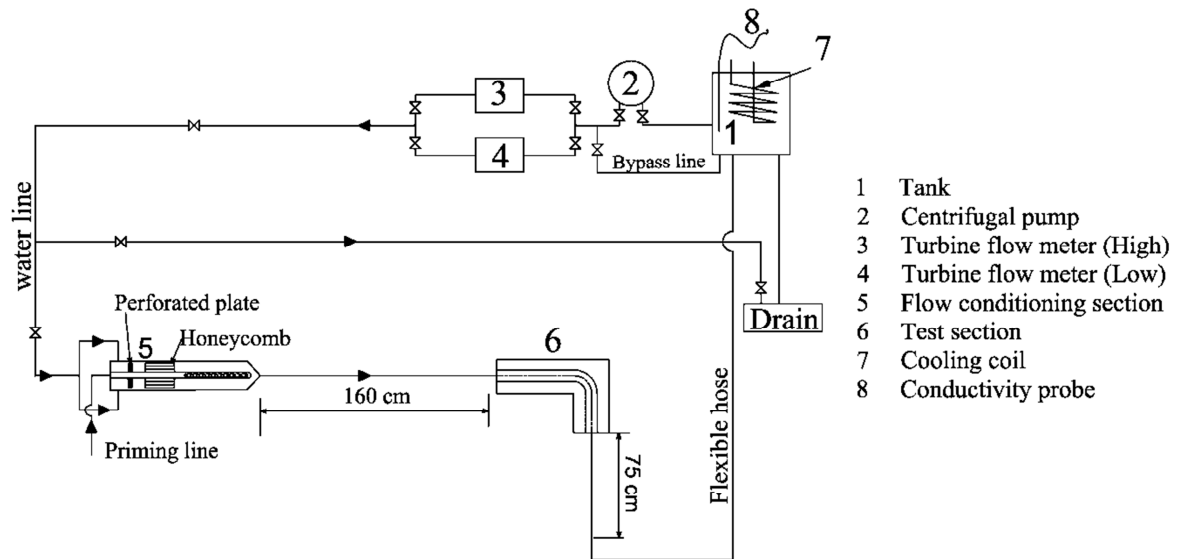


Figure 3.1: Schematic of the test facility showing the main components of the flow loop

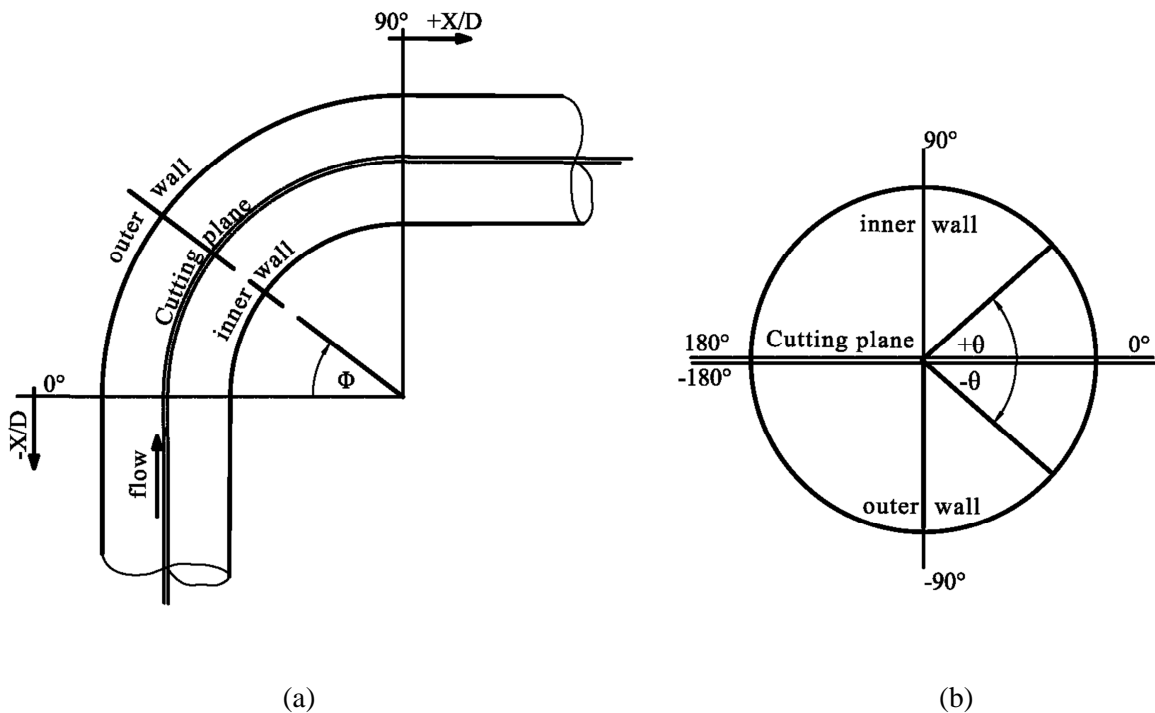


Figure 3.2: Schematic of the test section showing the sections plane relative to, (a) streamwise orientation (b) crosswise orientation

**Table 3.1: Nomenclature of quantities and terms.**

Nomenclature

$dm/dt$	<i>Mass transfer rate</i>	$[kg/s]$
$C_w$	<i>Hydrocal ions concentration at the wall</i>	$[kg/m^3]$
$C_b$	<i>Hydrocal ions concentration in the bulk fluid</i>	$[kg/m^3]$
$\Delta C_o$	<i>Initial concentration difference</i>	$[kg/m^3]$
$\delta$	<i>Local instantenous wear of the test section</i>	$[m]$
$D$	<i>Bend cross sectional diameter</i>	$[m]$
$D_m$	<i>Mass diffusivity for Hydrocal in water determined at 25° C</i>	$[m^2/s]$
$e$	<i>Roughness height</i>	$[m]$
$e/D$	<i>Relative roughness height</i>	$[m]$
$e^+$	<i>Roughness scale</i>	
$h$	<i>Mass transfer coefficient</i>	$[m/s]$
$Sc$	<i>Schmidt number (<math>\nu/D_m</math>)</i>	
$Sh$	<i>Sherwood number (<math>h \times D/D_m</math>)</i>	
$X/D$	<i>Streamwise dimensionless distance</i>	
$\rho$	<i>Density of the gypsum</i>	$[kg/m^3]$
$\theta$	<i>Bend cross sectional angle</i>	
$\phi$	<i>Bend angle of curvature</i>	
$\nu$	<i>Kinematic viscosity</i>	$[m^2/s]$

The worn surface topography of the test section at the end of each test was determined by cutting the section into two halves along the bend middle line using a thin blade band saw. This process led to a loss of approximately 10 degrees of the bend circumference on each of the side walls. The topography was obtained using a laser digitizer that scans the entire surface and provides the 3d Cartesian locations on a resolution of approximately 0.2 mm relative to a common datum. Figure 3.2 shows a schematic of the test section orientation and the profile along which the bend is sectioned. Multiple scans with overlap between scans were performed to increase the scanned spatial resolution and to ensure that all surface details were captured. The scanned surface coordinates were initially aligned to a common coordinate system using commercial image processing software by fitting three orthogonal planes on the scan image of the test section. The non-uniform laser scan data points were re-gridded to a uniform grid with a resolution of 0.25 by 0.25 mm using in-house developed routines by averaging the points within each grid cell. The alignment of the scans was refined using in-house data reduction routines by considering the local deviations from an ideal model of the test section on different longitudinal strips around the circumference. The test sections were aligned based on the assumption of symmetry of the average mass transfer along the test section and axi-symmetry in the upstream pipe. The circumferential strips were compared along the test section to determine the deviation from symmetry. The alignment of the bend and the downstream pipe was also verified by checking profiles in the different Reynolds number cases for any systematic bias. The alignment process was done in an iterative manner with the symmetry check used as the convergence criterion. The two parts of each test section

were analyzed separately and then brought together to check the trends of the two profiles at the terminals of each section to verify the alignment. The total mass removed from the test section during the experiment was determined by three methods: (i) comparing the mass of the test section before and after the test, (ii) from the concentration of the dissolved gypsum in the water at the end of every test and (iii) from the integrated mass removed computed from the laser digitized 3d surface scan. The mass calculated from the different methods agreed to within  $\pm 7\%$ .

The normal local deviations of the worn scan surface from the unworn scan surface determine the thickness removed  $\delta$  at every point on the surface. The local mass transfer coefficient is determined from

$$\rho \frac{d\delta}{dt} = h\Delta C \quad (1)$$

where  $\delta$  is the thickness of local mass removed normal to the surface,  $\Delta C$  is the difference between species concentration at the wall and in the bulk flow and  $h$  is the mass transfer coefficient. The concentration difference decreases over the course of the experimental time due to the dissolution of the gypsum in water, and thus the driving potential for the mass transfer decreases. The mass transfer coefficient was computed using a modified time to account for the change in concentration difference change as

$$\rho \frac{d\delta}{d\tau_{\text{mod}}} = h\Delta C_o \quad (2)$$

where  $\tau_{\text{mod}}$  is the modified time given by

$$\tau_{\text{mod}} = \frac{1}{\Delta C_o} \int_0^t [C_w - C_{b_i}] \cdot dt \quad (3)$$

Then the Sherwood number is calculated as

$$Sh = \frac{h \times D}{D_m} \quad (4)$$

where  $D$  is the pipe diameter and  $D_m$  is the mass diffusivity. The rate of change in the wear is computed at every local point to determine the spatial distribution of the mass transfer rate. The uncertainty in the mass transfer coefficient is estimated to be  $\pm 18\%$ .

Experiments were performed for Reynolds numbers of 40,000, 60,000, 70,000, 100,000 and 130,000. The repeatability of the results was examined here by performing experiments for different testing times of 40, 60 and 80 minutes for a Reynolds number of 70,000. The mass transfer coefficient obtained by considering multiple testing times together was compared with a single test time. The stream wise profiles of the mass transfer coefficient along the centerline of the inner wall and outer wall halves obtained from different times averaged over  $\pm 15$  degree in the azimuthal direction are shown in figure 3.3. The average profile obtained using three realizations together agreed well with the profiles obtained using individual testing times. The mass transfer coefficients for the different Reynolds number experiments were conducted using individual realizations with testing times that resulted in similar nominal mass removal to the longer time experiments for the  $Re=70,000$  case.

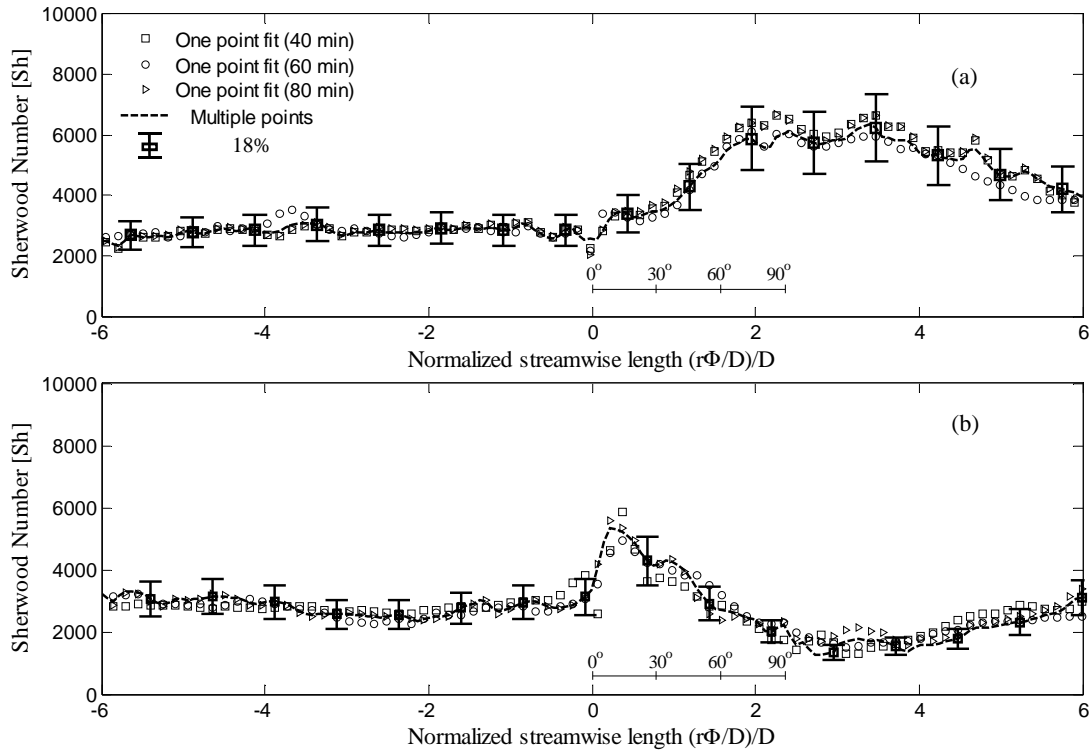


**Figure 3.3: Stream wise Sherwood number profiles along the centerline for (a) outer wall (b) inner wall of the bend section at  $Re=70,000$ ,  $Sc=1280$ .**

### 3.3 Mass transfer in single $90^\circ$ bend

The local Sherwood number distribution over the entire test section for Reynolds number of 70,000 obtained from the experimental measurement is shown in figure 3.4. The Sherwood number distribution is shown from 3 diameters upstream to 4 diameters downstream of the bend. The mass transfer is nearly constant in the section of the upstream pipe. The mass transfer rate on the inner wall increases near the inlet and then decreases gradually along the bend curvature. The mass transfer on the outer wall increases along the bend profile and extends a short distance into the downstream pipe,

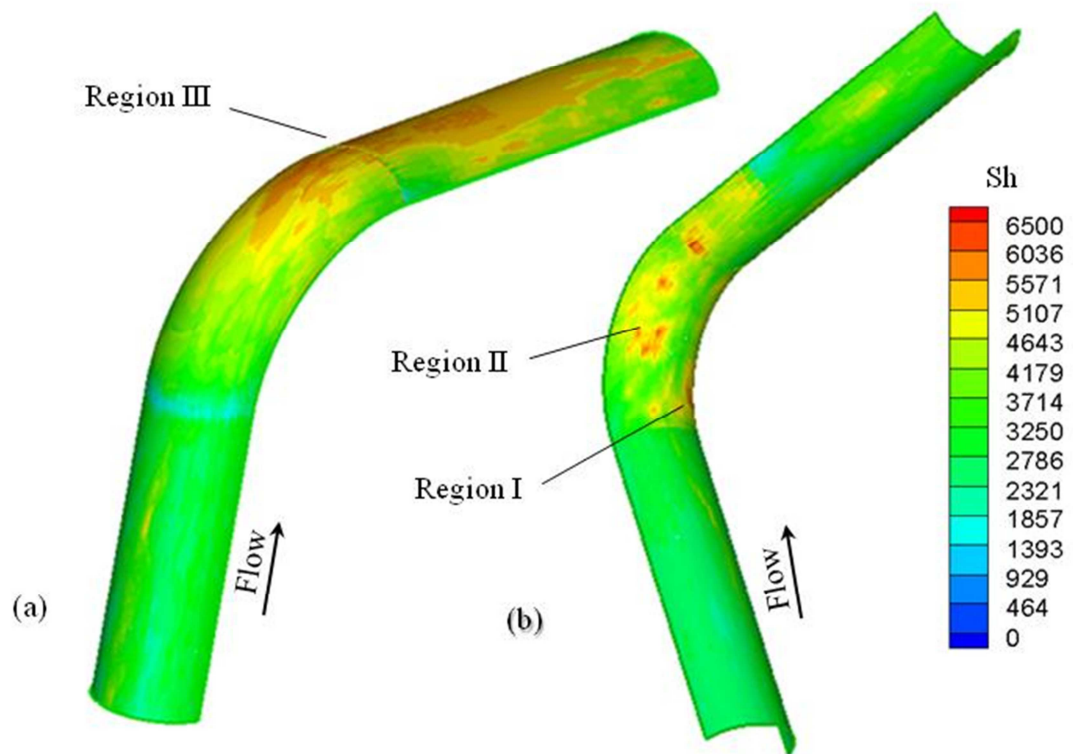


**Figure 3.4: Typical mass transfer distribution over the entire single bend test section. (a) outer wall side view and (b) inner wall side view, measured for  $Re=70,000$ ,  $Sc=1280$**

and then decays beyond that. The results show three regions of significant mass transfer enhancement relative to the mass transfer in the upstream pipe: (i) on the inner wall of the bend near the inlet, (ii) on the bend side wall midway into the bend and (iii) on the outer wall near the bend outlet. The surface of the inner wall shows a streaky wear pattern that is inclined toward the centerline. This likely corresponds to the anticipated high mean shear stress region due to flow acceleration into the bend [15]. The enhancement on the sidewalls was formed with a wear pattern of streaks directed normal to the center line, which can be attributed to the counter rotating vortices generated by the bend curvature. The strength of these vortices was reported to change and move from one side of the bend

to the other in a phenomenon referred to as swirl switching flow mechanism [15-19]. However, the averaged flow field is symmetric which correspond to the symmetric mass transfer distribution observed in the current results. These vortices intensify along the bend curvature and shifts from the wall to the core region near the outlet of the bend due to flow separation driving the high velocity core flow to the outer wall [19]. The maximum enhancement was observed on the bend outer wall near the outlet extending into the downstream pipe with longitudinal surface streaks in the flow direction. This may be attributed to the high velocity core flow which is directed by the effect of flow separation toward the outer wall resulting in a region of high shear stress. The surface features observed were qualitatively similar to the surface topography reported in [20] for the first part of an 180° bends using copper tube as the test specimen.

The  $Sh$  profiles normalized by the average  $Sh$  in the corresponding upstream pipe along the center line of the bend outer and inner walls, averaged over  $\pm 20$  degrees in the azimuthal direction, are shown in figure 3.5. The  $Sh_{local}/Sh_{pipe}$  profiles are consistent for the different Reynolds numbers within the experimental uncertainty. The stream wise trends are in good agreement with the profiles of [6]; however, the enhancement levels were different. The difference in level may be attributed to the effect of roughness and  $Sc$  on mass transfer enhancement, since the results in [6] were obtained from smooth surface experiments at low  $Sc$  of 2.5.

Azimuthal profiles of the mass transfer enhancement ( $Sh/Sh_{pipe}$ ) at different axial locations upstream, through and downstream of the bend curvature on the inner and outer walls are shown in figure 3.6. The mass transfer enhancement profile in the upstream pipe

( $x/D=-2$ ) is nearly uniform over the entire cross section. Along the bend outer wall, figure 3.6-a, the mass transfer at  $\phi=10$  is lower than in the upstream pipe; however, it is still laterally uniform. The mass transfer rate increases along the bend curvature to reach a maximum near the bend outlet. The maximum enhancement level is approximately 1.85 and extends around the symmetry plane between approximately  $\theta$  of  $-115^\circ$  and  $-65^\circ$ . This agrees well with the maximum enhancement location reported by [6, 8].

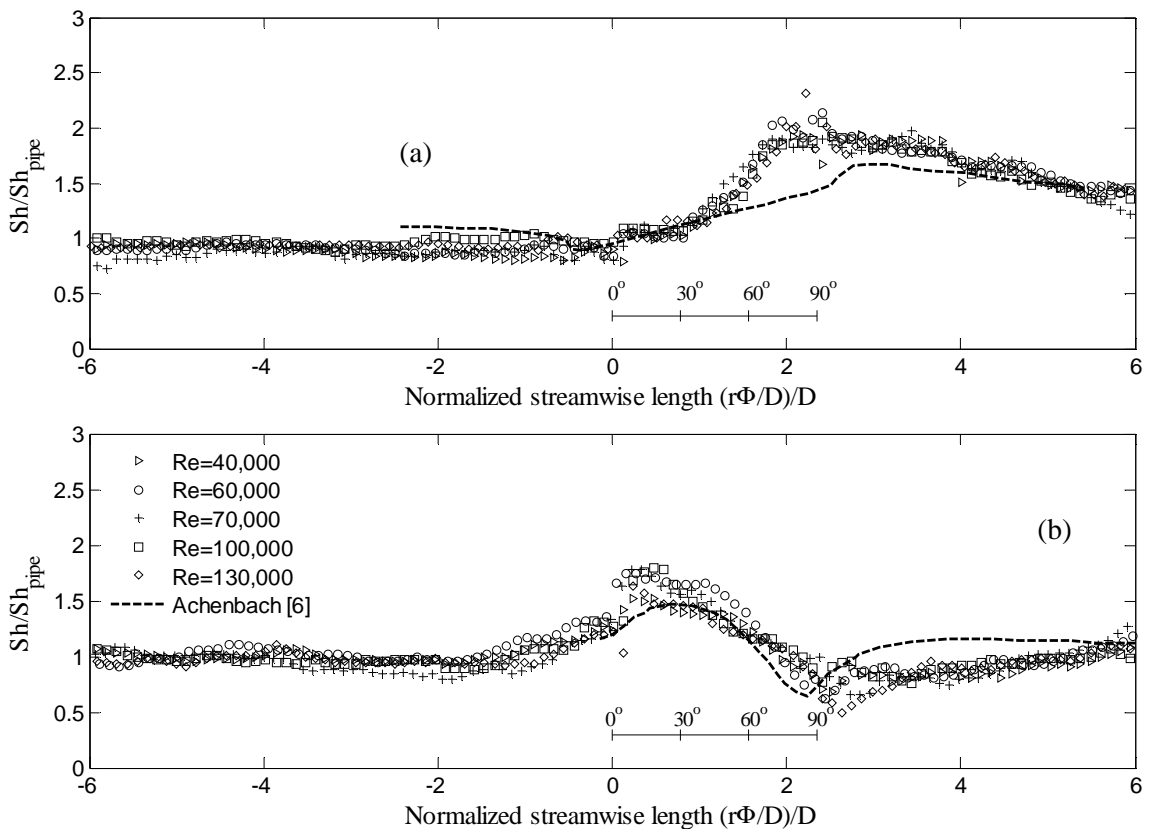


**Figure 3.5: Profiles of  $Sh/Sh_{pipe}$  along the (a) outer wall side and (b) inner wall side of the bend. The results are averaged over  $\pm 20^\circ$  in the azimuthal direction plotted along the centerline.**

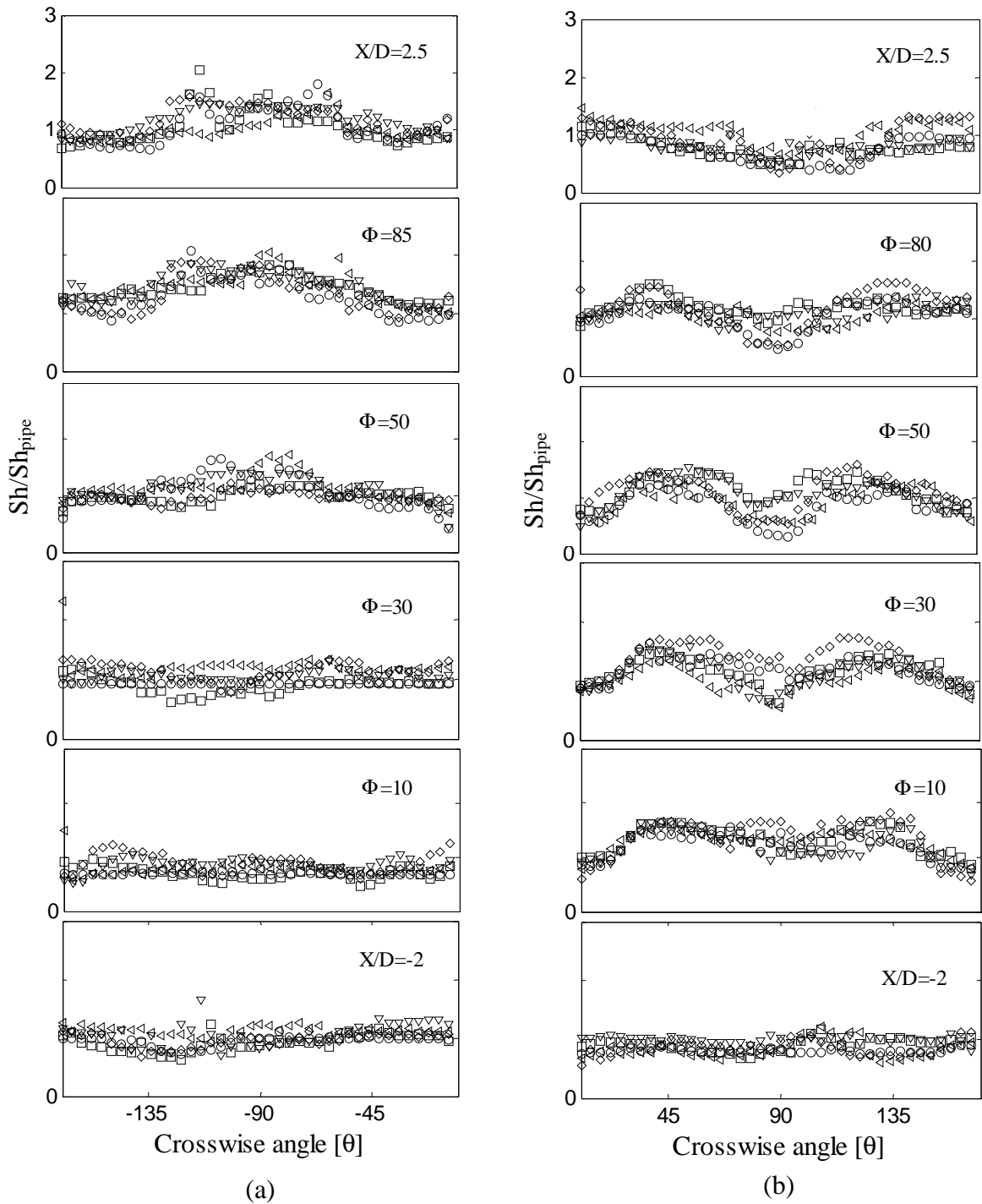


**Figure 3.6: Azimuthal profiles of  $Sh/Sh_{pipe}$  along the streamwise direction along the bend curvature for: a) bend outer wall side, b) bend inner wall side for  $Re$  of  $\nabla$  40,000,  $\square$  60,000,  $\circ$  70,000,  $\triangleleft$  100,000,  $\diamond$  130,000**

Along the bend inner wall, Figure 3.6-b, the mass transfer enhancement increases along the bend curvature to reach a maximum of approximately 1.65 near the inlet,  $\phi=10$ . The maximum spans between  $\theta$  of  $50^\circ$  to  $130^\circ$  on each side of the symmetry plane of the bend. The location of high mass transfer shifts away from the center line toward the sidewalls near  $\phi$  of  $30^\circ$  to  $50^\circ$ . This shift leaves two similar peaks on the sidewalls with a valley at the centerline. The level of enhancement on the side walls decreases to reach approximately 1.55 and forms approximately at  $\theta=40^\circ$  and  $\theta=140^\circ$ .

The difference in the mass transfer enhancement at the inlet of the inner wall at the different Reynolds number, especially between  $\phi$  of  $30^\circ$  and  $60^\circ$ , is attributed to the change of the onset of the flow separation. Since the separation region commences where the velocity reaches a minimum followed by a recovery zone in the mean velocity, the mass transfer behaves similarly. The mass transfer decreases near the onset of separation and then increases downward from this location. The location of the onset of flow separation moves downstream with increasing Reynolds number which results in an axial shift in the accompanying mass transfer/surface topography features. The mass transfer pattern is similar at different Reynolds number but the onset of the low enhancement region starts at different axial locations. This was confirmed by examining the physical samples at different Reynolds numbers. The images of the inner wall at  $Re$  of 40,000, 60,000 and 100,000 are shown in figure 3.7. The separation zone is characterized by a smooth surface morphology compared to the neighboring topography. The onset of this smooth area is observed to move further into the bend with increasing Reynolds number.

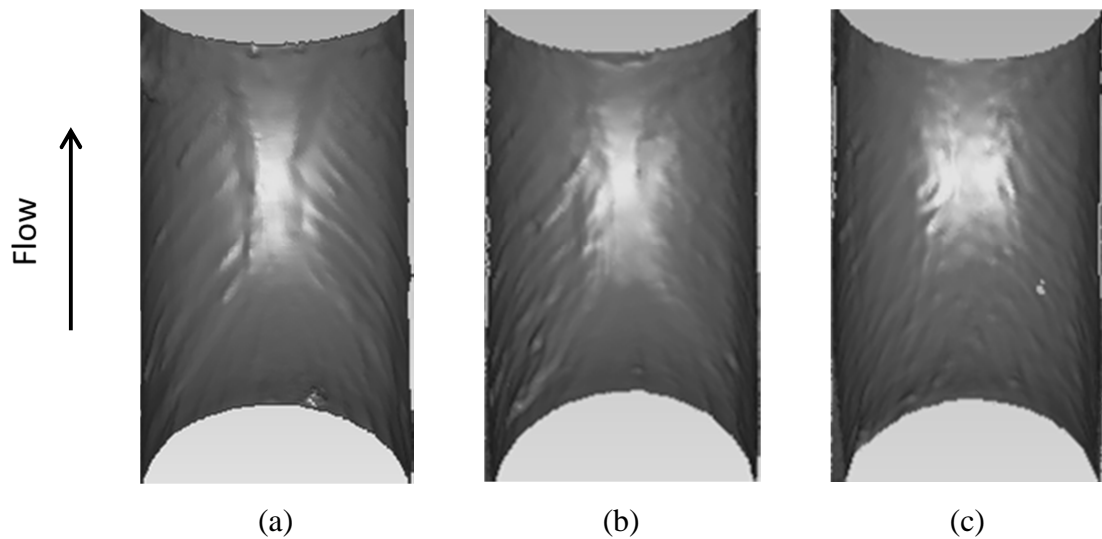


**Figure 3.7: Physical images of the test sections showing the inner wall side, at Reynolds numbers of a)  $Re=40,000$ , b)  $Re=60,000$  and c)  $Re=130,000$**

Several azimuthal profiles around the location of the maximum are used to determine the location and level of the maximum enhancement. The locations of the maxima are found to be consistent between the different Reynolds numbers. The effect of Reynolds number on the maximum Sherwood number at the different locations of elevated mass transfer, at the inlet to the inner wall, midway on the inner wall and near the outlet of the outer wall, is shown in figure 3.8. The  $Sh$  for the three mass transfer peak locations is found to be proportional to  $Re^{0.92}$  for the range of Reynolds numbers examined here, and agrees with the results for the average mass transfer in bends by [5]. The current mass transfer results for the upstream straight pipe are similar in trend to the rough wall experimental results of [12-14]. The magnitude is higher than the smooth wall experimental results of [5]. The local mass transfer maxima in the bend increase with Reynolds number at approximately

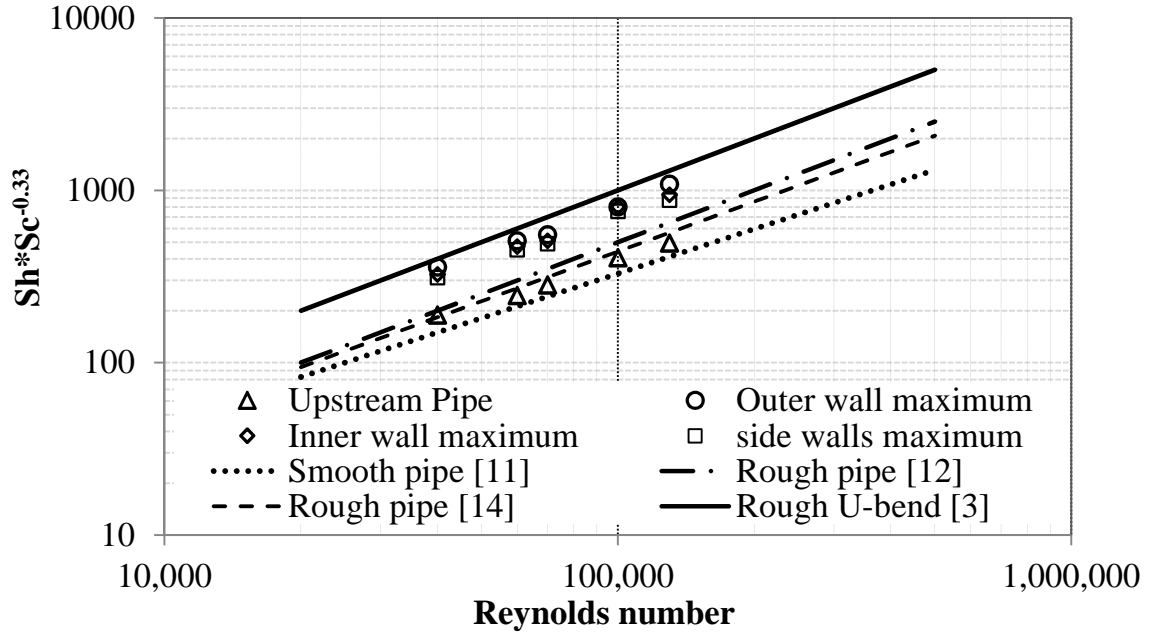


Figure 3.8: Variation of the local maximum Sherwood number with Reynolds number,  $-\cdot-$   $0.005 Re Sc^{0.33}$  [12],  $--$   $0.007 Re^{0.96} Sc^{0.33}$  [14],  $\cdots$   $0.0165 Re^{0.86} Sc^{0.33}$  [11],  $—$   $0.01 Re^1 Sc^{0.33}$  [3]

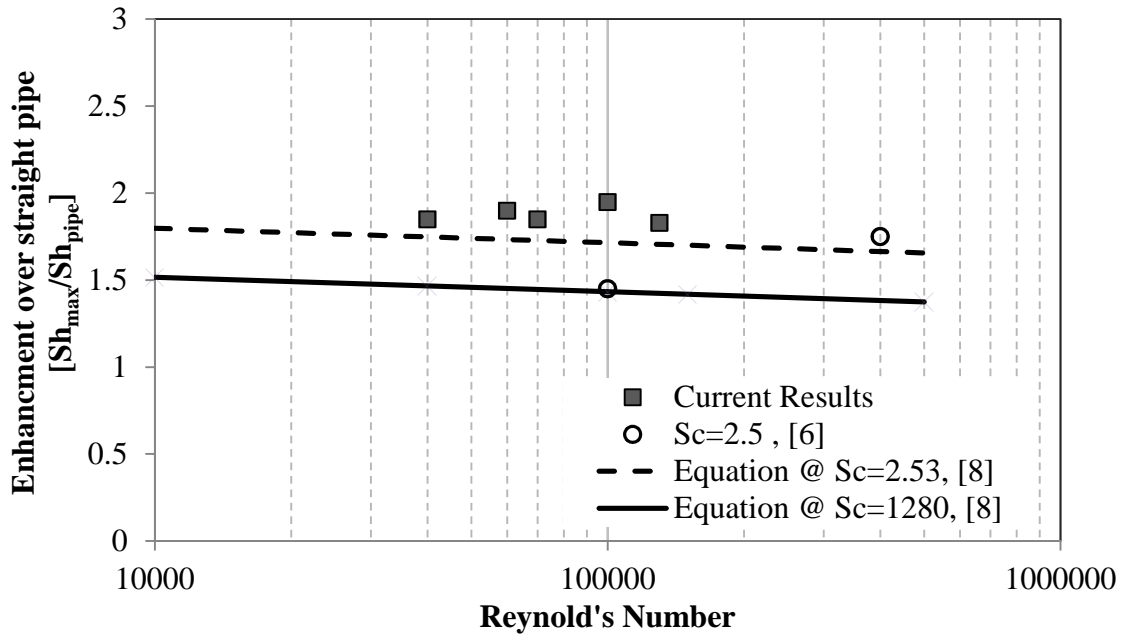
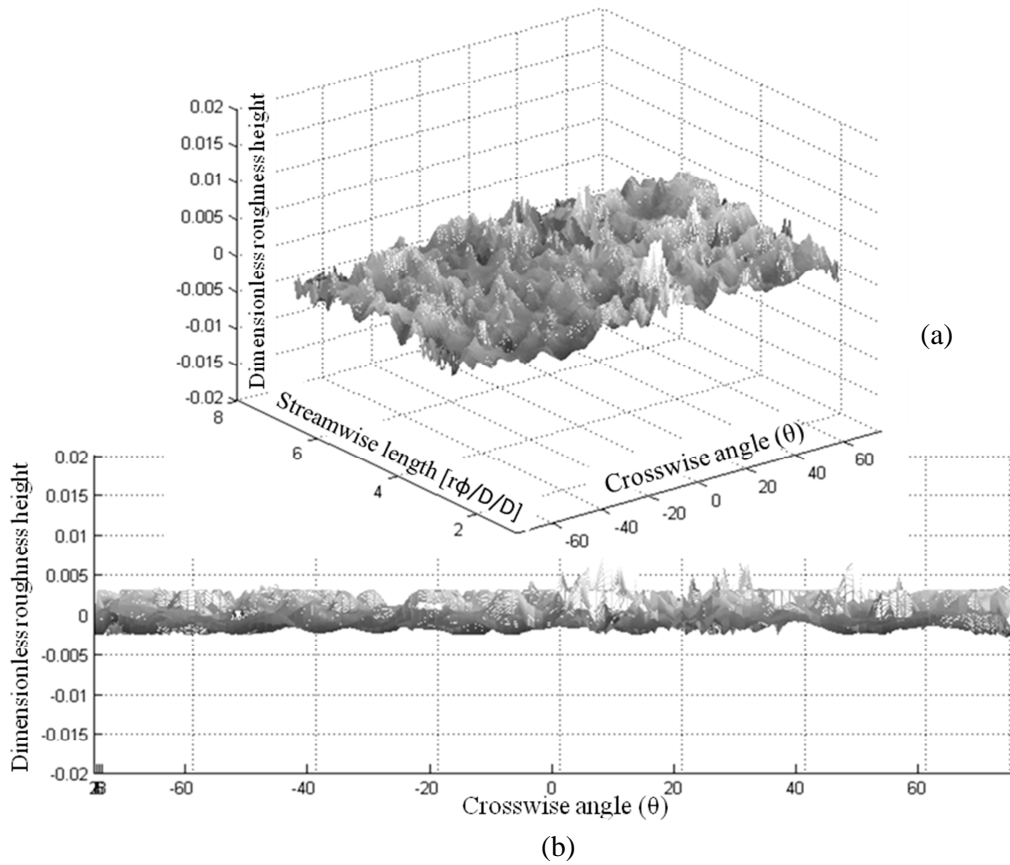


Figure 3.9: Variation of mass transfer enhancement in the bend compared with existing data for the same radius of curvature ( $r/D=1.5$ ) and different Schmidt numbers

a similar rate to the upstream pipe. The change in the ratio of the maximum mass transfer downstream of the bend outer wall to that in the upstream straight pipe ( $Sh_{max}/Sh_{pipe}$ ) with Reynolds number is shown in Figure 3.9. The results indicate that the ( $Sh_{max}/Sh_{pipe}$ ) is nearly independent of Reynolds number with a value of 1.85. The enhancement factor is higher than the results for low Reynolds number but similar to that at high Reynolds number by [5] for flow with a  $Sc$  of 2.5 and the same bend radius. The results obtained from [6] were only for two Reynolds numbers with a significant increase in the enhancement with Reynolds number. The results are also higher than the values of [8], obtained using numerical simulations of the flow with different bend  $r/D$ , and do not decrease with Reynolds as predicted by the correlation. The correlation proposed by [8] under predicts the experimental results reported by Coney [4] for long radius bends. Since the  $r/D$  range for Coney's correlation is much higher than the present results, a comparison to conclude the effect of roughness on mass transfer enhancement is not applicable.

### 3.4 Roughness analysis

The worn surface topography obtained from the laser scans were used to estimate the surface roughness. The entire scanned surface is gridded into cells to quantify the local average mass removal. The grid size was iterated to capture the roughness and a size of  $2 \times 4$  mm was used. The comparison of the mass removal obtained from the laser scan and the local averaged mass removal yields the local surface undulations within each cell. The roughness height is estimated from examining the peak to valley levels in the surface undulations. The typical undulations of the upstream pipe surface, for  $Re$  of 40,000, are



**Figure 3.10: Relative roughness pattern in the upstream pipe for  $Re=40,000$ , (a) 2-d roughness height pattern, (b) Spatial distribution of the roughness undulations from the physical sample scan**

shown in figure 3.10. The undulations were nearly uniform and similar in height. The initial test section was nominally smooth with a roughness of approximately  $e/D=0.0007$ , which was nearly 10 times less than the final roughness levels. The relative change in roughness with testing time was examined by comparing the roughness level for Reynolds number of 70,000 in three sections tested for different time intervals of 40, 60 and 80 minutes. The roughness level was similar for all three times as shown in figure 3.11, which indicates that 40 minutes was sufficient for the surface to reach a stable

roughness pattern. The results are consistent with [21] where the dissolution roughness was found to increase until it reached an equilibrium quasi-steady scalloped pattern. The experimental times for the other Reynolds numbers were selected to achieve similar nominal mass removal, approximately 1 to 2 mm in depth, to that obtained at 80 minutes under the Reynolds number of 70,000. The change in the relative roughness at the locations of the local maxima in the mass transfer for the upstream pipe, inner wall inlet, side walls and outer wall outlet with  $Re$  is shown in figure 3.12. The relative roughness in the upstream straight pipe was approximately 0.0065 for a Reynolds number of 40,000 and decreased slightly with an increase in Reynolds number, a trend also observed by [21].

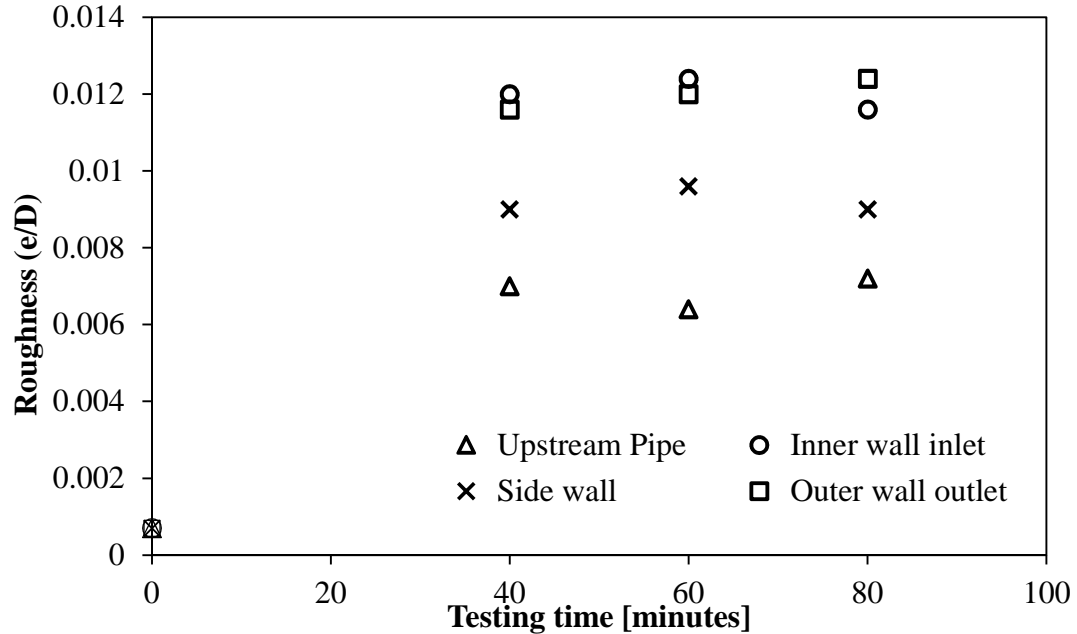


**Figure 3.11: Development of average relative roughness with time in the upstream pipe at  $Re= 70,000$**

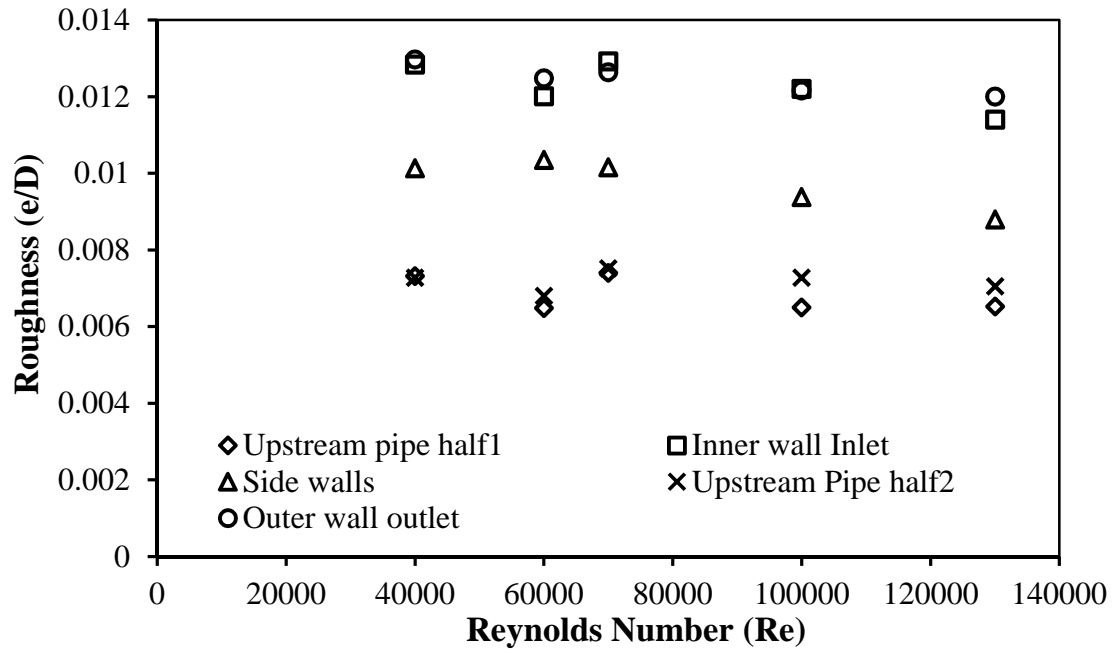


**Figure 3.12: Variation of the roughness evaluated based on the peak to valley at the upstream pipe, inlet to the bend inner wall and at the outlet from the bend outer wall with different Reynolds numbers**

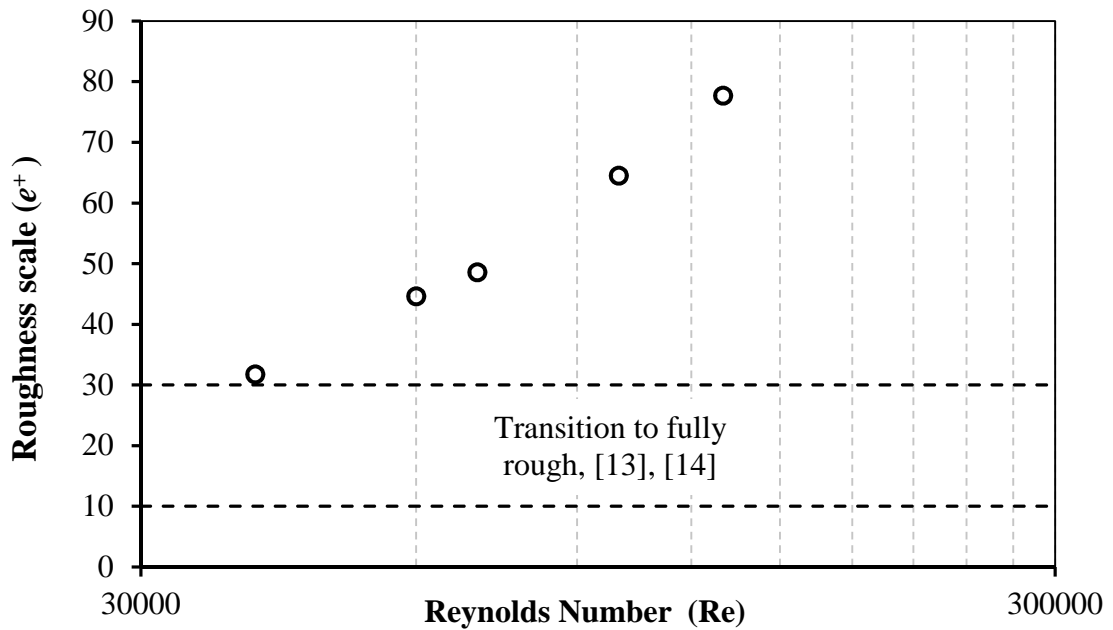


**Figure 3.13: Variation of the roughness scale in the upstream pipe with Reynolds number**

Similarly, the roughness at the bend inner wall inlet, side walls and outer wall outlet decreased with Reynolds number. The roughness levels within the bend were higher than the upstream pipe. The variation of the roughness scale  $e^+$  ( $=eu_r/\nu$ ) with Reynolds number in the upstream pipe section is shown in figure 3.13. The minimum value of  $e^+$  at  $Re$  of 40,000 is approximately 30 which corresponds to the fully rough pipe data level based on the results of [13, 14]. The roughness scale increased with Reynolds number which suggests that it is driven by some intermediate flow structure scale between the wall and the core scales; this may require further investigation to understand the relationship to the turbulence scales. The increase in the roughness scale did not affect the mass transfer similarity at the different Reynolds number. Similarly, Dawson and Trass [13] observed that increasing the  $e^+$  above the fully rough limit resulted in similar trends regardless of the physical roughness size.

### 3.5 Summary and conclusions

A dissolvable wall mass transfer measurement technique is developed and the local mass transfer distribution in a  $90^\circ$  bend was measured at Reynolds numbers in the range 40,000 to 130,000 for a Schmidt number of 1280. The technique allows for the surface roughness to develop due to the flow and thus mimics practical mass transfer applications. The mass transfer distributions were in good agreement with existing experimental and numerical data. The surface features are well correlated to the flow features reported in the existing literature. Three regions of high mass transfer enhancement were determined, (i) at the inlet to the bend inner wall, (ii) midway into the bend on the sides of the inner wall and (iii) near the outlet of the bend outer wall. The  $Sh$  scaled with  $Re$  in a similar manner in

all regions of high mass transfer with an exponent of 0.92. The maximum mass transfer enhancement occurs on the bend outer wall near the outlet and extends approximately 1 diameter into the downstream pipe. The magnitude of the maximum enhancement is 1.85 relative to the upstream pipe. The maximum mass transfer enhancement is nearly independent of Reynolds number. The relative roughness  $e/D$  in the upstream pipe was approximately 0.0065 and this corresponds to a fully rough wall for the range of Reynolds number studied here. The relative roughness in the bends varies between 1.5 and 2 times that in the upstream pipe. The measured relative roughness at the locations of local maxima in the mass transfer decreased with Reynolds number indicating that the tests are in the fully rough region.

### 3.6 References:

- [1] Heitz, E., Mechanistically Based Prevention Strategies of Flow-Induced Corrosion, *Electrochimica Acta*, vol. 41, No. 4, pp. 503-509, (1996)
  
- [2] Weske, J.R., Experimental Investigation of Velocity Distribution Downstream of a Single Duct Bend, N.A.C.A, TN 1471, (1948)
  
- [3] Poulson, B., The Local Enhancement of Mass Transfer at 180 Degree Bend, *International Journal of Heat Mass Transfer*, vol. 31, No. 6, pp. 1289-1297, (1988)
  
- [4] Coney, M. Erosion Corrosion, The Calculation of Mass Transfer Coefficients, CERL Report RD/L/N197, (1980)

- [5] Wilkin, S. J., Oates, H.S., Coney, M., Mass Transfer on Straight Pipes and 90° Bends Measured by the Dissolution of Plaster, (1st Edn). Central Electricity Research Laboratories, TPRD/L/2469/N83, (1983)
- [6] Achenbach, E., Mass Transfer from Bends of Circular Cross Section to Air, Future Energy Production Systems, Academic Press, New York, vol. 1, pp. 327-337, (1976)
- [7] Sparrow, E.M., and Chrysler, G.M., Turbulent Flow and Heat Transfer in Bends of Circular cross section: i-Heat transfer experiments, ASME J. Heat Transfer, 108 , 40-47, (1986)
- [8] Wang, J., Shirazi, S. A., A CFD Based Correlation for Mass Transfer Coefficient in Elbows, International Journal of Heat and Mass Transfer, vol. 44, 1817-1822, (2001)
- [9] Sprague, P.J., Patrick, M.A., Wragg, A.A., Coney, M.W.E., Mass Transfer and Erosion Corrosion in Pipe Bends, 8<sup>th</sup> Congress European de Corrosion, Vol. 12 (2), 19-21 (November 1985)
- [10] Poulson, B., Advances in Understanding Hydrodynamic Effects on Corrosion, Corrosion Science 35, no. 1-4, p. 655-665, (1993)
- [11] Berger, F. P. and Hau, K. F. F. L., Mass Transfer in Turbulent Pipe Flow Measured by the Electrochemical Method, International Journal Heat Mass Transfer 20, p. 1185-1194, (1977)

- [12] Blumberg, A study of stable, Periodic Dissolution Profiles Resulting from The Interaction of the Soluble Surface and an Adjacent Turbulent Flow, the university of Michigan , PhD, Engineering, Chemical, (1970)
- [13] Dawson, D. A. and Trass, D., Mass Transfer at Rough Surfaces, Int. J. Heat and Mass Transfer 15- p. 1317-1336, (1972)
- [14] Postlethwaite, J., Lotz, U., Mass Transfer at Erosion–Corrosion Roughened Surfaces, Canadian Journal of Chemical Engineering, p. 66 – 75, (1988)
- [15] Enayet, M. M., Gibson M.M., Yianneskis, M., Laser Doppler Measurements for Laminar and Turbulent Flow in Pipe Bend, International Journal of Heat and Fluid Flow 3, p. 213-220, (1982)
- [16] Tunstall, M. J., Harvey, J. K., On the Effect of a Sharp Bend in a Fully Developed Turbulent Pipe-Flow, Journal of Fluid Mech 34, no. 3 (1968) 595-608
- [17] Rütten, F. , Meinke, M. , Schröder, W., Large-Eddy Simulations of 90° Pipe Bend Flows, Journal of Turbulence, Volume 2, Art. No. 3, (2001)
- [18] Yamano, H., Tanaka, M., Murakami, T., Iwamoto, Y., Yuki K., Sago, H., Hayakawa, S., Unsteady Elbow Pipe Flow to Develop a Flow-Induced Vibration Evaluation Methodology for Japan Sodium-Cooled Fast Reactor, Journal of Nuclear Science and Technology, Vol. 48, No. 4, p. 677–687, (2011)

- [19] El-Gammal, M., Mazhar, H., Cotton, J.S., Schefski, C., Pietralik, J. and Ching, C. Y., The Hydrodynamic Effects of Single Phase Flow on Flow Accelerated Corrosion in a 90 Degree Elbow, Nuclear Engineering and Design 240, p.1589-1598, (2010)
- [20] Poulson, B., Complexities in Predicting Erosion Corrosion, Wear 233- 235, pp. 497-504, (1999)
- [21] Blumberg, P. N., Curl, R. L., Experimental and Theoretical Studies of Dissolution Roughness, Journal of Fluid Mechanics, Vol. 65, part 4, p. 735-751, (1974)



## **CHAPTER 4**

---

### **Mass transfer in dual pipe bends arranged in an S-configuration**

#### **Complete citation:**

H. Mazhar, D. Ewing, J. S. Cotton, C. Y. Ching, Mass transfer in dual pipe bends arranged in an S-configuration, International Journal of Heat and Mass Transfer- Submitted July (2013)

#### **Relative Contributions:**

H. Mazhar: Performed all experiments, interpretation and analysis of the data and wrote the first draft of the manuscript including all figures and text.

D. Ewing: was involved in the interpretation and discussion of results.

J. S. Cotton: Co-supervisor of H. Mazhar and revised the initial drafts of the manuscript

C. Y. Ching: Co-supervisor of H. Mazhar and was responsible for the final draft submittal to the journal

**Abstract:**

The mass transfer in dual in-plane short radius bends arranged in an S-configuration was measured for different separation distances ( $L/D$ ) between the two bends. Experiments were performed using a wall dissolution technique with gypsum test sections at a Schmidt number ( $Sc$ ) of 1280 for  $L/D$  from 0 to 5 at a Reynolds number ( $Re$ ) of 70,000. The maximum mass transfer was found to occur between the outlet of the first bend outer wall and the inlet of the second bend inner wall in all cases. The maximum mass transfer occurred for  $L/D=0$  and was 3.2 times larger than the average mass transfer in a fully developed pipe flow under the same flow condition. The maximum mass transfer decreased as the separation distance between the two bends was increased. The effect of  $Re$  on the mass transfer enhancement for a separation distance of  $L/D=0$  was examined for  $Re$  in the range 40,000 to 130,000. The peak mass transfer was found to scale as  $Re^{0.93}$  and was similar to that of the peak mass transfer in a single bend.

#### 4.1 Introduction

A serious safety and reliability problem in power generation plant piping systems and in particular nuclear power plants is flow accelerated corrosion (FAC). FAC occurs in two successive processes: (i) corrosion by oxidation of the carbon steel piping resulting in the formation of a porous oxide layer followed by (ii) the dissolution mass transfer of the formed corrosion layer to the adjacent fluid. This is different from erosion corrosion (EC) wear, where the mass removal process is dominated by mechanical forces, which is more prevalent in multiphase flows. In FAC, the mass transfer process depends on the hydrodynamics of the flow in the piping component and is normally the rate limiting factor for pipe wall thinning [1]. The flow turbulence level and shear stress, which are dependent on the geometry of the piping configuration, are found to be the dominant parameters in determining the overall mass transfer rate and thus the FAC rate [2]. Pipe bends in different arrangements are major components in almost all piping systems, and the flow in such components, especially when arranged back-to-back, exhibits a high level of flow complexity and turbulence level [2].

The mass transfer in bends is affected by the angle of curvature ( $\phi$ ), bend radius relative to the pipe diameter ( $r/D$ ), flow Reynolds number ( $Re$ ), Schmidt number ( $Sc$ ) and surface roughness ( $e/D$ ). Complex flow features are observed in bends due to the change in flow direction, such as flow acceleration, flow separation and generation of secondary flow structures in the form of swirling vortices [3]. The radius of curvature of the bend and Reynolds number are the dominant parameters in determining the strength of the swirling flow [3, 4]. The flow in dual bends is more complex than in single bends, due to the

interaction of the flow dynamics within the two bends [5]. The flow dynamics in back-to-back 90° bends arranged in U-, out of plane- and S- configurations, shown schematically in figure 4.1, were studied by [6-11]. The highest turbulence level and pressure drop was observed for the S- configuration compared to the U and out of plane dual bend configurations for turbulent flow conditions [6]. This is likely due to the sweeping motions within the first and the second bends in the U, and partially in the out of plane configurations, being in the same direction, which allows for a quicker velocity field recovery compared to the S configuration [6]. Twin vortices are generated within the first bend of the S configuration, similar to that in a single bend. These are stretched along the curvature, decreasing in diameter and increasing in strength. Similar secondary flows are developed within the second bend, but in the opposite direction; the strength of the secondary flow in each bend will determine the prevailing flow structure in the entire S dual bend. Small angles of curvature were found to suppress the swirling structures in the second bend in laminar flows, since the curvature was found to be not large enough for the flow in the second bend to recover from the first swirl [5, 7]. In this case, two double swirls turning in opposite directions were observed in the second bend and downstream of the dual bends. Very large angles could result in very strong vortices in the second bend that can diminish the intensity of vortices in the first bend. In dual 90° S-shape bends [8], the second bend could generate secondary structures that are able to overcome those generated in the first bend. The average turbulence level measured at several locations downstream of an S shape dual bend was found to decrease when the separation distance  $L/D$  was increased from 0 to 1 [9]. The velocity field was found to be oscillating non-

symmetric in the cross section downstream of the dual bend. This asymmetry was attributed to the developing flow at the inlet to the S-bend.

The effect of radius of curvature on the mass transfer distribution in bends was investigated by [12, 13, 14, 15]. The maximum mass transfer enhancement is found to increase as the bend radius to diameter ratio ( $r/D$ ) is decreased, which could be attributed to the increase in strength of the secondary flow structures and/or increase in turbulence levels. The effect of Reynolds number on the Sherwood number has been investigated for single  $90^\circ$  bends [12, 13]. For rough wall bends, the average  $Sh$  over the bend test section was found to scale as  $Re^{0.925}$  over a range of turbulent flow conditions [12], while the local maximum was found to scale as  $Re^{0.84}$  for smooth wall bends [13]. The maximum  $Sh$  in single bends was measured using a dissolving wall experimental technique and found to scale as  $Re^{0.92}$  [16], which agreed with the average  $Sh$  scaling by [12]. In the case of dual bends, only the U- bend configuration has been investigated using small and large curvature bends ( $r/D$  of 2.5 and 7.3) for a range of laminar and turbulent flows [17]. The maximum mass transfer in this case was reported to scale as  $Re^{0.86}$  for the smooth wall case and  $Re^1$  for the rough wall case. The Reynolds number range at which the mass transfer coefficient shifts from smooth to fully rough levels is found to decrease with an increase in the angle of curvature [4].

Heretofore, there have been no mass transfer studies in dual S-bend configurations. Thus, the objective of the current study is to investigate the local mass transfer distribution in dual bends arranged in an S-configuration. In particular, the effect of separation distance between the two bends and the effect of Reynolds number on the mass transfer

enhancement were determined. The dissolution of gypsum test sections in water was used to measure the mass transfer rate. The methodology provides a Schmidt number ( $Sc$ ) of 1280 which is analogous to the diffusion of ferrous ions  $Fe^{+2}$  in water [16]. Experiments were performed for separation distances of 0, 1 and 5 pipe diameters between the bends at  $Re$  of 70,000 and at  $Re$  in the range 40,000 to 130,000 for the  $L/D=0$  separation case.

#### **4.2 Experimental methodology and data reduction**

Experiments were performed in a 2.54 cm diameter flow loop shown schematically in figure 4.2. This facility has been used in previous mass transfer studies and is described in detail in [16]. Water is circulated from a 100 liter reservoir through the test facility by a centrifugal pump. The flow rate is regulated by globe valves and measured by a turbine flow meter with an accuracy of  $\pm 1\%$  of the flow reading. The flow is passed through a perforated plate followed by a honey-comb before entering a straight pipe with a length of 160 cm leading to the test section. The flow exited the test section to a 75 cm long straight pipe before being directed back to the reservoir. The water temperature was measured in the reservoir and controlled to within  $\pm 0.5$  °C using a compensation cooling loop. The amount of Gypsum dissolved in the water during the experiment was determined by measuring the electrical conductivity of the water. A calibration experiment was performed to correlate the amount of dissolved Gypsum to the increase in conductivity of the water.

The bend test sections consisted of an upstream 20 cm long straight pipe, two standard 90 degree bends with a radius of curvature of 3.81 cm ( $r/D=1.5$ ) arranged in an S-

configuration and a downstream 10 cm long straight pipe with a nominal diameter of 2.54 cm. The test sections were cast from gypsum in segments with delay intervals between every two segments to allow for partial curing. The gypsum was generated by mixing Hydrocal ( $\text{CaSO}_4 \cdot 1/2\text{H}_2\text{O}$ ) with water that yields gypsum with a density of  $1550 \text{ (kg/m}^3\text{)}$ . The repeatability of the cast test sections was qualified by comparing the surface scan obtained from a laser coordinate measurement machine (CMM) of three different unworn test sections. The variability in the test section diameter among the samples was  $\pm 0.7\%$ .

The gypsum test sections were tested in the facility by flowing water through it for a specific period of time, typically 40 to 100 minutes. After each test, the test section was allowed to dry until the weight reached a constant value, in typically 7 to 10 days. The worn surface topography of the test section at the end of each test was determined by cutting the section into two halves along the bend middle line using a 0.5mm blade band saw. This process led to a loss of approximately 10 degrees of the bend circumference on each of the side walls. A schematic of the test section angles, orientation and the profiles along the bend cut is shown in figure 4.3. The two halves of the test section were laser scanned separately to obtain the worn surface topography to a resolution of 0.2 mm. Multiple scans with overlap between scans were performed to increase the scanned spatial resolution and to ensure that all surface details were captured. The scanned surface coordinates were initially aligned to a common coordinate system using commercial image processing software by fitting three orthogonal planes on the scan image of the test section block outer surface. This process was followed by post processing using in-house Matlab routines to re-grid the data points to a spatially uniform grid of  $0.25 \times 0.25 \text{ mm}$ .

The test section alignment is checked based on axi-symmetry of the surface topography in the upstream pipe and symmetry in the entire test section, as outlined in [16].

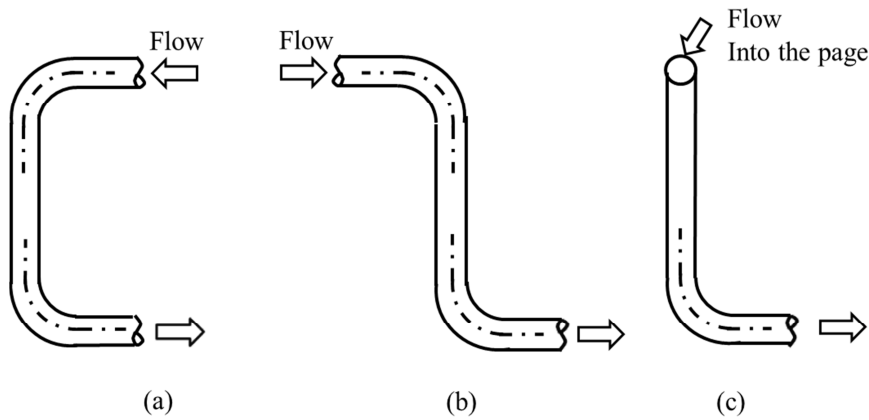


**Figure 4.1: Schematic of the different dual bend configurations in a) U -shape, b) S - shape and c) out of plane configurations**

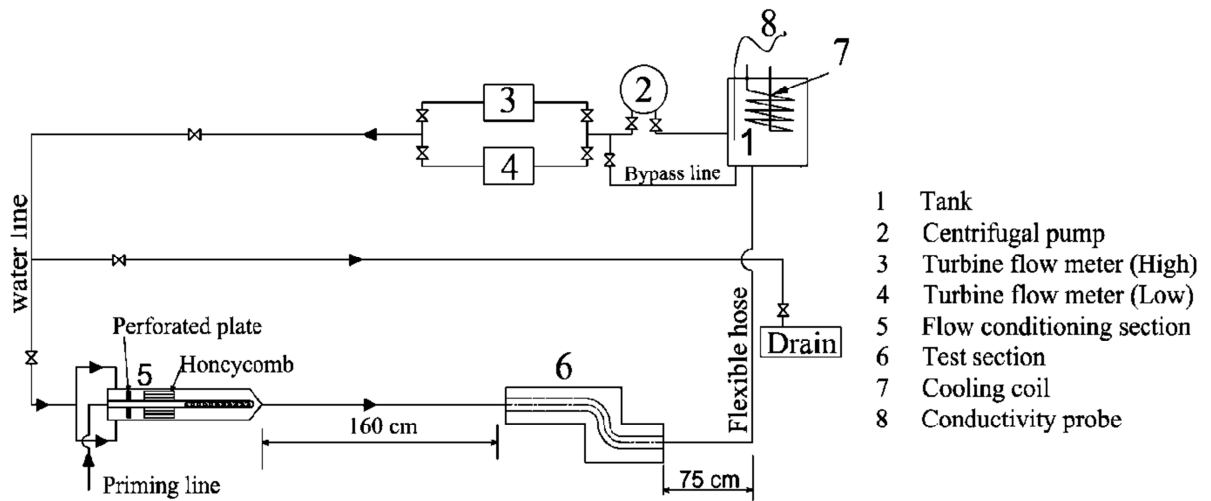


**Figure 4.2: Schematic of the test facility showing the main components of the flow loop**

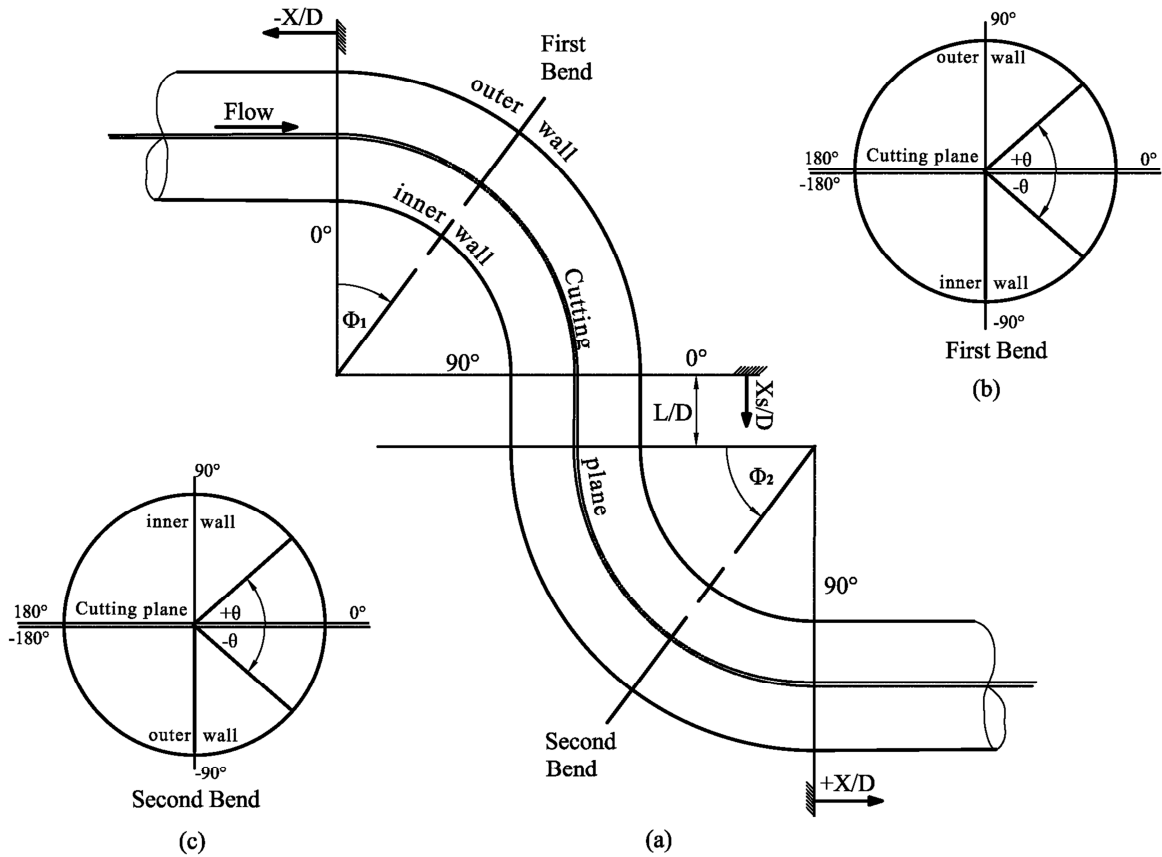


**Figure 4.3: Schematic of the test section showing the section planes relative to (a) streamwise orientation, (b) crosswise orientation in the first bend (c) crosswise orientation in the second bend**

**Table 4.1: Nomenclature of quantities and terms.**

Nomenclature

$dm/dt$	Mass transfer rate	$[Kg/s]$
$C_w$	Hydrocal ions concentration at the wall	$[Kg/m^3]$
$C_b$	Hydrocal ions concentration in the bulk fluid	$[Kg/m^3]$
$\Delta C_o$	Initial concentration difference	$[Kg/m^3]$
$\delta$	Local instantenous wear of the test section	$[m]$
$D$	Bend cross sectional diameter	$[m]$

$D_m$	Mass diffusivity for Hydrocal in water determined at 25 °C	$[m^2/s]$
$e$	Roughness height	$[m]$
$e/D$	Relative roughness height	$[m]$
$e^+$	Roughness scale	
$h$	Mass transfer coefficient	$[m/s]$
$Sc$	Schmidt number $(\nu/D_m)$	
$Sh$	Sherwood number $(h \times D/D_m)$	
$X/D$	Streamwise dimensionless distance	
$X_s/D$	Location along separation pipe	
$L/D$	Separation distance	
$\rho$	Density of the gypsum	$[Kg/m^3]$
$\theta$	Bend cross sectional angle	
$\phi_1$	Bend angle of curvature (along first bend)	
$\phi_2$	Bend angle of curvature (along second bend)	
$\nu$	Kinematic viscosity	$[m^2/s]$

Table 1: Factors affecting total uncertainty in local mass transfer coefficient

Parameter		Uncertainty
Depth scanning	[mm]	$\pm 3.9\%$ Nominal wear
Casting variability	[mm]	$\pm 8\%$ Nominal wear
Concentration ( $\Delta C$ )	[g/l]	$\pm 4\%$
Testing time	[min]	$\pm 1\%$
Density ( $\rho$ )	[kg/m <sup>3</sup> ]	$\pm 4\%$

A moving average using a 2mm x 2mm window is used to obtain the local average surface topography. The roughness is evaluated by subtracting the surface obtained from the moving average from the original uniform grid surface scan. The total mass removed from the test section during the experiment was determined by three methods: (i) from the mass of the test section before and after the test, (ii) from the concentration of the dissolved gypsum in the water at the end of the test and (iii) from the integrated mass removed computed from the laser digitized 3d surface scan. The mass removed calculated from the different methods agreed to within  $\pm 7\%$ .

The normal local deviations of the worn scan surface from the unworn scan surface is used to determine the thickness  $\delta$  removed at every point on the surface. The local mass transfer coefficient is determined from

$$\rho \frac{d\delta}{dt} = h\Delta C \quad (1)$$

where  $\delta$  is the thickness of local mass removed normal to the surface,  $\Delta C$  is the difference between species concentration at the wall and in the bulk flow and  $h$  is the mass transfer coefficient. The concentration difference decreases over the course of the experimental time due to the dissolution of the gypsum in water, and thus the driving potential for the mass transfer decreases. The mass transfer coefficient was computed using a modified time to account for the change in concentration difference during the run time as

$$\rho \frac{d\delta}{d\tau_{\text{mod}}} = h\Delta C_o \quad (2)$$

where  $\tau_{\text{mod}}$  is the modified time given by

$$\tau_{\text{mod}} = \frac{1}{\Delta C_o} \int_0^t [C_w - C_b] \cdot dt \quad (3)$$

Then the Sherwood number is calculated as

$$Sh = \frac{h \times D}{D_m} \quad (4)$$

where  $D$  is the pipe diameter and  $D_m$  is the mass diffusivity. The rate of change in the wear is computed at every local point to determine the spatial distribution of the mass transfer rate. The uncertainty in the local mass transfer coefficient was evaluated considering all the contributing parameters listed in Table 4.2. The major contributing factors to the overall uncertainty in the mass transfer was in the variability in the casting and the scanning accuracy for the local wear measurement. The uncertainty in the calculation of the local mass transfer coefficient was determined to be approximately  $\pm 18\%$ . Experiments were performed with different initial bulk gypsum concentrations in the water to determine the role of erosion, if any, to the mass removal. The local  $Sh$  distribution did not change to within experimental uncertainty with the different initial bulk concentrations, confirming that erosion was not present in the current tests.

The effect of separation distance on the mass transfer distribution was investigated for separation distances of  $L/D=0, 1$  and  $5$  at  $Re=70,000$ . The effect of Reynolds number on the mass transfer enhancement was also examined for the  $L/D=0$  separation case for  $Re$  in the range  $40,000$  to  $130,000$ . The mass transfer coefficient for the  $Re=70,000$  experiments is obtained using multiple test times of  $40, 60, 80$  min. The mass transfer at the other Reynolds numbers are obtained using individual time tests with testing times that resulted

in similar nominal mass removal to the longer time experiments for the  $Re=70,000$  case, as described in [16].

### 4.3 Results and discussion

The local Sherwood number ( $Sh$ ) distribution in the S-shape dual bends for the three different separation distances at  $Re=70,000$  obtained from the experimental measurements are shown in figure 4.4. The  $Sh$  contours are shown starting from 4 diameters upstream of the first bend and continuing up to 3 diameters downstream of the second bend. The  $Sh$  distribution is nearly uniform in the upstream pipe with a value of approximately 3000. This value is higher than the smooth pipe data [17] and slightly below the rough pipe data [18], and will be discussed later. There are three regions of significant mass transfer enhancement: (i) on the inner wall at the inlet to the first bend, (ii) over the latter part of the first bend outer wall and extending into the first part of the second bend inner wall, and (iii) midway into the second bend inner wall. The scan images of the surface topography of the worn sections are shown in figure 4.5. Surface wear patterns in the form of streaks that are inclined to the centerline are clearly seen on the inner wall at the inlet to the first bend, corresponding to the first region of high mass transfer. These surface wear pattern streaks indicate flow acceleration into the bend and development of a swirling flow, similar to those observed for a single bend [16]. The depth of these streaky wear patterns are much shallower for  $L/D=0$  and increase as the separation distance increases. This could be attributed to the suppression of the swirls in the first bend by the opposite swirls in the second bend [13]. The second region of high mass transfer is accompanied by a longitudinal streaky wear pattern on the outer wall of the first bend, which

extends into the second bend inner wall. This region is attributed to the superimposition of the acceleration due to the shift of the core flow toward the outer wall in the first bend, similar to the single bend case. The acceleration into the second bend due to the curvature likely intensifies this acceleration and results in a significant increase in the mass transfer enhancement in this region. The mass transfer enhancement decreases as the separation distance increases as the effect of the second bend decreases with increasing separation distance. The third region of high mass transfer observed on the second bend inner wall is in the form of two similar localized regions offset from the bend center line. The surface topography show inclined streaks toward the centerline in this region that is likely due to the developing swirling flow in the second bend. These localized regions are most prominent in the  $L/D=0$  case and diminish as the separation distance increases.

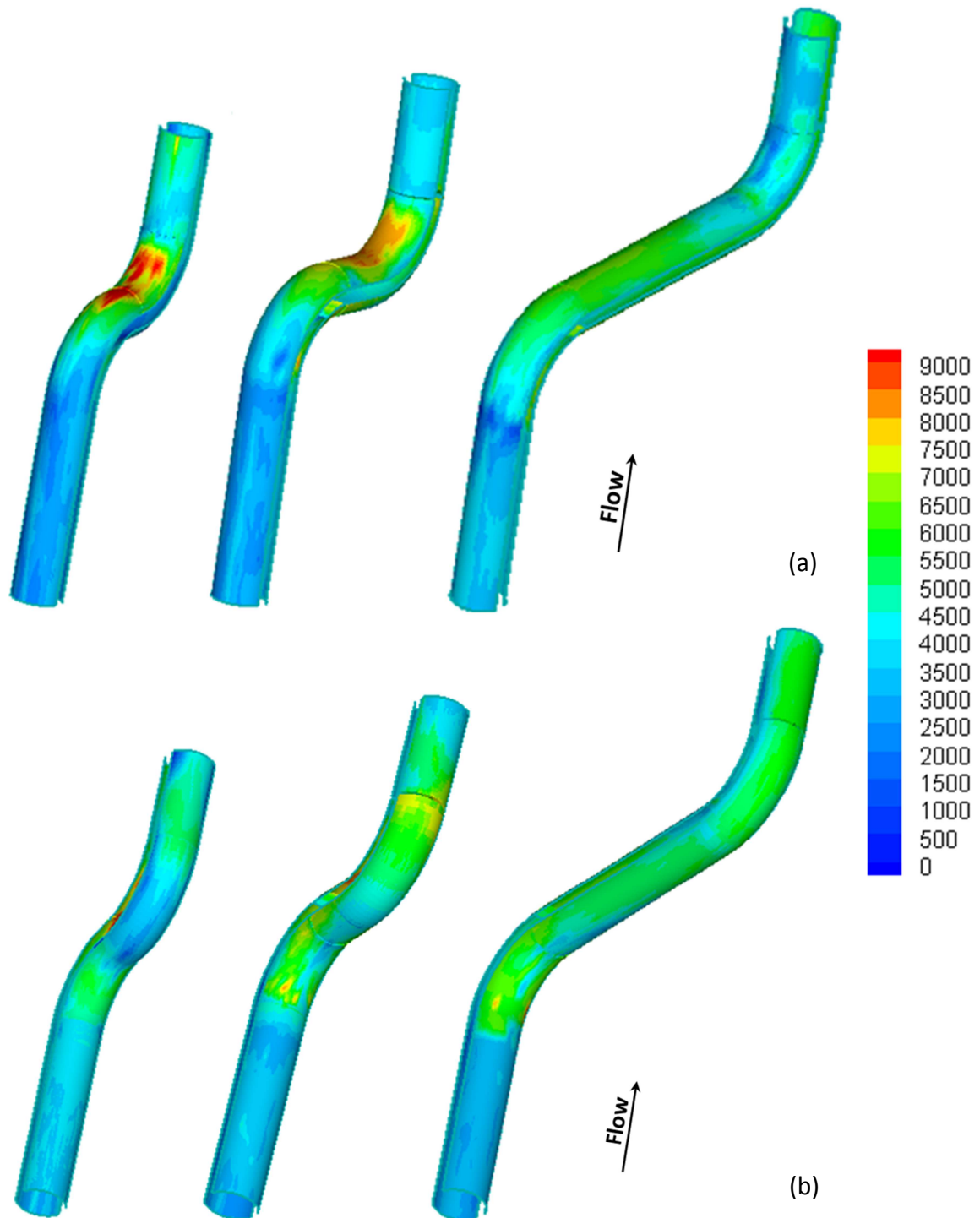
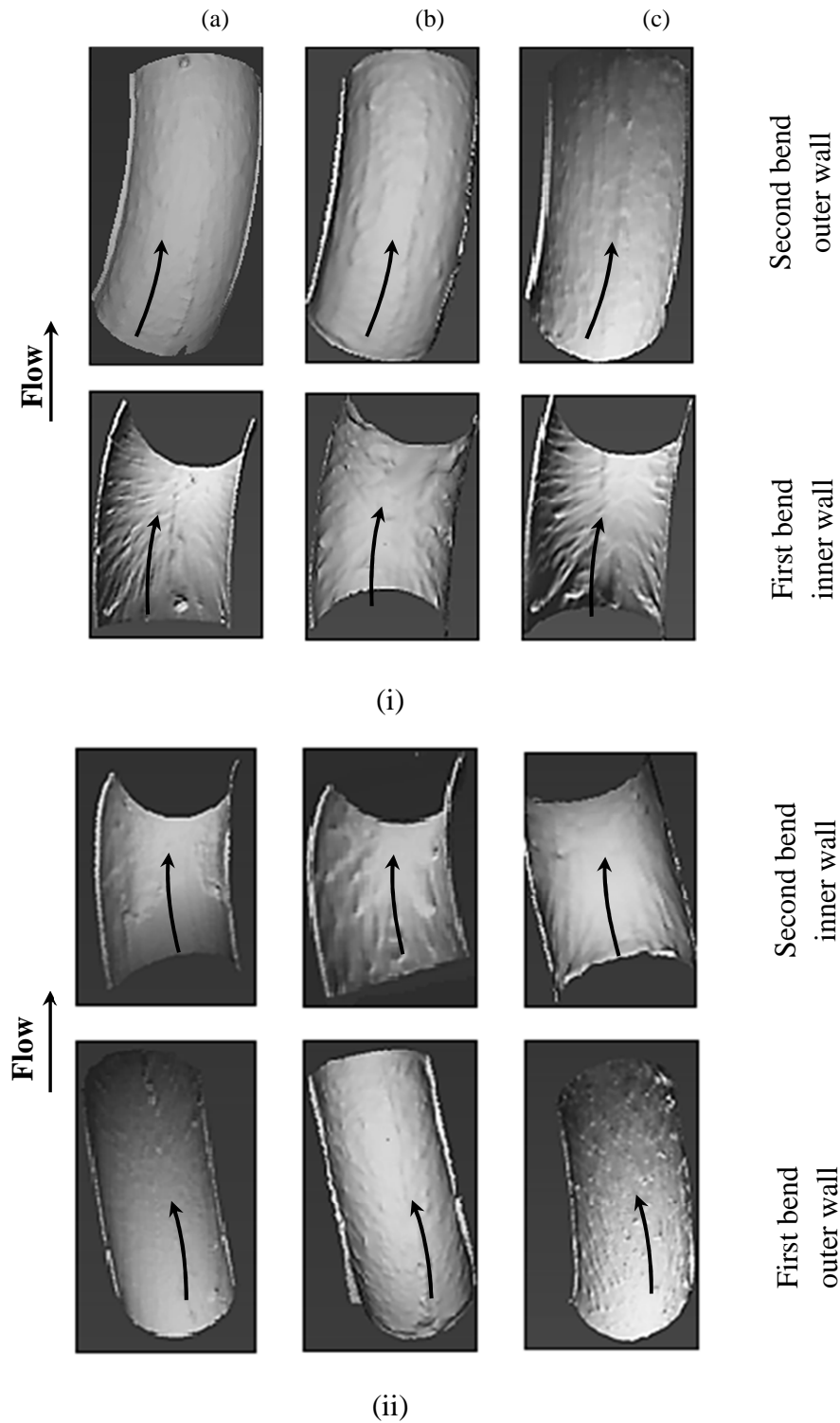


Figure 4.4: Local Sherwood number distribution at  $Re=70,000$  and  $Sc=1280$  for separation distances of  $L/D= 0, 1$  and  $5$ , arranged from left to right. (a) Side view consisting of the first bend outer wall and second bend inner wall (b) Side view consisting of the first bend inner wall and second bend outer wall

The  $Sh$  profiles normalized by the value in the upstream pipe ( $Sh/Sh_{pipe}$ ) along the streamwise direction at  $\theta = \pm 90^\circ$  for the three separation distances are compared with the single bend case [16] in figure 4.6. The mass transfer near the inlet to the first bend tends to increase where the flow acceleration into the bend inner wall is expected and decrease where flow deceleration into the outer wall side is expected. Along the centerline of the outer wall of the first bend the mass transfer increases to reach a maximum close to the outlet for the  $L/D=0$  case (figure 4.6,a). The slope of the  $Sh$  profile in the first bend outer wall is significantly higher than that of the single bend case for  $L/D=0$  and decreases with separation distance to approach that of the single bend for  $L/D=5$ . For the bends with separation distances  $L/D=1$  and 5, the mass transfer continues to increase into the separation pipe and reaches a maximum at  $X_s/D$  of approximately 0.95 and 2, respectively. Here,  $X_s$  is the streamwise distance along the centerline measured from the end of the first bend. The peak value was largest for the  $L/D=0$  case and decreased with an increase in the separation distance. A local maximum occurs on the inner wall of the second bend for  $L/D=0$  and 1 separations; however, it was not observed in the  $L/D=5$  case.



**Figure 4.5: Scan images of the test sections for separation distances of (a)  $L/D = 0$  (b) 1 (c) 5 for: (i) first bend inner wall and second bend outer wall, (ii) first bend outer wall and second bend inner wall**

The  $Sh/Sh_{pipe}$  increases along the inner wall of the first bend with a local maximum near the inlet (figure 4.6b), which can be attributed to the flow acceleration. The peak value is smaller in the  $L/D=0$  case, and increases as the separation distance increases to approach the value for the single bend case at  $L/D=5$ . The mass transfer decreases along the latter part of the first bend that could be due to flow separation followed by flow deceleration on the second bend outer wall [4]. The  $Sh$  profile along the first bend inner wall was similar to that of the single bend, however, it was lower in magnitude for  $L/D=0$  and increases with separation distance to approach the single bend for  $L/D=5$ . The mass transfer on the outer wall of the second bend increases gradually toward the outlet of the bend to form a second peak. This peak is also lower for the  $L/D=0$  case and increases with the separation distance.

Azimuthal profiles of  $Sh/Sh_{pipe}$  at different locations along the bend curvature are shown in figure 4.7. The mass transfer distribution in the upstream pipe at  $X/D=-2$  is nearly uniform for the different separation cases. The profiles across the inner and outer walls of the first bend have several features in common for the different separation distances. The maximum that occurs near the inlet of the first bend inner wall at  $\phi_I=10^\circ$  spans over approximately  $\theta$  from 45 to 135°. The magnitude of the maximum increases from approximately 1.5 for the  $L/D=0$  case to 1.6 and 1.7 for  $L/D=1$  and 5, respectively. The peak shifts outward from the centerline along the bend curvature, near  $\phi_I$  of 30°, resulting in a mass transfer valley around the centerline ( $\theta=-90^\circ$ ). The valley in the mass transfer distribution can be attributed to flow separation due to the bend curvature. The depth

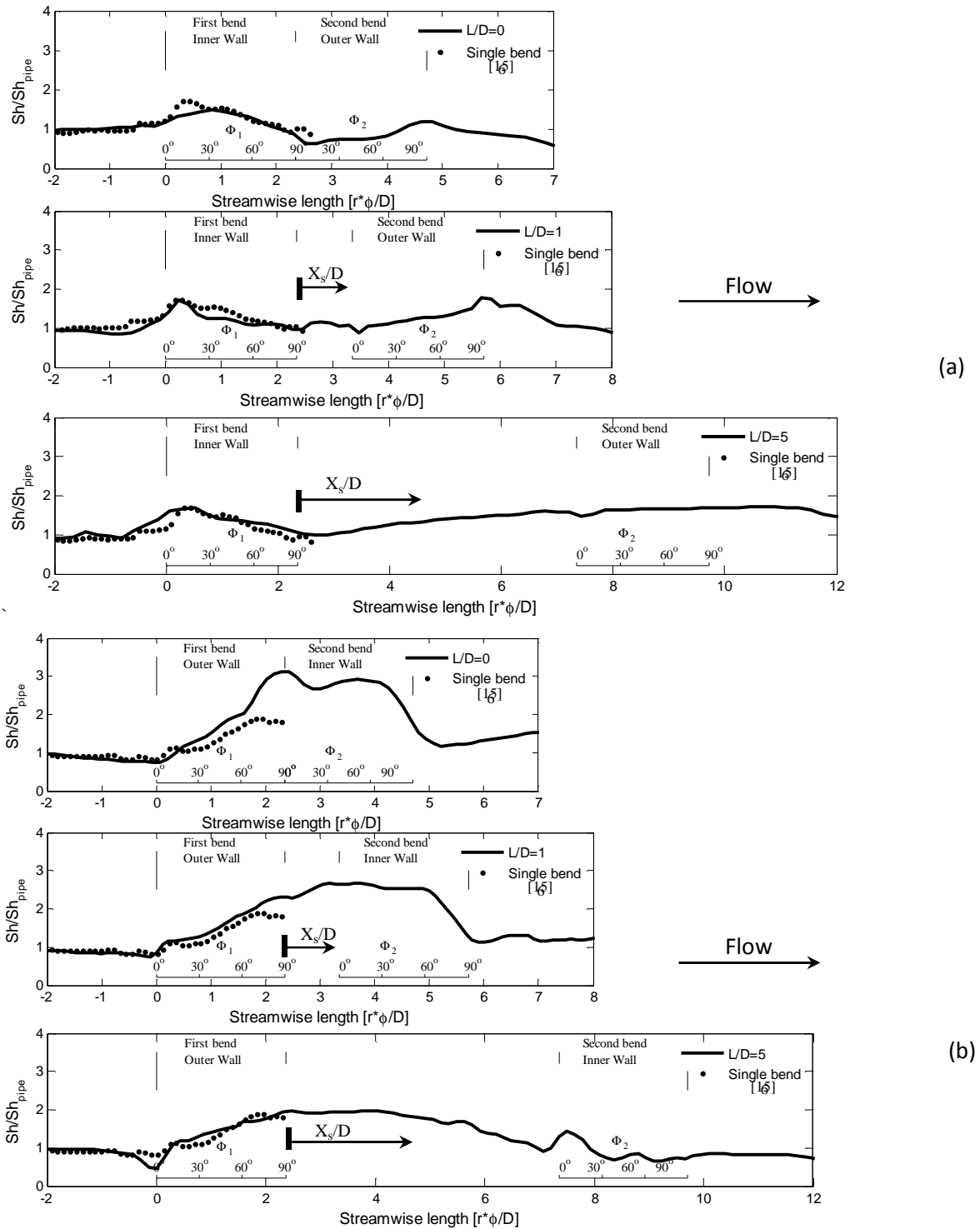


**Figure 4.6: Profiles of  $Sh/Sh_{pipe}$  along (a) first bend outer wall and second bend inner wall and (b) first bend inner wall and second bend outer wall at  $Re=70,000$  and  $Sc=1280$ .**

of the valley decreases as the separation distance is decreased which could be due to suppression of the flow structures in the first bend by that of the second bend. For the  $L/D=0$  separation case, the mass transfer continues to decay toward the second bend outer wall up to approximately  $\phi_2=10^\circ$ . The mass transfer then increases from this location to reach a local maximum outside the second bend outer wall near  $X/D=1$ . The peak covers approximately  $45^\circ$  on each side of the centerline and reaches a magnitude of approximately 1.4. For the  $L/D=1$  separation case, the mass transfer reaches a nearly constant value in the separation pipe and increases gradually from the inlet to the second bend outer wall to reach a peak near the bend outlet of nearly the same magnitude as the  $L/D=0$  case and decays from this location onward. For  $L/D=5$ , the mass transfer remains constant from the outlet of the first bend inner wall until one diameter into the separation pipe and then gradually increases along the pipe and into the second bend outer wall to reach a peak near the outlet and over the first part of the downstream pipe,  $X/D=1$ . The peak spans over approximately 45 degrees on each side of the centerline and is nearly 1.7 in magnitude.

On the first bend outer wall for  $L/D=0$ , the mass transfer reaches a maximum at the location between the first bend outer wall and the second bend inner wall ( $\phi_1=90^\circ$  and  $\phi_2=0^\circ$ ). The maximum region spans over approximately  $20^\circ$  on each side of the centerline with a magnitude of 3.2. The mass transfer decays from this location into the second bend inner wall and moves outwards to the sidewalls near  $\phi_2=50^\circ$ , while the magnitude decreases to approximately 2.8 at  $\theta=-45$  and  $-135^\circ$ . The mass transfer peaks off the

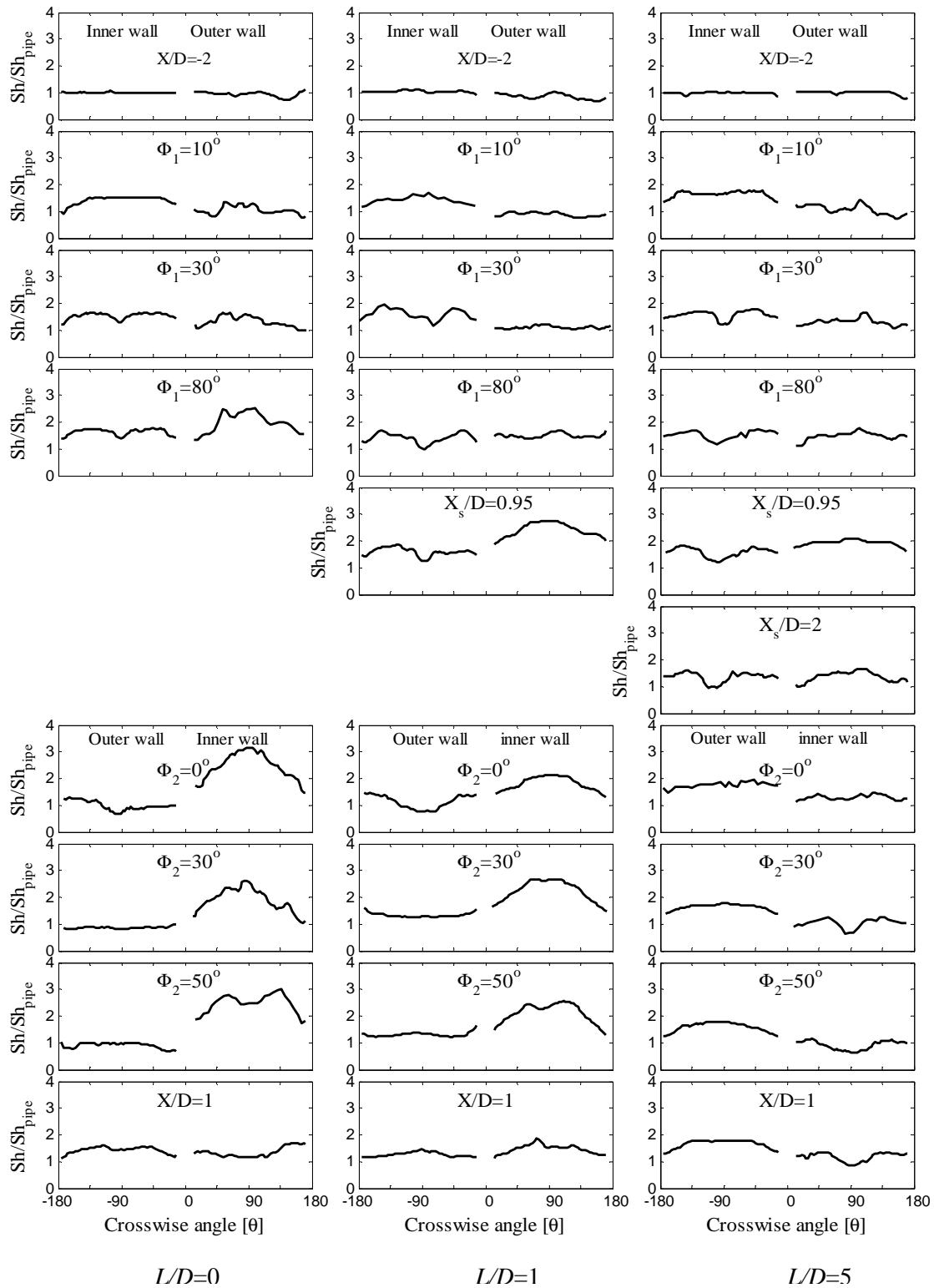


**Figure 4.7: Azimuthal profiles of  $Sh/Sh_{pipe}$  at different locations along the Dual bend profile for separation distances of 0D, 1D and 5D, arranged from left to right**

centerline are likely caused by the counter rotating vortices developed in the second bend [11]. The mass transfer decreases from this location onward. No clear features for flow separation are observed in the inner wall of the second bend. For  $L/D=1$ , the mass transfer continue to increase downstream of the first bend outer wall to reach a peak near the end of the separation pipe,  $X_s/D \sim 0.95$ . The span of the peak is wider than the  $L/D=0$  case, from  $\theta = -45$  to  $-135^\circ$  with a magnitude of approximately 2.8. Similar to the  $L/D=0$  case, the mass transfer decreases through the second bend inner wall and moves outward and form two peaks off the centerline near  $\theta = -45$  and  $-135^\circ$ . The mass transfer then decays from this location onward. For  $L/D=5$ , the mass transfer continue to increase downstream of the outlet of the first bend outer wall to reach a peak near  $X_s/D \sim 2$ . The peak in this case spreads over  $65^\circ$  on each side of the centerline with a magnitude of 1.9. The mass transfer then decays along the separation pipe. On the second bend inner wall the mass transfer features are relatively similar to the first bend but the magnitude is smaller, which could be due to the effect of the counter swirl in the first bend on that of the second bend.

The peak Sherwood number ( $Sh$ ) in the bend is obtained from the longitudinal and azimuthal profiles of  $Sh$ . The magnitude is then determined using multiple azimuthal profiles around the peak location. The variation of the mass transfer enhancement at the peak locations with separation distance  $L/D$  is shown in figure 4.7. The maximum mass transfer enhancement occurred for  $L/D=0$  with a magnitude of 3.2 compared to 1.8 for the single bend geometry [16]. The enhancement decreases with increasing separation distance to approximately 1.9 for  $L/D=5$ . The enhancement on the second bend inner wall

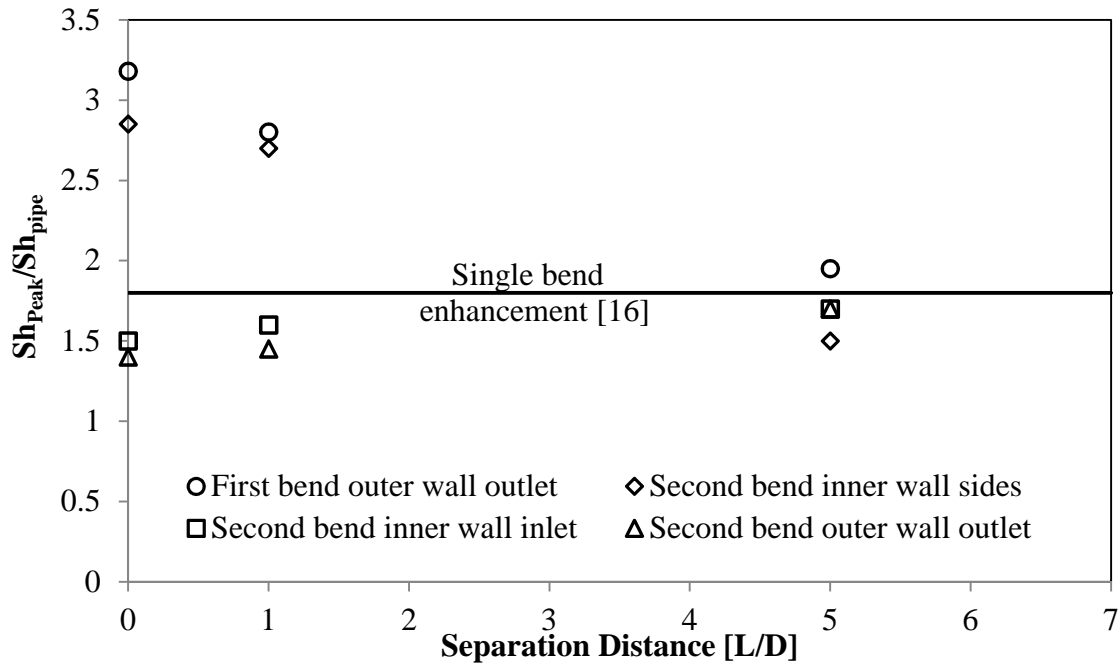


**Figure 4.8: Variation of peak mass transfer enhancement  $Sh_{peak}/Sh_{pipe}$  with separation distance.**

sides is 2.8 and decreases with separation distance. On the first bend inner wall and second bend outer wall, the mass transfer is relatively low and increases slowly with separation distance.

#### 4.4 Effect of Reynolds number

The mass transfer enhancement ( $Sh/Sh_{pipe}$ ) was a maximum for  $L/D=0$ ; therefore, this case is further investigated to determine the effect of Reynolds number on the mass transfer enhancement. Azimuthal profiles of the normalized Sherwood number ( $Sh/Sh_{pipe}$ ) along the dual bend for  $Re$  in the range 40,000 to 130,000 are shown in figure 4.8. There is a collapse of the normalized profiles with slight differences on the latter part of the first bend inner wall, which could be attributed to the downstream shift in the onset of the flow

separation with  $Re$ , similar to what was observed in the single bend case [16]. The mass transfer distributions were similar for the different  $Re$ , and followed the same trends as for the  $Re=70,000$  case, discussed earlier.

The change in the local maximum Sherwood number, observed at the outlet of the first bend outer wall, with Reynolds number is shown in figure 4.9. The current results are compared with existing results in the literature. The local  $Sh$  maxima follow a similar trend with Reynolds number, scaling as  $Re^{0.92}$ , similar to that for a single bend [16]. The variation of the maximum mass transfer enhancement relative to the straight pipe value,  $Sh_{max}/Sh_{pipe}$ , with Reynolds number is shown in figure 4.10, along with the results for a single bend [16] and U- bend [1]. The maximum enhancement when scaled by the value in the pipe is nearly independent of Reynolds number. The maximum mass transfer enhancement in the S- shape is higher than that for the single bend [16] and the U- bend [1]. The trend with  $Re$  agreed with the single bend case [16], but not with the U- bend. The pipe  $Sh$  used to normalize the U- bend results is not known. If smooth pipe data were used, it would explain the difference in the trends since the exponent in the Reynolds number scaling for smooth pipes is always smaller than for rough pipes.

#### **4.5 Roughness discussion**

The worn surface topography obtained from the laser scans was used to estimate the surface roughness. Comparison of the local topography from surface scans with the local averaged topography from a running average yields the local surface undulations. The roughness is evaluated from the undulations of the surface around the local average

surface pattern. The peak to valley of the undulations is used to determine the value of the surface roughness  $e$ . The initial roughness of the test specimen is found to be  $e/D=0.007$ , approximately 10 times less than the final relative roughness level in the upstream pipe. The local relative roughness ( $e/D$ ) distribution over the first and second bends for  $L/D= 0, 1$  and  $5$  are shown in figure 4.12. The surface roughness is formed as surface streaks which correspond to the flow features in this region.

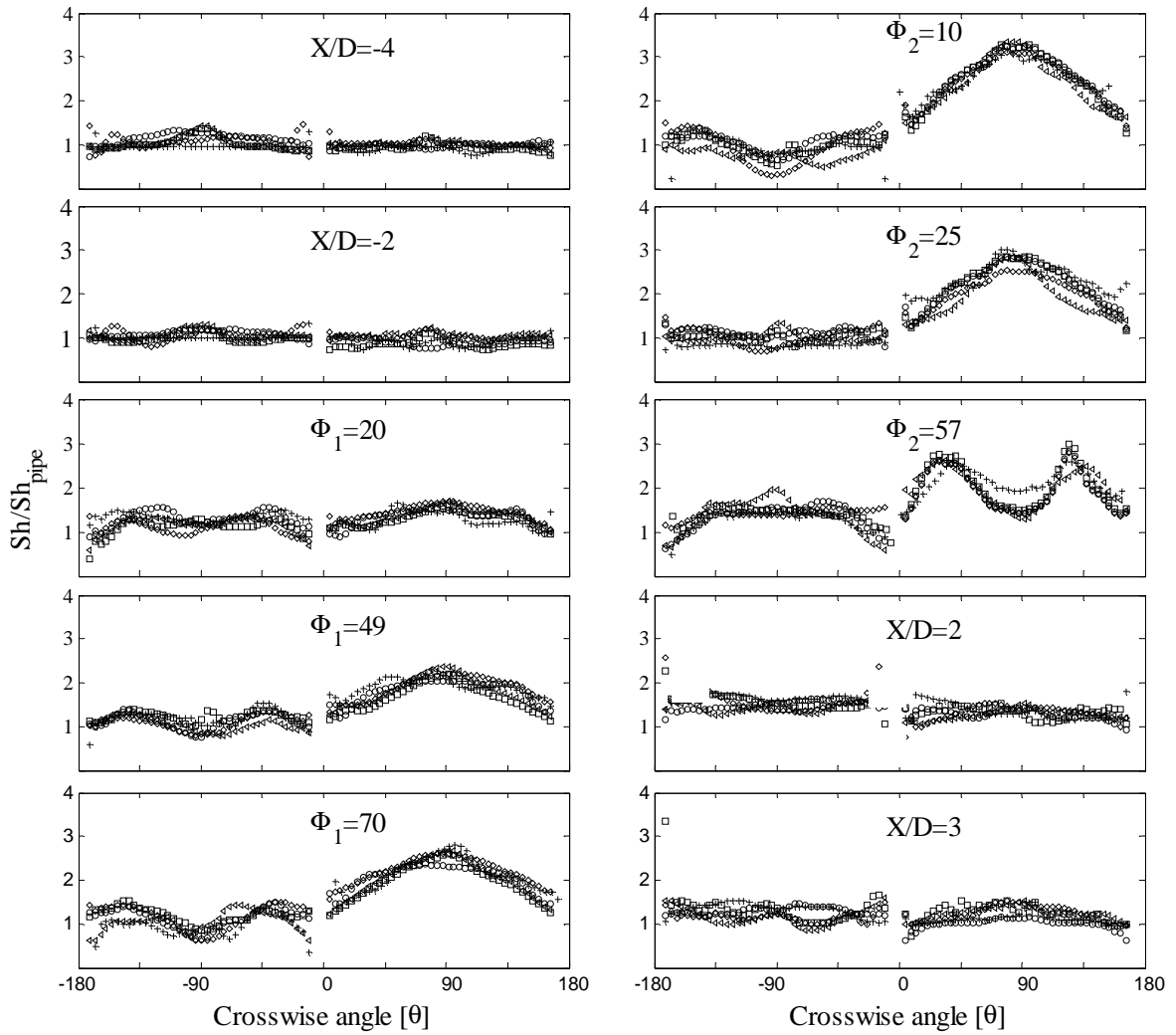


**Figure 4.9: Azimuthal profiles of  $Sh/Sh_{pipe}$  along the streamwise direction along the bend for  $L/D=0$  at  $Re$  of  $\square$  40,000,  $\circ$  60,000,  $\triangleleft$  70,000,  $\nabla$  100,000,  $\diamond$  130,000**

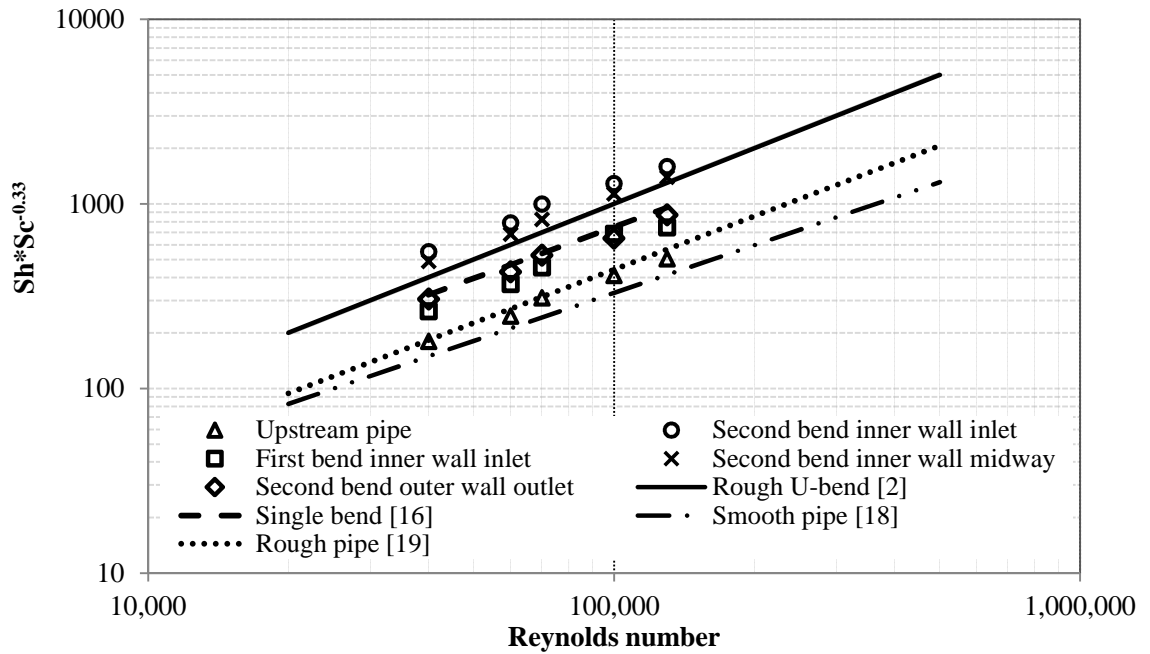


**Figure 4.10:** Variation of the local maximum Sherwood number with Reynolds number, —  $0.01 Re Sc^{0.33}$  [2], - -  $Re^{0.92}$  [16], - · - ·  $0.0165 Re^{0.86} Sc^{0.33}$  [18], ····  $0.007 Re^{0.96} Sc^{0.33}$  [19]

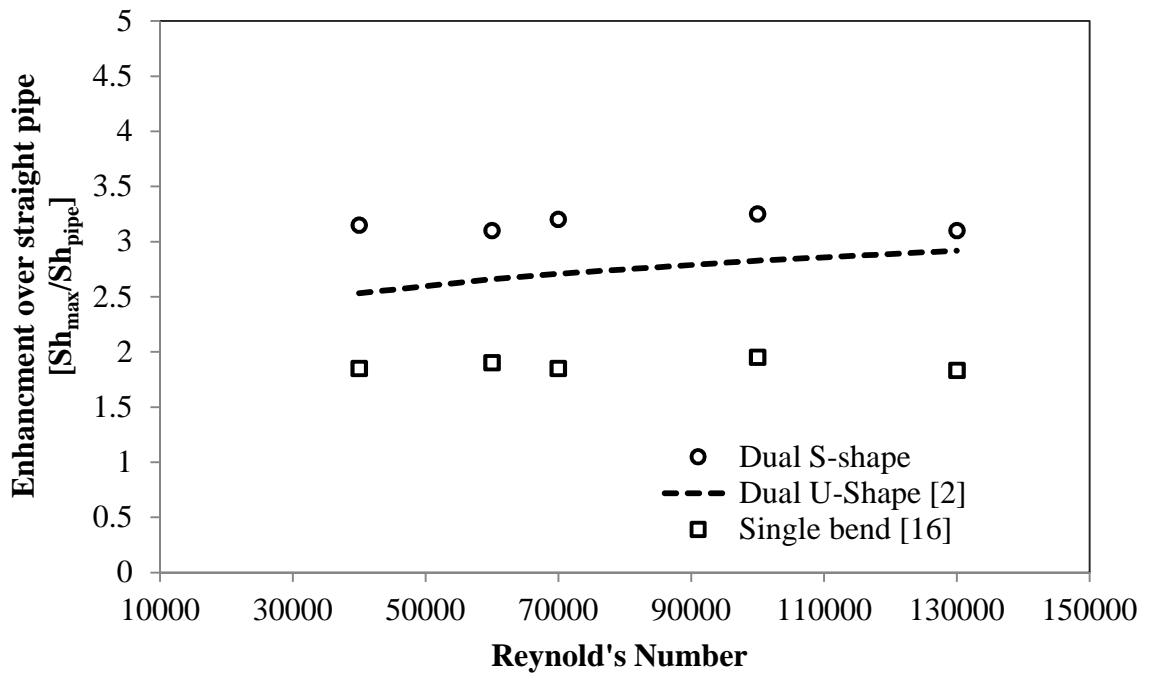


**Figure 4.11:** Variation of mass transfer enhancement in the S-bend compared with existing data for a single bend ( $r/D=1.5$ ) and U-bend ( $r/D=2.5$ ).

The variation of the local relative roughness, obtained from the roughness contours, with separation distance between the first and second bend is shown in figure 4.12. High roughness levels are observed on the latter part of the first bend outer wall and midway into the second bend inner wall and decreases with increase in separation distance. This high roughness corresponds to the areas of flow acceleration and the secondary swirling flow structure observed on the second bend inner wall. On the other side, the first bend inner wall and second bend outer wall, the roughness was found to increase with separation distance, which could be due to suppression of the swirling flow structure in short separation and flow relaxation in the large separation distance. The variation of the peak mass transfer at the different locations with  $L/D$  shows a similar trend to that of the roughness. This suggests that the roughness affects the magnitude of the peak mass transfer. The change in the relative roughness at the locations of the local maximum mass transfer, upstream pipe, first bend inner wall inlet, second bend outer wall outlet, second bend inner wall inlet and midway into the second bend inner wall with  $Re$  is shown in figure 4.13. The relative roughness in the upstream straight pipe was approximately 0.0065 for a Reynolds number of 40,000 and decreased slightly with an increase in Reynolds number which agrees with the observed trend by [19]. Similarly, the roughness at the bend inner wall inlet, side walls and outer wall outlet decreased with Reynolds number.

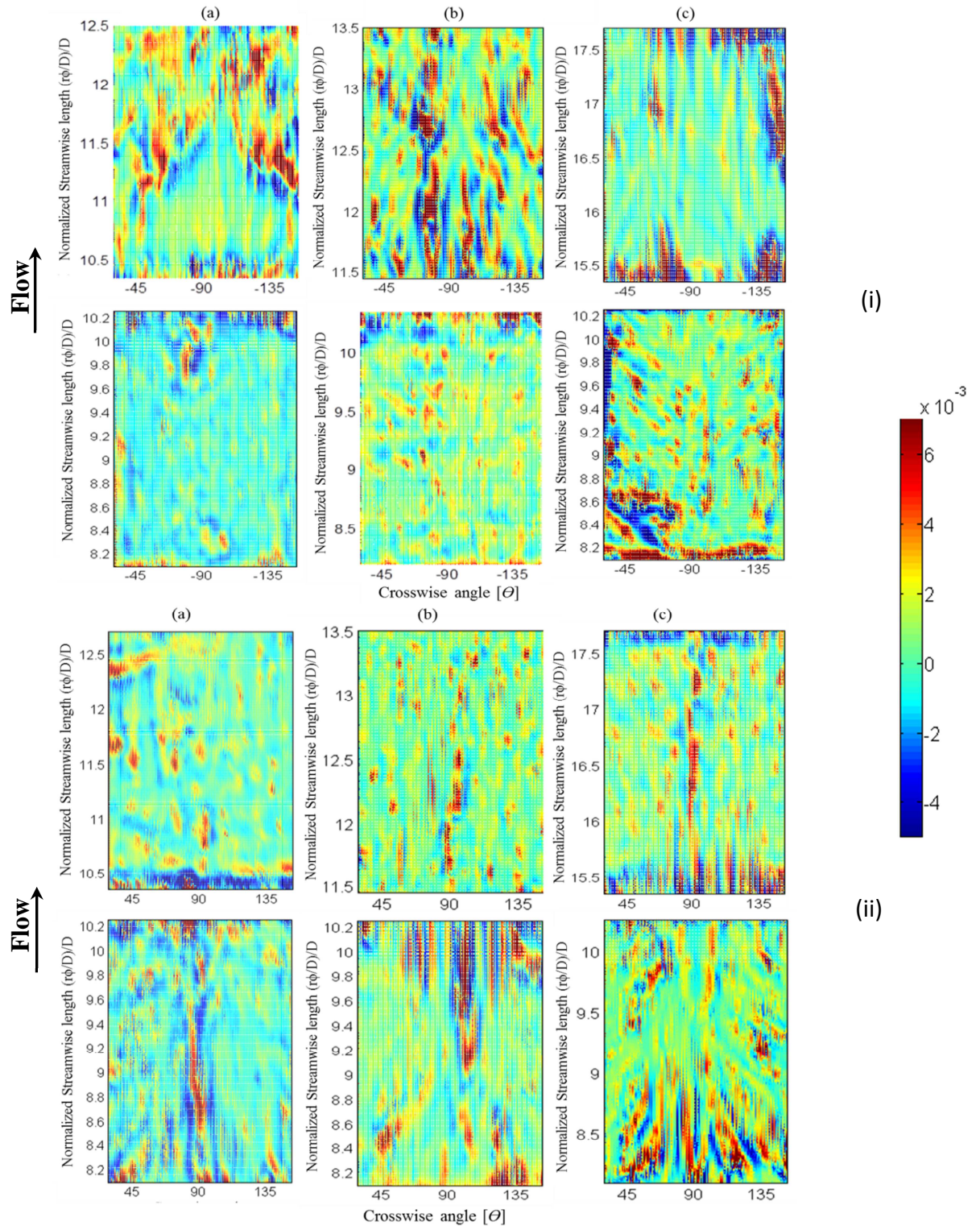


**Figure 4.12: Relative roughness distribution contours for separation distances of (a)  $L/D = 0$  (b) 1 (c) 5 for (i) first bend outer wall and second bend inner wall (ii) first bend inner wall and second bend outer wall**

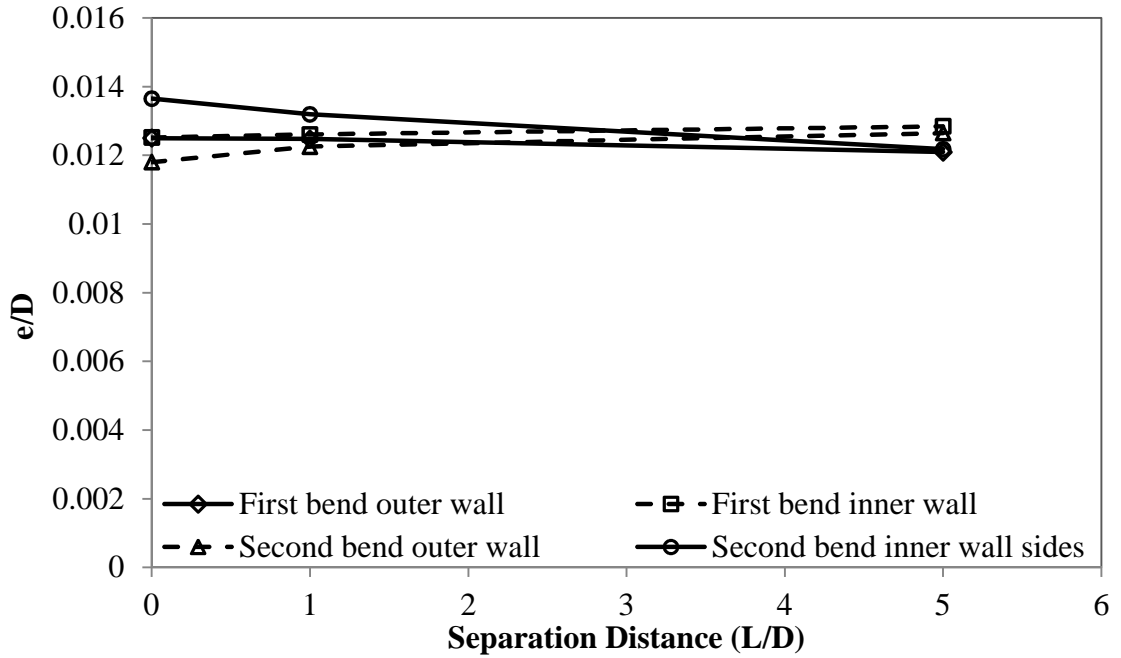


**Figure 4.13: Variation of the relative roughness at different locations along the bend for the different separation distances ( $L/D$ ).**

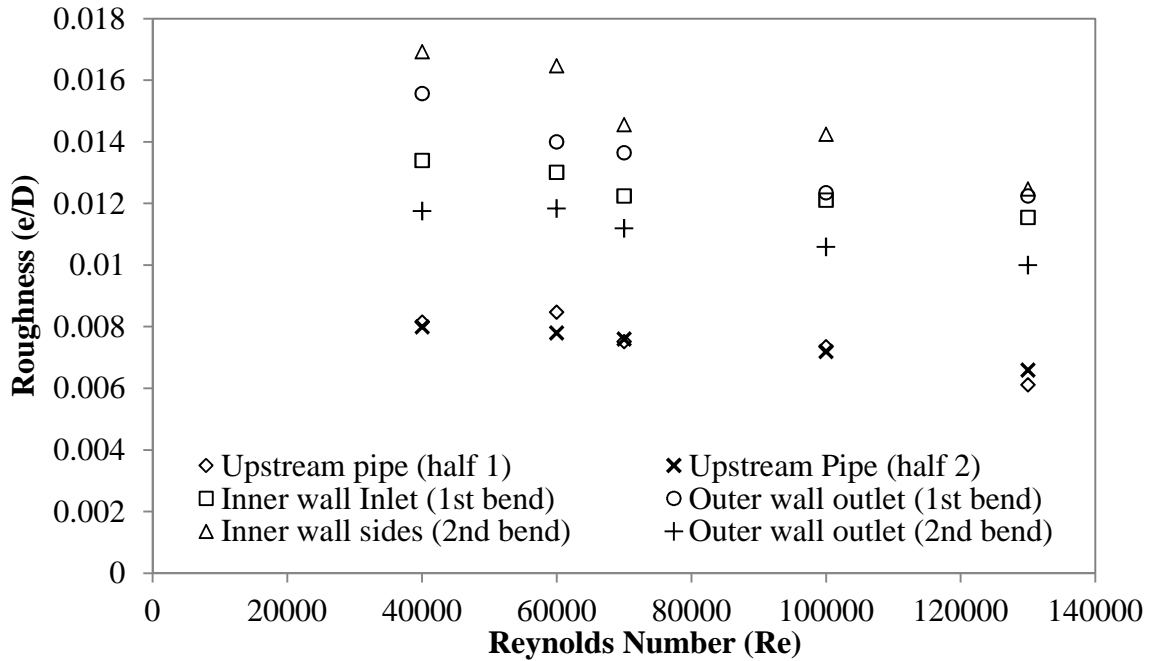


**Figure 4.14: Variation of the relative roughness at the upstream pipe, inlet to bend inner wall and at the outlet of the bend outer wall with Reynolds numbers for  $L/D=0$ .**

#### 4.6 Summary and conclusions

Tests were performed with different lengths of straight pipe between the two bends at a Reynolds number of 70,000. The effect of the Reynolds number was determined by testing at  $Re$  in the range 40,000 to 130,000 for the  $L/D=0$  separation case. Three regions of high mass transfer enhancement were determined: (i) at the inlet to the first bend inner wall, (ii) near the inlet to the second bend inner wall and (iii) midway into the second bend inner wall. The maximum mass transfer occurs in the  $L/D=0$  separation case over the latter part of the first bend outer wall and the first part of the second bend inner wall. The location of this maximum moved downstream of the first bend outer wall as the separation distance was increased. The magnitude of the local maximum enhancement relative to that in a straight pipe was 3.2 for  $L/D=0$ , and decreased to 2.8 and 1.9 as  $L/D$  was increased to 1 and 5, respectively. The surface features in the first bend were shallower than that of the single bend case, and approached the single bend as the separation distance increased. The  $Sh$  scaled with  $Re$  in a similar manner in all regions of high mass transfer with an exponent of 0.93. The location and magnitude of the maximum mass transfer enhancement ( $Sh_{max}/Sh_{pipe}$ ) for the  $L/D=0$  case is nearly independent of Reynolds number. The trend of the roughness and mass transfer enhancement at the peak locations agreed which suggest a direct correlation. The relative roughness is found to decrease slightly with Reynolds number, similar to the case of a straight pipe.

**4.7 References:**

- [1] Poulson, B., The Local Enhancement of Mass Transfer at 180 Degree Bend, International Journal of Heat Mass Transfer, vol. 31, No. 6, p. 1289-1297, (1988)
- [2] Weske, J. R., Experimental Investigation of Velocity distribution Downstream of a Single Duct Bend, N.A.C.A, TN-1471, (1948).
- [3] Sprague, P.J., Patrick, M.A., Wragg, A.A., Coney, M.W.E., Mass Transfer and Erosion Corrosion in Pipe Bends, 8<sup>th</sup> Congress European de Corrosion, Vol. 12 (2), 19-21 (November 1985)
- [4] Taylor, A. M., Whitelaw, J. H., Yianneskis, M., Developing Flow in S-shaped ducts 2: Circular Cross-Section Duct, NASA Contractor Report 3759, (1984)
- [5] Rudolf, P., Desova, M., Flow Characteristics of Curved Ducts, Applied and Computational Mechanics, vol. 1, p. 255- 264, (2007)
- [6] Niazmand, H., Jaghargh E. R., Bend Sweep Angle and Reynolds Number Effects on Hemodynamics of S-shaped Arteries, Annal of Biomedical Engineering, vol. 38, no. 9, p. 2817-2828, (2010)
- [7] Doorly, D., Sherwin, S. J., Geometry and Flow, Cardiovascular Mathematics: Modeling and Simulation of the circulatory System, Springer 2009
- [8] Yoshida, K., Kazuhisa, Y., Hashimue, H., Specificity of flow structure in a dual elbow and its visualization by PIV measurement, Proceedings of the 16th International

conference on Nuclear Engineering, ICONE 16, Florida, USA, May 11-15, p. 293- 299, (2008)

[9] Yuki, K., Hasegawa, S., Sato, T., Hashizume, H., Aizawa, K., Yamano, H., Matched refractive-index PIV visualization of complex flow structure in a three-dimensionally connected dual elbow, Nuclear Engineering and Design, vol. 241, p. 4544–4550, (2011)

[10] Sudo, K., Sumida, M., Hibara, H., Experimental investigation on turbulent flow through a circular 180 degree bend, Experiments In Fluids, vol. 28, p. 51- 57, (2000)

[11] Coney, M. Erosion Corrosion, The Calculation of Mass Transfer Coefficients, CERL Report RD/L/N197, (1980)

[12] Wilkin, S. J., Oates, H. S., Coney, M., Mass Transfer on Straight Pipes and 90° Bends Measured by The Dissolution of Plaster, (1st Edn). Central Electricity Research Laboratories, TPRD/L/2469/N83, (1983)

[13] Achenbach, E., Mass Transfer From Bends of Circular Cross Section to Air, Future Energy Production Systems, Academic Press, New York, vol. 1, p. 327-337, (1976)

[14] Sparrow, E. M., and Chrysler, G. M., Turbulent Flow and Heat Transfer in Bends of Circular Cross Section: i-Heat transfer experiments, ASME J. Heat Transfer, vol. 108, p. 40-47, (1986)

- [15] Mazhar, H., Ewing, D., Cotton, J. S., Ching, C. Y., Experimental Investigation of Mass Transfer in 90 Degree Pipe Bends using a Dissolvable Wall Technique, *International Journal of Heat and Mass Transfer*, 65, p. 280–288, (2013)
- [16] Poulson, B., Advances in Understanding Hydrodynamic Effects on Corrosion, *Corrosion Science*, vol. 35, no. 1-4, p. 655-665, (1993)
- [17] Berger, F. P., Hau, K. F., Mass Transfer in Turbulent Pipe Flow Measured by the Electrochemical Method, *International Journal of Heat Mass Transfer*, vol. 20, p. 1185-1194, (1977)
- [18] Postlethwaite, J., Lotz, U., Mass transfer at erosion–corrosion roughened surfaces, *Canadian J. Chem. Eng.*, p. 66- 75, (1988)
- [19] Poulson, B., Complexities in Predicting Erosion Corrosion, *Wear* 233- 235, pp. 497-504, (1999)

## CHAPTER 5

---

### Flow field characteristics in single and dual S- shape 90° bends

#### Abstract:

The flow field in single and dual S- shape short radius 90° bends was measured using Particle Image Velocimetry (PIV) at Reynolds numbers of 40,000 and 70,000. The flow upstream of the bend was fully developed and in good agreement with the literature. The highest velocity was on the first part of the second bend inner wall of the dual S- shape bend. An increasing turbulent kinetic energy is observed along the first bend outer wall and downstream of the separation zone of the first bend inner wall and extends into the second bend outer wall. Counter rotating vortices develop in the first bend and propagates into the second bend. High velocity secondary flows are observed near the second bend inner wall at approximately  $\phi_2$  of 40° into the bend.

## 5.1 Introduction

Flow Accelerated Corrosion (*FAC*) results in pipe wall thinning and failure in some cases. *FAC* is affected by several parameters such as flow cycle chemistry, piping material, operating conditions (pressure and temperature) and the flow hydrodynamics. The latter depends on the piping geometry and affects the mass transfer rate and hence *FAC* rate, [1]. Piping inspections and failure observations in industrial applications have shown that pipe bends are one of the components that are most prone to *FAC*. Several attempts to relate the flow dynamics in bends in order to better understand the *FAC* in these components have been performed [7,8]. The mass transfer was reported to be a significant function of flow shear stress where the effect of kinetic energy was believed to be insignificant [7].

The flow in pipe bends has been studied since Dean (1927) who observed counter rotating vortices in a single 90° bend under laminar flow conditions. Similar features have been observed in sharp 90° bend under turbulent flow conditions [2]. The flow in bends is affected by centrifugal forces which drive the flow toward the outside radius through the central region of the flow. The pressure gradient in the cross section, due to this centrifugal force, drives the flow again toward the inner radius. The two mechanisms result in double counter rotating vortices within the cross section of the bend [2]. Meanwhile, the adverse pressure gradient along the inner radius may lead to flow reversal and separation from the wall. The dynamics of the double counter rotating vortices is highly sensitive to the upstream conditions. The flow separation on the bend inner wall near the outlet is reported to be transient and causes pressure fluctuations in the bend

cross section [3]. Periodic change in the strength of the counter rotating vortices downstream of a single bend was observed by [4-6] which is reported to cause significant pressure fluctuations.

The flow dynamics in dual bends is even more complex due to the flow interaction within the two bends [9]. The flow dynamics in back-to-back bends arranged in U-, out of plane- and S- configurations have been investigated [9-15]. The turbulence level and pressure drop in the S configuration was highest when compared to the U- and out of plane- dual bend configurations under turbulent flow condition [10]. This could be due to the effect of direction of the bend curvature in the first and the second bends, which is the same in the U- shape and partially the same in the out of plane- shape. This produces a pair of vortices in the second bend aligned in the same direction of the first pair, and allows for quicker velocity field recovery compared to the S configuration [10].

In S- shape dual bends, the first bend generates twin vortices similar to that in a single bend. These are stretched along the curvature, their diameter decreases and strength increases. The second bend tends to drive the flow in the same pattern but in the opposite direction. The strength of the secondary flow structures in each bend will determine the prevailing flow pattern over the entire S- shape dual bend. For small angles of curvature the swirling structures in the second bend are suppressed since the curvature is not large enough for the second bend to recover from the first swirl and develop new secondary vortices, in the case of laminar flow [9,12]. In this case two double swirls turning in opposite directions were observed to coexist in the second bend and downstream of the dual bends. Significantly large angles may result in strong vortices in the second bend

that can diminish the intensity of vortices in the first bend. In dual 90° S-shape bends [12], the second bend would generate secondary structures that are able to overcome those generated in the first bend.

The average turbulence level measured at several stations downstream of an S shape dual bends was found to decrease with increasing separation distance between the back to back bends [13]. The flow velocity field was oscillating non-symmetric in the cross section downstream of the dual bend. This asymmetry was attributed to the non-developed flow at the inlet to the S-bend. Most flow field measurements in S- shape bends have been performed under laminar flow conditions [11, 12]. The flow field downstream of an S-shape dual bends was reported [13]. Flow asymmetry in the pipe cross section was observed but was attributed to a non-developed flow upstream of the bend geometry.

The objective of the current study is to investigate the flow field within the S- shape dual bends in order to better understand the driving mechanisms for the mass transfer within the bend. The flow field was measured using Particle Image Velocimetry for Re of 40,000 and 70,000 in standard 90° bends with a radius of curvature  $r/D$  of 1.5 in single and dual S- bend configurations with zero separation distance between the bends.

## **5.2 Experimental facility and methodology**

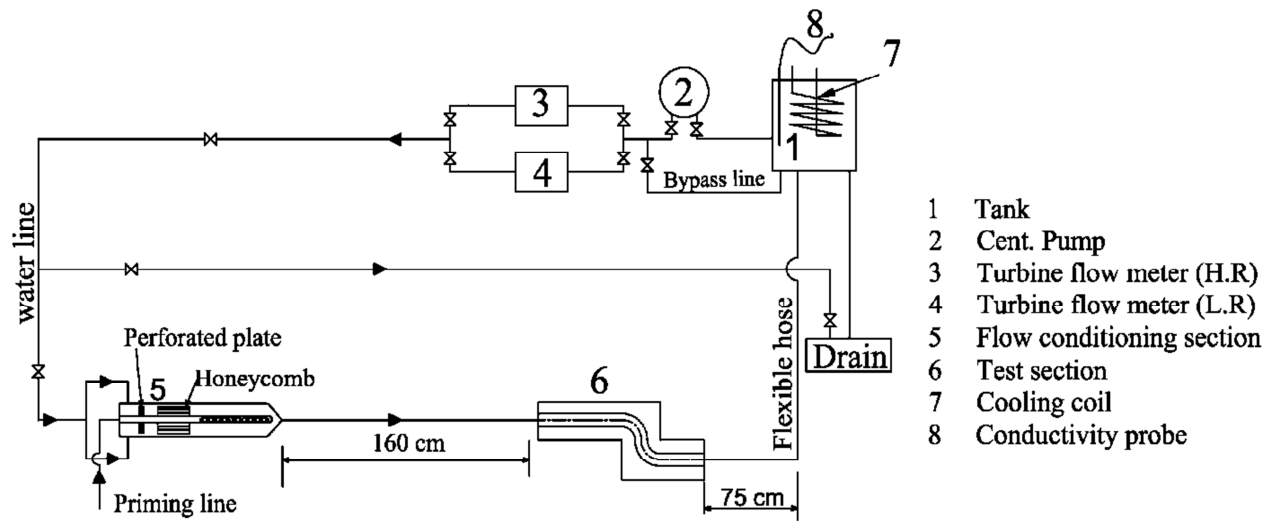
The measurements were performed in a 2.54 cm diameter flow loop shown schematically in figure 5.1. This facility has been used in previous mass transfer studies and is described in detail in [16]. Water is circulated from a 100 liter reservoir through the test facility by a centrifugal pump. The flow rate is regulated by globe valves and measured by a turbine

flow meter with an accuracy of  $\pm 1\%$  of the flow reading. The flow is passed through a perforated plate followed by a honey-comb before entering a straight pipe with a length of 160 cm leading to the test section. The test section was manufactured from transparent acrylic with a bend diameter of 2.54 cm and radius of curvature  $r/D$  of 1.5. The flow exited the test section to a 75 cm long straight pipe before being directed back to the reservoir. The water temperature was measured in the reservoir and controlled to within  $\pm 0.5$  °C using a compensation cooling loop. The velocity field is measured using a 2-dimensional particle image velocimetry system with a single PowerView 4MP 12 bit digital camera with a resolution of 2048×2048 pixels. The flow field illumination was performed using a 532nm New Wave Solo 120XT pulsed Nd:YAG laser with a maximum output of 120mJ per pulse. A combination of plano-cylindrical and spherical lenses was used to focus the laser beam into a sheet. Camera optics were determined by the required field of view for each flow field being captured, with a Sigma 105mm  $f$  2.8 lens being used in combination with 1.4x and 2.0x teleconverters and extension tubes. Synchronization of the laser pulses and camera images was performed using a TSI Laser Pulse Model 610035 synchronizer with external triggering and software adjustable time delay.

Seeding of the flow for *PIV* imaging was performed using metal coated glass particles with nominal size of 17 $\mu$ m. The glass coated seeding particle was selected to match the density of the fluid. Sodium iodide (*NaI*) was dissolved in water at 60% ratio (salt to water) by weight. This proportion maintains approximately the same index of refraction

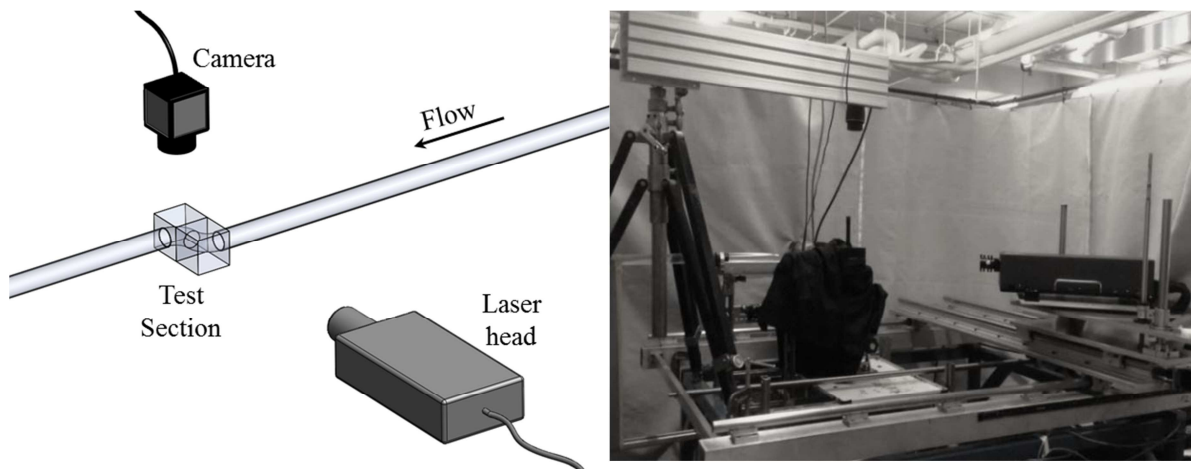
as the acrylic test section [14]. Calibration of the *PIV* system was performed using a Starett machinists' grade straight edge.

Each *PIV* vector field was obtained using a deformation based scheme incorporating  $32 \times 32$  pixel interrogation regions, which corresponds to a spatial resolution of approximately  $1 \times 1$ mm, with approximately 75% overlap in both the  $x$  and  $y$ -directions. All *PIV* measurements presented in this paper have a minimum validation rate of 99% for single instantaneous flow fields before applying vector replacement or interpolation schemes. Spurious vectors are determined based on the neighbouring vectors and replaced by interpolation scheme. Classic *PIV* analysis is followed where instantaneous frames are analyzed and the velocity vectors are obtained. A sum of 200 frames is then averaged to obtain the mean flow field and determine the turbulent kinetic energy using post processing commercial software.



- 1 Tank
- 2 Cent. Pump
- 3 Turbine flow meter (H.R)
- 4 Turbine flow meter (L.R)
- 5 Flow conditioning section
- 6 Test section
- 7 Cooling coil
- 8 Conductivity probe

(a)



(b)

**Figure 5.1: The main components of the test facility, (a) schematic of the main components of the flow loop (b) schematic and picture of the *PIV* setup**

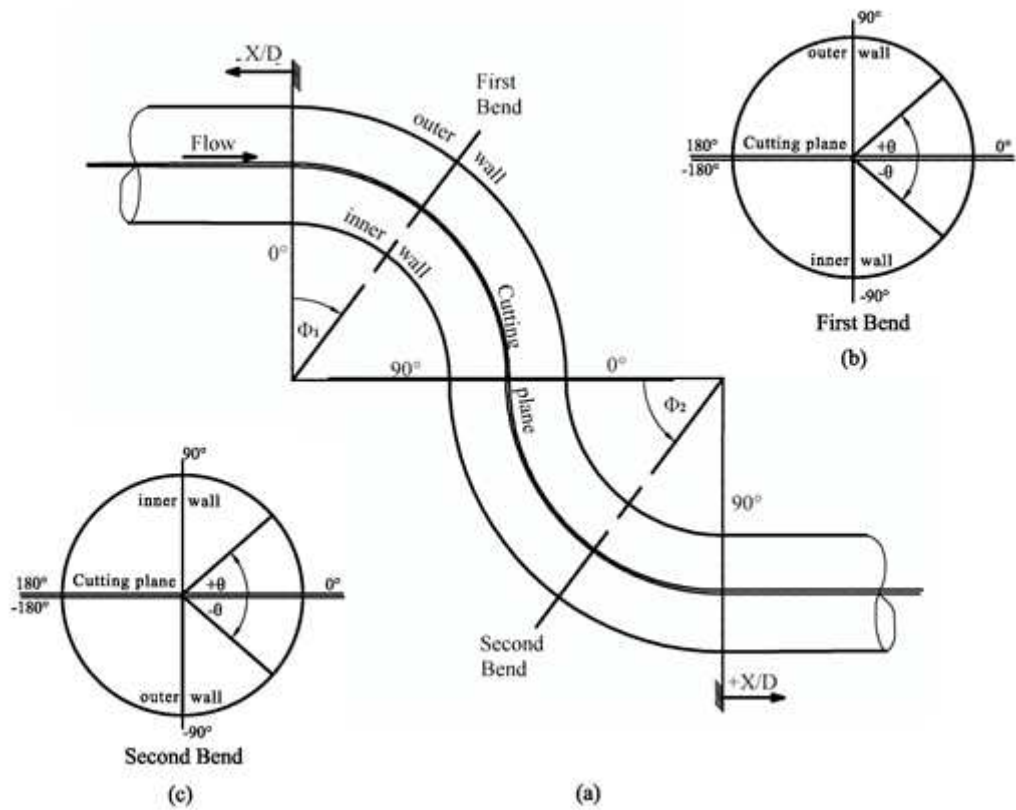


**Figure 5.2:** Schematic of the test section showing the section planes relative to: (a) streamwise orientation, (b) crosswise orientation in the first bend, (c) crosswise orientation in the second bend - Adapted [17]

**Table 5.1: Nomenclature of quantities and terms.**

Nomenclature

$dm/dt$	<i>Mass transfer rate</i>	$[kg/s]$
$D$	<i>Bend cross sectional diameter</i>	$[m]$
$h$	<i>Mass transfer coefficient</i>	$[m/s]$
$r$	<i>Local position in the pipe cross section</i>	$[m]$
$R$	<i>Pipe radius of curvature</i>	$[m]$
$T.K.E$	<i>Total turbulent kinetic energy</i>	$[m^2]$
$u$	<i>Local flow velocity</i>	$[m/s]$
$U_o$	<i>Mean flow velocity in the upstream pipe</i>	$[m]$
$\delta$	<i>Local instantaneous wear of the test section</i>	$[m]$
$\theta$	<i>Bend cross sectional angle</i>	
$\phi_1$	<i>Bend angle of curvature (along first bend)</i>	
$\phi_2$	<i>Bend angle of curvature (along second bend)</i>	
$\nu$	<i>Kinematic viscosity</i>	$[m^2/s]$

### 5.3 Results and discussion:

Flow field measurements were performed in the pipe upstream of the bend test section and velocity profiles at  $X/D$  of -3 and -2.5 are shown in figure (5.3-a). The velocity profiles are in good agreement with the experimental results of [16]. The flow rate calculated from these profiles agreed to within  $\pm 3\%$  with that measured from the turbine flow meter. The flow is found to be symmetric when the profile from right side was compared to the left side of pipe as shown figure (5.3-b).

The velocity field contour on a plane along the centerline of a single bend at  $Re=70,000$  is shown in figure 5.4. Flow acceleration and deceleration are observed on the inner and outer wall sides, respectively, similar to previous studies [3,4]. The high velocity region on the inner wall side tends to shift away from the inner wall toward the bend outer wall near  $\phi$  of 40 to 50 degrees. This is due to the flow separation caused by the adverse pressure gradient in this region [8]. Normalized velocity profiles along the central diameter at different angular locations for  $Re$  of 40,000 and 70,000 are shown in figure (5.4-b). The profiles at the two Reynolds numbers were in good agreement at the different locations. The velocity profile is symmetric upstream of the bend,  $X/D=-2$ . The mean velocity increased on the inner wall side ( $r/R < 0$ ) and decreased near the outer wall side at  $\phi$  of  $10^\circ$  and  $25^\circ$ . The high velocity core offset from the inner wall toward the centerline of the bend curvature, between  $\phi$  of  $45^\circ$  and  $70^\circ$ . The core velocity is observed to shift toward the outer wall between  $\phi$  of  $70^\circ$  and  $80^\circ$ .

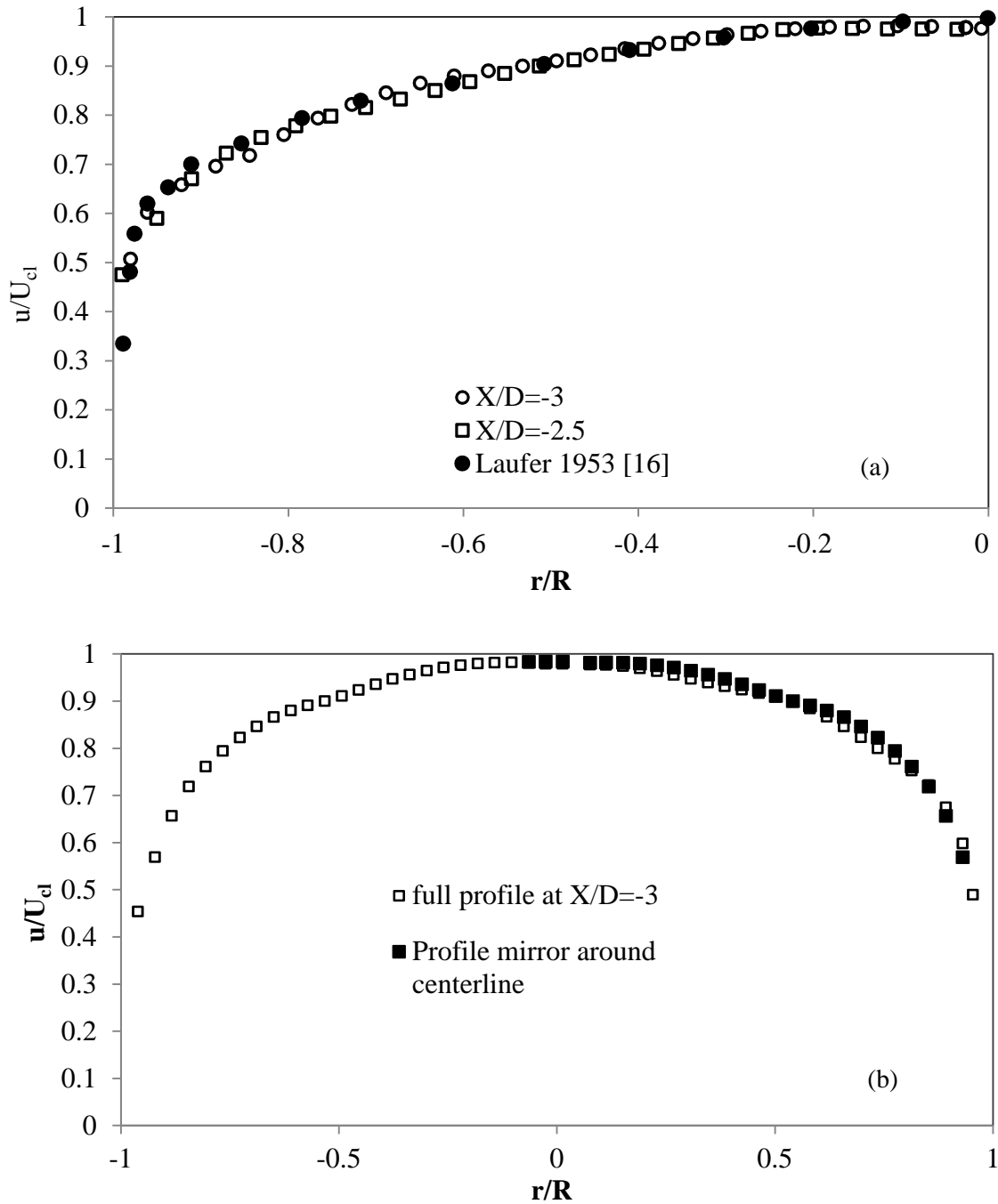


**Figure 5.3: Velocity profiles in the upstream pipe, (a) comparison of profiles at different locations with [16], (b) comparison of the profile from the two sides of the pipe (symmetry check)**

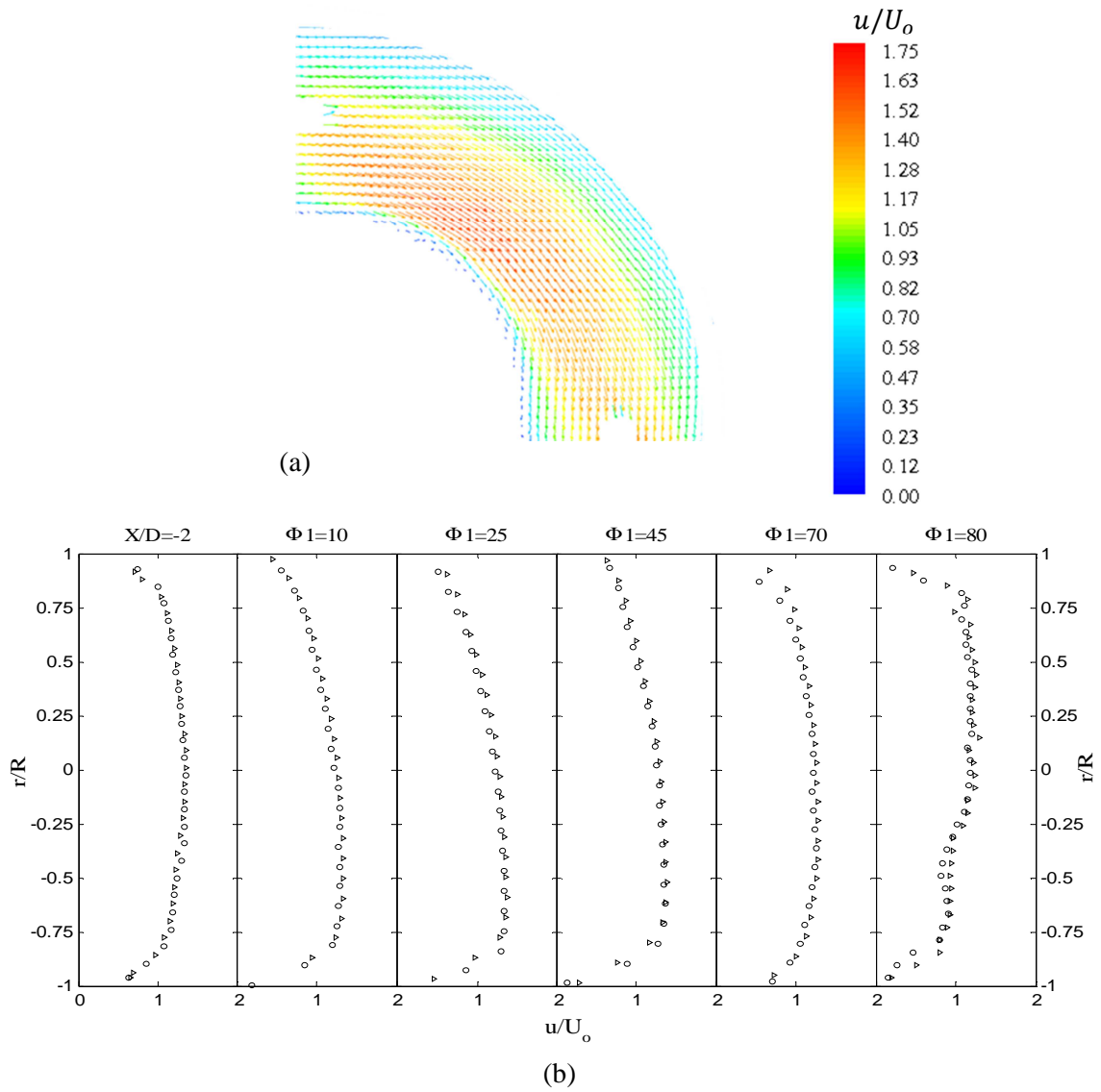


**Figure 5.4: Velocity field in single bend (a) contour along symmetry plane (b) Normalized velocity profiles at different angular locations for  $\circ$   $Re=40,000$ ,  $\blacktriangleright$   $Re=70,000$**

Normalized turbulence kinetic energy ( $T.K.E/U_o^2$ ) contours for the single bend are shown in figure (5.5-a). The  $T.K.E$  was relatively low at the inlet to the bend outer wall and increased along the bend curvature. On the inner wall side, the  $T.K.E$  was generally low except on the latter part near the separation zone, where elevated  $T.K.E$  levels were measured, similar to [8]. The profiles of ( $T.K.E/U_o^2$ ) at different angular locations are shown in figure (5.5-b). The turbulent kinetic energy was relatively uniform in the upstream pipe. On the bend inner wall side ( $r/R < 0$ ), the  $T.K.E$  remained low till  $\phi$  of  $45^\circ$ , and then increases toward the outlet of the bend. This agrees with the results of the numerical simulation reported by [8]. On the outer wall side, the  $T.K.E$  increased along the curvature toward the bend outlet.

The velocity field contours on the symmetry plane along of the dual S- shape bend are shown in figure 5.6. The flow accelerates on the inner wall and decelerates on the outer wall of the first bend of the S- shape, similar to that in the single bend case. The centripetal forces in the second bend due to bend curvature result in a lower pressure on the inner wall side and a higher pressure on the outer wall side. This adverse pressure gradient opposes the flow from the first bend inner wall side. The low pressure region on the second bend inner wall results in flow acceleration into the second bend. These two mechanisms result in a shift of the high velocity core to the outer wall and further acceleration into the second bend inner wall. The high velocity stream is observed to shift slightly from the inner wall as the flow turns around the second bend curvature. Normalized velocity profiles ( $u/U_o$ ) are shown in figure (5.6-b), where  $U_o$  is the mean

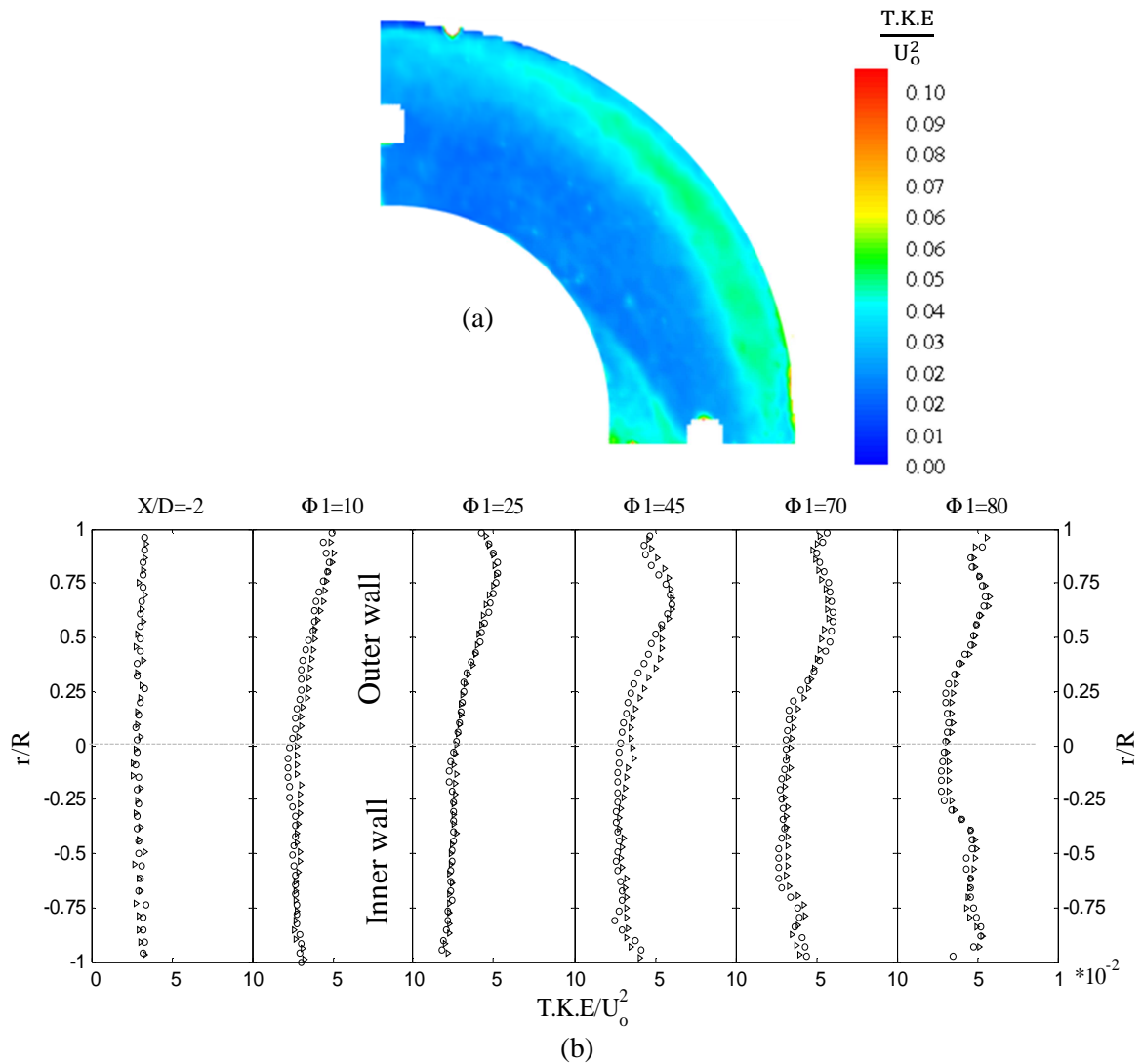


**Figure 5.5: Turbulent kinetic energy distribution in single bend (a) T.K.E contour at midplane (b) cross sectional profiles of T.K.E for  $\circ$  Re=40,000,  $\blacktriangleright$ Re=70,000**

flow velocity in the upstream pipe. The normalized velocity is observed to increase on the first bend inner wall to reach a high of 1.4 near  $\phi_1$  of  $25^\circ$  and then decreases as the high velocity core moves toward the outer wall. The normalized velocity near the outer wall increased toward the end of the first bend. The velocity continued to increase on the second bend inner wall to reach a magnitude of approximately 1.5 at  $\phi_2$  of  $10^\circ$ . The velocity continued to increase to reach a maximum of nearly 1.6 near  $\phi_2$  of  $45^\circ$  however the profile peak was shifting from the inner wall side toward the core region. The peak velocity decreased from this point onward.

The velocity contours at different cross sectional locations along the dual bend profile are shown in figure 5.7. The gap between the two sides of the bend in the contours is due to the seam line in the test section which was observed to obscure the camera view in this region. The cross sectional contours indicate the development of secondary flow structures starting from  $\phi_1$  of 10 degrees. High velocity twin cells are formed on the inner wall side of the first bend due to the action of centripetal force and the resultant cross sectional pressure gradient. As the flow turns around the bend the vortex moves on the circumference toward the side walls near  $\phi_1$  of 40 degrees. The contour at  $\phi_1$  of 70 degrees indicate further development of the double vortices and a shift of the high velocity flow core from the inner wall toward the outer wall. As the flow turns into the second bend near  $\phi_2$  of 10 degrees high velocity region is observed in the centerline plane contour, which is due to flow acceleration into the second bend. The vortex pair propagates from the first bend inner wall to the second bend outer wall with much lower

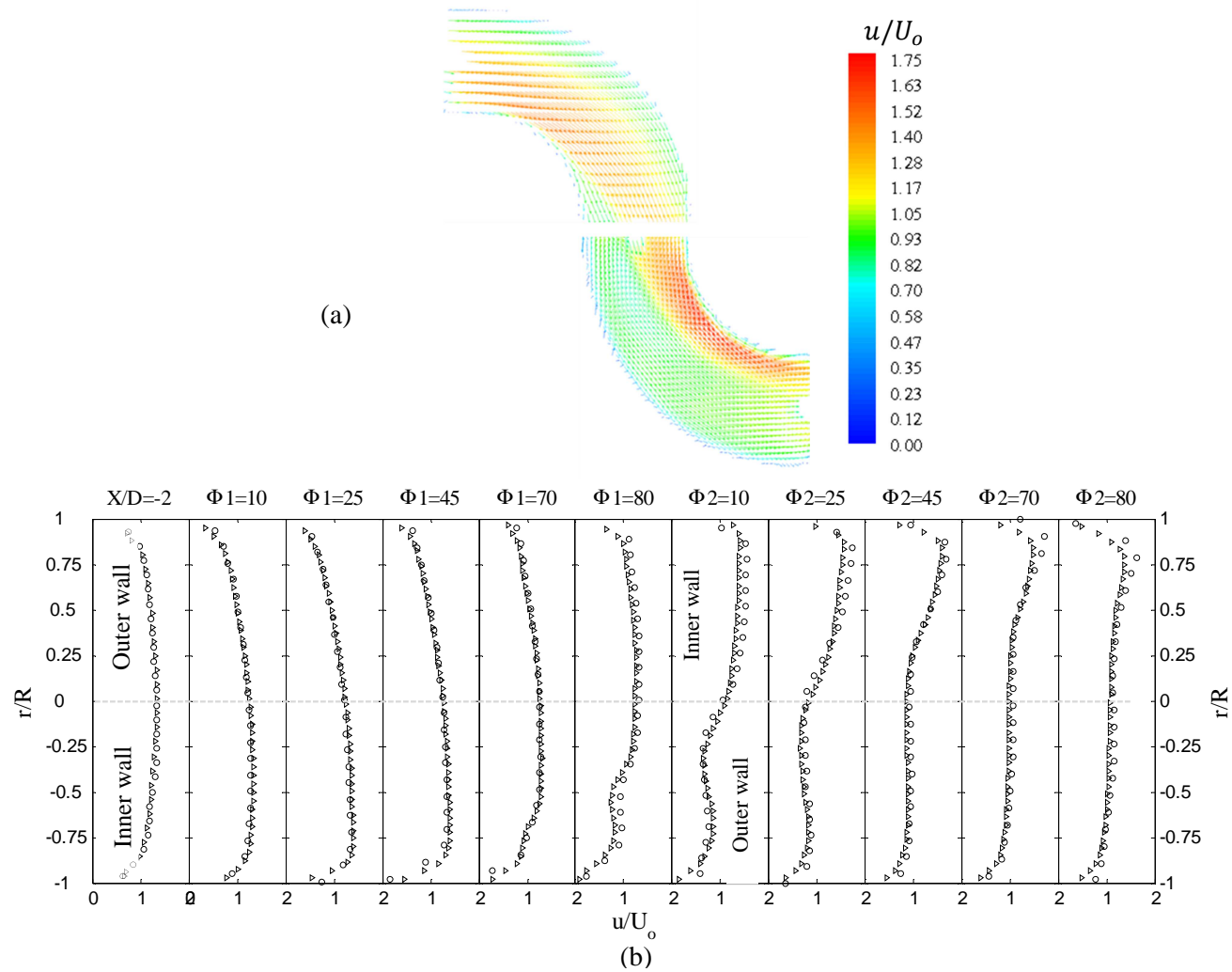


**Figure 5.6: Velocity field in the S- shape dual bends (a) T.K.E contour at midplane (b) cross sectional profiles of T.K.E for  $\circ$   $Re=40,000$ ,  $\blacktriangleright$   $Re=70,000$**

intensity. These vortices are observed to shift away from the outer wall toward the inner wall driving a high secondary velocity stream at the inner wall near of  $\phi_2$  40°. The high velocity secondary flow shifts along the circumference toward the side wall to reach  $\theta$  of approximately 90° near  $\phi_2$  of 70 degrees. At this position, the vortex pair moved to fill the center region of the cross section. The secondary flow structures were symmetric at the different locations along the bend profile which contradicts the findings of [13]. However the velocity field upstream of the S- dual bend in [13] was believed to be non-developed [13].

Contours of turbulent kinetic energy along the symmetry plane of the dual bend are shown in figure 5.8. Higher *T.K.E* was observed on the outer wall side of the first bend and downstream of the flow separation on the inner wall side, similar to the single bend case however the *T.K.E* magnitude in the first bend was relatively lower than for the single bend. The *T.K.E* level is observed to increase significantly downstream of the separation zone to approximately 2 times the maximum level in the first bend. Crosswise profiles of  $(T.K.E/U_o^2)$  at different angular locations around the dual bend profile are shown in figure (5.8-b). Low *T.K.E* is observed on the first part of the bend inner wall ( $r/R < 0$ ) and increases on the latter part, while a gradual increase in *T.K.E* along the first bend curvature is observed on the outer wall side ( $r/R > 0$ ). The *T.K.E* near  $\phi_1$  of 80° was found to be approximately equal on the two sides of the bend. This could be attributed to the low mean flow velocity near the inner wall outlet due to flow separation. On the second bend outer wall, high *T.K.E* is observed downstream of the flow separation zone and decreased from this point onward into the bend curvature. The *T.K.E* was low at the

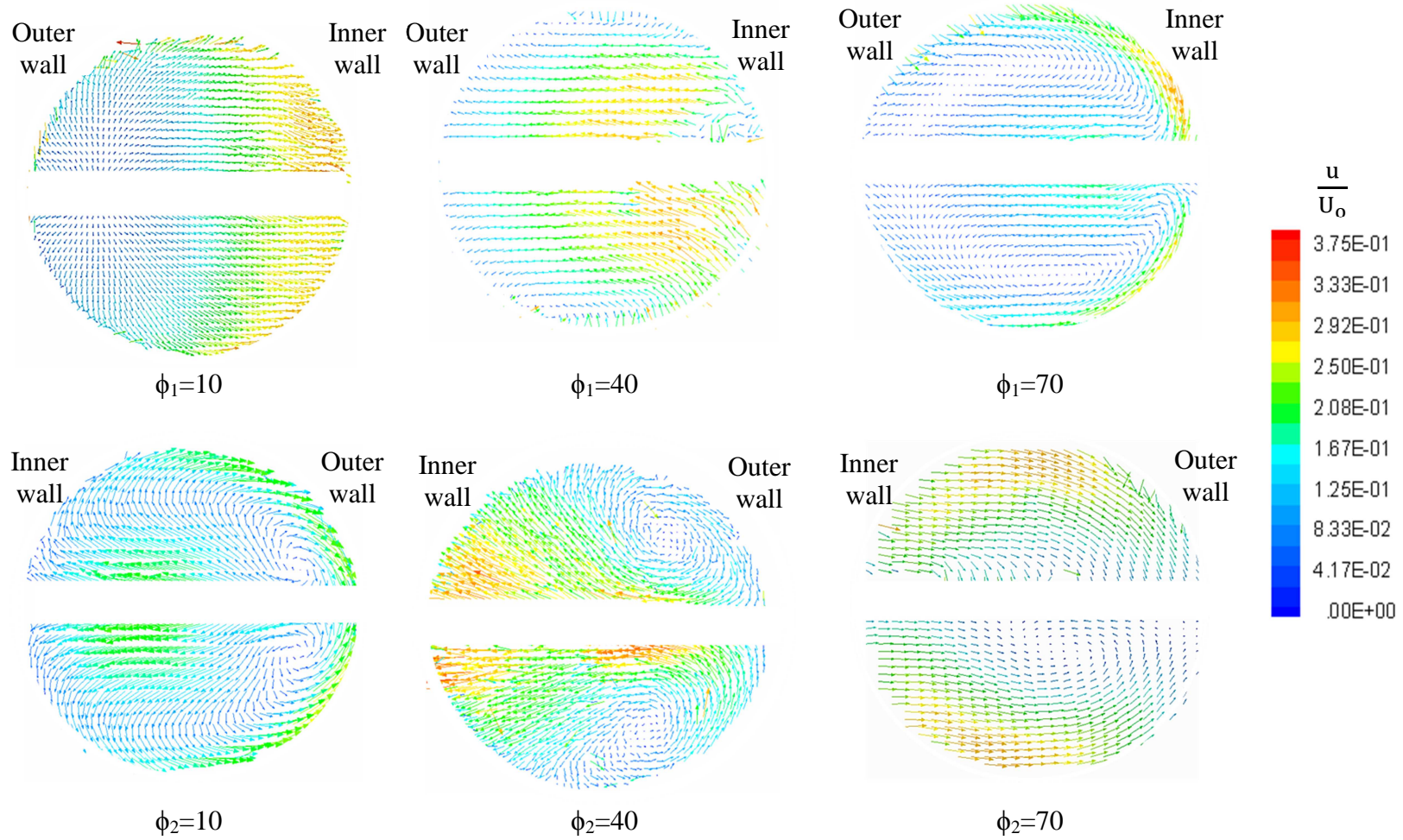


Figure 5.7: Crosssectional velocity contours at different locations along the bend curvature for  $Re=70,000$

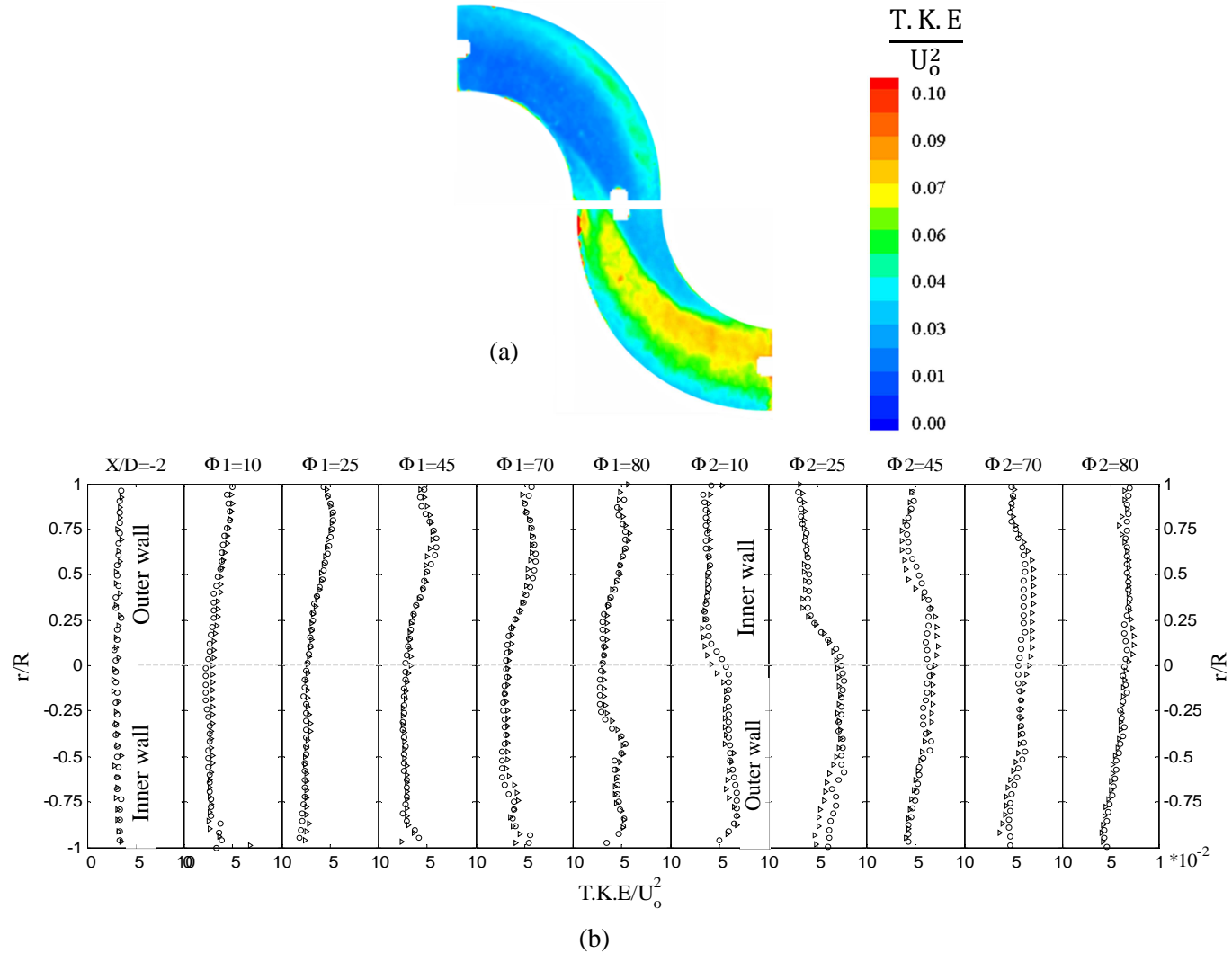


Figure 5.8: Turbulent kinetic energy distribution in S-shape dual bends: (a) T.K.E contour at midplane, (b) cross sectional profiles of T.K.E for  $\circ$  Re=40,000,  $\blacktriangleright$  Re=70,000

inlet at the second bend inner wall near  $\phi_2$  of  $10^\circ$  to  $25^\circ$  and increased from this point as the high  $T.K.E$  shifted from the outer wall to the inner wall.

#### **5.4 Summary and conclusions:**

Flow field characteristics in single and dual S- shape bends were investigated using particle image velocimetry (*PIV*) technique. The fluid and acrylic test section index of refraction were matched to reduce optical distortion. Measurements were performed in the stream wise plane as well as at different cross sectional planes. Fully developed flow profiles were measured upstream of the test section. Relatively high mean flow velocities and  $T.K.E$  were observed at the outlet of the outer wall side in the single and dual bends. High turbulent kinetic energy  $T.K.E$  was observed downstream of the separation zone of the first bend with a magnitude of approximately twice that in the first bend. Symmetric secondary flow velocity was measured along the bend profile. High velocity secondary flow is observed on the second bend inner wall near  $\phi_2$  of  $40^\circ$ .

#### **Acknowledgments**

The support of the CANDU Owners Group (COG) and the Natural Sciences and Engineering Research Council of Canada (NSERC) is gratefully acknowledged. The authors would like to thank Dr. Dave Arthurs for his valuable help in the setup and calibration of the *PIV* system and Mr. Lin Zhong for his contribution in the manufacturing of the *PIV* setup.

**5.5 References:**

- [1] Poulson, B., The Local Enhancement of Mass Transfer at 180 Degree Bend, International Journal of Heat Mass Transfer, *vol.* 31, No. 6, p. 1289-1297, (1988)
- [2] Weske, J. R., Experimental Investigation of Velocity distribution Downstream of a Single Duct Bend, N.A.C.A, TN-1471, (1948).
- [3] Yamano, H., Tanaka, M., Murakami, T., Iwamoto, Y., Yuki K., Sago, H., Hayakawa, S., Unsteady Elbow Pipe Flow to Develop a Flow-Induced Vibration Evaluation Methodology for Japan Sodium-Cooled Fast Reactor, Journal of Nuclear Science and Technology (48), no. 4, (2011): 677-687
- [4] Tunstall, M. J., Harvey, J. K., On The Effect of a Sharp Bend in a Fully Developed Turbulent Pipe-Flow, Journal of fluid Mech (34), no. 3 (1968): 595-608.
- [5] Rutten, F., Meinke, M., Schröder, W., Large-eddy Simulations of 90° Pipe Bend Flows, Journal of Turbulence (2), (2001): 1-13
- [6] Takamura, H., Ebara, S., Hashizume, H., Aizawa, K., Yamano, H., Flow Visualization and Frequency Characteristics of Velocity Fluctuations of Complex Turbulent Flow in a Short Elbow Piping Under high Reynolds Number Condition, Journal of Fluids Engineering, (134), (2012),1-8
- [7] Homicz, G. F., Computational Fluid Dynamics Simulations of Pipe Elbow Flow., New Mexico and Livermore: Sandia National Laboratories Albuquerque, (2004).

- [8] El-Gammal, M., Mazhar, H., Cotton, J.S., Schefski, C., Pietralik, J. and Ching, C. Y., The Hydrodynamic Effects of Single Phase Flow on Flow Accelerated Corrosion in a 90 Degree Elbow, *Nuclear Engineering and Design* 240, p.1589-1598, (2010)
- [9] Taylor, A. M., Whitelaw, J. H., Yianneskis, M., Developing Flow in S-shaped ducts 2: Circular Cross-Section Duct, NASA Contractor Report 3759, (1984)
- [10] Rudolf, P., Desova, M., Flow Characteristics of Curved Ducts, *Applied and Computational Mechanics*, vol. 1, p. 255- 264, (2007)
- [11] Niazmand, H., Jaghargh E. R., Bend Sweep Angle and Reynolds Number Effects on Hemodynamics of S-shaped Arteries, *Annal of Biomedical Engineering*, vol. 38, no. 9, p. 2817-2828, (2010)
- [12] Doorly, D., Sherwin, S. J., Geometry and Flow, *Cardiovascular Mathematics: Modeling and Simulation of the circulatory System*, Springer (2009)
- [13] Yoshida, K., Kazuhisa, Y., Hashimue, H., Specificity of Flow Structure in a Dual Elbow and its Visualization by PIV Measurement, *Proceedings of the 16th International conference on Nuclear Engineering, ICONE 16, Florida, USA, May 11-15*, p. 293- 299, (2008)
- [14] Yuki, K., Hasegawa, S., Sato, T., Hashizume, H., Aizawa, K., Yamano, H., Matched Refractive-Index PIV Visualization of Complex Flow Structure in a Three-Dimensionally Connected Dual Elbow, *Nuclear Engineering and Design*, vol. 241, p. 4544-4550, (2011)

[15] Sudo, K., Sumida, M., Hibara, H., Experimental Investigation on Turbulent Flow Through a Circular 180 Degree Bend, Experiments In Fluids, vol. 28, p. 51- 57, (2000)

[16] Laufer, J., The Structure of Turbulence in Fully Developed Pipe Flow, NACA- TN 2954, (1953)

[17] Mazhar, H., Ewing, D., Cotton, J. S., Ching, C. Y., Experimental Investigation of Mass Transfer in 90° Pipe Bends using a Dissolvable Wall Technique, International Journal of Heat and Mass Transfer, 65, p. 280–288, (2013)

## **CHAPTER 6**

---

### **Mass transfer in single bends under annular two phase flow conditions**

#### **Complete citation:**

H. Mazhar, D. Ewing, J. S. Cotton, C. Y. Ching, Mass Transfer in Single Bends under Annular Two Phase Flow Conditions, Journal of Heat Transfer Submitted April 2013

#### **Relative Contributions:**

H. Mazhar: Performed all experiments, interpretation and analysis of the data and wrote the first draft of the manuscript including all figures and text.

D. Ewing: was involved in the interpretation and discussion of results.

J. S. Cotton: Co-supervisor of H. Mazhar and revised the initial drafts of the manuscript

C. Y. Ching: Co-supervisor of H. Mazhar and was responsible for the final draft submittal to the journal

**Abstract**

The distributions of the mass transfer coefficient in horizontal 90° bends were measured under a range of two phase annular flow conditions. A dissolving wall technique at a high Schmidt number ( $Sc=1280$ ) is used for the measurements. The maximum mass transfer occurred on the centerline of the bend outer wall at an angle of approximately 50 degrees from the bend inlet under all tested conditions. The area of maximum mass transfer rate was found to span approximately 30 degrees in the circumferential direction. A second region of enhanced mass transfer occurred on the latter part of the bend with a local maximum occurring slightly off the bend centerline in some cases. Changing the air and water superficial velocities ( $J_v=22$  to 29.5 m/s,  $J_L=0.17$  to 0.41 m/s) showed that the air velocity had a larger effect on the mass transfer rates than the water velocity; however the effect of the water velocity on the mass transfer was not insignificant.

## 6.1 Introduction

The measurement of wall mass transfer rates under two phase flow conditions in different pipe geometries is important for the understanding of several practical applications, including Flow Accelerated Corrosion (FAC). Flow accelerated corrosion is attributed to the mass transfer of the metal surface or corrosion layer to the adjacent fluid and can result in pipe wall thinning, piping systems deterioration and sometimes abrupt failure [1]. Flow accelerated corrosion is more pronounced in two phase flows and in particular in pipe singularities, such as T-Joints and bends. The need to understand and predict the locations of high mass transfer has motivated investigations of the mass transfer rates in different pipe geometries.

Ninety degree bends, of interest here, cause changes in flow direction that result in phase separation and redistribution [2, 3]. Investigations of two phase flow in pipe bends have focused on evaluating the pressure drop along the bend curvature [4, 5, 6], visualization of the flow [7, 8, 9], and characterizing the heat and mass transfer in the bend [10, 11, 12]. The phase redistribution in long radius bends for high void fraction annular flows revealed distributions of the two phases that could be related to the interaction between gravity, centripetal and inertial forces [7, 8, 9]. The liquid film was found to detach from the bend inner wall and deposit onto the bend outer wall by [3]. The flow detachment phenomenon was shown to be periodic and intensified inversely with the bend radius of curvature [13].

The mass transfer in bends is found to increase with the void fraction to reach a maximum under annular flow conditions [11]. Poulson [10, 11] measured the mass transfer in 180°

bends under annular flow conditions for radius of curvature  $r/D$  of 3 and 7.3. Here, measurements were performed along the centerline of the outer wall. The location of maximum mass transfer was near the line of sight seen location, where the centerline of the upstream pipe intersects with the bend outer wall. The high mass transfer rate was attributed to the interplay between the impingement of liquid droplets within the core on the outer wall and the liquid film re-distribution due to the centripetal forces generated by the bend curvature. The interplay of these two mechanisms is expected to vary with the annular flow condition. The air superficial velocity had a significant effect on the mass transfer [10, 11] but the role of the water velocity is unclear with data showing it had a minor effect on the mass transfer [10]. Poulson [11] also reported a correlation for the location of the maximum mass transfer rate along the curvature based on the bend radius of curvature. The maximum mass transfer rate was found to move downstream when the radius of curvature of the bend was reduced.

The objective of this investigation was to measure the local surface distribution of mass transfer rates in short radius ( $r/D=1.5$ )  $90^\circ$  bends under annular air-water two phase flow conditions. The measurements were performed using a dissolving wall method with test sections cast from Gypsum. The dissolution of Gypsum in water has a high Schmidt number ( $Sc=1280$ ) which is similar to that for the diffusion of the iron magnetite layer of carbon steel piping in water, thus providing a mass transfer environment analogous to that in FAC. The full worn surface topography was measured using a three dimensional laser scanner and the results are used to determine the distribution of the mass transfer rates.

The test facility and methodology is reported in the next section followed by a discussion of the results and the conclusions from this study.

## **6.2 Experimental facility and methodology**

Experiments were performed in the 2.54 cm diameter test flow loop facility shown in Figure 6.1. Water is circulated from a reservoir through the test loop by a centrifugal pump. The flow rate is regulated by globe valves and measured by a turbine flow meter with an accuracy of  $\pm 1\%$  of the flow reading. Air from a compressed air line is filtered and supplied to the test facility. The air flow rate is measured using two rotameters connected in parallel with an accuracy of  $\pm 2\%$  of the full scale. The pressure is measured downstream of the rotameters and just upstream of the test section to correct the rotameter readings to the actual air flow rate. The uncertainty in the testing conditions is presented in table 6.1. The flow of water passed through a perforated plate followed by a honeycomb before it mixed with the air stream. The mixing chamber is in the form of two concentric tubes with the inner tube, carrying the air, being perforated on the periphery to homogeneously inject the air into the water stream running in the annulus between the inner and outer tubes.

The mixed air–water flow then passes through a straight pipe of 160 cm (60 diameters) in length upstream of the test section. The air-water flow exited the test section to a 75 cm (15 diameters) long straight pipe before being directed to a reservoir with an air vent to release the separated air. The water temperature was measured in the reservoir and kept constant to within  $25 \pm 0.5^\circ\text{C}$  using a compensation cooling loop.

**Table 6.1: Uncertainty in flow conditions**

Parameter	Minimum reading	Maximum reading	Uncertainty	Average Reading
Water flow rate [GPM]	0	8	1% reading	2.5±0.025 GPM
Air flow rate [SCFM]	0	25	2% full scale	20±0.5 SCFM
Air pressure [Pa]	0	100	2% full scale	40±2 Pa

**Table 6.2: Factors affecting total uncertainty**

Factor	Uncertainty	
Scanning uncertainty	±0.1	[mm]
Casting variability	±0.15	[mm]
Concentration ( $\Delta C$ )	±0.005	[kg/m <sup>3</sup> ]
Wear gradient ( $\partial\delta/\partial t$ )	$\pm 2.5 \times 10^{-6}$	[m/s]
Density ( $\rho$ )	±40	[kg/m <sup>3</sup> ]

**Table 6.3: Experimental test conditions**

Parameter	Range								
Air flow rate [SCFM]	25	25	25	28	28	28	35	35	35
Water flow rate [GPM]	1.5	2.5	3.5	1.5	2.5	3.5	1.5	2.5	3.5
Air pressure (test section inlet) [Pa]	20	28	37	24	32	40	37	48	60
Air temperature [°C]	22	22	22	22	22	22	22	22	22
Water temperature [°C]	25	25	25	25	25	25	25	25	25
$J_v$ [m/s]	22.2	22	21.7	24.7	24.5	24.2	29.4	29	28.7
$J_L$ [m/s]	0.17	0.28	0.41	0.17	0.28	0.41	0.17	0.28	0.41

The dissolution of Gypsum in water during the test increases the water electrical conductivity and this measure was used to determine the overall dissolved mass of gypsum in the water. An electrical conductivity probe placed in the reservoir was used to measure the water conductivity. Calibration experiment was performed to correlate the amount of Gypsum dissolution to the change in conductivity of the water by dissolving small weights of ground powder of the test section in pure water and record the corresponding change in conductivity.

The test sections consisted of an upstream 20 cm long straight pipe, a standard 90° bend with a radius of curvature of 3.81 cm ( $r/D=1.5$ ) and a 10 cm long downstream straight section. The test section has a nominal diameter of 2.54 cm throughout. Test sections were cast from Hydrocal ( $\text{CaSO}_4 \cdot 1/2 \text{H}_2\text{O}$ ), which produces high density Gypsum when mixed with water. The cast sections were left to dry and the weight recorded periodically. When the weight reached a constant level, in approximately 15 days, the sections were tested under annular air-water flow conditions. Experiments were performed with the test section oriented horizontally. Test durations were chosen to reach a maximum nominal wear under 10% of the diameter to avoid excessive geometry distortion and changes to the flow dynamics. Once the tests were complete, the samples were dried till they reached a steady weight. The difference in sample weights before and after each test is taken as a measure of the overall mass removed. The dried samples are then sectioned in two halves along the bend profile as shown schematically in Figure 6.2. Each half is scanned on a laser coordinate measurement machine (CMM) with a resolution of 0.2 mm to obtain the

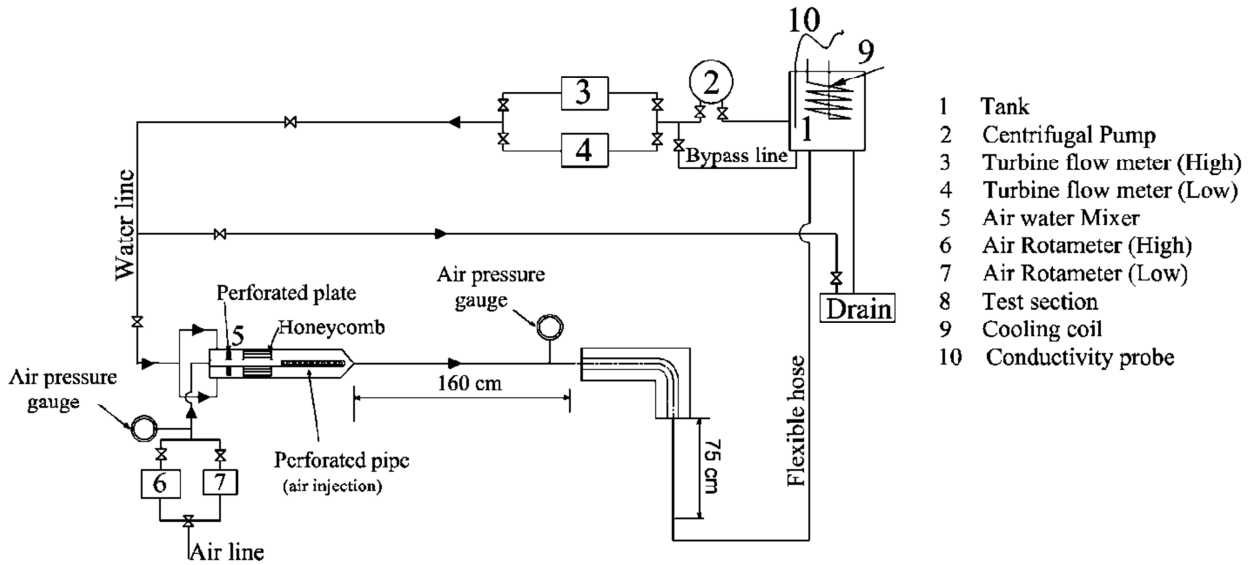


**Figure 6.1: Schematic of the test facility showing the main components of the flow loop**

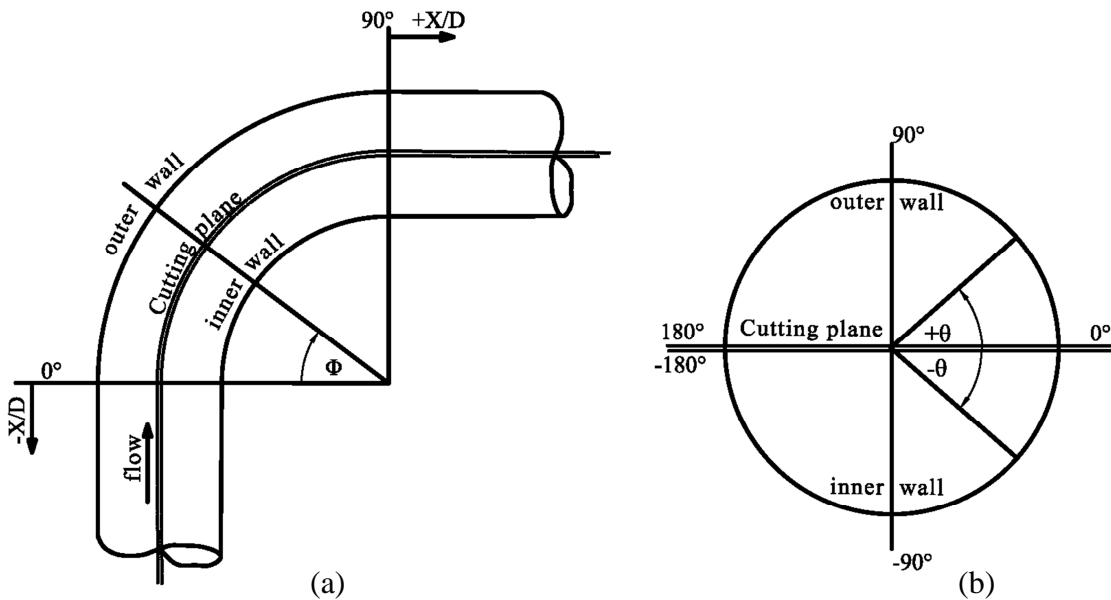


**Figure 6.2: Schematic of the test section showing the section planes relative to (a) streamwise orientation (b) crosswise orientation**

**Table 6.4: Nomenclature of quantities and terms.**

Nomenclature		
$dm/dt$	Mass transfer rate	$[Kg/s]$
$C_w$	Hydrocal ions concentration at the wall	$[Kg/m^3]$
$C_b$	Hydrocal ions concentration in the bulk fluid	$[Kg/m^3]$
$\Delta C_o$	Initial concentration difference	$[Kg/m^3]$
$\delta$	Local instantaneous wear of the test section	$[m]$
$D$	Bend crosssectional diameter	$[m]$
$D_m$	Mass diffusivity for Hydrocal in water determined at 25° C	$[m^2/s]$
$h$	Mass transfer coefficient	$[m/s]$
$J_v$	Air superficial velocity	$[m/s]$
$J_L$	Water superficial velocity	$[m/s]$
$Sc$	Schmidt number $(\nu/D_m)$	
$Sh$	Sherwood number $(h \times D/D_m)$	
$X/D$	Streamwise dimensionless distance	
$\rho$	Density of the gypsum	$[Kg/m^3]$
$\theta$	Bend cross sectional angle	
$\phi$	Bend angle of curvature	
$\nu$	Kinematic viscosity	$[m^2/s]$
$\delta$	Local mass removal	$[mm]$

surface topography. Multiple scans were taken from different directions to ensure complete surface coverage and increase the scanned surface resolution. The laser digitized surfaces are initially aligned to a common coordinate system using commercial software and then more precisely aligned and analyzed using in house developed routines. The digitized surfaces scans are re-gridded to a uniform grid with a resolution of 0.25 mm with typically multiple points within each cell. Section alignment is then refined based on the surface symmetry in the upstream and downstream pipe sections where checks are made for any systematic bias. The scanned topography for a non-tested sample is subtracted from the topography of the tested samples to obtain the local amount of mass removed during each experiment. The overall mass removed is determined by integrating over the entire surface and compared against the total mass removed from the difference in weight of samples before and after testing and from the concentration of gypsum dissolved in the water during each test. In all cases the measured mass removal values agreed to within  $\pm 7\%$ . The mass transfer coefficient is evaluated from [14]

$$\rho \frac{d\delta}{d\tau_m} = h\Delta C_0 \quad (1)$$

where  $h$  is the mass transfer coefficient (m/s), and  $\rho$  is the Gypsum density. The dissolution of gypsum in water increases the concentration of the Gypsum ions in water and in turn reduces the mass transfer potential and the dissolution time scale with test progression. The time scale used in the calculation of the mass transfer coefficient is modified to account for the increase in concentration with time in equation (1) as

$$\tau_m = \frac{1}{\Delta C_o} \int_0^t [C_w - C_b] \cdot dt \quad (2)$$

where  $C_w$  and  $C_b$  are the Gypsum concentration at the wall and in the bulk respectively. The gypsum concentration at the wall was taken as the saturation concentration for gypsum ions in water (2.6 g/L) [14, 15]. The bulk concentration in the tank was measured over the testing time at the recirculation water reservoir. The mass transfer coefficient  $h$ , is then used to compute the Sherwood number given by

$$Sh = \frac{h \times D}{D_m} \quad (3)$$

where  $D$  is the bend diameter and  $D_m$  is the mass diffusivity with a value of  $6.5 \times 10^{-10}$  at  $25^\circ \text{C}$  [15, 16].

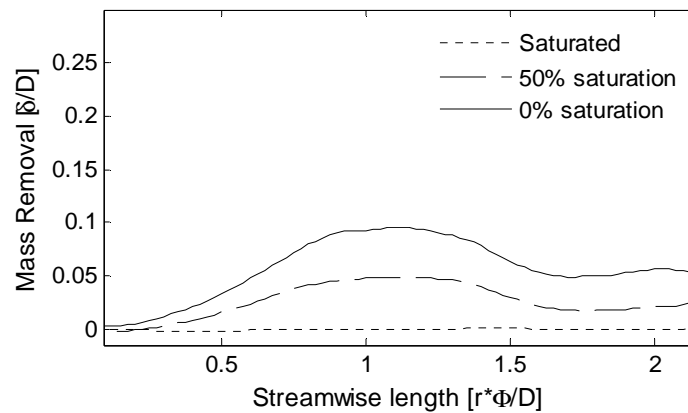
The mass transfer can be a result of surface dissolution due to concentration potential or erosion under aggressive flow conditions [10]. The role of the two mechanisms was examined through a set of experiments with different initial bulk gypsum concentrations (0, 50% of saturation, and fully saturated) similar to the experiments of Poulson [10]. The experiments were performed under annular flow conditions with gas and liquid superficial velocities  $J_v=24.5$  m/s,  $J_L=0.28$  m/s. Ground gypsum is dissolved in the water to change the initial bulk concentration. The mass removal rate was found to be nearly zero for the saturated case and proportional to the concentration difference in the other cases. Typical profiles of the thickness removed and the mass transfer coefficient profiles on the outer wall are shown in Figure 6.3. The results indicate that the mass transfer under

the current testing conditions is driven by dissolution only. The uncertainty in the measurements was evaluated considering all the contributing parameters, listed in table 6.2, following [17]. The uncertainties in scanning and casting were used to quantify the uncertainty in the local depth measurement and this was used to quantify the uncertainty in the wear gradient. The total uncertainty was determined from the factors affecting the mass transfer coefficient which are wear gradient, gypsum density and gypsum concentration difference based on equation 1. The uncertainty in the calculation of the local mass transfer coefficient was determined to be approximately  $\pm 19\%$  based on the upstream pipe and  $\pm 15\%$  based maximum mass transfer level.

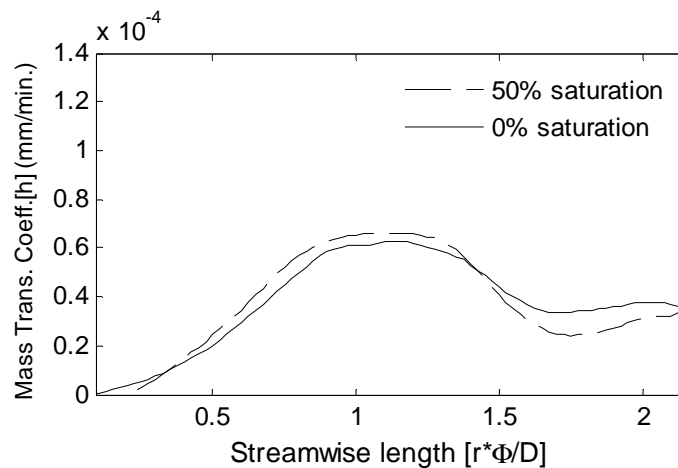
### 6.3 Results and discussions

Experiments were performed for the range of air and water flow rates tabulated in table 6.3 which maintain annular flow conditions. The mass transfer rates were measured under annular flow condition for air superficial velocities of  $J_v=22, 24.5$  and  $29.5$  m/s, and water superficial velocities of  $0.17, 0.28$  and  $0.41$  m/s which yield a void fraction in the range of  $0.9$  to  $0.93$ , based on the Martinelli model [18]. Typical surface distributions of local Sherwood number  $Sh$  are shown in Figure 6.4. The distributions for different liquid superficial velocity at air superficial velocity of  $\sim 29.5$  m/s are shown in Figure (6.4-a), while the distributions for different air superficial velocities for a liquid superficial velocity of  $0.28$  m/s are shown in Figure (6.4-b). The local distribution of  $Sh$  had a number of features in common for the different flow conditions. The  $Sh$  was relatively uniform in the inlet pipe. The maximum  $Sh$  was approximately half way into the bend on

the outer wall, consistent with the results of Poulson [10] in all cases. The region of this maximum extends across a significant portion of the outer wall. The maximum increased with an increase in liquid superficial velocity and air superficial velocity. The results in some cases also show a second region of significant enhancement in  $Sh$  on the latter part of the bend.



(a)



(b)

**Figure 6.3: Comparison of the (a) mass removal and (b) mass transfer coefficient for different initial water bulk concentrations for  $J_v=24.5$  and  $J_L=0.28$  m/s**

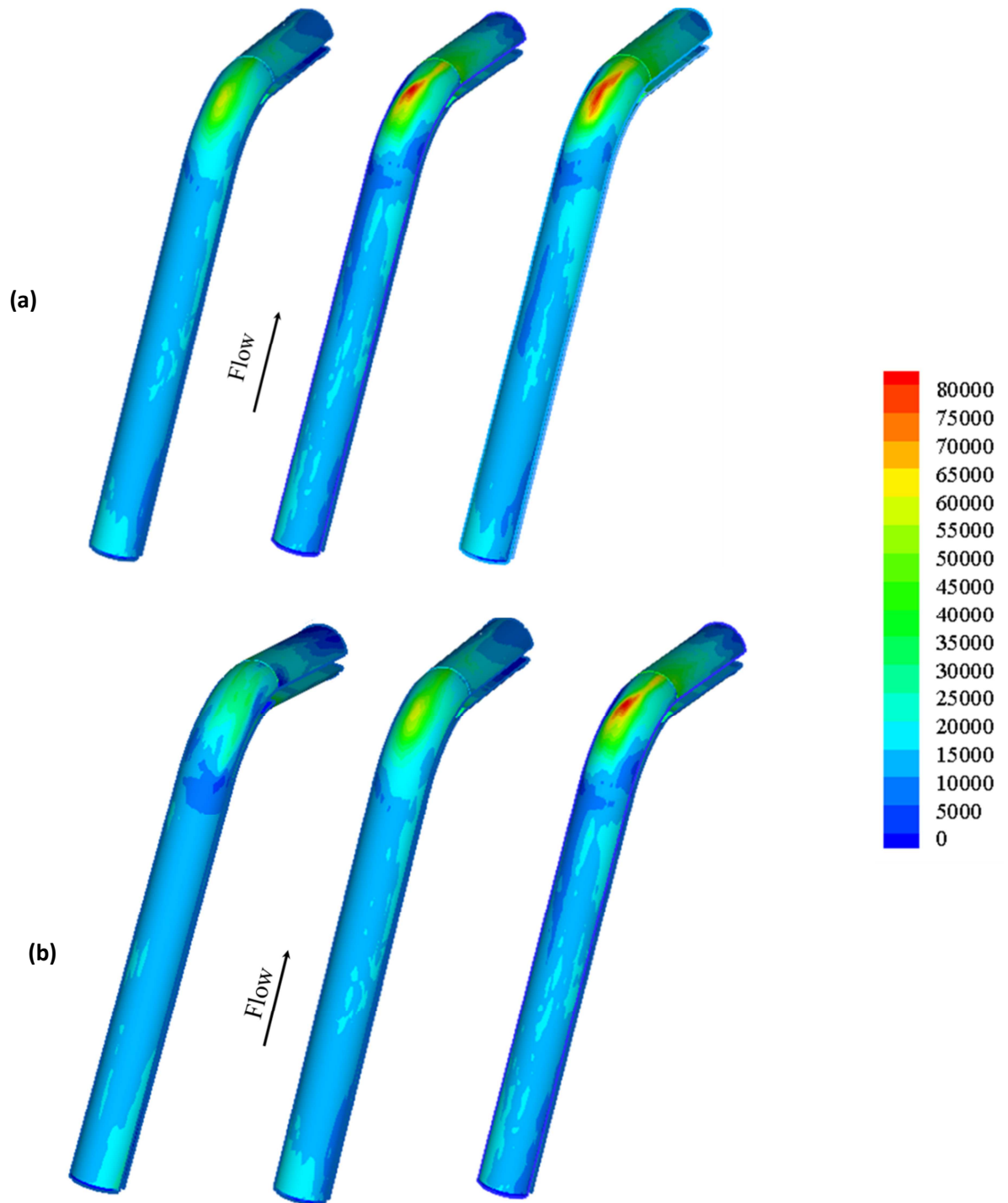
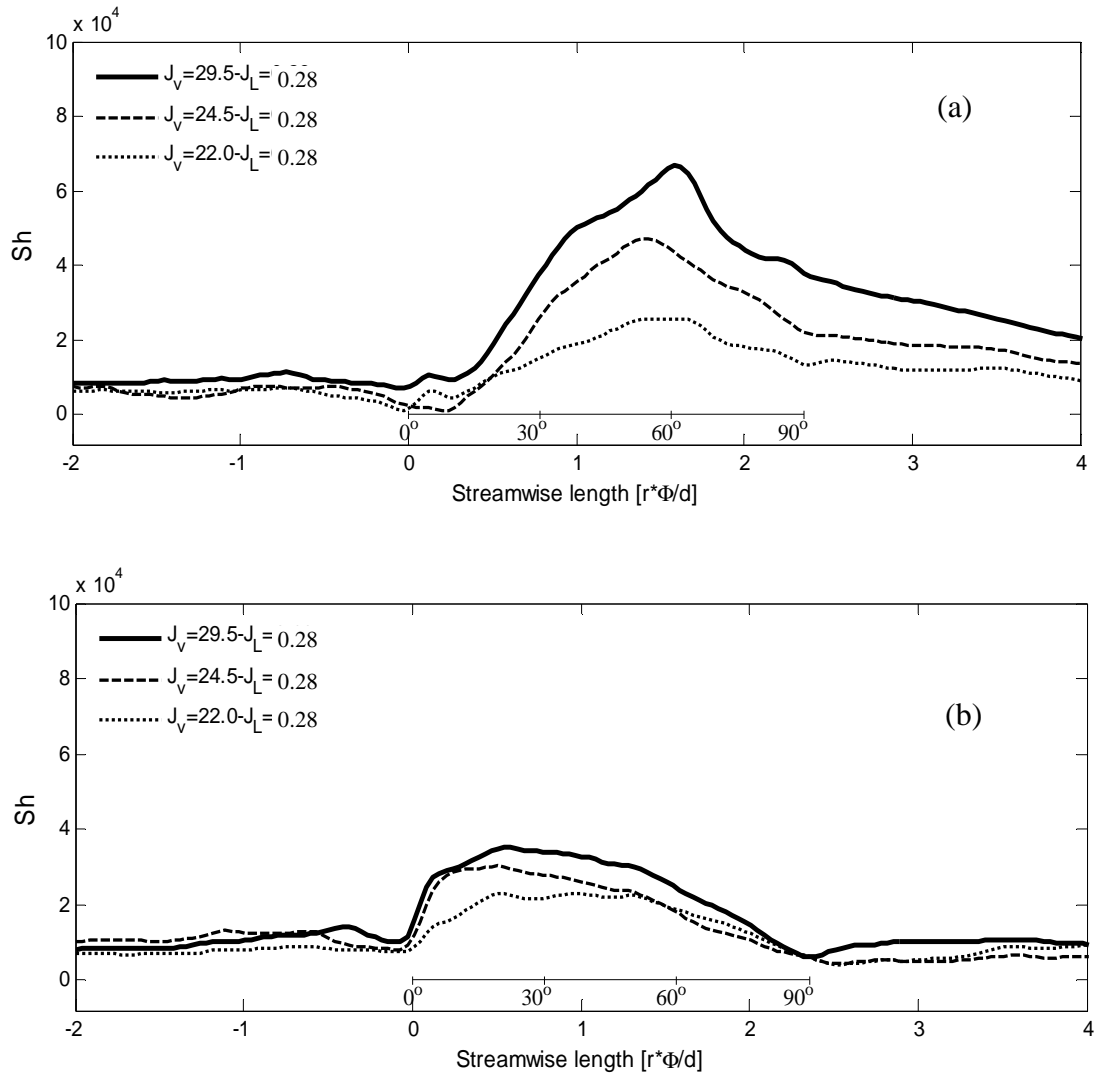


Figure 6.4: Effect of (a) water velocity and (b) air velocity on the Sherwood number distribution in the 90° bend with a radius of 1.5D under annular flow conditions, (a)  $J_v \sim 29.0 \text{ m/s}$ ,  $J_L = 0.17, 0.28 \text{ and } 0.41 \text{ m/s}$ , (b)  $J_L = 0.28 \text{ m/s}$ ,  $J_v = 22, 24.5 \text{ and } 29.5 \text{ m/s}$

This is again consistent with the results of Poulson [11] who found a plateau in the mass transfer in 180° bends downstream of the location of maximum mass transfer. The results here show that the downstream peak in  $Sh$  is significantly narrower than the upstream peak. The magnitude of the downstream peak in  $Sh$  was also affected by the air and water superficial velocity.

Streamwise profiles of the  $Sh$  along the center line of the outer and inner walls, highlighting the effect of the air and water velocities, are presented in Figure 6.5 and 6.6, respectively. The mass transfer data along pipe sections immediately upstream and downstream of the bend are also shown in these figures. The mass transfer coefficient was nearly uniform along the inlet pipe. The mass transfer rate along the outer wall of the bend increased to a maximum at approximately  $\phi$  of 55°. The mass transfer rate then dropped before reaching the second region of elevated mass transfer. There was evidence of a local minimum in the mass transfer between the peaks in some cases, consistent with the results of Poulson [11]. The mass transfer rate along the bend inner wall increases at the inlet of the bend, reaching a maximum level approximately 30° into the bend curvature. The  $Sh$  then decays toward the inner wall outlet, where it reaches a constant level slightly lower than the upstream pipe level. The enhancement in the mass transfer rate at the inlet is likely due to the acceleration of the flow on the inner wall. The acceleration as the flow enters the bend is due to the reduced pressure near the inner wall, similar to what is seen at lower void fractions [12]. Here, though, it only occurs in the film rather than across the full flow.



**Figure 6.5: Streamwise Sherwood number profiles along the (a) outer wall and (b) inner wall for  $J_L=0.28$  m/s and different  $J_v$ .**

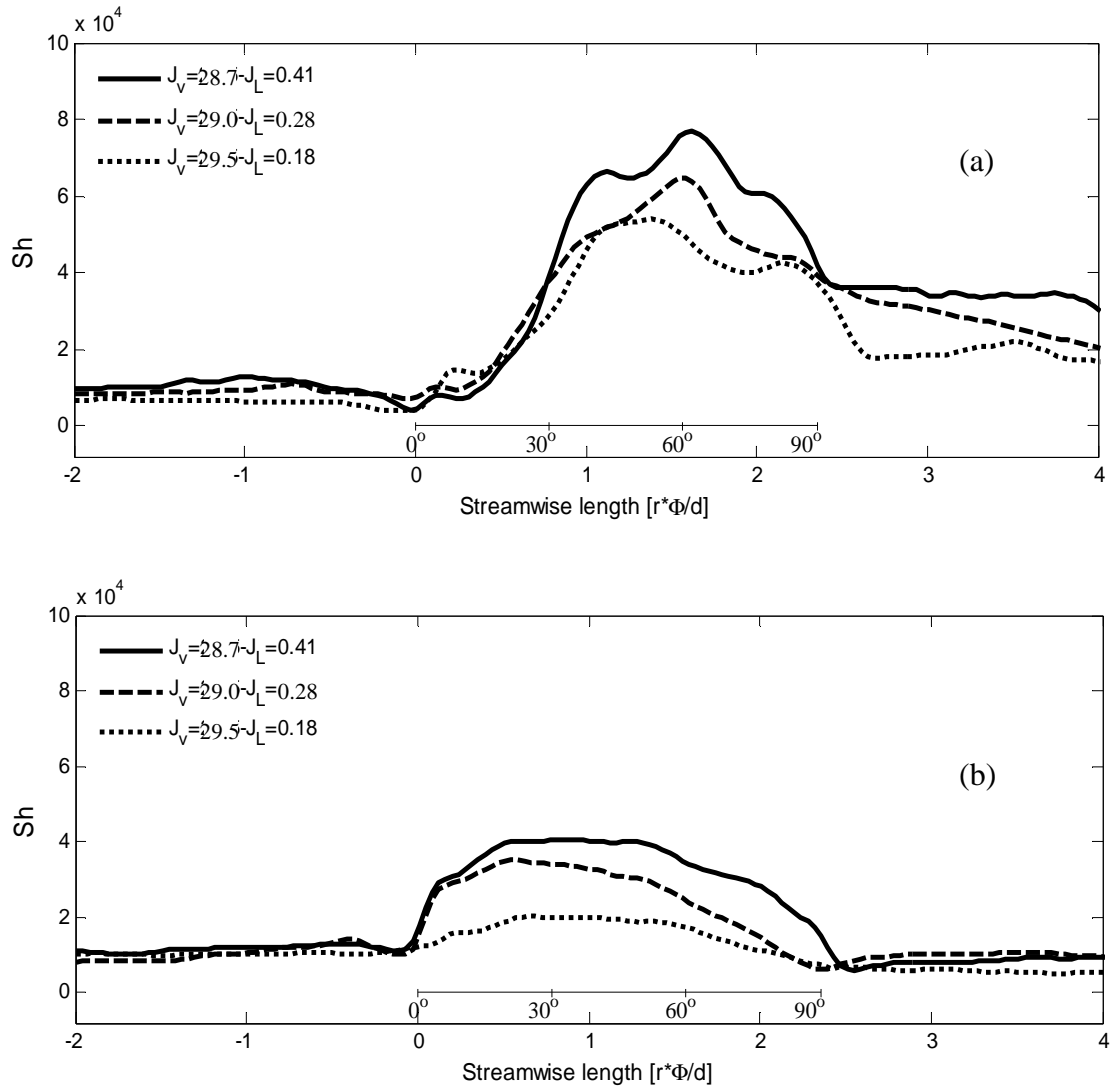


**Figure 6.6: Streamwise Sherwood number profiles along the (a) outer wall and (b) inner wall for  $J_v \sim 29.0$  m/s and different  $J_L$ .**

The effect of the air and water superficial velocities on the mass transfer are further examined through the azimuthal profiles of  $Sh$  at different stream wise locations as shown in Figures 6.7 and 6.8. The lateral distribution of  $Sh$  is nearly uniform in the upstream pipe ( $X/D = -4$  and  $-2$ ) at the different superficial air velocities (22, 24.5 and 29.5 m/s) for a constant superficial water velocity of 0.28 m/s (Figure 6.7). Similar results were obtained at a constant air velocity of 29.5 m/s and different water velocities (0.17, 0.28 and 0.41 m/s), as shown in Figure 6.8. The  $Sh$  on the outer wall at the inlet of the bend is uniform across the bend and similar in magnitude to the upstream pipe. Further into the bend, the mass transfer reaches a maximum around the centerline while the side walls are still similar in magnitude to the upstream pipe. The mass transfer rates on the outer wall at  $\phi$  of  $50^\circ$  and  $60^\circ$ , where there was a maximum in the stream wise profile, shows a uniform peak level with a width of approximately of  $30^\circ$  in the circumferential direction. The mass transfer rate decreased rapidly on either side of this peak and reaches a uniform level at approximately  $50^\circ$  off the centerline. Poulson [10, 11] attributed this peak to the impingement of the liquid droplets entrained within the core at the sight seen location on the bend outer wall. The fact that the maximum mass transfer occurs at the center line in the form of a localized sharp peak supports the proposed model by Poulson [10, 11]. The change in water superficial velocity has a significant effect on the mass transfer enhancement which agrees with the impinging jet experimental results presented by [10]; however, the results did not agree with those of Poulson [11] for annular flow which showed the water velocity had a negligible effect on the mass transfer rates. The change in air superficial velocity, however, causes a higher rate of enhancement compared to the

change in water superficial velocity. The mass transfer decreases downstream of the maximum until approximately  $\phi$  of  $80^\circ$ , and remains approximately constant from this location to the end of the bend curvature. The secondary high mass transfer location on the outer wall at the end of the bend curvature (at  $\phi > 60^\circ$ ) is more pronounced at high superficial air velocity and was not evident at low superficial air velocity. The results show that when the mass transfer is high the peak mass transfer occurred off the centerline and thus, is under represented if mass transfer measurements are performed only along the centerline. The location of the second impingement is shifted from the centerline toward the bottom half of the test section which could be due to the gravity effect. At high superficial air velocity, the magnitude of the second maximum mass transfer was evolving with the water velocity at a similar rate to the first maximum. The magnitude of  $Sh$  at the second peak is approximately 0.75 times the first maximum. The second maximum observed on the outer wall could be due to the impingement of the liquid separating from the inner wall of the bend. The liquid film on the outer wall may also be unstable due to the curvature effect and the no slip condition at the wall. There was no evidence of this in the early stages of the bend curvature so it is not clear if this has a substantial effect on the mass transfer rates. There was no significant mass transfer on the sidewalls, which suggests there is no flow sweeping around the bend. This reinforces the explanation that the second high mass transfer region on the outer wall is due to separation of the film from the inner wall impinging on the outer wall.

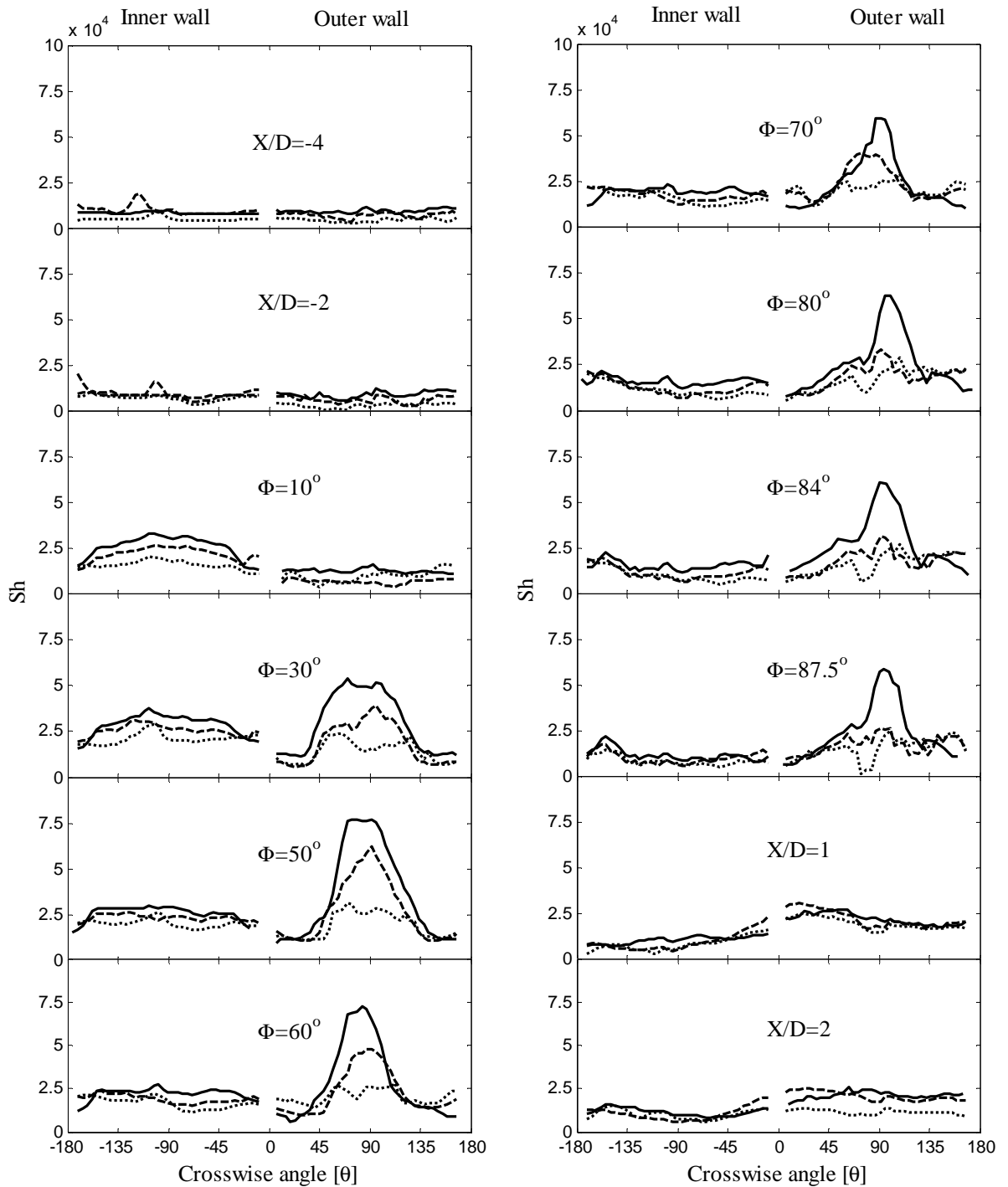


**Figure 6.7:** Azimuthal profiles of the Sherwood number for  $J_L=0.28$  m/s and  $J_v = 29.5$  m/s (—), 24.5 m/s (---), 22 m/s (.....).

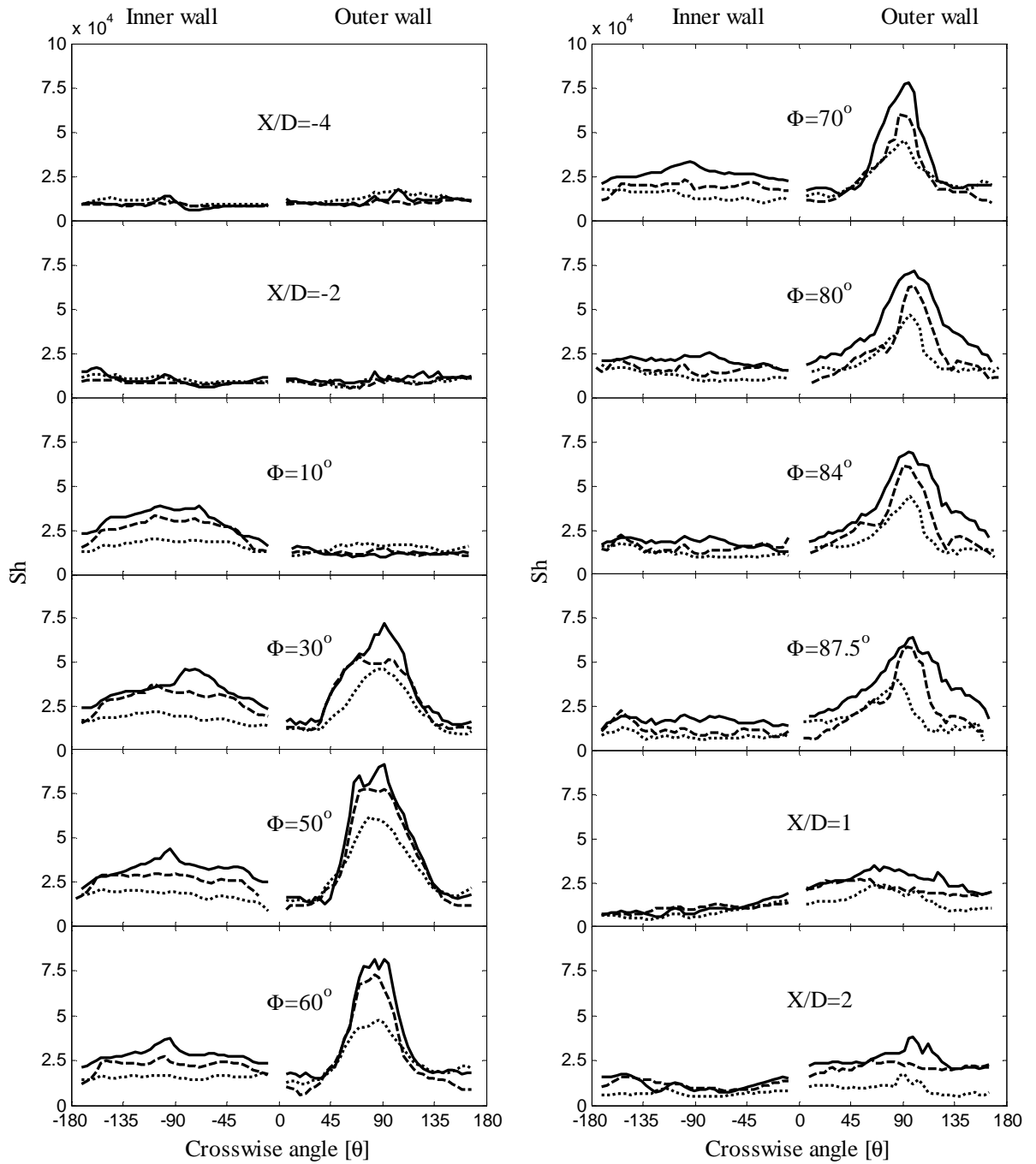


**Figure 6.8:** Azimuthal profiles of the Sherwood number for  $J_v = 29.5 \text{ m/s}$  and  $J_L = 0.41 \text{ m/s}$  (—),  $0.28 \text{ m/s}$  (---),  $0.17 \text{ m/s}$  (.....).

The  $Sh$  profiles on the inner wall show a uniform distribution across the upstream inlet pipe. The mass transfer rate on the inner wall increases to reach a maximum at approximately  $\phi$  of  $30^\circ$ . This maximum occurs in the center region in the form of a broad uniform plateau covering  $100^\circ$  in the circumferential direction and tails off toward the side walls. This enhancement may be attributed to the low pressure formed on the bend inner wall causing flow acceleration at the bend inlet. The  $Sh$  profiles then decay towards the bend outlet, as also evident in the streamwise profiles. The effect of increasing either the superficial water or air velocity on the trend of mass transfer enhancement was similar. In the outlet pipe the mass transfer rate drops slightly below the upstream pipe with the side walls trending upward.

The mass transfer enhancement, defined as the ratio of the local maximum  $Sh$  to that in the upstream pipe ( $Sh_{pipe}$ ), at the first and second peak mass transfer rate locations, is presented in figure 6.9. The results are presented for the different liquid and air superficial velocities with the numbers representing the magnitude of the mass transfer enhancement. The results of Poulson [11] are also shown in figure (6.9-a) for comparison. The maximum mass transfer rates in this instance are determined from the azimuthal profiles. The trend of the mass transfer enhancement with the superficial air velocity of the present results agreed with the proposed trend of Poulson [10]. Poulson [11], however, did not find a significant effect of the liquid superficial velocity on the enhancement, which are contrary to the present results. The mass transfer enhancement at the first peak increased by a factor of 2.3 as the superficial air velocity was increased from 22 to 29.5 m/s, while it increased by a factor of 1.5 when the superficial water velocity was increased from 0.17

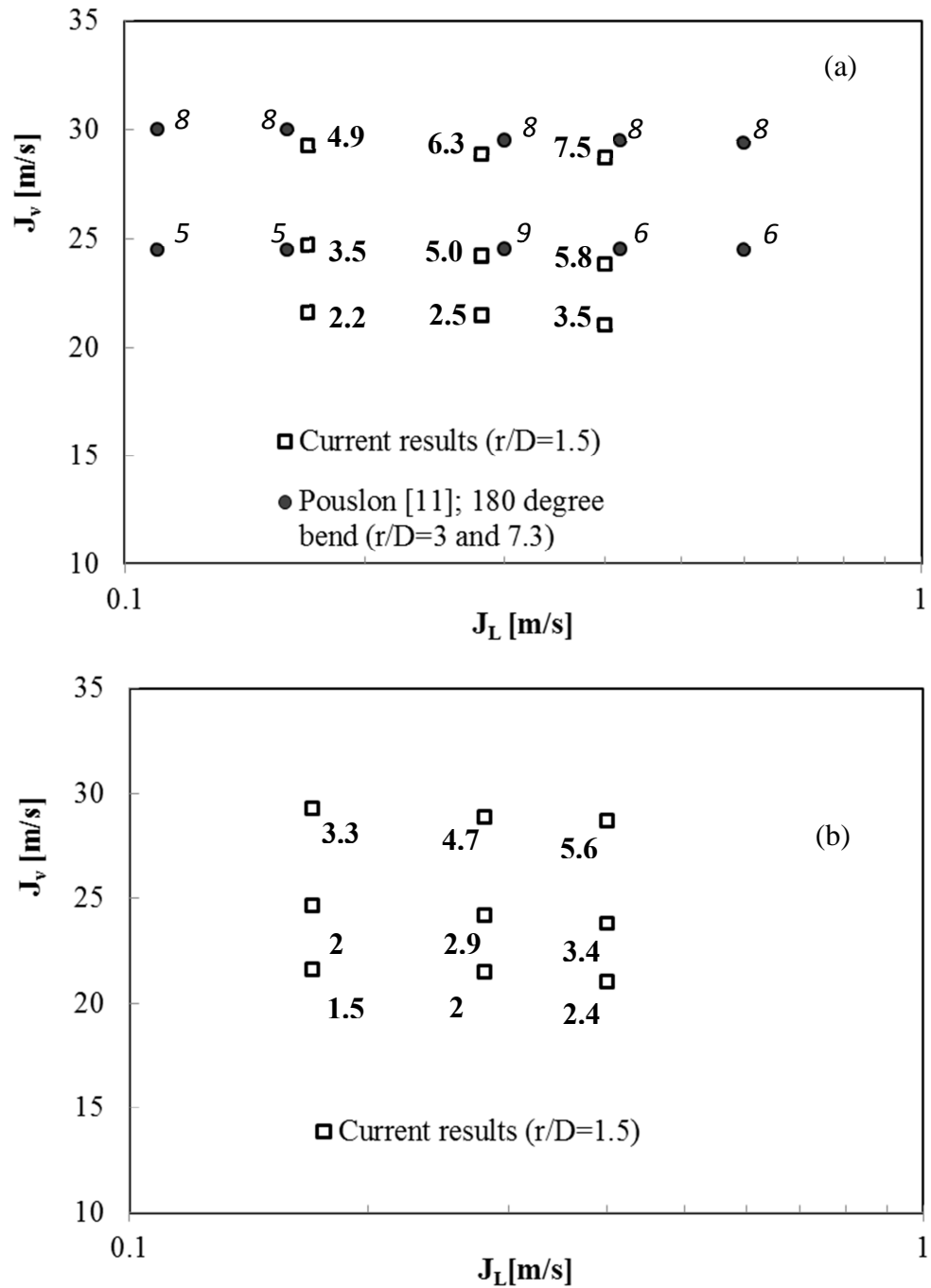


**Figure 6.9: Effect of air and water superficial velocities on the mass transfer enhancement over straight pipe ( $Sh/Sh_{pipe}$ ) for different annular flow conditions, (a) at the first peak, compared with [11] results, (b) at the secondary peak. Note: numbers in bold represent the current results**

to 0.41 m/s, figure (6.9-a). The relative changes in mass transfer enhancement at the second mass transfer maximum on the outer wall with the air and water velocity were very similar to that at the first mass transfer maximum; figure (6.9-b).

#### **6.4 Conclusions**

Mass transfer measurements in horizontal single 90° bends under a range of inlet annular air-water flow conditions at high Schmidt number ( $Sc=1280$ ) were performed. The air and water superficial velocities were in the range 22 to 29.5 m/s and 0.17 to 0.41 m/s, respectively. The local distribution of the mass transfer rate over the entire surface was obtained. Two local maxima in the mass transfer were found on the outer wall of the bend. The location of the maximum mass transfer was midway through the bend on the outer wall centerline, in agreement with Poulson [10]. The maximum in the mass transfer spanned 30° in the azimuthal direction. The second peak occurs further downstream on the bend outer wall at  $\phi$  of 80 to 85° and shifted off the center line. The mass transfer enhancement increased with an increase in either the water or air superficial velocity. Mass transfer enhancement levels between 2.5 and 7.5 relative to that in the upstream pipe are measured at the first maximum, while the second maximum enhancement levels were between 1.5 and 5.6.

#### **Acknowledgement**

The support of the Natural Sciences and Engineering Research Council of Canada (NSERC) and CANDU Owners Group (COG) is gratefully acknowledged.

## 6.5 References

- [1] Poulson, B., 1999, Complexities in predicting erosion corrosion, *Wear* 233-235: 497-504.
- [2] Kim, S., Park, J. H., Kojasoy, G., Kelly, J. M., Marshall, S. O., 2007, Geometric effects of 90-degree elbow in the development of interfacial structures in horizontal bubbly flow, *Nuclear Engineering and Design* 237 : 2105-21
- [3] Spedding, P.L., Benard, E. and Crawford, N.M., 2008, Fluid flow through a vertical to horizontal 90° elbow bend III phase flow, *Exp. Thermal Fluid Sci.*32, pp827-843
- [4] Crawford, N. M., Cunningham, G., Spedding, P.L., 1974, Prediction of pressure drop for turbulent fluid flow in 90 degree bends, *Proc. Inst. Mech. Eng.* 217E, 1–3.
- [5] Spedding, P.L., Benard, E., McNally, G.M., 2004, Fluid flow through 90 degree bends, *Dev. Chem. Eng. Min. Process* 12, 107–128.
- [6] Supa-Amornkul, S., Steward F.R., Lister D.H., 2005, Modeling two-phase flow in pipe bends, *Journal of Vessel Technology* 127: 204-209
- [7] Maddock, C. Lacey, P. M. C. Patrick, M. A., 1974, “The structure of two phase flow in a curved pipe”, *J. of Chem. E. Symp.* 38.
- [8] Anderson, G.H., Hills, P.D., 1974, “Two-phase annular flow in tube bends”, Presented at Symp. *Multiphase Flow Systems, Inst. Chem. Engineers Symp. Ser. No. 38*, Univ. of Strathclyde, Paper J1
- [9] Usui K., Aoki S, Inoue A, 2008, Flow behavior and pressure drop of two phase flow in C- Shaped bend in vertical plane, Upward flow (I), *J. Nuclear Science and Technology*, 17 (12) 875-887.
- [10] Poulson, B., 1993, Advances in understanding hydrodynamic effects on corrosion, *Corrosion Science* 35, no. 1-4: 655-665.

- [11] Poulson, B., 1991, Measuring and modeling mass transfer at bends in annular two phase flow, *J. of Chemical Engineering Science* 64, no. 4: 1069-1082.
- [12] Pecherkin N., Chekhovich V., 2011, Mass transfer in two-phase gas-liquid flow in a tube and in channels of complex configuration, 155, Chapter 8, Mass transfer in multiphase systems and its applications, Mohamed El-Amin (Ed.), ISBN: 978-953-307-215-9, In Tech.
- [13] Da Silva Lima, R. J., Thome, J.R., 2012, Two-phase flow patterns in U-bends and their contiguous straight tubes for different orientations, tube and bend diameters, *International Journal of Refrigeration*, 35: pp. 1439-1454
- [14] Villien, B., Zheng, Y., and Lister, D.H., 2001, “The scalloping phenomenon and its significance in flow assisted-corrosion”, *Twenty Sixth Annual CNS-CNA Student Conference*.
- [15] Wilkin, S. J., Oates, H.S., Coney, M., 1983, “Mass transfer on straight pipes and 90° bends measured by the dissolution of plaster (1st Edn)”. *Central Electricity Research Laboratories*, TPRD/L/24.569/N83.
- [16] Robinson, R. A., and R. H. Stokes, 1968, *Electrolyte Solutions*, 2nd Rev. Edit., Butterworths, London
- [17] Coleman, H.W. and Steele, W.G., 1999, *Experimentation and Uncertainty Analysis for Engineers*, 2<sup>nd</sup> Ed., John Wiley & Sons, New York
- [18] Chisholm, D., 1967, A theoretical basis for the Lockhart Martinelli correlation for two-phase flow, *Int. J. Heat Mass Transfer* 10 1767–1778.

## **CHAPTER 7**

---

### **Mass transfer in S-shape dual pipe bends under annular two phase flow conditions**

#### **Complete citation:**

H. Mazhar, J. S. Cotton, D. Ewing, C. Y. Ching, Mass Transfer in S-shape dual pipe bends under annular two phase flow conditions, Journal of Heat Transfer Submitted August 2013

#### **Relative Contributions:**

H. Mazhar: Performed all experiments, interpretation and analysis of the data and wrote the first draft of the manuscript including all figures and text.

J. S. Cotton: Co-supervisor of H. Mazhar and was involved in the discussion of Results and revised the initial drafts of the manuscript

D. Ewing: was involved in the interpretation and discussion of results.

C. Y. Ching: Co-supervisor of H. Mazhar and was responsible for the final draft submittal to the journal

**Abstract:**

The mass transfer in S- shape dual in-plane short radius bends is investigated under annular air-water flow conditions. Experiments were performed for a Schmidt number ( $Sc$ ) of 1280 for different lengths of straight pipe ( $L/D$ ) between the bends. Standard  $90^\circ$  bends with radius of curvature ( $r/D$ ) of 1.5 were tested for  $L/D$  from 0 to 40 for water ( $J_L$ ) and air ( $J_V$ ) superficial velocities of 0.28 and 29 m/s, respectively. The maximum mass transfer was found to occur on the outer wall of the first bend in all cases. The region of high mass transfer in the second bend is located near the outlet of the bend outer wall and was approximately 60% of that in the first bend for the  $L/D=0$  case. This value increased and the location moved upstream as the separation distance was increased, with a magnitude of approximately 85% of that in the first bend at  $L/D$  of 40. The effect of  $J_V$  and  $J_L$  on the mass transfer for  $L/D=0$  was determined for  $J_V$  and  $J_L$  in the range 0.17 to 0.4 m/s and 22 to 30 m/s, respectively. The local mass transfer distribution was similar in all cases, with  $J_V$  having a more significant effect on the mass transfer enhancement. The phase redistribution within the dual bend for  $L/D=0$  was visualized using laser induced fluorescence. The high mass transfer locations were found to correlate well with the locations of liquid impingement.

## 7.1 Introduction

Flow accelerated corrosion (*FAC*) is a piping degradation mechanism that develops over several years and results in pipe wall thinning with potential for abrupt pipe failure. *FAC* occurs in two stages: (i) oxidation of the pipe metal known as corrosion followed by (ii) the mass transfer of the formed corrosion layer to the adjacent fluid by dissolution. Mass transfer is the rate limiting factor in *FAC*, and is affected by flow velocity and turbulence level. The frequency of pipe failure due to *FAC* is reported to be higher under two phase flow conditions than under single phase flow [1].

Two phase flow through pipe bends results in significant changes in flow direction leading to phase redistribution due to the difference in density between the two phases [2, 3]. The phase redistribution is more severe under high void fraction flow conditions and can result in high mass transfer enhancement levels [4]. Thus, *FAC* studies have primarily focused on annular two phase flow conditions. Several investigations focused on understanding the annular two phase flow in bends through pressure drop measurements and flow visualizations [5- 9], and through heat and mass transfer in the bends [10-12]. The phase redistribution is reported to cause a significant mass transfer enhancement on the pipe bend outer wall and develop distinctive mass transfer distribution features. Continuous liquid flow separation from the first bend inner wall and deposition on the second bend outer wall was observed by [7, 13]. A high mass transfer enhancement was reported at the location of the anticipated liquid deposition [12].

Comparison of mass transfer in straight pipes under annular two phase flow and single phase flow at an equivalent surface shear stress yielded an enhancement of 1- 1.6 for the

two phase flow over single phase flow [11]. The mass transfer enhancement for slug two phase flow relative to single phase flow at similar Reynolds number was reported to be approximately 3 times [14]. This enhancement was attributed to the effect of the entrained bubbles and the effect of liquid slugs on disturbing the near wall liquid region.

The mass transfer in  $180^\circ$  bends was measured under annular flow conditions for radius of curvature  $r/D$  of 3 and 7.3 by Poulson [10, 11]. Only centerline measurements were performed along the bend outer wall. The location of maximum mass transfer was on the bend outer wall and corresponded to the location of the entrained liquid droplet deposition. The high mass transfer rate was attributed to the interplay of liquid droplets within the core impinging on the outer wall and the film re-distribution due to the centripetal forces generated by the bend curvature. The interplay of these two mechanisms is expected to vary with the annular flow condition. The air superficial velocity had a significant effect on the mass transfer but the role of the water velocity was unclear with results showing it had only a minor effect on the mass transfer [10]. The location of the maximum mass transfer along the curvature is found to depend on the bend tightness ( $r/D$ ) and a correlation for this location was proposed by [11]. The maximum mass transfer was found to move downstream as the radius of curvature of the bend was reduced.

Mass transfer by erosion was reported by [11] in test sections cast from plaster of paris for a gas superficial velocity of 60 to 70 m/s. The velocity threshold for liquid droplet impingement wear in steel pipes is reported to be in the range 70 to 125 m/s [15-17]. Droplet impingement has a significant effect under mist flow conditions, like wet steam

flows, where no liquid film exists on the pipe surface. In the case of annular flow with sufficient film thickness on the pipe wall, the film tends to cushion the impact of the liquid droplets on the surface and reduces its effect on the mass removal enhancement [18].

The development length for annular flow through straight pipes is reported to be approximately 30 diameters [19]. The development length downstream of a U- shape dual bend is reported to be longer than 30 pipe diameters which was the maximum length for the experiments by [20] and more than 141 diameters by [21]. This could be due to the drastic phase redistribution within the bends, where most of the liquid phase collects on one side of the bend.

The objective of this investigation was to investigate the mass transfer distribution in short radius ( $r/D=1.5$ )  $90^\circ$  dual bends arranged in an S- configuration with different lengths of straight pipe between the two bends under a range of annular flow conditions. The measurements were performed using a dissolving wall method with test section cast from Gypsum with a Schmidt number ( $Sc$ ) of 1280. The surface wear topography at the end of each experiment is measured using a laser scanning system. The phase redistribution within the bend was visualized using laser induced fluorescence (*LIF*) to help understand the mechanism responsible for the mass transfer distribution. The test facility and methodology is reported in the next section followed by a discussion of the results.

## 7.2 Experimental methodology

Experiments were performed in the test facility shown schematically in figure 7.1, which is described in detail in [22]. Water is circulated from a reservoir through the test loop by a centrifugal pump. The flow rate is regulated by globe valves and measured by a turbine flow meter with an accuracy of  $\pm 1\%$  of the flow reading. Air from a compressed line is filtered and supplied to the test facility. The air flow rate is measured using two rotameters connected in parallel with accuracies of  $\pm 2\%$  of the full scale. The supply air pressure is measured and recorded for each test condition using a pressure gauge at the supply line. The air pressures after the rotameters and before the test section are measured to correct the air flow rate and obtain the air superficial velocity at the inlet to the test section. The flow of water passed through a perforated plate followed by a honeycomb before it is mixed with the air stream. The mixing chamber is in the form of two concentric tubes with the inner tube, carrying the air, being perforated on the periphery to homogeneously inject the air into the water stream running in the annulus between the inner and outer tubes.

The mixed air–water flow then passes through a straight pipe of 160 cm in length upstream of the test section. The air-water flow exited the test section to a 75 cm long straight pipe before being directed to a phase separation reservoir with an air vent to release the separated air. The water temperature was measured in the reservoir and is kept constant to within  $\pm 0.5$  °C using a compensation cooling loop. The dissolution of the Gypsum test section in water during the test increases the water electrical conductivity

which is used to determine the overall dissolved mass from the test section in the water. The water reservoir included an electrical conductivity probe to measure the water conductivity. A calibration experiment was performed offline to correlate the amount of dissolved Gypsum to the change in conductivity of the water.

The test sections are cast from Hydrocal ( $\text{CaSO}_4 \cdot 1/2 \text{H}_2\text{O}$ ), which produces Gypsum with a density of  $1580 \text{ kg/m}^3$ . The test sections had a nominal diameter of 2.54 cm and consisted of an upstream 20 cm long straight pipe, two standard  $90^\circ$  bends with a radius of curvature of 38.1 cm each, arranged in an S- configuration with pipe lengths of 0, 1 and 5 diameters between the bends, and finally a 10 cm long downstream straight section. For the tests with separation distances between 10 to 40 diameters, only the second bend was manufactured from Gypsum with a 20 cm upstream pipe segment and 10 cm downstream pipe segment. In this case the first bend and a segment of the separation pipe were made of Acrylic. The cast sections are left to dry and their weight is recorded periodically. When the weight attains a constant level, the sections are tested under annular flow conditions. The same process is repeated after each experiment and when the samples weights are constant, the difference in samples weights before and after experiments is taken as a measure of the overall mass removed. The test sections are then cut along the bend profile (figure 7.2) to measure the surface topography using a laser scanning coordinate measurement technique to obtain the local mass transfer coefficients.

The total mass removed from the test section during the experiment was determined from: (i) comparing the mass of the test section before and after the test, (ii) the concentration of the dissolved gypsum in the water at the end of each test and (iii) the integrated mass

removed obtained from the laser digitized three dimensional surface scan. The mass calculated from the different methods agreed to within  $\pm 7\%$ .

The mass transfer coefficient is evaluated from

$$\rho \frac{d\delta}{dt} = h\Delta C \quad (1)$$

where  $\rho$  is the average density of the Hydrocal,  $\delta$  is the thickness of local mass removed normal to the surface,  $\Delta C$  is the difference between species concentration at the wall and in the bulk flow and  $h$  is the mass transfer coefficient. The concentration difference decreases over the course of the experimental time due to the dissolution of the gypsum in water, and thus the driving potential for the mass transfer decreases. The mass transfer coefficient was calculated using a modified time to account for the change in concentration difference using the following

$$\rho \frac{d\delta}{d\tau_{\text{mod}}} = h\Delta C_o \quad (2)$$

where  $\tau_{\text{mod}}$  is the modified time given by

$$\tau_{\text{mod}} = \frac{1}{\Delta C_o} \int_0^t [C_w - C_b] \cdot dt \quad (3)$$

Then the Sherwood number is calculated as

$$Sh = \frac{h \times D}{D_m} \quad (4)$$

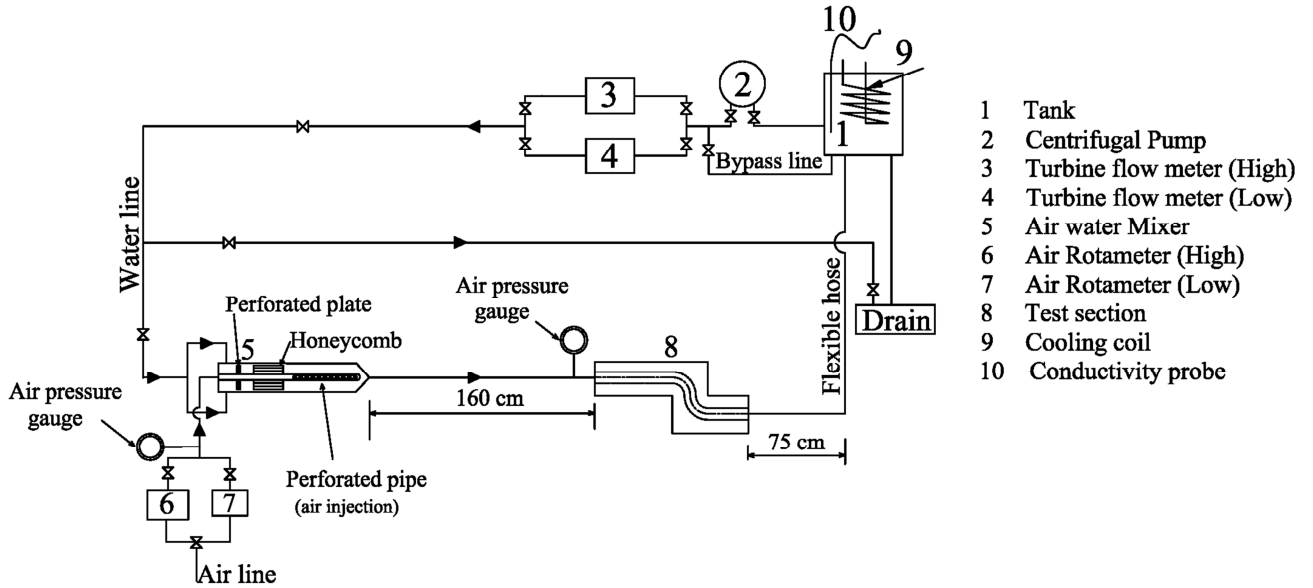


Figure 7.1: Schematic showing the principle components of the test facility.

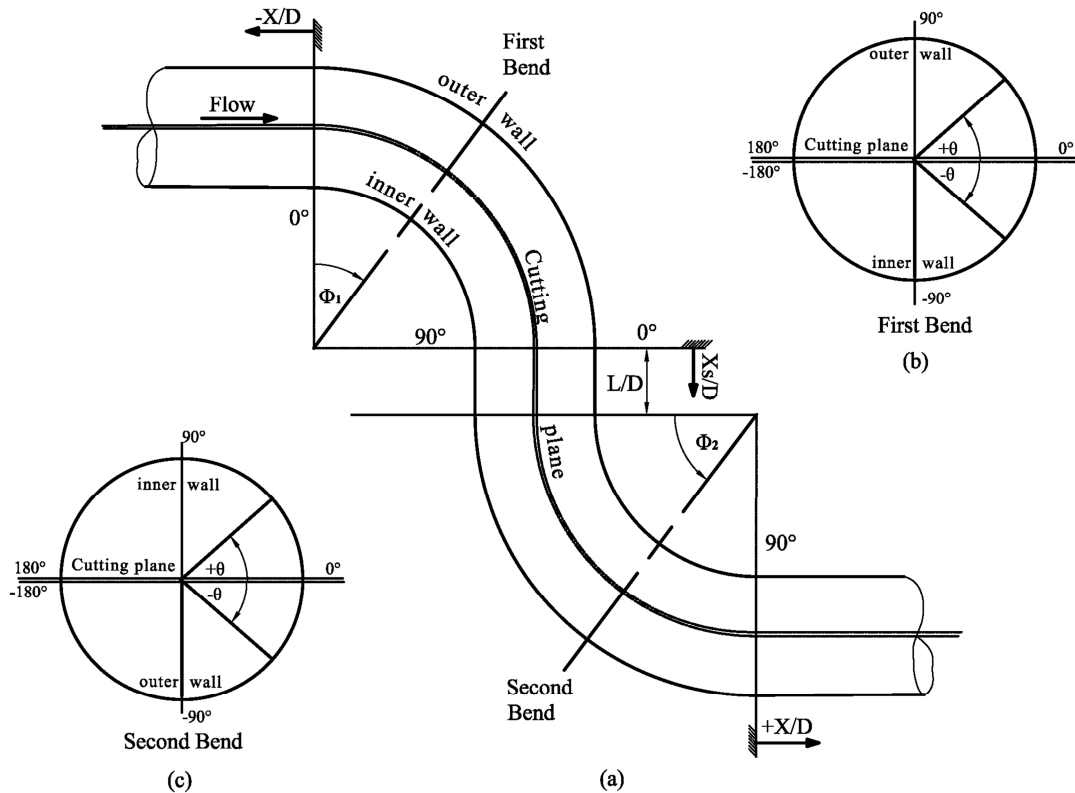


Figure 7.2: Schematic of the test section showing the section planes relative to : (a) streamwise orientation, (b) crosswise orientation in the first bend and (c) crosswise orientation in the second bend.

**Table 7.1: Nomenclature of quantities and terms.**

Nomenclature		
$dm/dt$	Mass transfer rate	$[kg/s]$
$C_w$	Hydrocal ions concentration at the wall	$[kg/m^3]$
$C_b$	Hydrocal ions concentration in the bulk fluid	$[kg/m^3]$
$\Delta C_o$	Initial concentration difference	$[kg/m^3]$
$\delta$	Local instantaneous wear of the test section	$[m]$
$D$	Bend cross sectional diameter	$[m]$
$D_m$	Mass diffusivity for Hydrocal in water determined at 25° C	$[m^2/s]$
$e$	Roughness height	$[m]$
$e/D$	Relative roughness height	$[m]$
$e^+$	Roughness scale	
$h$	Mass transfer coefficient	$[m/s]$
$J_v$	Air superficial velocity	$[m/s]$
$J_L$	Water superficial velocity	$[m/s]$
$Sc$	Schmidt number $(\nu/D_m)$	
$Sh$	Sherwood number $(h \times D/D_m)$	
$X/D$	Streamwise dimensionless distance	
$X_s/D$	Location along separation pipe	
$L/D$	Separation distance	
$\rho$	Density of the gypsum	$[kg/m^3]$
$\theta$	Bend cross sectional angle	
$\phi_1$	Bend angle of curvature (along first bend)	
$\phi_2$	Bend angle of curvature (along second bend)	
$\nu$	Kinematic viscosity	$[m^2/s]$

where  $D$  is the pipe diameter and  $D_m$  is the mass diffusivity. The rate of change in the mass removal is computed at every local point to determine the spatial distribution of the mass transfer rate. The uncertainty in the measurements was evaluated considering all the contributing variables, e.g. uncertainty in the digitized image, water electrical conductivity, variability from different testing times, following [23]. The uncertainty in the calculation of the local mass transfer coefficient was determined to be approximately  $\pm 19\%$  based on the upstream pipe and  $\pm 15\%$  based on the average peak level.

Since the mass transfer in two phase flow systems could result from dissolution and/or erosion, the contribution of the two processes was evaluated by performing experiments with different initial gypsum bulk concentrations of 0%, 50% and fully saturated in the water. The fully saturated experiments resulted in no mass removal, while the mass transfer coefficients from the other two initial concentrations were within the experimental uncertainty. This indicates that mass transfer for the current experimental conditions is purely by dissolution.

The phase redistribution for the  $L/D=0$  separation case was visualized using a transparent acrylic section manufactured to the same geometric specifications as the mass transfer test section. The flow was illuminated using a 532nm New Wave Solo 120XT pulsed Nd:YAG laser with a maximum output of 120mJ per pulse. A combination of plano-cylindrical and spherical lenses was used to focus the laser beam into a sheet. Rhodamine 6G fluorescence dye was injected upstream of the test section, which is excited by the laser wave length and emits light at a longer wave length. A PowerView 4MP 12 bit digital camera with a resolution of 2048×2048 pixels was used for flow imaging. A high

pass optical filter with a cut-off wave length of 545 nm was installed on the camera lens to filter the 532 nm green laser light scattered by the air-water interfaces, and distinguish between the air and water in the visualization image [24]. The laser pulses and camera frames were synchronized using a TSI Laser Pulse Model 610035 synchronizer with external triggering and software adjustable time delay.

The experiments were performed for  $J_v$  of 29 m/s and water superficial velocity  $J_L$  of 0.28 for bend separation distances of  $L/D$  of 0, 1, 5, 10, 20 and 40. The effect of annular flow conditions on the mass transfer enhancement was examined for the  $L/D=0$  case for  $J_v$  in the range of 22 to 30 m/s and  $J_L$  in the range 0.17 to 0.4 m/s. This yields a void fraction level of approximately 0.89 to 0.93 according to the model of Lockhart and Martinelli [25]. The test matrix is presented in appendix C, and is in the annular flow regime on the two phase flow map developed by Taitel and Duckler [26], which was also confirmed using high speed imaging in the upstream pipe.

### **7.3 Results and discussion:**

The distribution of the Sherwood number ( $Sh$ ) for the different separation distances at  $J_v=29$  m/s and  $J_L=0.28$  m/s is shown in figure 7.3. The  $Sh$  distribution in the first bend for the three separation distances of  $L/D = 0, 1$  and 5 is similar to that for the single bend [12]. The  $Sh$  in the upstream pipe was generally uniform along the stream wise direction in all cases, which suggest that the flow is fully developed in the upstream pipe. On the first bend outer wall, the  $Sh$  decreases near the inlet and then increases gradually and reaches a maximum midway through the bend curvature (figure 7.3-a). A second

localized high mass transfer region is observed along the centerline near the outlet, similar to the single bend case. The relatively high  $Sh$  level extends into the second bend inner wall for the  $L/D=0$  separation case, while it decays along the separation pipe for the other cases. The  $Sh$  along the second bend inner wall starts relatively high and gradually decreases along the bend curvature and the downstream pipe. On the other side of the test section, the mass transfer starts relatively high near the inlet of the first bend inner wall and decreases from this location onward into the bend curvature (figure 7.3-b). For the  $L/D=0$  separation, the mass transfer increases gradually along the second bend outer wall to form another region of high mass transfer near the outlet of the bend curvature, which extends to the first part of the downstream pipe. The increase in separation distance does not result in a significant change in the mass transfer in the first bend; however, it changes the magnitude and location of the maximum mass transfer on the second bend outer wall. The location of the maximum shifts upstream and the magnitude increases with an increase in separation distance. The maximum region in the second bend is in the form of a wide region over most of the bend cross section and the breadth of this peak decreases with an increase in the  $L/D$  to approach a similar pattern to the first bend at  $L/D$  of 40; however, the magnitude is still lower. Streamwise  $Sh$  profiles along the centerline of the test section,  $\theta = \pm 90^\circ$ , are shown in figure 4. The mass transfer increases along the first bend outer wall to reach a maximum near  $\phi_I = 50^\circ$  (figure 7.4-a). The mass transfer decays from this point and reaches a plateau on the latter part of the first bend outer wall. The mass transfer on the first bend inner wall increases to reach a peak near  $\phi_I = 20^\circ$  and

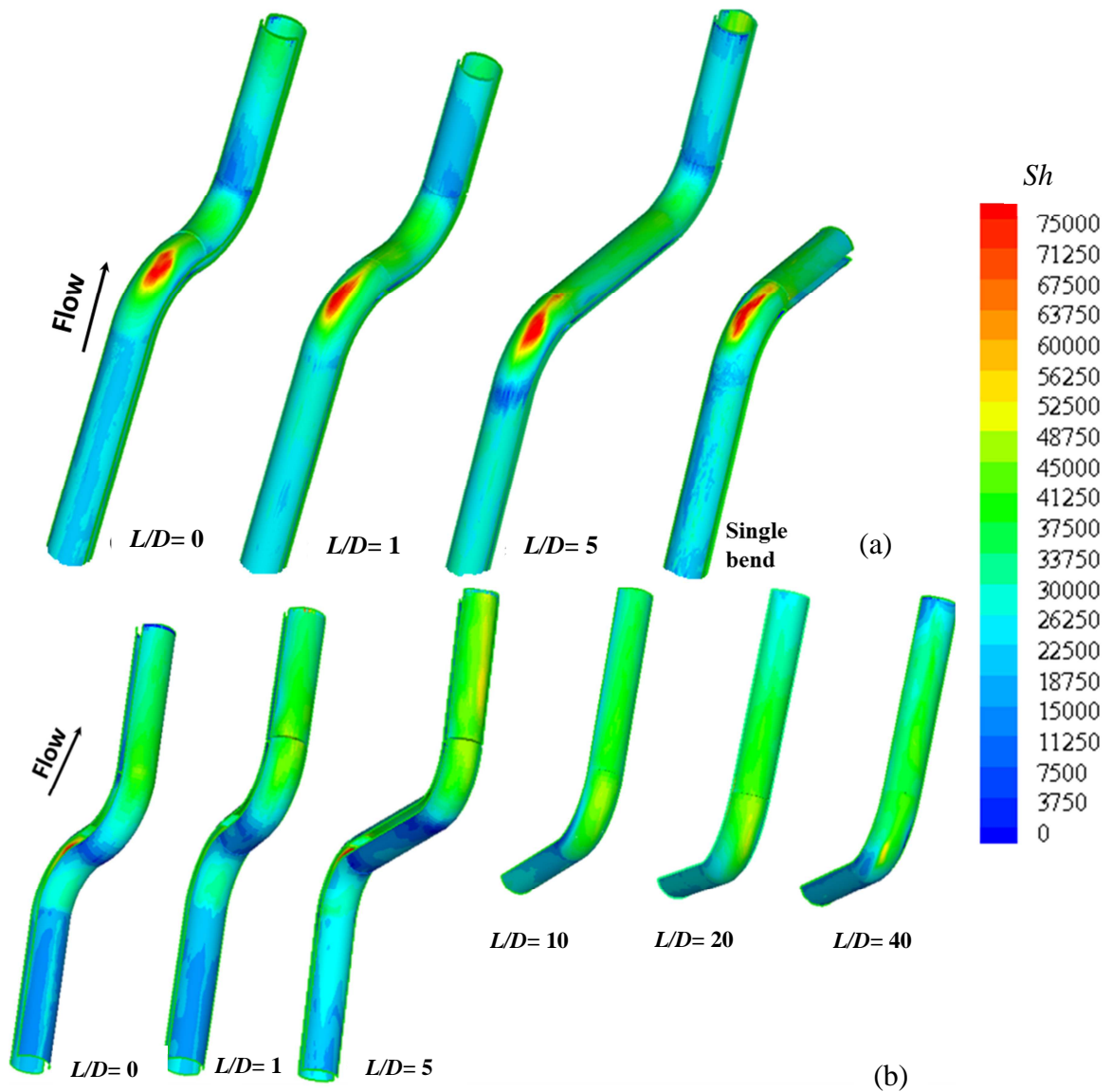


**Figure 7.3: Mass transfer distribution in the S-shape dual bend at  $L/D$  from 0 to 40 for (a) first bend outer wall (b) second bend outer wall for  $J_v=29$  m/s and  $J_L=0.28$  m/s and  $Sc=1280$ .**

then gradually decreases along the bend curvature (figure 7.4-c). There is little difference in the profiles along the first bend for the different separation distances and they are all similar to the single bend profiles [12]. On the second bend inner wall, the mass transfer starts at the same level of the plateau region occurring at the end of the first bend outer wall and decays gradually along the bend profile for the zero separation case. The mass transfer at the inlet of the second bend inner wall is lower as the separation distance increases, as there is more distance for the mass transfer to relax in the separation pipe. For the  $L/D=0$  case, the mass transfer starts lower than the level in the straight pipe on the second bend outer wall, and increases along the bend curvature to reach a maximum near the outlet. The maximum mass transfer on the outer wall of the second bend increases as the separation distance is increased while the location of the maximum moves upstream to approach the location of the maximum on the first bend for the  $L/D=40$  case.

Azimuthal profiles of the mass transfer at different locations along the bend curvature are shown in figure 7.5. On the first bend outer wall side, the mass transfer reaches a maximum near  $\phi_1=50^\circ$  and spans approximately  $30^\circ$  in the circumferential direction. The mass transfer decays from this point onward, following the same trend as the single bend [12]. On the first bend inner wall, an elevated mass transfer region with  $Sh$  of  $28 \times 10^3$  occur near  $\phi_1$  of  $20^\circ$  and spans from  $\theta$  of  $-135^\circ$  to  $-45^\circ$ . The mass transfer decreases gradually from this point onward and is similar for the different separation distances. On the second bend inner wall, figure (7.5-b), the  $Sh$  has a maximum of approximately  $38 \times 10^3$  near  $\phi_2$  of  $20^\circ$  for  $L/D=0$  and the region spans between  $\theta$  of  $65^\circ$  and  $115^\circ$ , and decreases gradually along

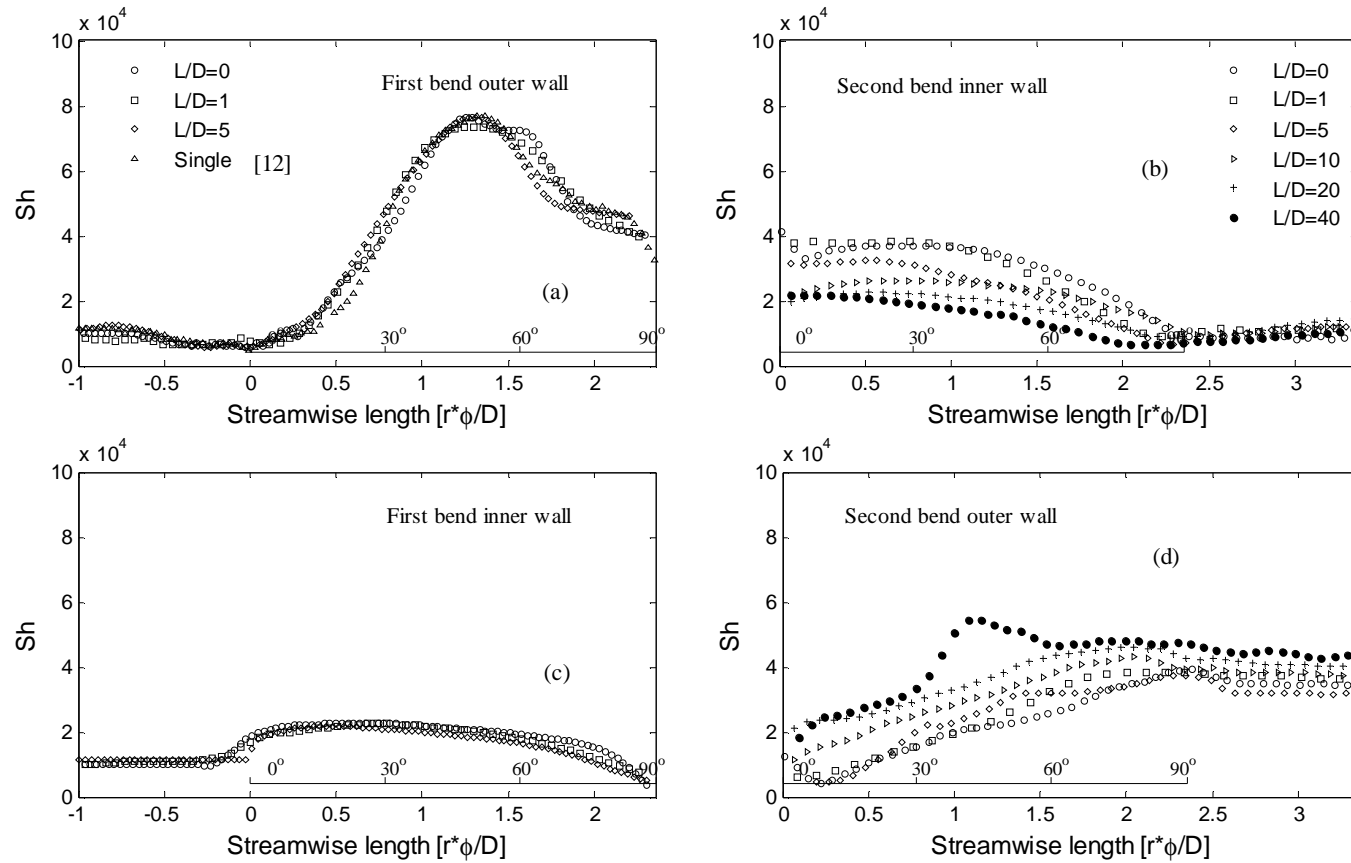


**Figure 7.4: Profiles of Sherwood number along the centerline of (a) first bend outer (b) second bend inner wall (c) first bend inner wall and (d) second bend outer wall.**

the bend curvature. The mass transfer at the different separation distances follow a similar trend to the zero separation case; however, the magnitudes are lower with increasing separation distance. On the second bend outer wall for the zero separation case, the mass transfer increases along the bend curvature to reach a maximum on the center line near  $\phi_2=90^\circ$  and spans between  $\theta$  of  $-135^\circ$  and  $-45^\circ$ . As the separation distance is increased, the maximum region moves upstream and at  $L/D=40$  it is located near  $\phi_2$  of  $50^\circ$ .

The variation of the maximum mass transfer enhancement,  $(Sh_{max}/Sh_{pipe})$  on the first and second bends are shown on figure (7.6-a). The  $Sh_{max}/Sh_{pipe}$  in the first bend for  $L/D$  of 0, 1 and 5 agree well with the results for a single bend under the same annular flow condition. On the second bend, the maximum enhancement is found to be lowest for the zero separation case with a magnitude of 2.75 and increases with an increase of separation distance to reach approximately 85% of the first bend enhancement at  $L/D= 40$ . The location of the mass transfer maxima for the different separation distances is shown in figure 6b. The location of the mass transfer maximum in the second bend moves upstream as the separation distance is increased, and is at a similar angular location to the maximum on the single bend at  $L/D=40$ .

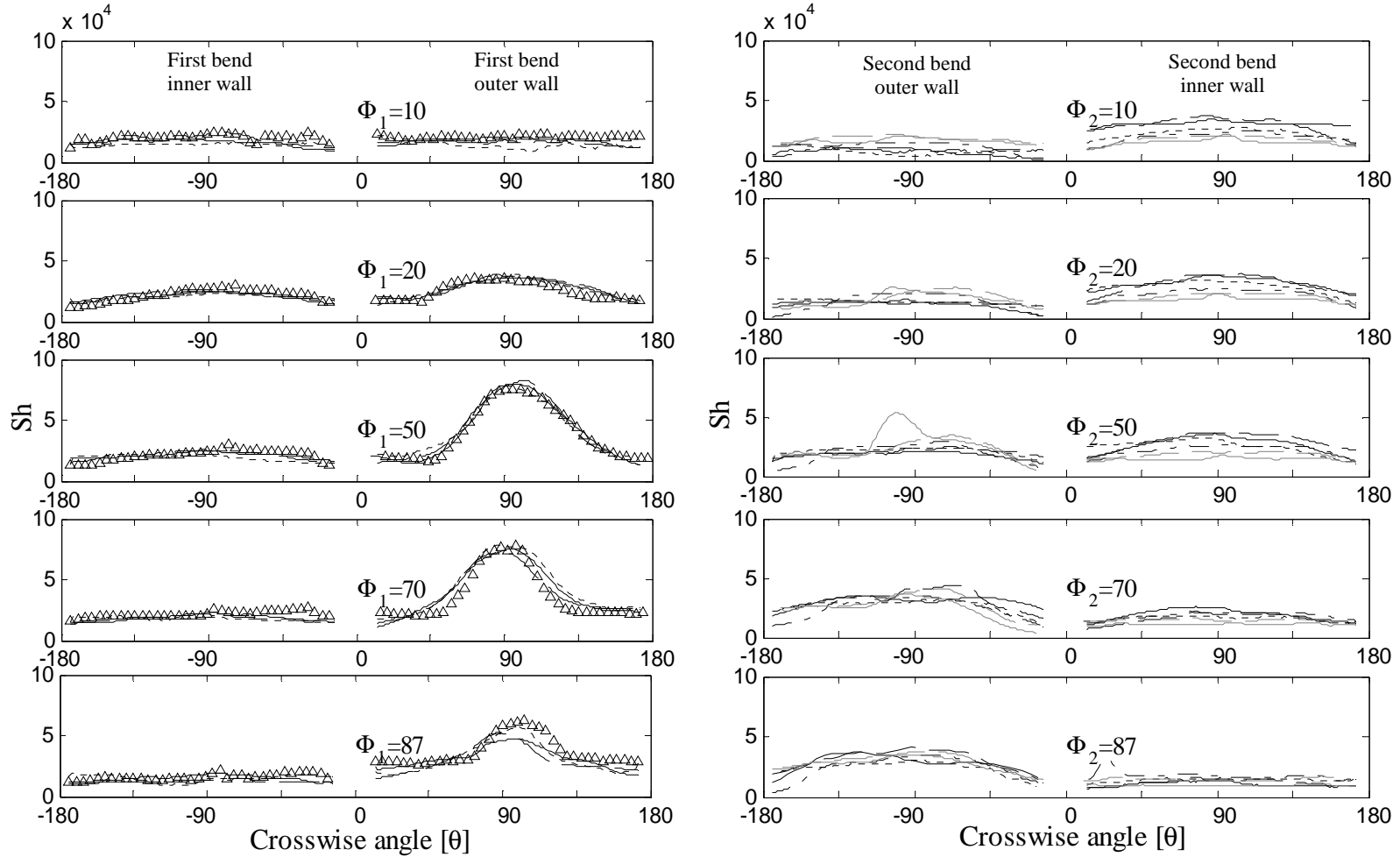


**Figure 7.5: Azimuthal profiles of  $Sh$  at different locations along the bend curvature for separation distances of  $L/D$  of — 0, - - · 1, ····· 5, — · - 10, - - · 20, — 40,  $\Delta$  Single bend [12].**

Since the mass transfer in the second bend of the zero separation case is significantly affected by the upstream bend, this case is further investigated to determine the effect of changing the air and water superficial velocities on the mass transfer enhancement. The mass transfer distributions were measured under annular flow conditions for  $J_v = 22, 24.5$  and  $29$  m/s, and  $J_L = 0.17, 0.28$  and  $0.41$  m/s. The local  $Sh$  distributions for the different flow conditions are shown in figure 7.7. The mass transfer distributions on the first and second bends had a number of features in common between the different flow conditions. The mass transfer pattern on the first bend under all flow conditions was similar to that of the single bend case [12].

Azimuthal profiles of the mass transfer distribution are plotted at selected locations along the bend curvature to elicit the effect of the  $J_v$  and  $J_L$  as shown in figure 7.8. The mass transfer reaches a maximum on the first bend outer wall near  $\phi_1$  of  $50^\circ$ , with a second local maximum near the outlet of the second bend outer wall near  $\phi_2$  of  $85^\circ - 90^\circ$ . The increase in mass transfer with an increase in the air and water superficial velocities was similar at the locations of these two maxima. The mass transfer enhancement  $Sh_{peak}/Sh_{pipe}$  with change in air and water superficial velocities at the two maxima locations is shown in figure 7.9. The enhancement at the maximum in the first bend is consistent with that of the single bend [12]. The enhancement within the second bend is in the range 50 to 60% of that in the first bend (figure 7.9b).

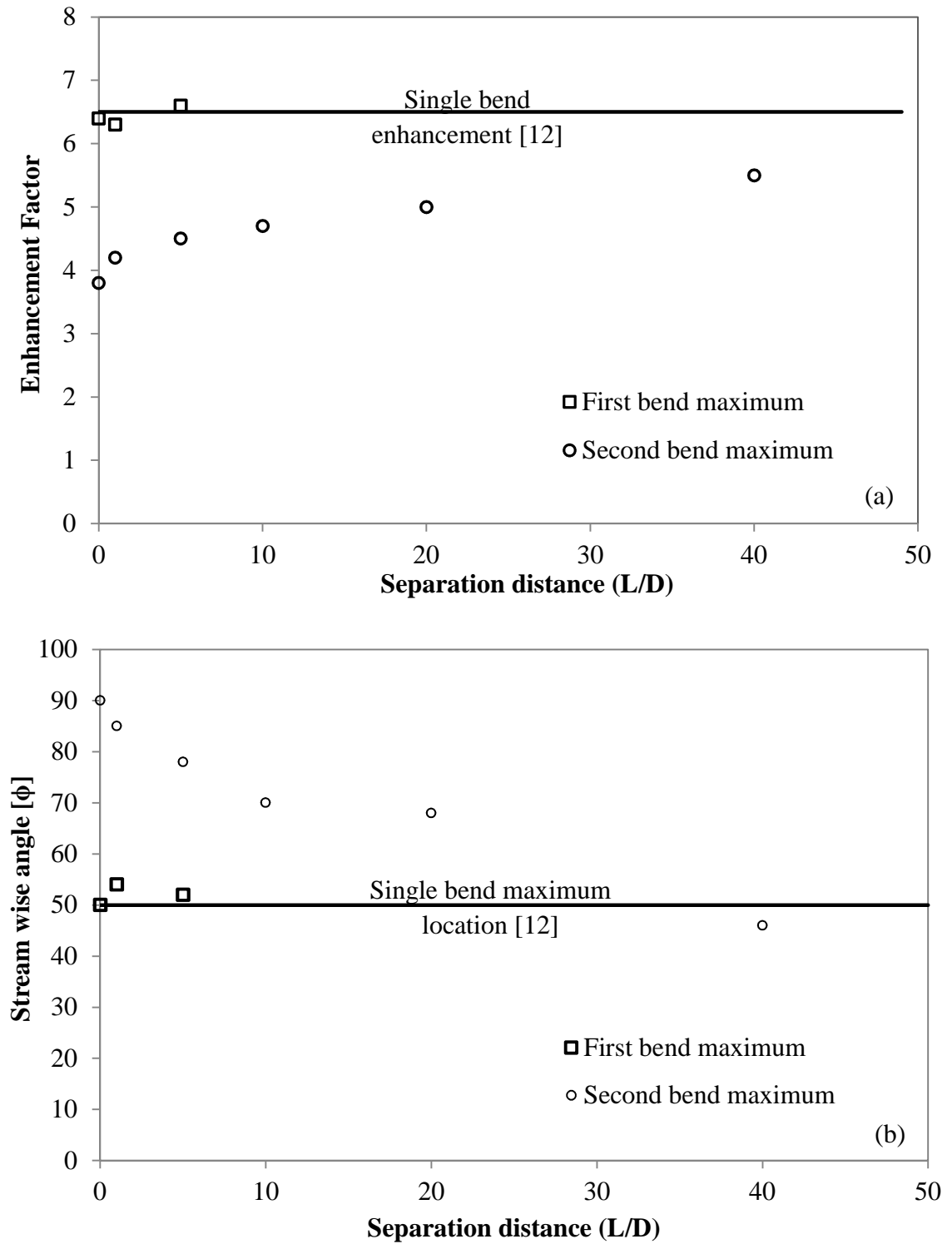
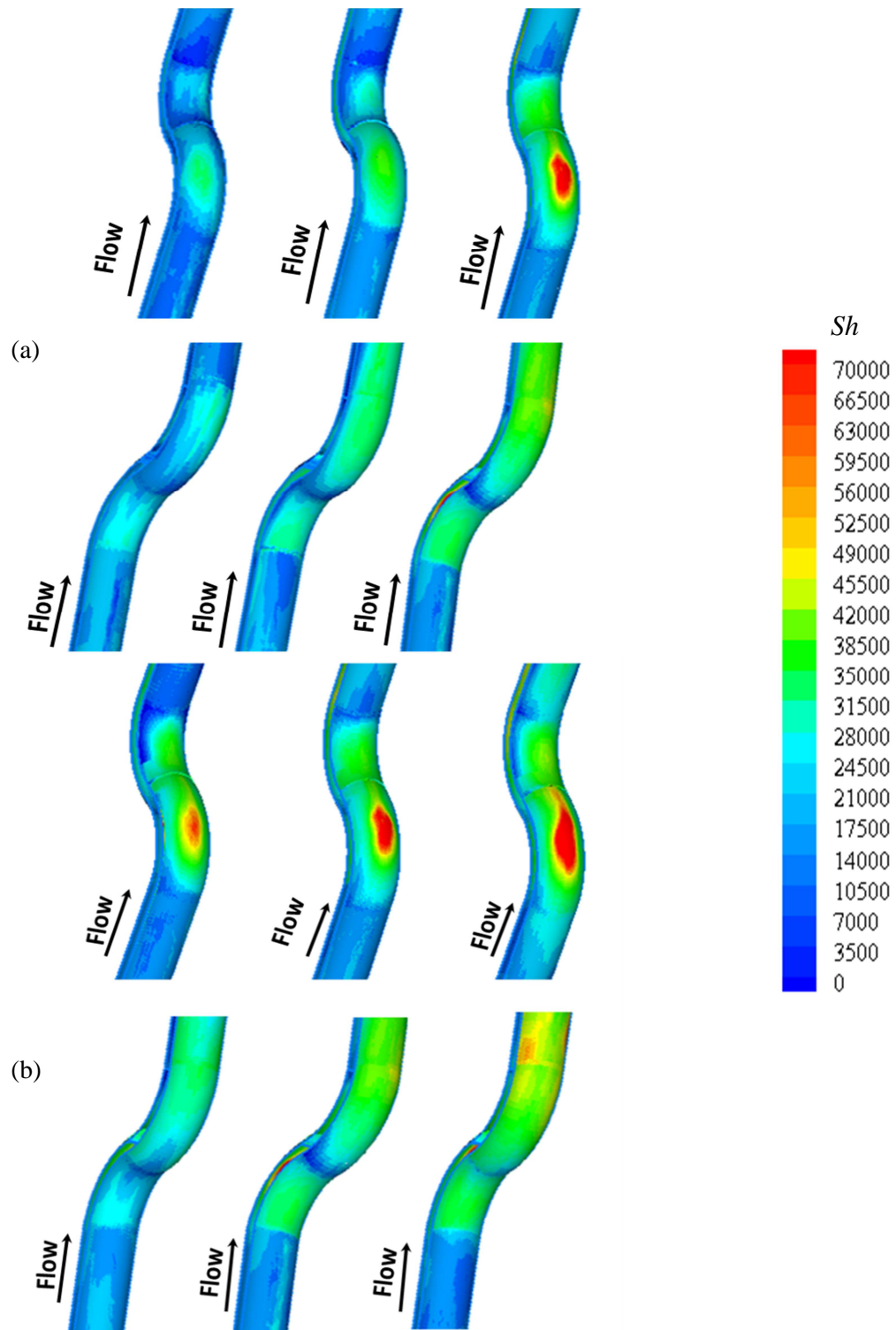


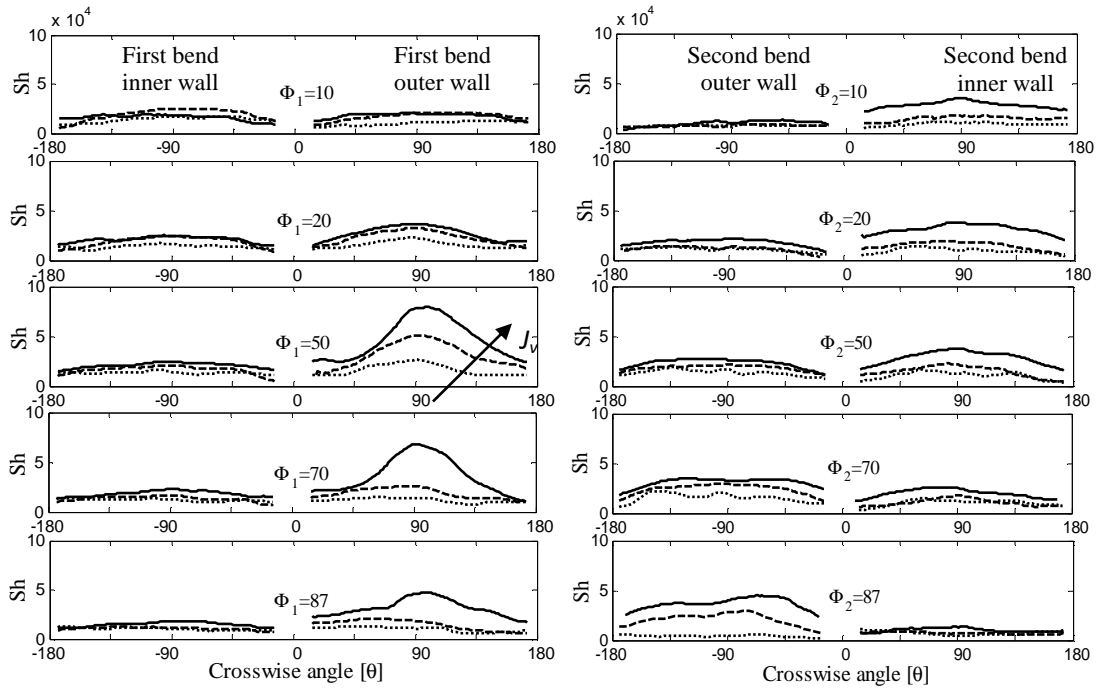
Figure 7.6: Effect of separation distance  $L/D$  on (a) maximum enhancement factor and (b) location of maximum enhancement in first and second bend.



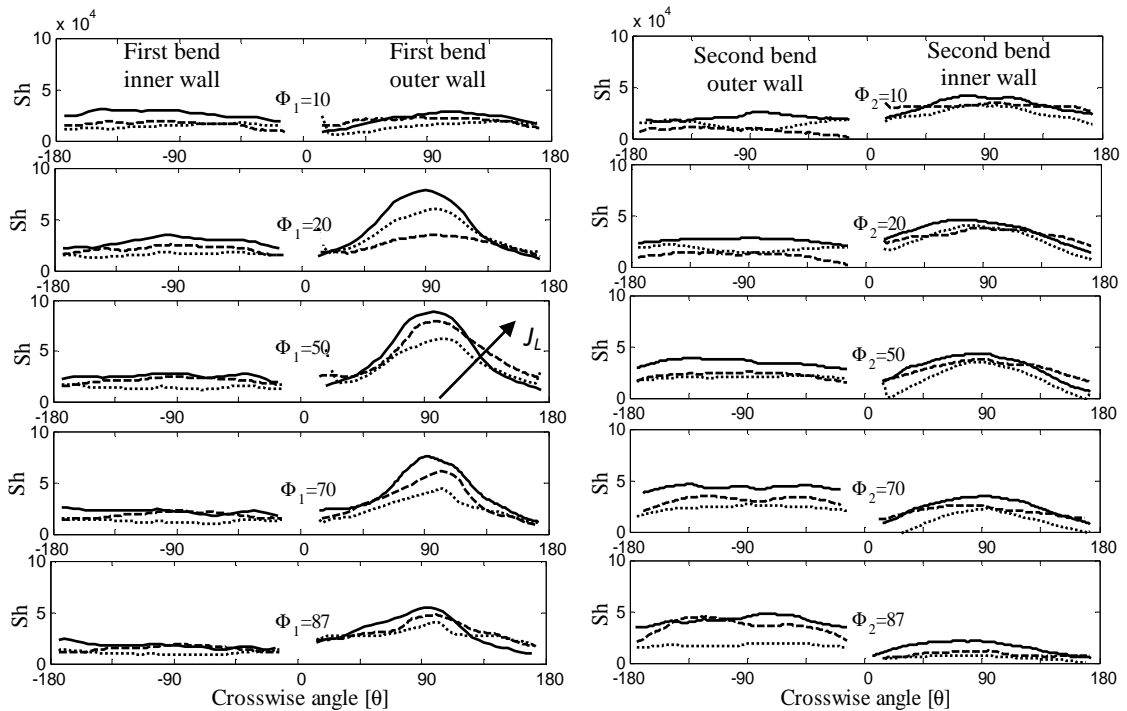
**Figure 7.7: Mass transfer distribution in S dual bend with change in (a) air superficial velocity for  $J_V = 29, 24.5$  and  $22$  m/s and  $J_L=0.28$  m/s (b) water superficial velocity for  $J_L = 0.17, 0.28$  and  $0.41$ m/s and  $J_V \sim 29$  m/s for  $L/D=0$ .**

#### 7.4 Flow visualization

The annular two phase flow redistribution within the bends was visualized for  $L/D=0$  case to better understand its effect on the mass transfer distribution. Three realizations of the flow at  $J_v=29$  m/s and  $J_L=0.28$  m/s are shown in figure 7.10. The liquid phase is distinguished by a brighter color due to the fluorescence laser light reflection. As the annular flow enters the first bend, the entrained droplets in the core region tend to deposit onto the outer wall midway through the first bend. The film thickness is observed to thin in this region which could be due to the impingement of the high velocity air core. This region is always distinguished with a very high mass transfer rate. This suggests that the high mass transfer at this region is a result of the interplay of the droplet deposition and liquid film velocity. The thicker film upstream of this region is likely due to the reverse flow in the upstream direction due to the core flow impingement. The mass transfer upstream of the peak location is low which could be explained by the possible flow deceleration due to reverse flow. The increase in film thickness downstream of the deposition region is possibly due to the liquid accumulation on the outer wall. Due to the bend curvature the liquid film tends to accelerate near the inlet of the first bend inner wall. This also corresponds to the relatively high mass transfer in this region. As the flow turns around the bend secondary flow structures within the gas core in the form of counter rotating vortices are developed along the bend curvature [7]. The inertia of the liquid film in addition to the drag caused by the counter rotating vortices tends to shear off the liquid film in the form of streaks directed toward the outer wall as seen in figure (7.10-b),



(a)



(b)

**Figure 7.8: Azimuthal Sherwood profiles with change in (a) air superficial velocity for  $J_V = 29, 24.5$  and  $22$  m/s and  $J_L=0.28$  m/s (b) water superficial velocity for  $J_L = 0.17, 0.28$  and  $41$  m/s and  $J_V=29$  m/s, for  $L/D=0$ .**

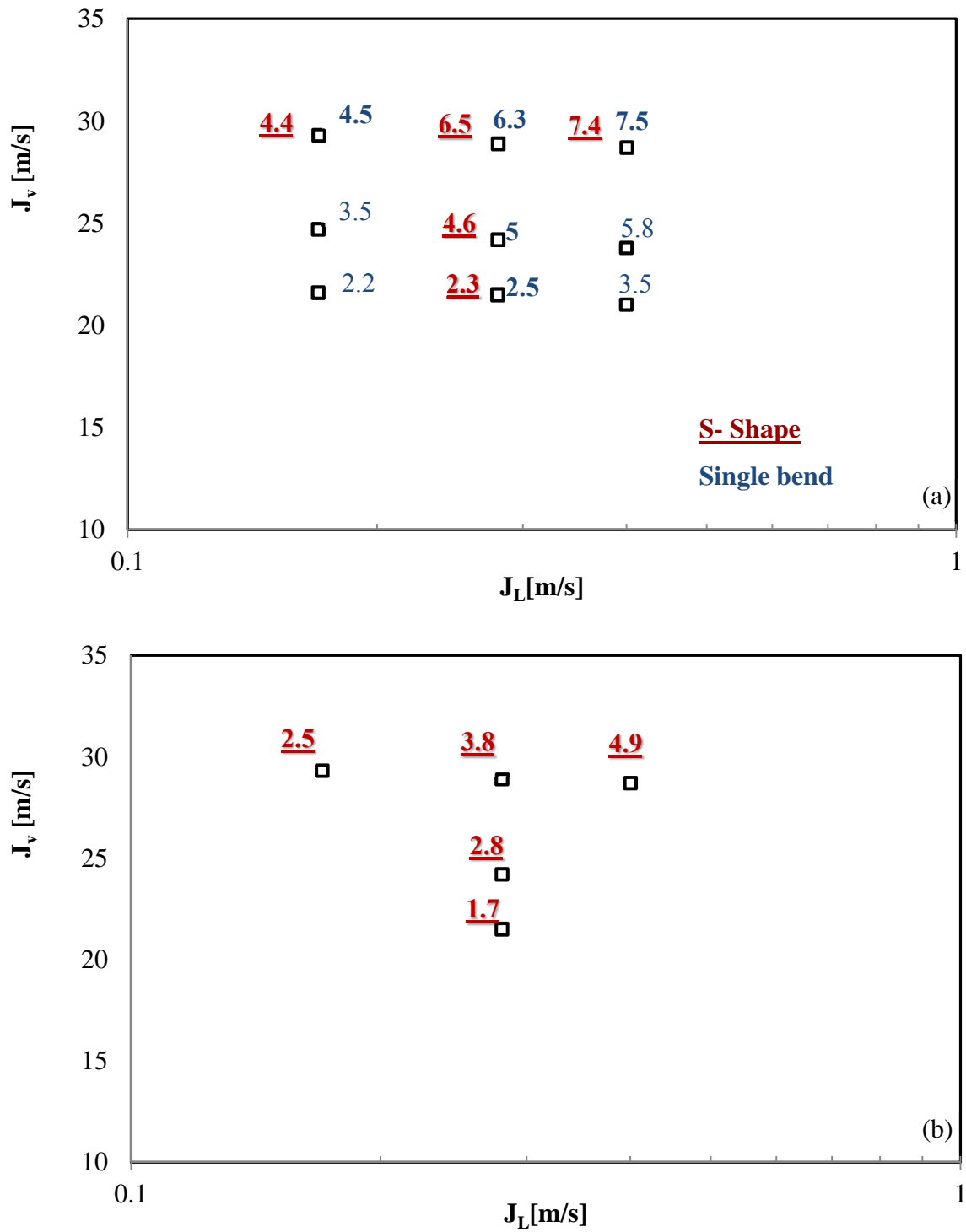
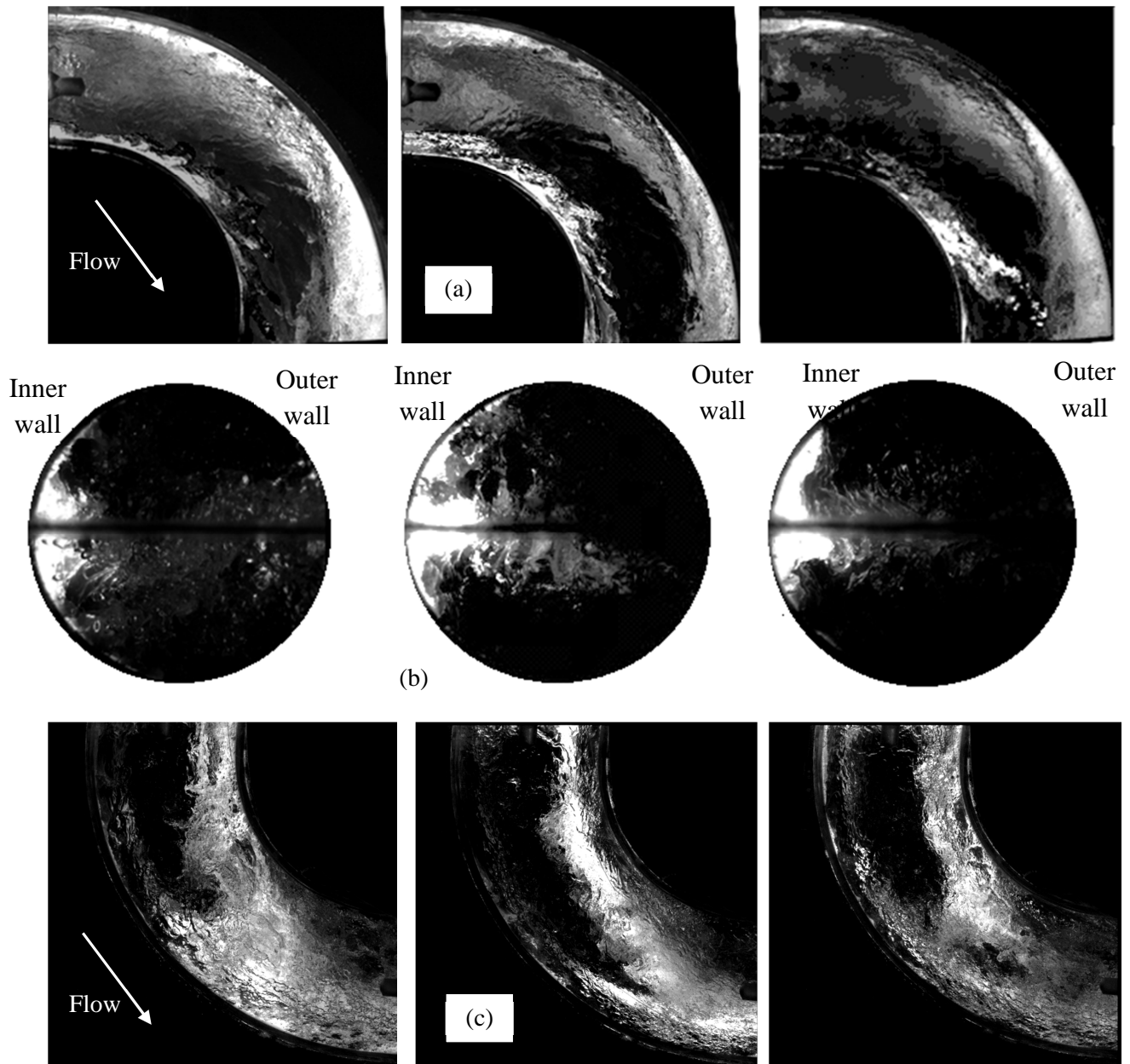
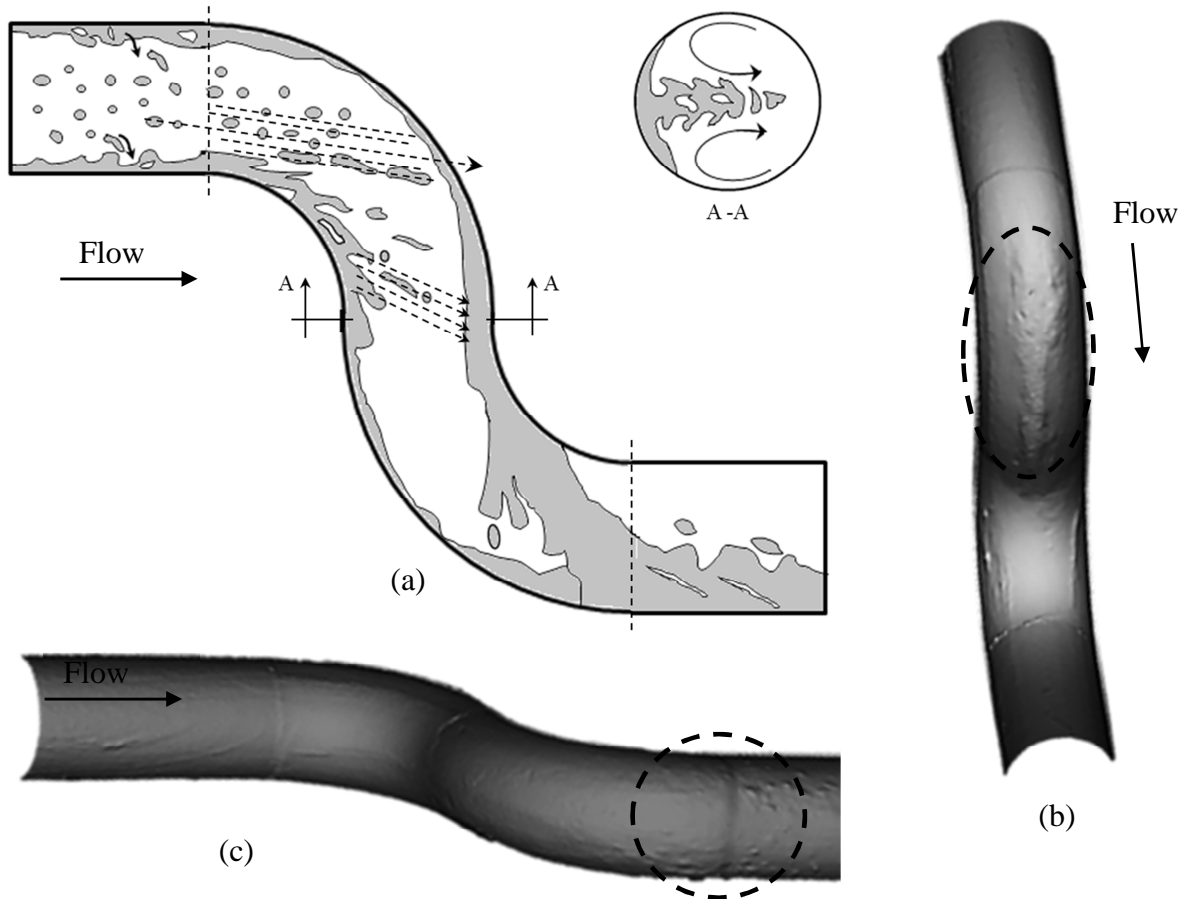


Figure 7.9: Variation of mass transfer enhancement for the different annular flow conditions for (a) first bend and (b) second bend.

similar to what was observed in U- shape bends by [13]. The deposition region of the liquid streaks on the outer wall corresponds to the mass transfer plateau in the mass transfer on the latter part of the bend. Most of the liquid separates from the flow and collects on the latter part of the first bend outer wall side. When the flow enters the second bend, the liquid travels on the inner wall side causing relatively high mass transfer in this region. The liquid film separates from the second bend inner wall near  $\phi_2$  of approximately  $30^\circ$  to  $40^\circ$  and deposits on the latter part of the outer wall and hence results in high mass transfer region (figure 7.10-c). Based on the flow visualization and mass transfer surface observations a flow redistribution model is proposed and shown schematically in figure 7.11. The proposed sketch suggests agreement between the locations of liquid phase deposition and elevated mass transfer regions as observed from the physical images in figure 7.11; however, the level of enhancement seemed to depend on the velocity and angle of impact of the liquid on the surface as well as the liquid film thickness at the location of liquid impact.



**Figure 7.10: Different realizations of the phase redistribution at (a) the first bend (b) cross section near the outlet of the first bend and (c) at second bend, using laser induced fluorescence for  $J_v=29$  m/s and  $J_L=0.28$  m/s.**



**Figure 7.11: Schematic of (a) the proposed model for the phase redistribution depicted from flow visualization in contrast with physical images of the surface topography for (b) first bend outer wall and second bend inner wall and (c) first bend inner wall and second bend outer wall.**

## 7.5 Summary and conclusions

The mass transfer in S- shape dual bends arranged in a horizontal orientation was measured for a range of annular air-water flow conditions at Schmidt number ( $Sc$ ) of 1280. Measurements were performed for bends with different lengths of straight pipe, from 0 to 40 pipe diameters, between the two bends at air and water superficial velocities of 29 m/s and 0.28 m/s, respectively. The maximum mass transfer enhancement occurred on the outer wall of the first bend, at a location midway into the bend, similar to the case of a single bend. The location and magnitude of this maximum was independent of the separation distance between the two bends. A second local maximum is observed on the second bend outer wall with a magnitude of approximately 60% of that in the first bend for the zero separation case. This magnitude increased with an increase in the separation distance to reach 85% for the  $L/D=40$  separation case. This suggests that effect of the first bend on the phase redistribution seems to prevail for lengths greater than 40 pipe diameters downstream of the bend. The mass transfer in the  $L/D = 0$  case was investigated for air and water superficial velocities in the range 22 to 29.5 m/s and 0.17 to 0.4 m/s, respectively. The ratio of the maximum mass transfer in the second bend to that in the first bend was independent of the air to water velocity ratio, and was approximately 60% in all cases. The location of the maximum mass transfer was found to correspond to the location of liquid droplet impingement on the outer wall of the first bend, which was corroborated through flow visualization using laser induce fluorescence. A second region of liquid deposition is observed on the latter part of the first bend where the mass transfer is characterized by a plateau. A significant amount of liquid is found to deposit of the

latter part of the second bend outer wall where the second local maximum in the mass transfer is observed.

### **Acknowledgments**

The support of CANDU owners group (COG) and the Natural Sciences and Engineering Research Council of Canada (NSERC) is gratefully acknowledged.

## 7.6 References

- [1] Dooley, R. B., “Flow Accelerated Corrosion in fossil and combined cycle/HRSG plants” *Power Plant Chemistry*, Vol 10 (2), 2008
- [2] Crawford, N. M., Cunningham, G., Spedding, P.L., “Prediction of pressure drop for turbulent fluid flow in 90 degree bends”, *Proceeding Institute of Mechanical Engineering*, 217E, 1–3, 1974
- [3] Kim, S., Park, J. H., Kojasoy, G., Kelly, J. M., Marshall, S. O., “Geometric effects of 90-degree elbow in the development of interfacial structures in horizontal bubbly flow” *Nuclear Engineering and Design* (237) : 2105-2113, 2007
- [4] Pecherkin N. and Chekhovich V., “Mass Transfer in Two-Phase Gas-Liquid Flow in a Tube and in Channels of Complex Configuration”, *Chapter 8, Mass transfer in multiphase systems and its applications*, vol (155)- 2011
- [5] Spedding, P.L., Benard, E. , McNally, G.M., “Fluid flow through 90 degree bends”, *Dev. Chemical Engineering Mineral Process* 12, 107–128, 2004
- [6] Supa-Amornkul, S., Steward F.R., Lister D.H., “Modeling two-phase flow in pipe bends”, *Journal of Vessel Technology* 127: 204-209, 2005
- [7] Maddock, C. Lacy, P. M. C. Patrick, M. A., “The structure of two Phase flow in a curved pipe”, *Journal of Chemical Engineering Symposium* (38), 1-22, 1974

- [8] Anderson, G.H., Hills, P.D., “Two-phase annular flow in tube bends”, Presented at *Symposium Multiphase Flow Systems, Institute of Chemical Engineers Symposium Ser. No. 38, Univ. of Strathclyde, Paper J1, 1974*
- [9] Usui, K., Aoki, S., Inoue, A., “Flow behavior and pressure drop of two phase flow in C- Shaped bend in vertical plane, Upward flow (I)”, *Journal Nuclear Science and Technology*, 17 (12) 875-887, 2008
- [10] Poulson, B., “Advances in understanding hydrodynamic effects on corrosion”, *Corrosion Science* 35, no. 1-4: 655-665, 1993
- [11] Poulson, B., “Measuring and Modeling Mass Transfer at Bends in Annular Two phase flow”, *Journal of Chemical Engineering Science*, (64) 4: 1069-1082, 1991
- [12] Mazhar, H., Ewing, D., Cotton, J. S., Ching, C. Y., “Mass Transfer in Single Bends under Annular Two Phase Flow Conditions”, *ASME Journal of Heat Transfer*, (Submitted).
- [13] Da Silva Lima, R. J., Thome, J. R., “Two-phase flow patterns in U-bends and their contiguous straight tubes for different orientations, tube and bend diameters” *International Journal of Refrigeration* 35, 1439-1454, 2012
- [14] Wang, H., Hong, T., Cai, J., Jepson, W., Enhanced mass transfer and wall shear stress in multiphase slug flow, *Corrosion* 02501, 2002

[15] “Recommended Practice -Erosive wear in piping systems”, DVN RP-guideline code 0501, 2007

[16] Hattori S.,” Effects of impact velocity and droplet size on liquid impingement erosion”, *International Symposium on the ageing Management & maintenance of Nuclear Power Plants*, 2010

[17] Deffenbaugh D. M. and Buckingham J. C., “A study of the erosional/ corrosional velocity criterion for sizing multi-phase flow lines”, San Antonio, Houston, USA, 1989

[18] Koshizuk, S., Naitoh, M., Uchida, S., Okada, H. “Evaluation procedures for wall thinning due to Flow Accelerated Corrosion and liquid droplet impingement” *International Symposium on the Ageing Management & Maintenance of Nuclear Power Plants*, 18-28, 2010

[19] Zhao, Y., Markides, N., Matar, O., Hewitt, F., ”Disturbance wave development in two-phase gas–liquid upwards vertical annular flow”, *International Journal of Multiphase Flow* (55), 111-129, 2013

[20] De Kerpel, K., Ameel B., Caniere H., De Paepe M., “Study of two phase flow in hairpins by means of image processing and pressure drop measurements”, *Multiphase Flow in Industrial Plants, 12th International Conference Proceedings*, 2011

[21] Da Silva Lima, R. J., Thome, J. R., “Two–phase pessure drops in adiabatic horizontal circular smooth U-bends and contiguous straight pipes (RP-1444)”, *HVAC & R RESEARCH*, Vol. (16) 3, 2010

- [22] Mazhar, H., Ewing, D., Cotton, J. S., Ching, C. Y., Experimental Investigation of Mass Transfer in 90 Degree Pipe Bends using a Dissolvable Wall Technique, *International Journal of Heat and Mass Transfer*, 65, p. 280–288, 2013
- [23] Coleman, H.W and Steele, W., “Experimentation and Uncertainty Analysis for Engineers”, 2<sup>nd</sup> Ed., John Wiley & Sons, New York, 1999
- [24] Farias, P. S., Martins, F. J., Sampaio, L. E., Serfaty, R., Azevedo, L. F., “Liquid film characterization of horizontal, annular, two-phase, gas-liquid flow using time-resolved LASER-induced fluorescence”, *15th International Symposium on Applications of Laser Techniques to Fluid Mechanics*, Lisbon, Portugal, 05-08 July, 2010
- [25] Chisholm, D., “A theoretical basis for the Lockhart Martinelli Correlation for two-phase flow”, *International Journal of Heat and Mass Transfer* (10), 1767–1778, 1967
- [26] Taitel, Y., Dukler, A. E., “A model for predicting flow regime transitions in horizontal and near horizontal gas-liquid flow” *American Institute of Chemical Engineers Journal*, Vol. 22 (1), 47–55, January 1976
- [27] Blumberg, “A study of stable, Periodic Dissolution Profiles Resulting from The Interaction of the Soluble Surface and an Adjacent Turbulent Flow”, The University of Michigan, PhD, Engineering, Chemical, 1970

## **CHAPTER 8**

---

### **Summary and Conclusions**

#### **8.1. Thesis summary**

The mass transfer in pipe bends is experimentally investigated in the current study in particular; the mass transfer in a standard short radius  $90^\circ$  bend arranged in single and dual S- shape configuration was measured under single and annular two phase flow conditions using a novel dissolving wall measurement technique. The effect of Reynolds number in the single phase flow and the air and water superficial velocities for the annular two phase flow case on the local mass transfer distribution and enhancement was determined. The mass transfer distribution was correlated to the single and two phase flow characteristics based on the surface topography results in the literature and current flow field measurements in single phase flow and visualizations.

Experiments were performed in a 2.54 cm diameter flow loop which could be operated under both single and two phase air-water flow conditions. Standard  $90^\circ$  bends arranged in single and dual S- shape configurations were tested. Test sections were cast from gypsum using molds which were manufactured from high density plastic. The test sections were cast with an upstream 20 cm (eight pipe diameters) long pipe section and downstream 10 cm (four pipe diameters) long pipe section two reduce inlet and outlet

effects. A transparent acrylic test section was manufactured with the same dimensions as the gypsum section for the flow field measurements and visualization.

The current study can be broadly categorized as:

1. Mass transfer in single  $90^\circ$  degree bends for  $Re$  range from 40,000 to 130,000. The effect of  $Re$  on the mass transfer distribution and on the surface roughness was investigated.
2. Mass transfer in dual S- shape  $90^\circ$  bends for different separation distances between the two bends. The effect of  $Re$  on the mass transfer enhancement was also investigated for the case with no separation distance between the bends. The roughness variation with separation distances as well as with  $Re$  was studied.
3. The flow field characteristics in single and dual bends under single phase flow conditions was investigated using Particle Image Velocimetry (*PIV*) system.
4. Mass transfer in single  $90^\circ$  short radius bend under annular two phase flow conditions. The effect of air and water superficial velocities on the mass transfer enhancement was investigated.
5. Mass transfer in dual S- shape bend configurations under annular two phase flow conditions. The effect of separation distance between the bends, from 0 to 40 diameters, on the mass transfer was investigated. The effect of air and water superficial velocities on the mass transfer enhancement for the zero separation case was also examined.

6. The phase redistribution for the zero separation case was visualized using Laser Induced Fluorescence (*LIF*) and correlated to the different mass transfer regions.

## 8.2. Conclusions

The key conclusions of the current investigation are:

### 8.2.1 Mass transfer in single and S- shape bends under single phase flow

For the single bend, three regions of high mass transfer were identified, (i) near the inlet of the bend inner wall, (ii) midway into the bend on the inner wall side and (iii) and on the outer wall outlet. The  $Sh$  at the locations of high mass transfer in the single bend was found to scale as  $Re^{0.92}$ . The maximum mass transfer enhancement was approximately 1.8 times relative to the upstream pipe and located on the bend outer wall outlet. The maximum enhancement is found to independent of  $Re$  for the tested range of  $Re$ . The region of high mass transfer extended over 2 diameters downstream of the bend outlet. The surface roughness in the single bend geometry was found to be in the fully rough range ( $e^+ > 30$ ) for the current range of  $Re$ . This indicates that the mass transfer coefficient exponent is independent of Reynolds number and can be extrapolated for higher  $Re$ .

High mean flow velocity was observed on the inner wall near the inlet and the outer wall near the outlet due to shift of high velocity core toward the outer wall. This region corresponded to high mass transfer regions observed in the single bend. The  $T.K.E$  increased gradually along the bend outer wall, similar to the mass transfer trend in this

region. The highest turbulent kinetic energy was observed on the latter part of the inner wall where low mass transfer was measured.

For the S- shape dual bend, the high mass transfer locations occurred on, (i) the inner wall at the inlet to the first bend, (ii) over the latter part of the first bend outer wall and extending into the first part of the second bend inner wall, and (iii) midway into the second bend inner wall. The maximum mass transfer enhancement in the S- shape dual bend geometry is found to occur on the outer wall of the first bend near the inlet of the inner wall of the second bend with a magnitude of approximately 3.2 and was found to be independent of  $Re$ . A second peak is observed on the second bend inner wall in short separation distances,  $L/D$  of 0 and 1 with a magnitude of approximately 85 % of the first peak and occur off the center line in the form of two symmetric locations around the bend centerline at  $\theta$  of  $-45^\circ$  and  $-135^\circ$ . The increase in separation distance resulted in a decrease in the mass transfer and surface roughness in the second bend. The  $Sh$  scaling with  $Re$  at the high mass transfer locations in this case was found to be similar to the single bend case,  $Re^{0.92}$ .

High mean flow velocity and relatively high turbulent kinetic energy was observed near the transition from the first bend outer wall to the second bend inner wall. This region corresponded to highest mass transfer in the zero separation case. High secondary flow velocity was observed midway into the second bend inner wall. This region was found to correspond to localized high mass transfer.

In general, regions of high velocity and potentially shear stress correspond to locations of high mass transfer while the effect of the turbulent kinetic energy was unclear since high *T.K.E* corresponded to regions of high mass transfer and low mass transfer.

### **8.2.2 Mass transfer in single and dual bends under annular two phase flow**

For the single bend, the peak mass transfer was located on the bend outer wall at  $\phi$  of approximately  $50^\circ$ . This location corresponded to the entrained liquid droplet impingement and anticipated high velocity region due to liquid film thinning. The effect of the air superficial velocity dominates that of the water superficial velocity in annular two phase flow; however the effect of water superficial velocity is not insignificant. The maximum mass transfer enhancement increased by a factor of 2.3 as the superficial air velocity was increased from 22 to 29.5 m/s, while it increased by a factor of 1.5 when the superficial water velocity was increased from 0.18 to 0.41 m/s.

For the S- shape dual bends, the maximum mass transfer in the different separation distances was always found to occur in the first bend similar to the single bend case. The second maximum mass transfer was found to occur on the second bend outer wall. The minimum enhancement was found to occur in the  $L/D=0$  case where the mass transfer reaches approximately 60% of that in the first bend and occur near the outlet of the bend outer wall. This location matches the location of the deposition of a significant portion of the liquid phase as the flow turns around the second bend. The mass transfer enhancement was found to increase as the  $L/D$  was increased to reach approximately 85% of that in the first bend for  $L/D$  of 40.

The mass transfer under two phase flow is relatively high compared to the single phase.

The comparison of the mass transfer of the mass transfer coefficient is explained in detail

### **8.3. Research contributions**

The current experimental study has provided, for the first time, local mass transfer distributions in bends under single and two phase flow conditions. Typically in the industrial application, life predictions codes such as CHECWORKS are used to estimate component life and schedule inspections of piping components based on geometry factors determining the piping geometry priority. The mass transfer enhancement factors for the single and back to back bend configurations which were obtained in the current study will be used to improve the geometry factors. The research contributions can be summarized as:

- a. Developed a robust local mass transfer measurement technique to measure the mass transfer for high  $Sc$  conditions in single and two phase flows for different piping geometries
- b. Investigated the effect of Reynolds number on mass transfer distribution and enhancement in single  $90^\circ$  bends under single phase flow. (“Experimental investigation of mass transfer in  $90^\circ$  pipe bends using a dissolvable wall technique”, *International Journal of Heat and Mass transfer*, 65, p. 280–288, 2013)

- c. Performed mass transfer measurements in S-configuration bend geometry under single phase flow condition and determined the effect of separation distance. (“Mass transfer in dual pipe bends arranged in an S-configuration”, International Journal of Heat and Mass transfer, Submitted July, 2013)
- d. Examined the mass transfer in single 90° bend under a range of annular two phase conditions and determined the effect of air and water superficial velocity changes on mass transfer. (“Mass Transfer in Single Bends under Annular Two Phase Flow Conditions”, Journal of Heat Transfer, Submitted April, 2013)
- e. Investigated the effect of separation distance between bends arranged in S-configuration under two phase annular flow conditions for separation distances  $L/D$  of 0, 1, 5, 10, 20 and 40 (“Mass Transfer in S-shape dual pipe bends under annular two phase flow conditions”, International Journal of Heat and Mass Transfer, Submitted August, 2013)
- f. Provided mass transfer enhancement factors in back to back bends which will be utilized to improve the geometry factors in the *FAC* predictive codes
- g. Elicited the mechanism of the mass transfer enhancement for two phase annular flow at the different locations of the dual S- shape bend

#### **8.4. Recommendations for future work**

The effect of Reynolds number on the mass transfer enhancement was performed in the range 40,000 to 130,000 while the Reynolds numbers in industrial applications can be

over a million. Dual bends exist in the industrial applications in different configurations depending on the angle between the first and the second bend. Some of these configurations were not investigated in the literature. The recommendations for future work can be summarized as follows

- The work discussed in this thesis was performed in a small bore pipe, 2.54 cm in diameter, and therefore relatively low  $Re$ . The effect of the pipe diameter on flow scales and boundary layer thickness and thus on mass transfer need to be investigated. Experiments need to be expanded to large bore pipe to verify the Reynolds number exponent against that obtained from the current small bore results.
- Bends in different orientations are common components in nuclear power stations and since the bend configuration is concluded to have a significant effect on the enhancement factor. The effect of the dual bend configuration for  $U$  shape and out of plane with  $90^\circ$  rotation is being investigated at McMaster. Out of plane dual bends with different angles of rotation, as shown in figure 8.1, need to be studied to determine the effect of the angular orientation of the second bend on the mass transfer enhancement.
- Shear stress is an important parameter in determining the mass transfer rate. Shear stress measurements along the bend wall (such as using wall mounted strain gauges) are required to better understand the correlation between shear stress and mass transfer.

- Bends with different radius of curvature exist in different industrial applications. Experiments at different  $r/D$  are required to understand the effect of radius of curvature on mass transfer enhancement.

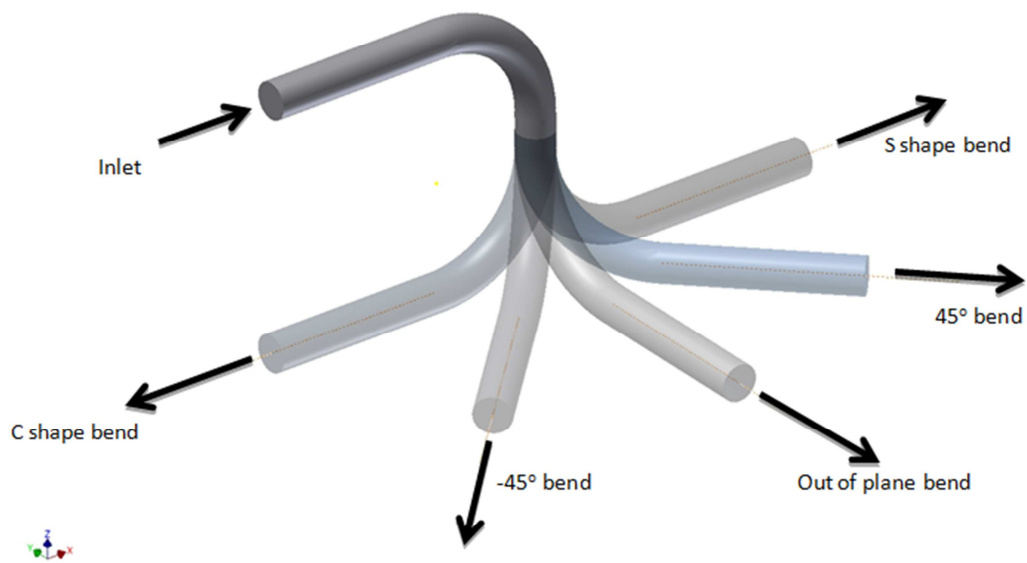


Figure 8.1: Schematic of the dual bend with different angular orientations of the second bend

## **Appendix A**

---

### Uncertainty analysis

## A.1 Uncertainty analysis

The uncertainties associated with the presented measurements are discussed in this appendix. For a given variable ( $Y$ ), that is a function of other independent parameters ( $X_i$ )

$$Y = f(X_1, X_2, X_3, X_4, \dots) \quad (A.1)$$

the total uncertainty in ( $Y$ ) can be expressed in terms of the uncertainties of the independent measured values ( $X_i$ ) using the Kline and McClintock method (Coleman & Steels, 1998), given as:

$$\Delta Y = \sqrt{\sum_{i=1}^N \left( \frac{\partial Y}{\partial X_i} \Delta X_i \right)^2} \quad (A.2)$$

where  $\Delta X_i$  is the uncertainty in each independent measured variable. The summation of the terms on the right hand side of Equation A.2 gives the overall uncertainty in the dependent variable ( $Y$ ). This analysis will be applied to the expression used to calculate the mass transfer coefficient.

## A.2 Uncertainty in the mass transfer coefficient

The mass transfer coefficient is calculated using the following equation

$$h = \rho \frac{d\delta}{dt} \times \frac{1}{\Delta C} \quad (A.3)$$

where  $\delta$  is the thickness of local mass removed normal to the surface,  $\Delta C$  is the difference between species concentration at the wall and in the bulk flow and  $h$  is the mass transfer coefficient. The total uncertainty in the mass transfer coefficient can be estimated using equation A.2 as follows:

$$\Delta h_{total} = \sqrt{\left(\frac{\partial h}{\partial S} \times \Delta S\right)^2 + \left(\frac{\partial h}{\partial \Delta C} \times \Delta \Delta C\right)^2 + \left(\frac{\partial h}{\partial \rho} \times \Delta \rho\right)^2} \quad (A.4)$$

$$: S(\text{gradient}) = \frac{\partial \delta}{\partial t}$$

Substituting from equation A.3 in equation A.4:

$$\Delta h_{total} = \sqrt{\left(\frac{\rho}{\Delta C} \times \Delta S\right)^2 + \left(-\frac{\rho S}{\Delta C^2} \times \Delta \Delta C\right)^2 + \left(\frac{S}{\Delta C} \times \Delta \rho\right)^2} \quad (A.5)$$

The uncertainty of the laser scanning was determined by scanning a standard block multiple times and was found to be on the order of  $\pm 0.1$  mm, with 95% confidence level. The random uncertainty due to variability in the initial casting diameter was estimated by scanning multiple original test sections to be approximately  $\pm 0.15$  mm. The average uncertainty in the slope  $\Delta S$  was estimated using equation A.6

$$\Delta S = \left(\frac{S_{max} - S_{min}}{2}\right)_{\text{at every point}} \quad (A.6)$$

The uncertainty in the slope is estimated to be  $\pm 2.5 \times 10^{-6}$  m/s. The uncertainty in the concentration measurement including the calibration correlation is approximately  $\pm 0.005$

kg/m<sup>3</sup>. The uncertainty in the measured density of the gypsum was  $\pm 40$  kg/m<sup>3</sup>. The total uncertainty in the mass transfer coefficient ( $\Delta h$ ) is estimated to be approximately  $\pm 18\%$

### A.3 Effect of change in pipe diameter on Re:

The Uncertainty in Re increased over the course of the experiment due to the change in the local water velocity associated with the increase in test section diameter. The uncertainty in the Reynolds number due to change in diameter is estimated as follows:

$$Re_t = \frac{\rho V D}{\mu} = \frac{4Q}{\pi v D_t} \quad \longrightarrow \quad D_t = D_o + 2 \times \delta$$

$$Re_t = \frac{4Q}{\pi v (D_o + 2 \times \delta_t)}$$

$$\Delta Re_t = Re_o - Re_t = \frac{4Q}{\pi v} \left( \frac{1}{D_o} - \frac{1}{(D_o + 2 \times \delta_t)} \right)$$

$$\Delta Re_t = C \left( \frac{2\delta_t}{D_o(D_o + 2 \times \delta_t)} \right) = Re_o \left( \frac{2\delta_t}{(D_o + 2 \times \delta_t)} \right)$$

$$\text{at } t=60 \text{ min, } \delta_{60} \sim 0.04 D_o$$

$$\frac{\Delta Re_t}{Re_o} = \frac{2\delta_t}{D_o + 2 \times \delta_t} \quad \therefore \frac{\Delta Re}{Re_o} = 0.074 \quad \dots \dots \dots \text{Over the total testing time}$$

$$\Delta Re_{av.} = 3.7\% Re$$

The average uncertainty in the Reynolds number over 60 minutes experiment is approximately 3.7% of the initial Re reported in the single phase results.

## A.4 Uncertainty in flow field measurements

The Uncertainty in the PIV measurements was estimated following Raffel et. al (2007).

The recording and processing parameters are as tabulated below.

**Table A.1: Recording parameters**

Field of View	76.2×76.2 mm
Total Sensor Size	2048×2048 pixel
Total Image size	1350×1350 pixel
Spatial Calibration	31 $\mu\text{m}/\text{pixel}$
Number of Acquisitions per case	200 shots
<b>Processing Parameters</b>	
Initial Window Size	64 pixels ×64 pixels
Subpixel Interpolation Scheme	Guassian
Window Distortion Scheme	1 <sup>st</sup> order Deformation Scheme
Final Window Size	32 pixels ×32 pixels
Overlap Ratio	75%
Validation Rate	>99%
<b>Error analysis</b>	
Uncertainty in Particle Displacement (Raffel et. al, 2007), $\varepsilon_{\Delta}$	0.1 pixel
Relative Uncertainty in Particle Displacement ( $\varepsilon_{\Delta}/\Delta$ )	2%

The uncertainty in the velocity is estimated from

$$\Delta U = \frac{\Delta X}{\Delta t} \quad (A.7)$$

The uncertainty in the delay time between laser pulses is on the order of nano-seconds, therefore can be neglected. The dominant uncertainty is that in the displacement the uncertainty in velocity is estimated to be 1.5% of the mean velocity.

## **Appendix B**

---

### Material Properties

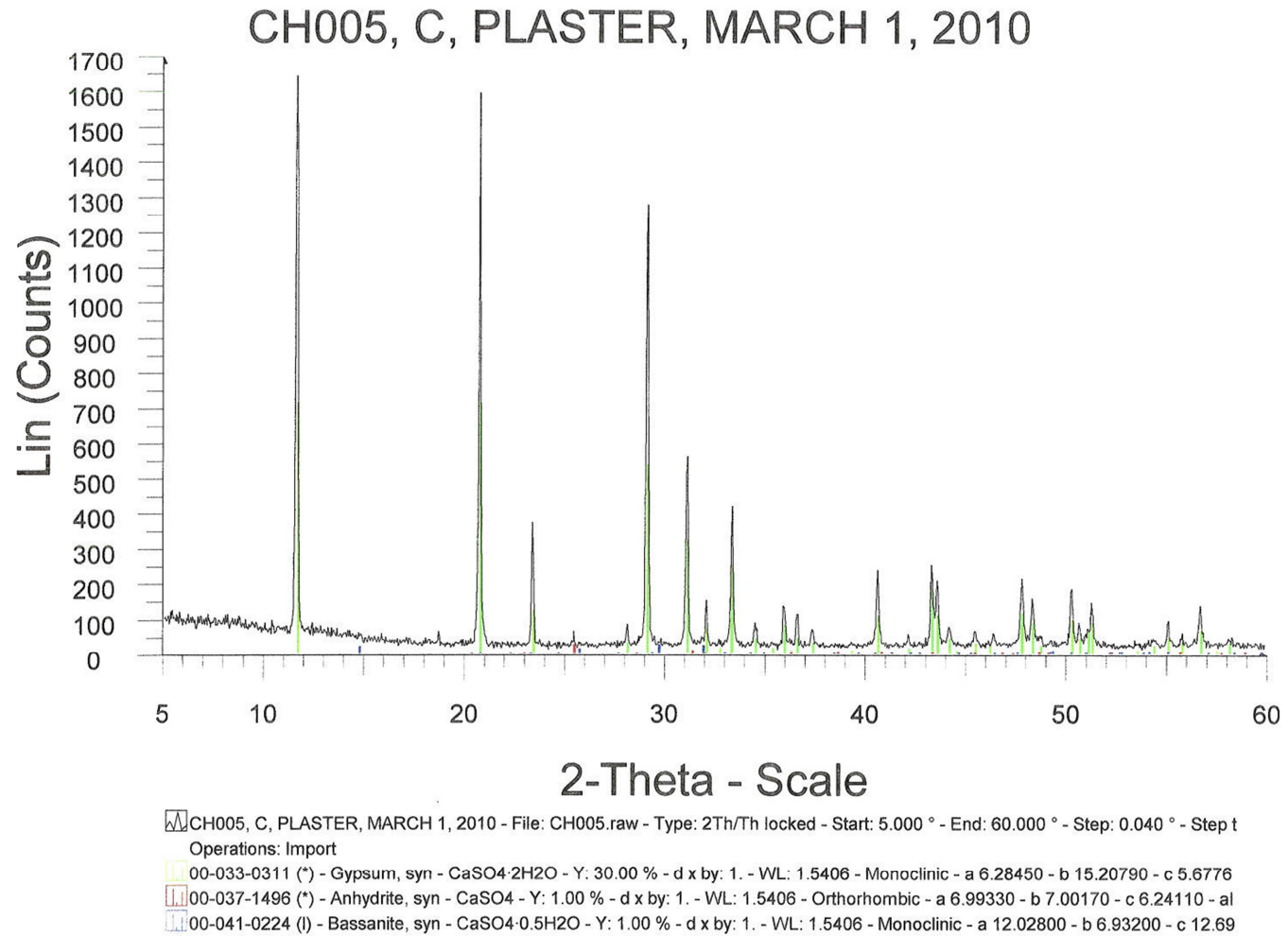


**Figure B.1: Material composition analysis (sample C)**

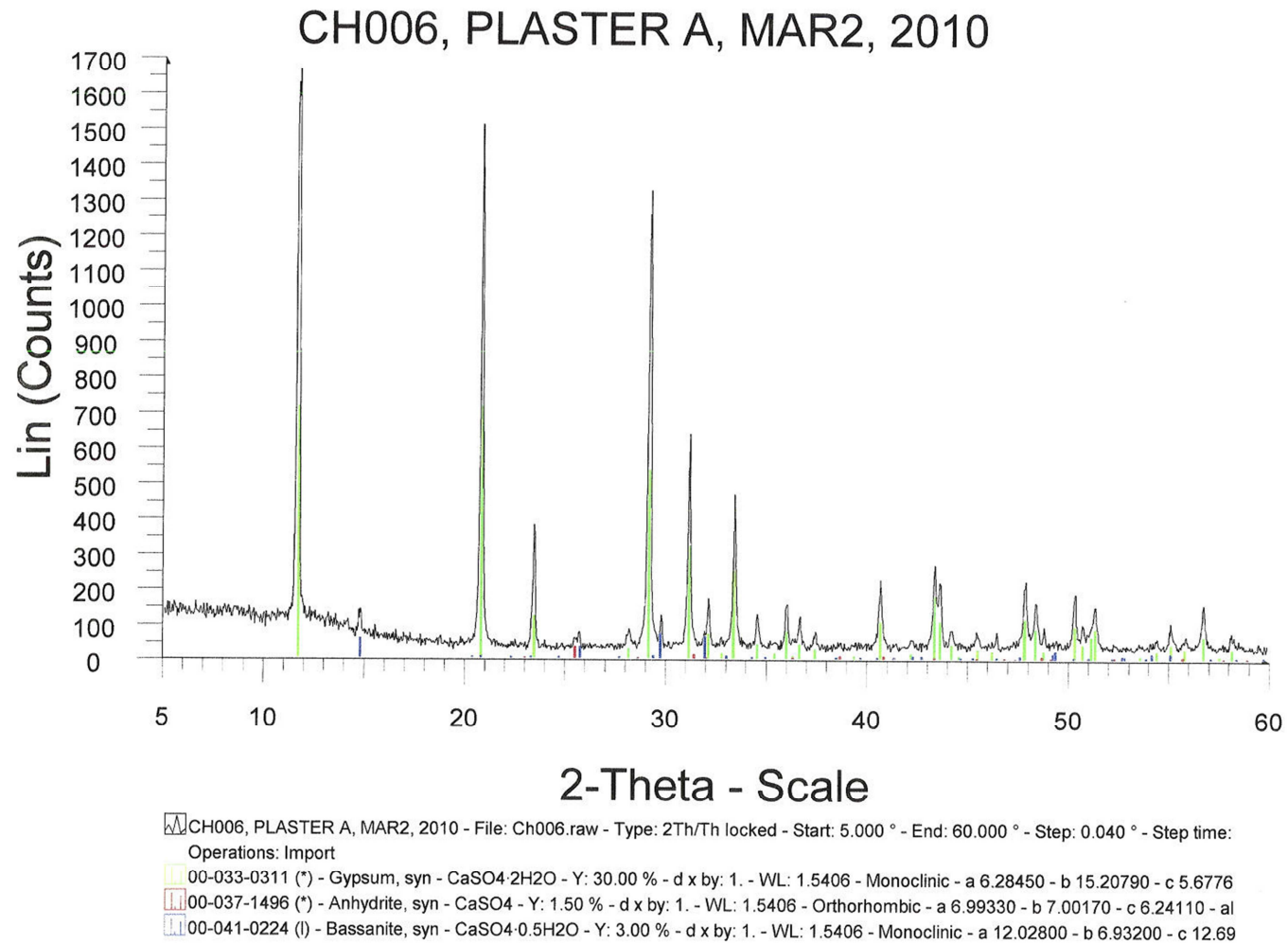


**Figure B.2: Material composition analysis (sample A)**

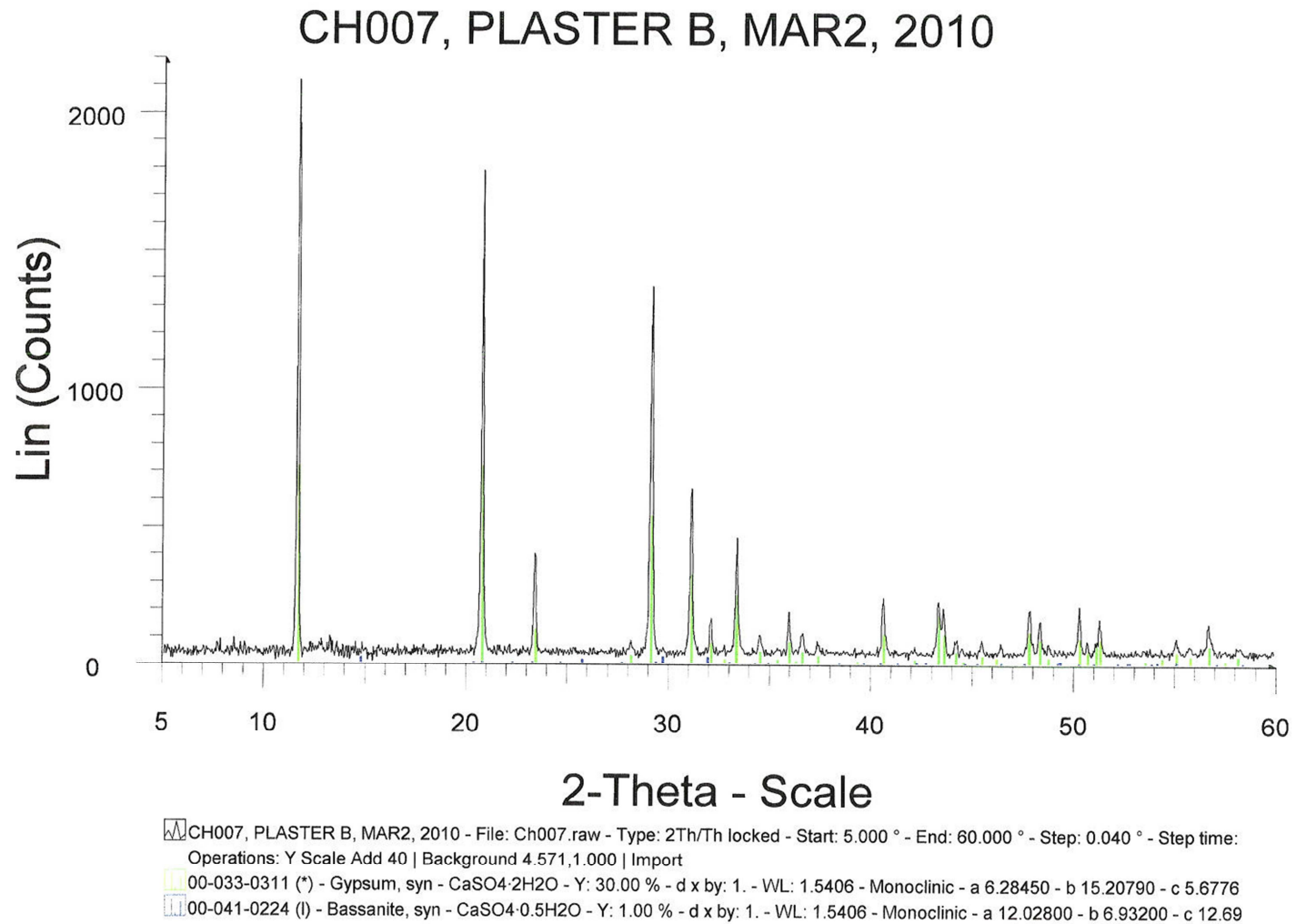


**Figure B3: Material composition analysis (sample B)**

	CH005	CH006	CH007
	C	A	B
$\text{CaSO}_4 \cdot 2\text{H}_2\text{O}$	~95%	92%	97%
$\text{CaSO}_4$	2%	~2%	-
$\text{CaSO}_4 \cdot 0.5\text{H}_2\text{O}$	1%	1%	~1%
OTHERS	2%	2%	2%

**Table B.1: Summary of the different material constituents from different random samples**

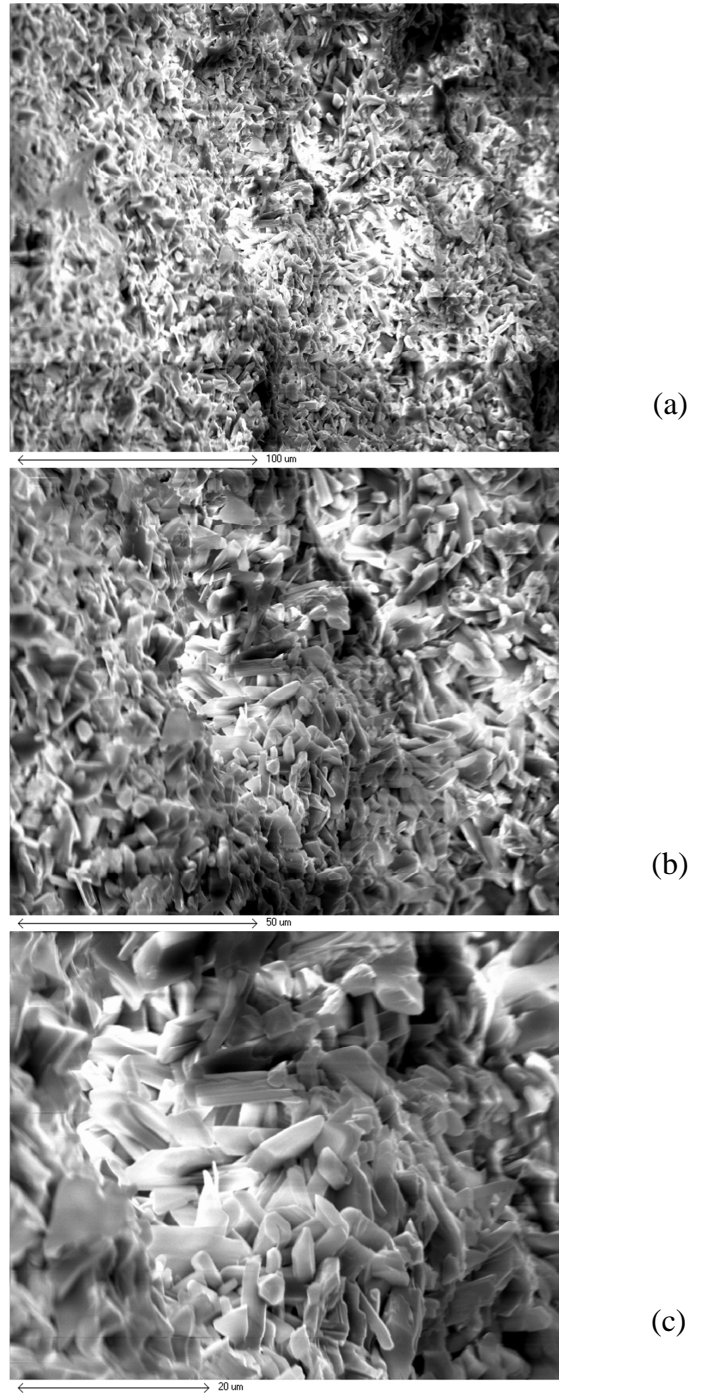


**Figure B.4: SEM microscopic image of the gypsum cast micro structure dendrites with magnifications of (a) 500x (b) 1000x (c) 2000x**

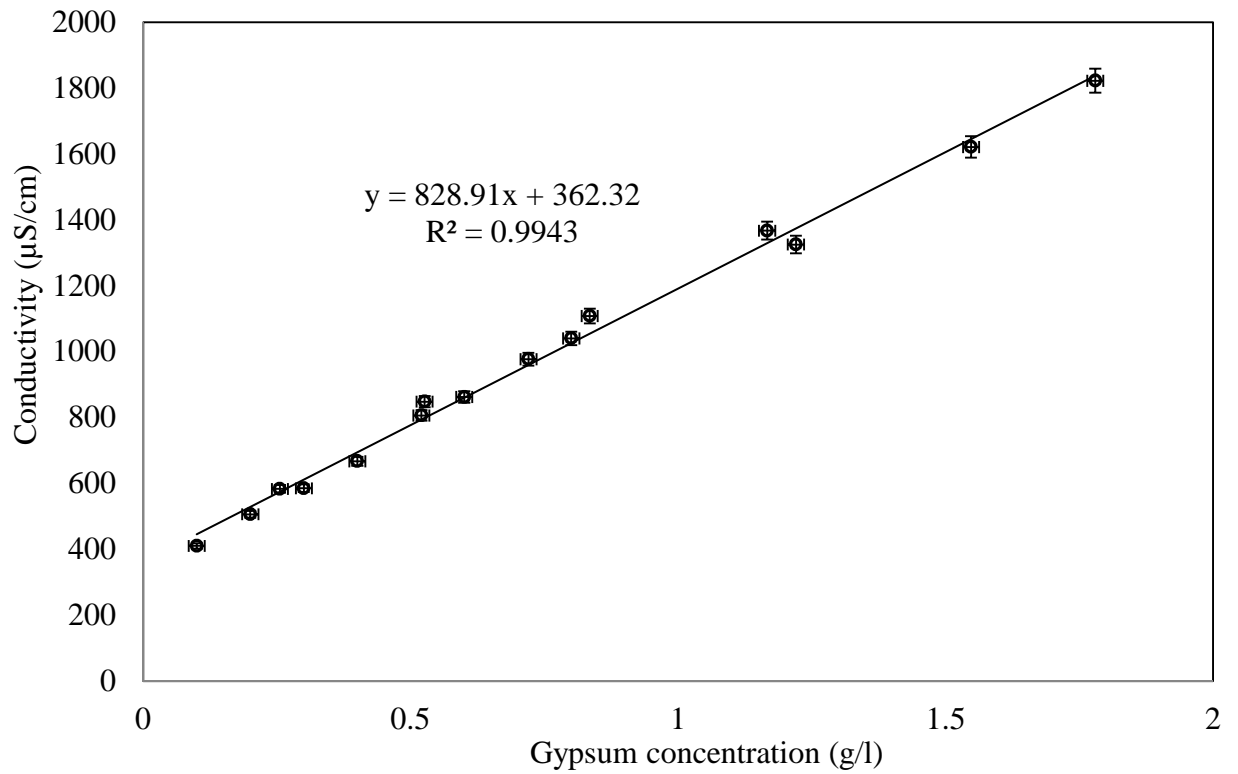


**Figure B.5: Calibration of the water electrical conductivity variation with gypsum dissolution**

## **Appendix C**

---

Comparison of single and two phase mass transfer

## C.1 Two phase test matrix

<b>Water flow rate &amp; <math>V_{\text{superficial}}</math></b>	2.5 [GPM] 0.28 [m/s]	2.5 [GPM] 0.28 [m/s]	2.5 [GPM] 0.28 [m/s]	1.5 [GPM] 0.17 [m/s]	3.5 [GPM] 0.41 [m/s]
<b>Air flow rate &amp; <math>V_{\text{superficial}}</math></b>	25 [SCFM] 22 [m/s]	28 [SCFM] 24.5 [m/s]	35 [SCFM] 29 [m/s]	35 [SCFM] 29.5 [m/s]	35 [SCFM] 28.7[m/s]
<b>Void fraction</b> (Martinelli's model)	0.91	0.92	0.93	0.94	0.91

**Table C.1: Test matrix and void fractions estimated based on Martinelli's Model**

[25]

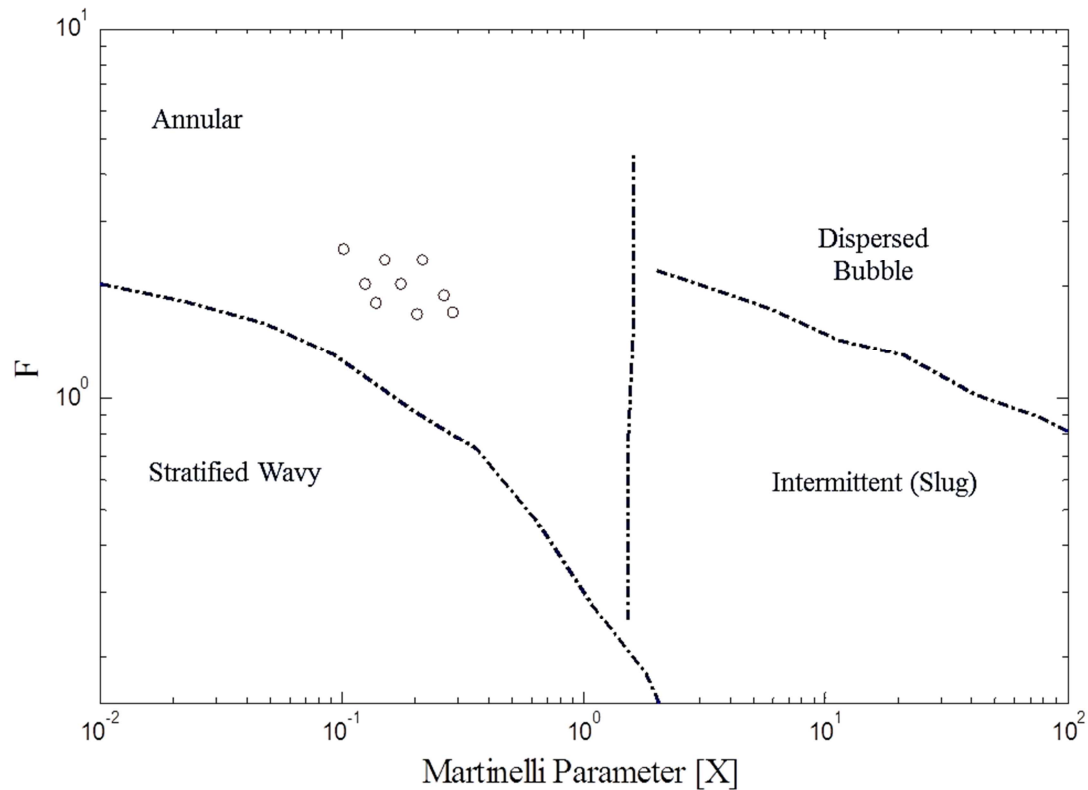


**Figure C.1: Test conditions located on the two phase flow map of Taitel and Duckler (1967)**

## **C.2 Comparison of mass transfer coefficient:**

The  $Sh$  in the straight pipe section obtained for annular two phase flow conditions obtained from the experimental measurements was compared to that for single phase flow at similar average liquid flow velocity and Reynolds number. The  $Sh$  for single phase flow was obtained from the straight pipe correlation, of Blumberg (1970), at the same average liquid velocity as the estimated annular liquid film velocity, similar to Wang et.

al (2002), assuming only liquid exists in the pipe cross section. The comparison shows approximately 30-50% increase in  $Sh$  for the two phase flow compared to the single phase flow as shown in figure C.2. This increase could be attributed to the effect of the liquid film waviness in addition to the process of liquid droplets deposition and re-entrainment to and from the liquid film. The latter may result in penetration of the liquid viscous sublayer which could affect the mass transfer rate from the wall. The Reynolds number for the annular two phase flow was based on the pipe diameter since the mass transfer occurs only on the interface between the liquid and the pipe wall.

$$Re_{single\ phase} = \frac{\rho v D_{pipe}}{\mu} \quad and \quad Re_{two\ phase} = \frac{\rho v_{film} D_{pipe}}{\mu}$$

This comparison requires measurement of the wall shear stress, since the single and two phase flow conditions were claimed to have the same  $Sh$  for the same shear stress by Wang et. al (2002).

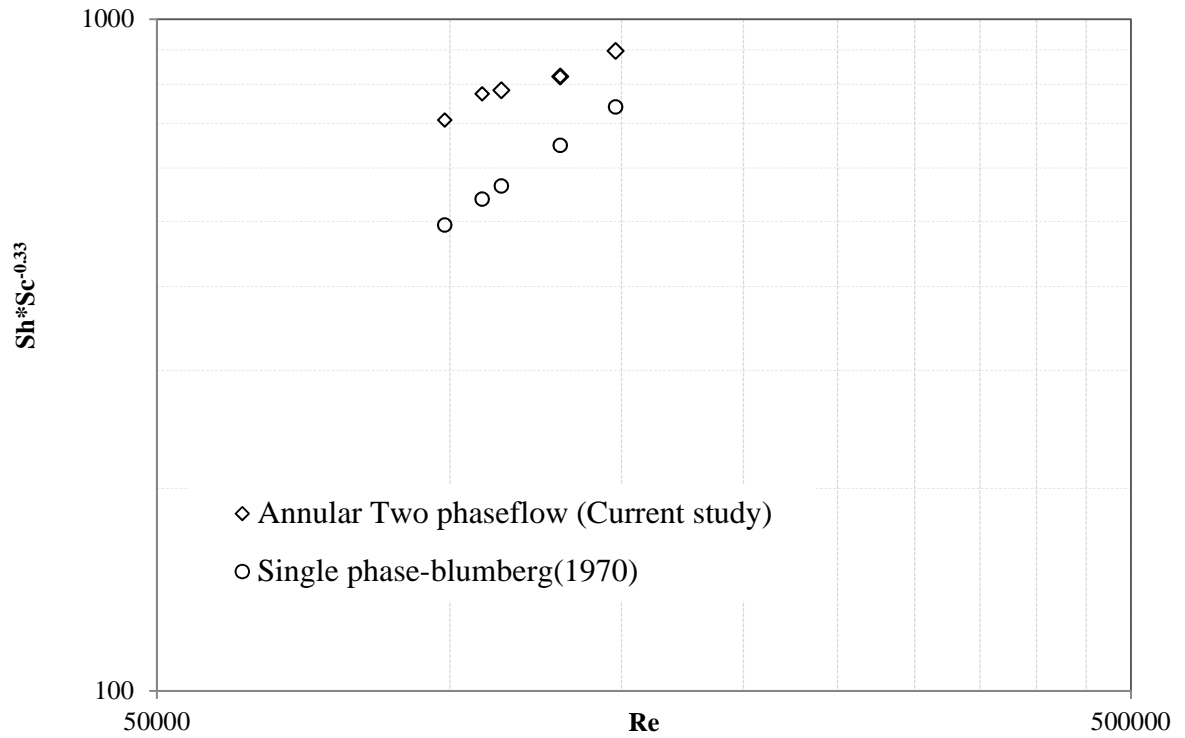


**Figure C.2: Comparison of the mass transfer coefficient for single and two phase flow in a straight pipe**

## **Appendix D**

### Processing Matlab Routines

## D.1 Subtracting the original cloud from an ideal mathematical model of the shape

```

close all
clear all
clc

load C:\Research\Analysis\Singlebend\ext40.txt
cloud=ext40;
cloudnew=sortrows(cloud,1);
x=(-cloudnew(:,1))/25.4;
y=-(38.1+cloudnew(:,2))/25.4;
z=(-50.8+cloudnew(:,3))/25.4;

transcloud=[x,y,z].*25.4;
dlmwrite('C:\Research\Analysis\Singlebend\Trans\transcloudext40.txt', transcloud, 'delimiter', '\t');
ans1='done transformation'

%% %%% Define the domain of every segment
j=0;
k=0;
l=0;
p=0;
v=0;
for i=1:length(x);
    if 0<x(i) & x(i)<=7.985;
        j=j+1;
        xpipeup(j)=x(i);
        ypipeup(j)=y(i);
        zpipeup(j)=z(i);
    end;
    if 8<x(i) & y(i)<=1.5;
        k=k+1;
        xbend1(k)=x(i);
        ybend1(k)=y(i);
        zbend1(k)=z(i);
    end;
    if 1.5<y(i)& y(i)<=6.5;
        l=l+1;
        xseppipe(l)=x(i);
        yseppipe(l)=y(i);
    end;
end;

```



```

pipeup=[thetapipeup;Lpipeup;deltapipeup];
bend1=[thetabend1;Lbend1;deltabend1];
seppipe=[thetaseppipe;Lseppipe;deltaseppipe];

%%% Write the output file
map=[pipeup;bend1;seppipe];
dlmwrite('C:\Research\Analysis\Singlebend\map40ext.txt', map, 'delimiter', '\t');
\t');

```

## D.2 Re-gridding the output of the first step into a uniform grid

```

%this program regrids the data and writes the output to the file called
%output.out

load C:\Research\Analysis\Singlebend\map40ext.txt %%%%%%%%% reads the file to 'matrix
matrix=map40ext;
cc = 120;
% input('Enter the number of angle subdivisions: '); %angle subdivision is about 100-150
thetastarting = -75;
% input('Enter the starting angle: '); %starting about is about 5 degrees.
rr =2000;
% input('Enter the number of length subdivisions: '); %length subdivision is about 600
zstarting = 0.1;
%input('Enter the starting z location (should be negative: '); %the starting z location is about-0.05
zending = 15.3;
%input('Enter the ending z location (should be negative: '); %the starting z location should be a bit
less than the actual length of the pipe

zgap = (-zending+zstarting)/rr;
thetaending = 150+ thetastarting;
thetagap = (thetaending-thetastarting)/cc;
rpipe = 0.5; %radius of the test pipe is 0.5 inches

dt = thetagap/2; %small change in theta angle
dz = zgap/2; %small change in z direction

theta = matrix(:,1);
zcart = matrix(:,2);

```



### D.3 Check the alignment of the samples scans based on symmetry of the upstream pipe surface topography

```

close all
clear all
clc
load C:\Research\Analysis\Singlebend\cont\contour40ext.txt
load C:\Research\Analysis\Singlebend\trans\transcloud40ext.txt
tic
%% left to right correction
ans='done loading'
a=0;
for gg=1:20;
a=a+1;
nn=length(contour40ext);
contour60up=contour40ext;
theta=contour60up(:,1);
L=contour60up(:,2);
delta60=contour60up(:,3);
L1=1039*120/2;L2=((309*120)/2)+L1;L3=length(L);    %% L1 need to be modified in the new analysis
to (761*120)
ans='make sure you correct L s for the good scanned samples'

%%%%%%%%%%%%%%%%%%%%%%%%%%%%%%%%%%%%%%%%%%%%%%%%%%%%%%%%%%%%%%%%%%%%%%%% part1 %%%%%%%%%%%%%
x_raw60(1:L1)=(0.5+delta60(1:L1)).*sin(theta(1:L1)*pi/180);
y_raw60(1:L1)=(0.5+delta60(1:L1)).*cos(theta(1:L1)*pi/180);
ycl60(1:L1)=y_raw60(1:L1);
z_raw60(1:L1)=L(1:L1);

%%%%%%%%%%%%%%%%%%%%%%%%%%%%%%%%%%%%%%%%%%%%%%%%%%%%%%%%%%%%%%%%%%%%%%%% part2 %%%%%%%%%%%%%
phi(L1+1:L2)=(L(L1+1:L2)-3.35)*180/(1.5*pi);
Inplane60(L1+1:L2)=(0.5+delta60(L1+1:L2)).*cos(theta(L1+1:L2)*pi/180);
x_raw60(L1+1:L2)=(0.5+delta60(L1+1:L2)).*sin(theta(L1+1:L2)*pi/180);
y_raw60(L1+1:L2)=(1.5+Inplane60(L1+1:L2)).*cos(phi(L1+1:L2)*pi/180);
z_raw60(L1+1:L2)=(1.5+Inplane60(L1+1:L2)).*sin(phi(L1+1:L2)*pi/180);
R60(L1+1:L2)=(y_raw60(L1+1:L2).^2+z_raw60(L1+1:L2).^2).^0.5;
ycl60(L1+1:L2)=R60(L1+1:L2)-1.5;

```

```
%%%%%%%%%%%%%%%%%%%%%%%%%%%%%%%%%%%%%%%%%%%%%%%%%%%%%%%%%%%%%%%%%%%%%%%% part3 %%%%%%%%%%%%%%%%%%%%%%%%%%%%%%%%%%%%%%%%%%%%%%%%%%%%%%%%%%%%%%%%%%%%%%%%%
```

```
x_raw60(L2+1:L3)=(0.5+delta60(L2+1:L3)).*sin(theta(L2+1:L3)*pi/180);
y_raw60(L2+1:L3)=(0.5+delta60(L2+1:L3)).*cos(theta(L2+1:L3)*pi/180);
ycl60(L2+1:L3)=y_raw60(L2+1:L3);
z_raw60(L2+1:L3)=L(L2+1:L3);
```

```
%%%%%%%%%%%%%%%%%%%%%%%%%%%%%%%%%%%%%%%%%%%%%%%%%%%%%%%%%%%%%%%%%%%%%%%% estimate the deviation of the
mean
```

```
%%%%%%%%%%%%%%%%%%%%%%%%%%%%%%%%%%%%%%%%%%%%%%%%%%%%%%%%%%%%%%%%%%%%%%%% from Zero
```

```
sample=20;
k=0;
f=1;
for i=5:120:nn;
    if i>(nn-120);
        break;
    end;

    for j=i:i+sample;
        k=k+1;
        xleft60(k,f)=contour60up(j,3);
        if f==floor(nn/120);
            break;
        end
        if k>=sample;
            k=0;
            f=f+1;
        end;
    end;
end;
k=0;
f=1;
for i=87:120:nn;
    if i>(nn-120);
        break;
    end;
    for j=i:i+sample;
        k=k+1;
        xright60(k,f)=contour60up(j,3);
```

```

    if f==floor(nn/120);
        break;
    end

    if k>=sample;
        k=0;
        f=f+1;
    end;
end;
end;

dev60=xright60-xleft60;

avgdev60=mean(dev60);

for count=1:nn/120;
    phi1(count)=[0+count*0.0155];
end;

figure (a);
subplot 311;
AXIS([0 15.7 -0.05 0.05]);
hold all
plot(phi1,avgdev60);
p1 = polyfit(phi1,avgdev60,1);
yfit60= [polyval(p1,phi1)];
plot(phi1,yfit60);

%%%%%% correct for the mean dev.
xshift60=yfit60(500)/1.75;
x_raw60new=x_raw60-xshift60;
r60=(x_raw60new.^2+y160.^2).^0.5;
delta60new=r60-0.5;
contour60new=[theta,L,delta60new'];

%%%%%% estimate the local error in the cross-wise direction
k=0;
f=1;
for i=5:120:nn;
    if i>(nn-120);

```

```
    break;
end;

for j=i:i+sample;
    k=k+1;
    xleft60new(k,f)=contour60new(j,3);
    if f==floor(nn/120);
        break;
    end;
    if k>=sample;
        k=0;
        f=f+1;
    end;
end;
end;
k=0;
f=1;
for i=87:120:nn;
    if i>(nn-120);
        break;
    end;
    for j=i:i+sample;
        k=k+1;
        xright60new(k,f)=contour60new(j,3);
        if f==floor(nn/120);
            break;
        end;

        if k>=sample;
            k=0;
            f=f+1;
        end;
    end;
end;
dev60new=xright60new-xleft60new;
avgdev60new=mean(dev60new);

figure(a)
subplot 312;
AXIS([0 15.7 -0.05 0.05]);
hold all
plot(phi1,avgdev60new);
```

```

p5 = polyfit(phi1,avgdev60new,50);
yfit60new= [polyval(p5,phi1)];
plot(phi1,yfit60new);
%%%%%%%%%%%%%%%%%%%%%%%%%%%%%%%%%%%%%%%%%%%%%%%%%%%%%%%%%%%%%%%%%%%%%%%%
%%%%%%%%%%%%%%%%%%%%%%%%%%%%%%%%%%%%%%%%%%%%%%%%%%%%%%%%%%%%%%%%%%%%%%%%
% yfit60new=yfit60new';

i=1;
for j=1:nn-119;
    x60(1,j)=x_raw60new(1,j)-yfit60new(1,i);
    if rem(j,120)==0;
        i=i+1;
    end;
end;

%%%%%%%%%%%%%%%%%%%%%%%%%%%%%%%%%%%%%%%%%%%%%%%%%%%%%%%%%%%%%%%%%%%%%%%% trimming loop
thetaneu=[];
yclnew60=[];
Lnew=[];
for i=1:length(x60);
    yclnew60(i)=ycl60(i);
    thetaneu(i)=theta(i);
    Lnew(i)=L(i);
end;

yclnew60=yclnew60';
thetaneu=thetaneu';
Lnew=Lnew';
x60=x60';
r60=(x60.^2+yclnew60.^2).^0.5;
delta60correct=r60-0.5;
cont60upcorrect=[];
cont60upcorrect=[thetaneu,Lnew,delta60correct];
delta60correct=[];

% cont60upcorrect=cont60upcorrect';
% dlmwrite('contunworncorrect2.txt', cont60upcorrect, 'delimiter', '\t');

%%%%%%%%%%%%%%%%%%%%%%%%%%%%%%%%%%%%%%%%%%%%%%%%%%%%%%%%%%%%%%%%%%%%%%%%

nnn=length(x60);

```

```
for count=1:floor(nnn/120);
    phi2(count)=[0+count*0.0155];
end;
k=0;
f=1;
for i=5:120:nnn;
    if i>(nnn-119);
        break;
    end;

    for j=i:i+sample;
        k=k+1;
        xleft60correct(k,f)=cont60upcorrect(j,3);

        if f==floor(nnn/120);
            break;
        end;
        if k>=sample;
            k=0;
            f=f+1;
        end;
    end;
end;
k=0;
f=1;
for i=87:120:nnn;
    if i>(nnn-119);
        break;
    end;

    for j=i:i+sample;
        k=k+1;
        xright60correct(k,f)=cont60upcorrect(j,3);

        if f==floor(nnn/120);
            break;
        end;
        if k>=sample;
            k=0;
            f=f+1;
        end;
    end;
end;
```

```

end;

dev60correct=[];
avgdev60correct=[];
dev60correct=xright60correct-xleft60correct;
avgdev60correct=mean(dev60correct);

%%%%%%%%%
figure(a);
subplot 313;
hold all
AXIS([0 15.7 -0.05 0.05]);
plot(phi2,avgdev60correct);
p5 = polyfit(phi2,avgdev60correct,10);
yfit60correct= [polyval(p5,phi2)];
plot(phi2,yfit60correct);

%%%%%%%%%
x60=x60';
i=1;
for j=1:nn-120;
    x260(1,j)=x60(1,j)-yfit60correct(1,i);
    if rem(j,120)==0;
        i=i+1;
    end;
end;

end;

yclnew260=[];
thetane2=[];
Lnew2=[];
for i=1:length(x260);
    yclnew260(i)=ycl60(i);
    thetane2(i)=theta(i);
    Lnew2(i)=L(i);
end;

yclnew260=yclnew260';
thetane2=thetane2';
Lnew2=Lnew2';
x260=x260';

```

```

r260=(x260.^2+yclnew260.^2).^0.5;
delta60corrected=r260-0.5;
cont60upcorrected=[];
cont60upcorrected=[thetaneu2,Lnew2,delta60corrected];
delta60corrected=[];
x60=[];x260=[];
yclnew60=[];yclnew260=[];

% filename=['cont40L2R' num2str(gg) '.txt'];
numg=num2str(gg);
dlmwrite(['C:\Research\Analysis\Singlebend\cont\cont40extcorrect.txt'], cont60upcorrected, 'delimiter',
'\t','precision',3);

%% streamwise tilt
L1inch=floor((1/0.0155)*120);
k=0;
f=1;
for i=5:120:(L1-1*L1inch);
    if i>((L1-1*L1inch)-119);
        break;
    end;
    for j=i:i+sample;
        k=k+1;
        xleft60tilt(k,f)=cont60upcorrected(j,3);

        if f==floor((L1-1*L1inch)/120);
            break;
        end;
        if k>=sample;
            k=0;
            f=f+1;
        end;
    end;
end;
k=0;
f=1;
for i=80:120:(L1-1*L1inch);
    if i>((L1-1*L1inch)-119);
        break;
    end;
    for j=i:i+sample;

```

```

k=k+1;
xright60tilt(k,f)=cont60upcorrected(j,3);

if f==floor((L1-1*L1inch)/120);
    break;
end;
if k>=sample;
    k=0;
    f=f+1;
end;
end;
end;

%%%% top
k=0;
f=1;
for i=60:120:(L1-1*L1inch);
    if i>((L1-1*L1inch)-119);
        break;
    end;
    for j=i:i+sample;
        k=k+1;
        xtop60tilt(k,f)=cont60upcorrected(j,3);
        if f==floor((L1-1*L1inch)/120);
            break;
        end;
        if k>=sample;
            k=0;
            f=f+1;
        end;
    end;
end;
%%
tilt60=xtop60tilt-((xright60tilt+xleft60tilt)/2);
tilt60all=[tilt60];
avgtilt60=mean(tilt60all);
phi3=(phi2(floor(L1inch/120):(floor((L1-1*L1inch)/120))));

%%%%%%%%%% plot the trend
c=a+5;
figure (c);
AXIS([0 15.7 -0.05 0.05]);

```

```

hold on
plot(phi3,avgtilt60(floor(L1inch/120):(floor((L1-1*L1inch)/120))),',' );
p6 = polyfit(phi3,avgtilt60(floor(L1inch/120):(floor((L1-1*L1inch)/120))),1);
yfit60tilt= [polyval(p6,phi2)];
plot(phi2,yfit60tilt);
title('axi-symmetry deviation in upstreamand downstreampipe','fontsize',15,'fontname','Times New Roman');
xlabel('Streamwise length [inch]','fontsize',15,'fontname','Times New Roman');
ylabel('deviation [inch]','fontsize',15,'fontname','Times New Roman');

yzero=p6(2)*25.4;
tiltang=(atan(p6(1)))*(180/pi)*3;
str1 = (['Streamwise tilt angle=',num2str(tiltang)]);
str2=([' & Streamwise shift=',num2str(p6(2))]) ;
text(7.5,-0.025,str1,'FontSize',14,'fontname','Times New Roman');
text(7.5,-0.035,str2,'FontSize',14,'fontname','Times New Roman');
h=gca;
set(h,'FontSize',15)
hold off

%%%%%% correct the tilt
x=transcloud40ext(:,1); y=transcloud40ext(:,2);z=transcloud40ext(:,3);
tilt=tiltang*(pi/180);
shift=yzero*3;
R=((x.^2+y.^2).^0.5)*tilt;
deltax=(R*sin(tiltang));
deltay=R*cos(tiltang);

ycorr=y+deltay+shift;
xcorr=x+deltax;
transcloud40ext=[];
transcloud40ext=[xcorr,ycorr,z];

if gg==19;
    dlmwrite('C:\Research\Analysis\Singlebend\trans\transcloud40ext2.txt', transcloud40ext, 'delimiter', '\t');
    break;
end;
if abs(tiltang)<=0.002;
    dlmwrite('C:\Research\Analysis\Singlebend\trans\transcloud40ext2.txt', transcloud40ext, 'delimiter', '\t');
    break;
end;

```

```

%% Re-analyzing
ans='Re-analyzing....'
cloud=transcloud40ext;
x=((cloud(:,1))/25.4);
y=((cloud(:,2))/25.4);
z=((cloud(:,3))/25.4);

ans1='done transformation'
j=0;
k=0;
l=0;
p=0;
v=0;
for i=1:length(x);
    if 0<x(i) & x(i)<=7.985;
        j=j+1;
        xpipeup(j)=x(i);
        ypipeup(j)=y(i);
        zpipeup(j)=z(i);
    end;
    if 8<x(i) & y(i)<=1.5;
        k=k+1;
        xbend1(k)=x(i);
        ybend1(k)=y(i);
        zbend1(k)=z(i);
    end;
    if 1.5<y(i)& y(i)<=6.5;
        l=l+1;
        xseppipe(l)=x(i);
        yseppipe(l)=y(i);
        zseppipe(l)=z(i);
    end;
end;

ans='done decomposition'
%%%%%%%%%% Pipe up
xpipeupc=xpipeup;
ypipeupc=ypipeup-0.02;
zpipeupc=(zpipeup)+0.01;
thetaslopepipeup=(zpipeupc./ypipeupc);

```

```

thetapipeup=(((atan(thetaslopepipeup)).*(180/pi)));
rpipe=(zpipeupc.^2+ypipeupc.^2).^0.5;
deltapipeup=rpipe-0.50;
Lpipeup=0+xpipeupc;

```

```

%%%%%%%%%%%%%%%%%%%%%%%%%%%%%%%%%%%%%%%%%%%%%%%%%%%%%%%%%%%%%%%%%%%%%%%%%% First bend

```

```

xbend1c=xbend1-8.0;
ybend1c=ybend1-1.5;
zbend1c=zbend1+0.01;
Rbend1=(xbend1c.^2+ybend1c.^2).^0.5;
yclbend1=1.5-Rbend1;
phiislopebend1=(xbend1c./ybend1c);
phibend1=abs(atan(phiislopebend1)).*(180/pi);
thetaslopebend1=(zbend1c./yclbend1);
thetabend1=(atan(thetaslopebend1)).*(180/pi);
rbend1=(yclbend1.^2+zbend1c.^2).^0.5;
deltabend1=rbend1-0.500;
Lbend1=8+(phibend1*1.5*pi/180);

```

```

%%%%%%%%%%%%%%%%%%%%%%%%%%%%%%%%%%%%%%%%%%%%%%%%%%%%%%%%%%%%%%%%%%%%%%%%%% Separation pipe segment

```

```

xseppipec=xseppipe-9.5;
yseppipec=yseppipe-1.5;
zseppipec=zseppipe+0.01;
thetaslopesepipe=(zseppipec./-xseppipec);
thetaseppipe=(atan(thetaslopesepipe)).*(180/pi);
rseppipe=(zseppipec.^2+xseppipec.^2).^0.5;
deltaseppipe=rseppipe-0.50;
Lbend1end=max(Lbend1);
Lseppipe=10.356+yseppipec;

```

```

ans2='Done subtraction'

```

```

%%%%%%%%%%%%%%%%%%%%%%%%%%%%%%%%%%%%%%%%%%%%%%%%%%%%%%%%%%%%%%%%%%%%%%%%%%

```

```

pipeup=[thetapipeup;Lpipeup;deltapipeup];
bend1=[thetabend1;Lbend1;deltabend1];
seppipe=[thetaseppipe;Lseppipe;deltaseppipe];

```

```

%%%%%%%%%%%%%%%%%%%%%%%%%%%%%%%%%%%%%%%%%%%%%%%%%%%%%%%%%%%%%%%%%%%%%%%%%%

```

```

pipeup=pipeup';

```

```

bend1=bend1';
seppipe=seppipe';
%%%%%%%%%%

map=[pipeup;bend1;seppipe];
%% Re-Gridding
matrix=map;

cc = 120;
% input('Enter the number of angle subdivisions: '); %angle subdivision is about 100-150
thetastarting = -75;
% input('Enter the starting angle: '); %starting about is about 5 degrees.
rr=1000;
% input('Enter the number of length subdivisions: '); %length subdivision is about 600
zstarting = 0.1;
%input('Enter the starting z location (should be negative): '); %the starting z location is about-0.05
zending = 15;
%input('Enter the ending z location (should be negative): '); %the starting z location should be a bit
less than the actual length of the pipe

zgap = (-zending+zstarting)/rr;
thetaending = 150+ thetastarting;
thetagap = (thetaending-thetastarting)/cc;
rpipe = 0.5; %radius of the test pipe is 0.5 inches

dt = thetagap/2; %small change in theta angle
dz = zgap/2; %small change in z direction

theta = matrix(:,1);
zcart = matrix(:,2);
wear = matrix(:,3);

%r = sqrt(xcart.*xcart+ycart.*ycart);
%theta = acosd(xcart./r);

%formulate zetta gridding matrix
zgridding = zeros(rr,cc);
for i = 1:cc
    zgridding(:,i) = linspace(zstarting,zending,rr)';
end

```

```

%formulate theta gridding matrix
thetagridding = zeros(rr,cc);
for i = 1:rr
    thetagridding(i,:) = linspace(thetastarting,thetaending,cc);
end

worn = griddata(zcart,theta,wear,zgridding,thetagridding); %triangle-based linear interpolation is the
default

%interpolating the radius by averaging the radius within the cell.
%zgridding-+ dz and thetagridding-+ dt
for i = 1:rr
    for j = 1:cc
        ind = find(zgridding(i,j)-dz<zcart & zcart<zgridding(i,j)+dz & thetagridding(i,j)-dt<theta &
theta<thetagridding(i,j)+dt);
        if ind > 0
            worn_ave(i,j) = sum(wear(ind))/length(ind);
        else
            worn_ave(i,j) = worn(i,j);
        end;
    end;
end;

zettavector = reshape(zgridding',rr*cc,1);
thetavector = reshape(thetagridding',rr*cc,1);
worn_avevector = reshape((worn_ave)',rr*cc,1);

outputmatrix = [thetavector, zettavector, worn_avevector];

contour40ext=outputmatrix;
xleft60new=[];xright60new=[];xleft60correct=[];xright60correct=[];
xleft60tilt=[];xright60tilt=[];xtop60tilt=[];xleft60tiltd=[];xright60tiltd=[];xtop60tiltd=[];
end;

```

## D.4 Calculate the mass removal rate and mass transfer coefficients

```

clc
clear all
close all

```

```

load C:\Research\Analysis\Singlebend\contunworncorrectext.txt
load C:\Research\Analysis\Singlebend\contunworncorrectint.txt
load C:\Research\Analysis\Singlebend\contextcorrected.txt
load C:\Research\Analysis\Singlebend\contintcorrected.txt

%% bulk concentration
load C:\Research\Analysis\Singlebend\bconc.txt

%%
bconc=bconc;

ans='done loading'
% Enter the total length of the input file
mm=length(contextcorrected);
nn=length(contintcorrected);

% Please assure the file names are placed right
time0int=contunworncorrectint; time0ext=contunworncorrectext; t0=0;
time1=contextcorrected; t1=[0 14]; ynew1=[time0ext time1(1:mm,3)]*0.0254*1500;
time2=contintcorrected; t2=[0 17]; ynew2=[time0int time2(1:mm,3)]*0.0254*1500;

%% %%% Develop the integral of the concentration difference trend equation
cwMINUSCb=2.4-bconc(:,2);
cwMINUSCb=2.4-bconc(:,2);
recordtime=bconc(:,1); %%% %%% %%% %%% set the testing time and recording
intervals

p1=polyfit(recordtime,cwMINUSCb,2); %%% %%% second order suggestion

init1=(((p1(1))/3)*t1.^3)+(p1(2))*t1.^2+(p1(3))*t1; %%% %%% Integral of the second order
init2=(((p1(1))/3)*t2.^3)+(p1(2))*t2.^2+(p1(3))*t2;

%% %%% %%% Calculate the rate of mass removal
y2new=[];
C1=[];C2=[]; C3=[];C4=[];
M1=[];M2=[];M3=[];M4=[];
X1=[];
Y1=[];

```

```
for i=1:mm;

    X1=[ones(2,1) init1(1:2)];
    X2=[ones(2,1) init2(1:2)];

    Y1=ynew1(i,1:2);
    Y2=ynew2(i,1:2);

    SOL1=X1\Y1; SOL2=X2\Y2;
    m1=SOL1(1); m2=SOL2(1);
    c1=SOL1(2); c2=SOL2(2);
    M1=[M1 m1]; M2=[M2 m2];
    C1=[C1 c1]; C2=[C2 c2];

end;

%% %% % Calculate the Sherwood number matrix
sh1=C1'*(0.0254)/6.49e-10/(60);
sh2=C2'*(0.0254)/6.49e-10/(60);

%% Write the output matrix
zet=time1(1:mm,1);
fi=time1(1:mm,2);

K1= [zet, fi, sh1];
K2= [zet, fi, sh2];

dlmwrite('C:\Research\Analysis\Singlebend\Shext.txt', K1, 'delimiter', '\t');
dlmwrite('C:\Research\Analysis\Singlebend\Shint.txt', K2, 'delimiter', '\t');
```

## **References**

---

- Achenbach, E. "Mass Transfer From Bends of Circular Cross Section to Air." *Future Energy Production Systems* 1 (1976): 327-337.
- Allen, J. R. L. "Note on the Use of Plaster of Paris In Flow Visualization and Some Geologocal Applications." *Journal of Fluid Mechanics* 25, no. 2 (1966): 331-335.
- Benoit Villien, Zheng, Y., Lister, D. H. "The Scalloping Phenomenon and its Significance in flow Assisted Corrosion." *Twenty sixth annual CNS-CNA student conference*, (2001).
- Berger, F.P. and Hau, K.F.F.L. "Mass Transfer in Turbulent Pipe Flow Measured by The Electrochemical Method." *International Journal of Heat and Mass Transfer* 20 (1977): 1185-1194.
- Blumberg. "Periodic Dissolution Profiles Resulting from The Interaction of the Soluble Surface and an Adjacent Turbulent Flow." University of Michigan, PhD, Chemical, Engineering, (1970).
- Blumberg, P.N., Curl, R.L. "Experimental and Theoretical Studies of Dissolution Roughness." *Journal of Fluid Mechanics* 65, no. 4 (1974): 735-751.
- Chen X., Mclaury B. S., Shirazi S. A. "Numerical and Experimental Investigation of The Relative Erosion Severity Between Plugged Tees and Elbows in Dilute Gas/Solid Two-Phase Flow ." *Journal of Energy Resources* 128 (2006): 70-78.
- Chen, J.C. "Correlation for Boiling Heat Transfer to Saturated Fluids in Convective Flow." *Industrial & Engineering Chemistry Process Design and Development* 5 (1966): 322-329.
- Coney, M. "Erosion Corrosion: The Calculation of Mass Transfer Coefficients." *CERL Report RD/L/N197*, (1980).
- Crawford, N. M., Cunningham, G., and Spedding, P. L., "Prediction of Pressure Drop for Turbulent Fluid Flow in 90° Bends," *Proceedings of the Institution of Mechanical Engineers*, Vol. 217, No. 3, 2003, pp. 153-155.

- Da Silva Lima, R. J., Thome, J. R., "Two-phase flow patterns in U-bends and their contiguous straight tubes for different orientations, tube and bend diameters" *International Journal of Refrigeration* 35, 1439-1454, 2012
- Dawson, D.A. and Trass, D. "Mass Transfer at Rough Surfaces." *International Journal of Heat and Mass Transfer* 15 (1972): 1317-1336.
- De Kerpel, K., Ameel B., Caniere H., De Paepe M., "Study of two phase flow in hairpins by means of image processing and pressure drop measurements", *Multiphase Flow in Industrial Plants, 12th International Conference Proceedings*, 2011
- Dooley, R. B., Mathews, J., "The Current State of Cycle Chemistry for Fossil Plants." *Fifth International Cycle Chemistry Conference*. EPRI TR-108469, (1997).
- Doorly, D., Sherwin, S.J. "Geometry and flow, Cardiovascular Mathematics: Modeling and Simulation of the circulatory System." *Springer*, (2009).
- El-Gammal, M., Mazhar, H., Cotton, J.S., and Ching, C. Y. "Flow Accelerated Corrosion in Piping Components Under single and two phase flow conditions." *COG report*, (2010).
- El-Gammal, M., Mazhar, H., Cotton, J.S., Schefski, C., Pietralik, J. and Ching, C. Y. "The Hydrodynamic Effects of Single Phase Flow on Flow Accelerated Corrosion in a 90 degree elbow." *Journal of Nuclear Engineering and Design* 240 (2010): 1589-1598.
- Elliot, A. J., Goding, M. S., Walker, Z. H. "In-Reactor Loop Experiments to Study the Impact of coolant PH on the Flow Accelerated Corrosion of Carbon Steels with Varying Chromium Concentrations under CANDU HTS Conditions." *Proceeding of the international conference on water chemistry of Nuclear systems* 1446, EPRI, (2004).
- Enayet, M. M., Gibson M.M., Yianneskis, M. "Laser Doppler Measurements for Laminar and Turbulent Flow in Pipe Bend." *International Journal of Heat and Fluid Flow* 3 (1982): 213-220.
- Hassan, Y. A., Schmidt, W., Ortiz-Villafuerte, J. "Investigation of Three-Dimensional Two-Phase Flow." *Measurement Science Technology* 9 (1998): 309-326.

- Henzel, N., Crosby, D. C., Eley, S. R. "Erosion/Corrosion in Power Plants Single and Two Phase Flow Experience, Predictions." *NDE management*, (1990).
- Hetiz, E. "Mechanistically Based Prevention Strategies of Flow-Induced Corrosion." *Electrochimica Acta* 41, no. 4 (1996): 503-509.
- Homicz, Gregory, F. "Computational fluid Dynamics Simulations of Pipe Elbow Flow." New Mexico and Livermore: *Sandia National Laboratories Albuquerque*, (2004).
- Jayattilleke, C. L. V. "Progress in Heat and Mass Transfer." *International journal of heat and mass transfer*, (1971).
- Jepson, W. P. "Modelling the Transition to Slug Flow in Horizontal Conduit." *Canadian Journal Of Chemical Engineering* 67-(1989): 731-740.
- John, P. S., Tracy, S., Gendron. "Flow Accelerated Corrosion and Cracking of Carbon Steel in primary Water- Operating Experience at the Point Lepreau Generating Station." *Proceedings of the 12th International Conference on Environmental degradation of Materials in Nuclear Power Systems*. (2005).
- Kanster, W., Erve, M., Henzel, N., and Stellwag, B. "Calculation Code for Erosion-Corrosion Induced Wall Thinning in Piping System." *Nuclear Engineering and Design* 119 (1990): 431-438.
- Kastner, W., Nopper, N., Resiner. "Protection of Piping From Corrosion Erosion." *Atomic Energy* 75 (4), (1993): 791-799.
- Kim, S., Park, J. H., Kojasoy, G., Kelly, J. M., Marshall, S. O. "Geometric Effects of 90-Degree Elbow in the Development of Interfacial Structures in Horizontal Bubbly flow." *Journal of Nuclear Engineering and Design* 237 (2007): 2105-2113.
- Kutateladze, S.S. "Problems of Heat Transfer and Hydraulics of Two Phase Media." (Pergamon Press, Oxford) (1969).
- Maddock, C. Lacy, P. M. C. Patrick, M. A. "The Structure of Two Phase Flow in a Curved Pipe." *Journal of Chemical Engineering Symposium* 38 (1974).

- Niazmand, H., Jaghargh, E.R. "Bend Sweep angle and Reynolds number Effects on Hemodynamics of S-shaped arteries, *Annal of Biomedical Engineering*." 38, no. 9 (2010): 2817-2828.
- Peshkin, M. A. "About the Hydraulic resistance of Pipe Bends to the Flow of Gas-Liquid Mixtures." *Teploenergetika* 8(6), (1961), 79-80.
- Postlethwaite, J. and Lotz, U. "Mass Transfer at Erosion–Corrosion Roughened Surfaces." *Canadian Journal of Chemical Engineering*, (1988): 66-75.
- Postlethwaite, J. "Erosion-Corrosion in Disturbed Two Phase Liquid/Particle Flow." *Corrosion* 35 (1979): 475.
- Poulson, B. "Advances in Understanding Hydrodynamic Effects on Corrosion." *Journal of Corrosion Science* 35, no. 1-4 (1993): 655-665.
- Poulson, B. "Complexities in Predicting Erosion Corrosion." *Wear* 233-235, (1999): 497-504.
- Poulson, B. "Measuring and Modeling Mass Transfer at Bends in Annular Two phase Flow." *Journal of Chemical Engineering Science* 64, no. 4 (1991): 1069-1082.
- Poulson, B., Robinson, R. "The Local Enhancement of Mass Transfer at 180 Degree Bend." *International Journal of heat and mass transfer* 31, no. 6 (1988): 1289-1297.
- Poulson, B., Robinson, R. "The Use of a Corrosion Process to Obtain Transfer Data." *Journal of corrosion science* 26, no. 4 (1986): 265-280.
- Raffel, M., Willert, E., Wereley, S., Kompenhans, J. "Particle Image Velocimetry- A Practical Guide." New York: *Springer*, (2007).
- Raines, M., Thomas Dewers. "Mixed Kinetics Control of Fluid-Rock Interaction in Reservoir Production Scenarios." *Journal of petroleum Science and Engineering* 17, no. 1-2 (1997): 139-155.
- Robinson, J. "Resolving Flow Accelerated Corrosion Problems in the Industrial Steam Plants." *Corrosion* (National Association of Corrosion Engineers) 346 (1999).

- Rütten, F. , Meinke, M. , Schröder, W. "Large-Eddy Simulations of 90° Pipe Bend Flows." *Journal of Turbulence* 2, no. 3 (2001).
- Sleicher, R. H., Notter, C. A. "Fully Developed and Entry Region Heat Transfer Rates." *Chemical Engineering Science* 26 (1971): 161.
- Sparrow, E.M., and Chrysler, G.M. "Turbulent Flow and Heat Transfer in Bends of Circular Cross Section: i- Heat Transfer Experiments." *ASME Journal of Heat Transfer* 108 (1986): 40-47.
- Spedding P.L., Benard, E., Crawford, N.M., "Fluid flow through a vertical to Horizontal 90° elbow III three phase flow" *Dev. Chem. Eng. Min. Process.* 14 (2006)
- Sprague, P.J., Patrick, M.A., Wragg, A.A., Coney, M.W.E. "Mass Transfer and Erosion Corrosion in Pipe Bends." *8th Congress European de Corrosion* 12, no. 2 (November 1985): 19-21.
- Supa-Amronkul, S., Steward Frank, R., Lister Derek H. "Modeling Two-Phase Flow in Pipe Bends." *Journal of Vessel Technology* 127 (2005): 204-209.
- Taylor, A.M.K.P., Whitelaw, J.H. and Yianneskis, M. "Developing Flow in S-shaped Ducts 2: Circular Cross-Section Duct." *NASA Contractor Report*, (1984).
- Tunstall, M. J., Harvey, J. K. "On the Effect of a Sharp Bend in a Fully Developed Turbulent Pipe-Flow." *Journal of Fluid Mechanics* 34, no. 3 (1968): 595-608.
- Usui, K., Aoki, S., Inoue, A., "Flow behavior and pressure drop of two phase flow in C-Shaped bend in vertical plane, Upward flow (I)", *Journal Nuclear Science and Technology*, 17 (12) 875-887, 2008
- Wang, H., Hong, T., Cai, J., Jepson, W. "Enhanced Mass Transfer and Wall Shear Stress in Multiphase Slug Flow." *Corrosion* 02501, (2002).
- Wang, J., Shirazi, S.A. "A CFD Based Correlation for Mass Transfer Coefficient in Elbows." (2001) 44: 1817-1822.
- Weske, J.R. "Experimental Investigation of Velocity Distribution Downstream of a Single Duct Bend." *N.A.C.A, TN no.1471*, (1948).

- Wilkin, S. J., Oates, H.S., Coney, M. "Mass Transfer on Straight Pipes and 90° Bends Measured by the Dissolution of Plaster" (*1st Edn*). *Central Electricity Research Laboratories*, TPRD/L/2469/N83, (1983).
- Yamano, H., Tanaka, M., Murakami, T., Iwamoto, Y., Yuki K., Sago, H., Hayakawa, S. "Unsteady Elbow Pipe Flow to Develop a Flow-Induced Vibration Evaluation Methodology for Japan Sodium-Cooled Fast Reactor." *Journal of Nuclear Science and Technology* 48, no. 4 (2011): 677-687.
- Yoshida, K., Kazuhisa, Y. and Hashimue, H. "Specificity of Flow Structure in a Dual Elbow and its Visualization by PIV Measurement." *Proceedings of the 16th International conference on Nuclear Engineering ICONE 16* (2008): 293- 299.
- Zhao, Y., Markides, N., Matar, O., Hewitt, F., "Disturbance wave development in two-phase gas-liquid upwards vertical annular flow", *International Journal of Multiphase Flow* (55), 111-129, 2013